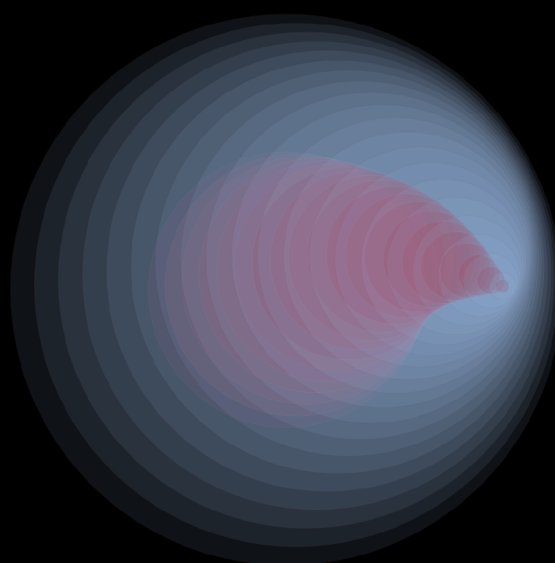
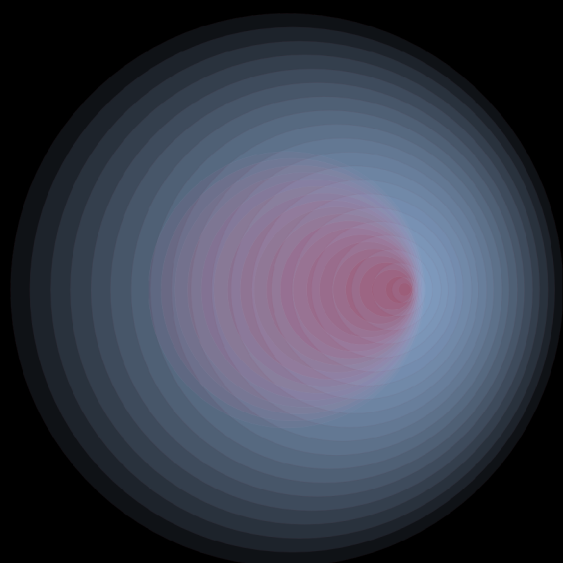
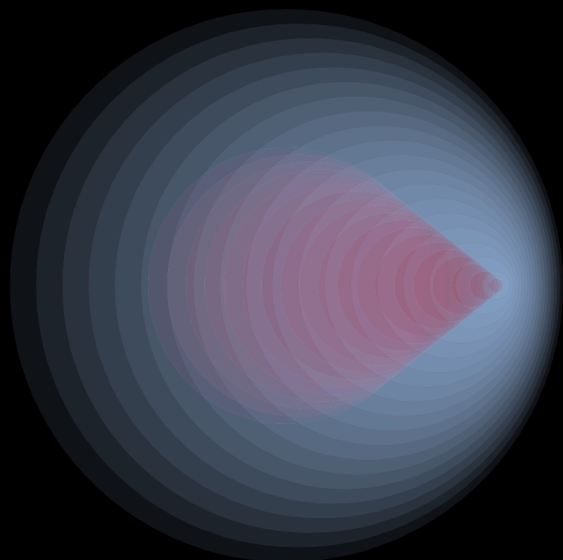
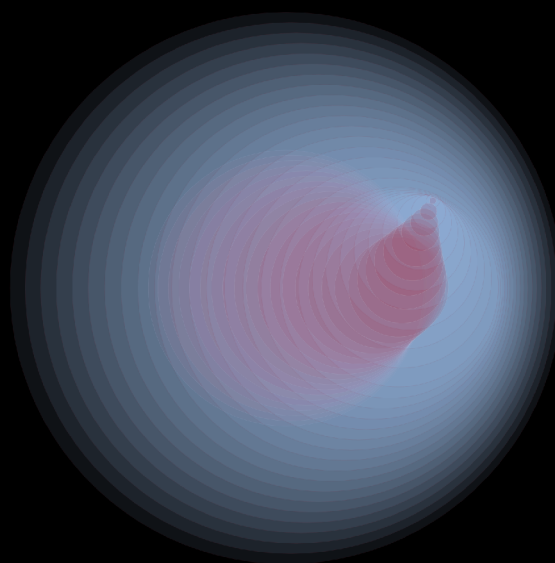
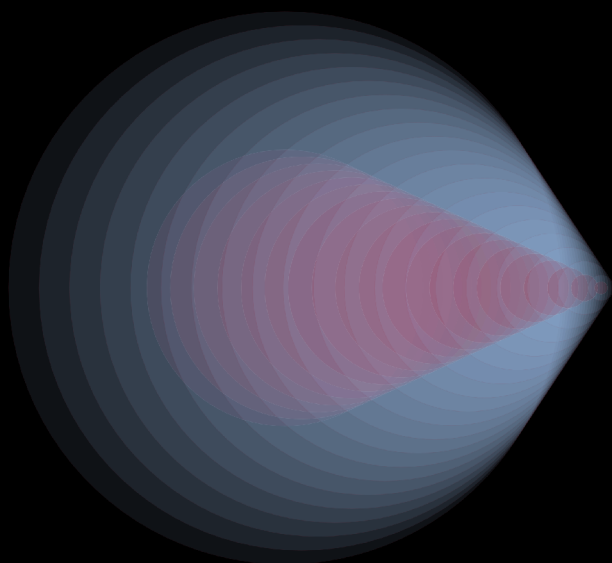


# SUPERSHEAR EARTHQUAKES

THEORY  
EXPERIMENTS  
OBSERVATIONS



HARSHA SURESH BHAT



HABILITATION À DIRIGER DES RECHERCHES  
ÉCOLE NORMALE SUPÉRIEURE



Copyright © 2020 Harsha S. Bhat

SELF PUBLISHED

TUFTE-LATEX.GITHUB.IO/TUFTE-LATEX

Licensed under the Apache License, Version 2.0 (the “License”); you may not use this file except in compliance with the License. You may obtain a copy of the License at <http://www.apache.org/licenses/LICENSE-2.0>. Unless required by applicable law or agreed to in writing, software distributed under the License is distributed on an “AS IS” BASIS, WITHOUT WARRANTIES OR CONDITIONS OF ANY KIND, either express or implied. See the License for the specific language governing permissions and limitations under the License.



# FOREWORD

This manuscript encloses all documents required to obtain a *Habilitation à Diriger des Recherches* from École Normale Supérieure. I have synthesised my research work on supershear earthquakes, listed below, that were conducted over the last 13 years in collaboration with students, postdocs and colleagues at various institutions around the world.

1. Jara, J., L. Bruhat, S. Antoine, K. Okubo, M. Y. Thomas, Y. Klinger, R. Jolivet, and **H. S. Bhat** (2020). “*Signature of supershear transition seen in damage and aftershock pattern*”. *submitted to Nat. Comm.*
2. Amlani, F., **H. S. Bhat**, W. J. F. Simons, A. Schubnel, C. Vigny, A. J. Rosakis, J. Efendi, A. Elbanna, and H. Z. Abidin (2020). “*Supershear Tsunamis and insights from the Mw 7.5 Palu Earthquake*”. *to appear in Nat. Geosci.*
3. Mello, M., **H. S. Bhat**, and A. J. Rosakis (2016). “*Spatiotemporal properties of sub-Rayleigh and supershear rupture velocity fields : Theory and Experiments*”. *J. Mech. Phys. Solids*. DOI: 10.1016/j.jmps.2016.02.031.
4. Mello, M., **H. S. Bhat**, A. J. Rosakis, and H. Kanamori (2014). “*Reproducing The Supershear Portion Of The 2002 Denali Earthquake Rupture In Laboratory*”. *Earth Planet. Sc. Lett.* DOI: 10.1016/j.epsl. 2013.11.030.
5. Passelègue, F. X., A. Schubnel, S. Nielsen, **H. S. Bhat**, and R. Madariaga (2013). “*From Sub-Rayleigh to Supershear Ruptures During Stick-Slip Experiments on Crustal Rocks*”. *Science*. DOI: 10.1126/ science.1235637.
6. Dunham, E. M. and **H. S. Bhat** (2008). “*Attenuation of radiated ground motion and stresses from three-dimensional supershear ruptures*”. *J. Geophys. Res.* DOI: 10.1029/2007JB005182.
7. **Bhat, H. S.**, R. Dmowska, G. C. P. King, Y. Klinger, and J. R. Rice (2007). “*Off-fault damage patterns due to supershear ruptures with application to the 2001 Mw 8.1 Kokoxili (Kunlun) Tibet earthquake*”. *J. Geophys. Res.* DOI: 10.1029/2006JB004425.



# ACKNOWLEDGEMENTS

We are nothing but a sum total of our experiences. We carry these experiences from our past to build a better future for ourselves. Many of these experiences are mere reflections of the people who have made profound influences in our lives. I would thus like to acknowledge these individuals who have made me into who I am today. I cherish each one of you and am lucky to have encountered you.

From the bottom of my heart, thank you Amma and Appa. I am forever grateful, and mindful, to the sacrifices you have made to ensure that I could carve out my own life. You have protected me from the enormous societal pressures to conform and have always encouraged me in satiating my thirst to learn. In your twilight years, my only regret is that I am unable to reciprocate as much as I should. Some were out of my hand and some were not. I hope you forgive me for the latter.

To Deepti, my constant. True to your name, you have been a shining light in my life. Your unwavering love keeps this crazy train on its tracks. To Chikkamma, how apt it is that an aunt is called 'Little Mother'. My fond memories of learning start with you.

I am eternally grateful to my advisors Jim and Renata, my parents in America. Thank you for taking on a twenty one year old boy from small town India under your tutelage. Your profound influence in my life is aptly summarised by a Kannada poet called Kuvempu. Thank you from the bottom of my heart.

ಮನುಜ ಮತ, ವಿಶ್ವ ಪಥ, ವಿಜ್ಞಾನ ದೃಷ್ಟಿ, ವಿಚಾರ ಬುದ್ಧಿ  
ಇವು ನಮ್ಮ ಹೃದಯದ ನಿತ್ಯಮಂತ್ರಗಳಾಗಬೇಕು

Humanism, universalism, scientific outlook, a spirit of inquiry  
These ought to be our daily hymns

– ಕುವೆಂಪು

To Virginia, Barbara and Chris for mothering me at Harvard. To Ares, who instilled a sense of self-confidence that was severely battered for almost a decade. Thank you my friend. To Charlie, for taking me on as a postdoc and sharing with me your unflappable enthusiasm. To Pritika who took a naive twenty one year old, fresh off the boat in America, under her wings and began his re-education as a social being.

When I took on another wild adventure of coming to work in France, a country whose language and culture were alien to me, I didn't imagine that I would make it this far. For this, I am eternally grateful to Claude Jaupart, Yann Klinger, Nobuaki Fuji, Djimédo Kondo, Ioanna Hérou and Yves Guéguen. To Geoff, my dear friend. Thank you for your support, your friendship and for those moments of discussing our shared love of an England of the yesteryears. I am especially grateful to Alex for encouraging me here in France and for giving a kick-start to my career that had flagged for almost half a decade. I was fumbling in the dark and in the pits about my future when you extended your friendly hand and pulled me out of it.

Thank you Lolo my true friend. From the moment you helped me after my accident to helping me through the vicissitudes of life in France, for a non-European non-American non-white foreigner, you have been the beach in the horizon when I thought I was floundering.

Thank you Marion for your friendship and your constant love. Every moment I share with you is cherished and savoured. Do not change.

To all my students and postdocs. I have truly learnt a lot from you and my experience with each and everyone of you has left a positive, indelible mark on me. Thank you.

To the two true loves of my life. Aziliz and Kiara. You and my science are the only things that matter to me. I love you both and will love you forever and ever and ever ...

काममया एवायं पुरुष इति  
सा यथाकामो भवति तत्कृतुर भवति  
यात्कृतुर भवति तत् कर्म कुरुते  
यत् कर्म कुरुते तद् अभिसम पद्यते

You are what your deep, driving desire is  
As your desire is, so is your will  
As your will is, so is your deed  
As your deed is, so is your destiny

– उपनिषद्

# CONTENTS

<b>Introduction</b>	11
• A Brief History of Earthquake Source Mechanics	11
• Supershear Earthquake Ruptures	15
<b>Theory</b>	21
• Classification and Stability of Ruptures	21
• 2D Steady State Singular Elastic Model	22
• 2D Steady State Cohesive Zone Models	31
• Far Field Stresses Along Mach Fronts	45
• 2D Spontaneous Rupture Models	47
• 3D Steady State Cohesive Zone Model	50
• Transition to Supershear Speed	72
• Scaling Relationship for Laboratory Earthquakes	79
• Mach Envelopes for Arbitrary Ruptures	81
<b>Experiments</b>	83
• Caltech Laboratory Earthquake Experiment	83
• ENS Laboratory Earthquake Experiment	111
<b>Observations</b>	117
• Ground Motion	117
2002 Denali earthquake	117
2018 Palu earthquake	128
• Far-Field Damage	129
2001 Kunlun earthquake	129
• Off-fault Damage at Transition	132
1999 Izmit ; 2001 Kunlun ; 2002 Denali & 2013 Craig earthquakes	132
• Supershear Tsunamis	136
2018 Palu earthquake	136
<b>Conclusions</b>	143



# 1

## INTRODUCTION

### 1.1 A Brief History of Earthquake Source Mechanics

One of the perennial mysteries of humankind, earthquakes have always fascinated, shocked and awe-inspired us. The earliest attempt to provide close to a scientific explanation, as always, dates back to the ancient Greeks. The most famous of these explanations was provided by Aristotle (384–322 B.C.) in his revolutionary treatise titled *Meteorologica* (Aristotle, 350 B.C.E.). In it he introduced the notion of the four elements (water, fire, air, earth) that compose all terrestrial elements. Aristotle proposed that the cause of earthquakes consisted in the shaking of the earth by dry heated underground exhalations of winds trapped in cavities of its interior, as they attempt to escape toward the exterior (Udias, 1999; Udías et al., 2014). It is worth noting that the Aristotelian idea of earth, “The earth is surrounded by water, just as that is by the sphere of air, and that again by the sphere called that of fire”, still describes the broad sections of earth and atmospheric sciences. It is also worth noting that this theory survived for twenty centuries until the seventeenth century, the era of the birth of modern scientific revolution!

The great Lisbon earthquake of 1755, estimated to have a moment magnitude of  $8.5 \pm 0.3$  (Solares & Arroyo, 2004), occurred on November 1 on the day of the feast of all saints. It caused the death of tens of thousands of people and turned Voltaire into a pessimist. He was finally forced to reject Leibniz’s notion of “the best of all possible worlds” argument. This earthquake resulted in Candide and his “Poème sur le désastre de Lisbonne”. It also launched a vigorous scientific inquiry taking earthquakes from the supernatural to the natural realm. It is now accepted that this earthquake led to the birth of modern seismology. The pioneering text of Revered John Michell, ‘Conjectures concerning the cause, and observations upon the phenomena, of earthquakes’, read at the Royal Society in 1760 firmly established the notion of an earthquake focus and that waves, traveling at a speed of about 0.5 km/s, propagated out of this focus all over the world. Using his version of triangulation he was able to estimate that the earthquake orig-

inated in the Atlantic ocean, somewhere between the latitudes comprising Oporto and Lisbon and about fifty to eighty kilometres from the coast (Michell, 1760).<sup>1</sup> It is worth keeping in mind that the mathematical theory of elastic waves came much later through the works of the giants like Cauchy, Poisson, Stokes among others. Michell made five key contributions in this work. One, he distinguished between aftershocks and mainshocks. He also noticed that large mainshocks return after long periods of time. Two, he noticed that areas near large volcanoes are always subject to frequent earthquakes. Three, the motion of the earth in earthquakes is partly tremulous and partly propagated by waves, which succeed one another sometimes at larger, sometimes at smaller, distances; and this latter motion is generally propagated much farther than the other. Four, the earthquakes occur at the same geographic location and the velocity of the waves moving out of them never changed. And finally, that the great Lisbon earthquake triggered several smaller earthquakes in Switzerland and elsewhere. It should be noted that the cause of the earthquake was attributed to some sort of a natural underground fire originating in a stratum of coal or shale. Sadly, Michell failed to impress his readers, and “he who succeeds in doing so”, said Charles Darwin, “deserves in my opinion all the credit.”(Davison, 1921).

<sup>1</sup> We leave it to the curious reader to see how good his calculations were and just urge to keep in mind that time keeping and mapping were not as accurate at those times

Later, Thomas Young, Robert Mallet and John Milne solidified the foundations of modern seismology. Mallet, an Irish civil engineer who studied the 1857 Naples earthquake, brought earthquake closer to exact science by noting that an earthquake is “the transit of a wave of elastic compression in any direction, from vertically upwards to horizontally, in any azimuth, through the surface and crust of the earth, from any centre of impulse, or from more than one, and which may be attended with tidal and sound waves dependent upon the former, and upon circumstances of position as to sea and land”. He notes that earthquakes are generated “either by the sudden flexure and constraint of the elastic materials forming a portion of the earth’s crust, or by the sudden relief of this constraint by withdrawal of the force, or by their giving way, and becoming fractured”. Concurrently with Alexis Perrey, a professor of Mathematics in Dijon, he compiled earthquake catalogues along with his son and summarised them in a map (Figure 1.1) that clearly delineates seismic and aseismic regions of the world. It is also to him that we owe the words ‘seismology’ and ‘epicentre’. The time following this saw great advances happen in instrumental seismology. In the interest of time the reader is referred to the magnificent chapter of D. Agnew (Agnew, 2002) and the references therein.

Although the distinction between the origin of earthquakes and the propagating waves was made, and the fault relationship with earthquake was established, the emergence of the faulting origin hypothesis of earthquakes would only happen in late 19th century.

During the 19th century systematic field studies after earthquakes were started and the first attempts to relate them to tectonic processes were also made by Koto (Neo, Japan, 1891), and Oldham (Assam, India, 1897) among

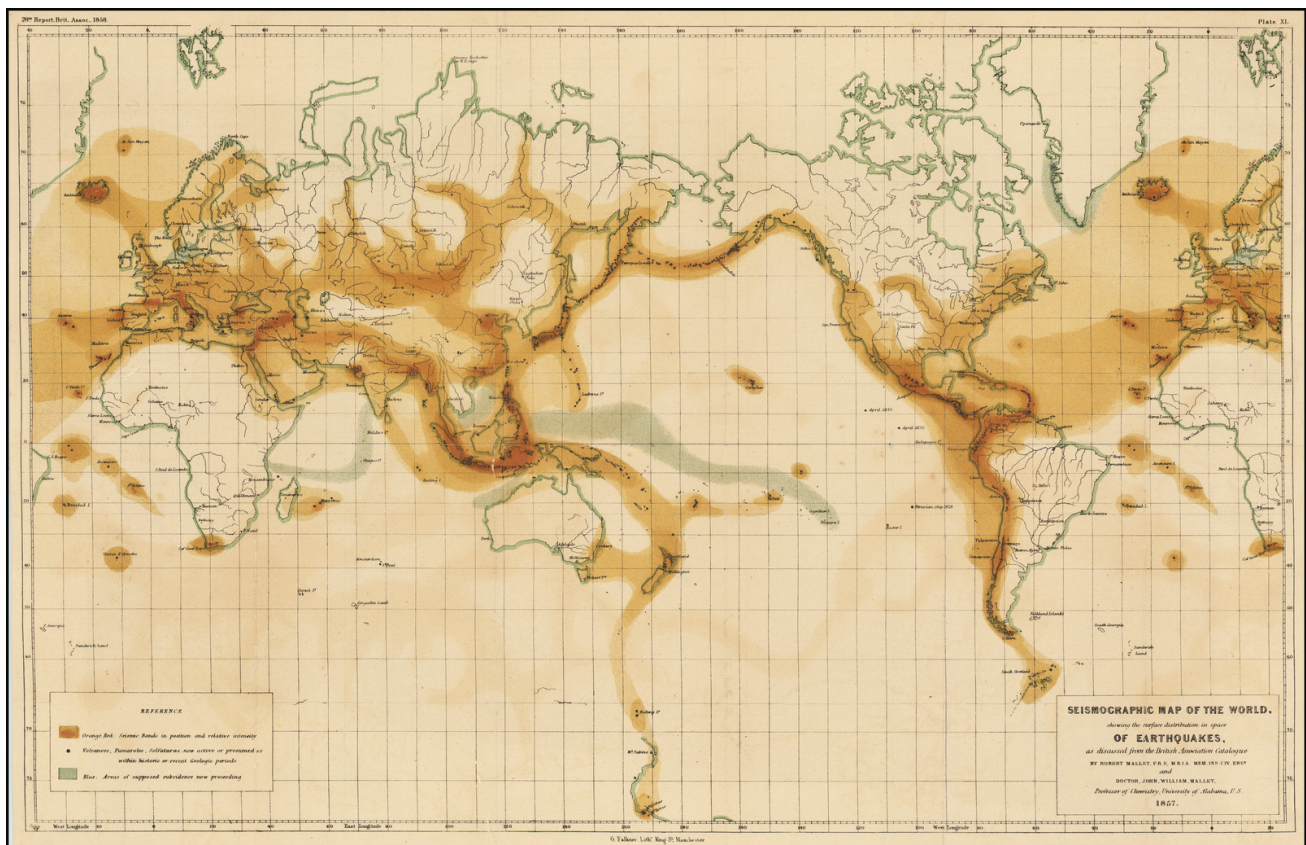


Figure 1.1: Map of global earthquakes published by Mallet and his son in 1858. Taken from Lee et al. (2002)

others. With the increase in number of field observations and in precision of localisation of epicentres, the correlation between earthquakes and faults became clearer. Authors such as Suess, Koto, Montessus de Ballore, and Sieberg assigned the cause of earthquakes to stresses accumulated in the Earth's crust by tectonic processes and their release by its fracture.

Grove Carl Gilbert (1843-1918) was a geologist, working on normal fault system in the Basin and Range province of west America Segall (2010). He was the first to recognise that a strain release along fault was the source of earthquakes. He also understood earthquake phenomenon as a stick slip phenomena 80 years before the famous paper of Brace & Byerlee (1966), Gilbert (1884) wrote :

The upthrust produces a local strain in the crust . . . and this strain increases until it is sufficient to overcome the starting friction on the fractured surface. Suddenly, and almost instantaneously, there is an amount of motion sufficient to relieve the strain, and this is followed by a long period of quiet, during which the strain is gradually reimposed. The motion at the instant of yielding is so swift and so abruptly terminated as to constitute a shock, and this shock vibrates through the crust with diminishing force in all directions.

At the same time as Gilbert understood the faulting origin of earthquakes, at least two authors Alexander McKay (1841-1917) and Bunjiro Koto (1856-1935) made observations of new fresh scarp concomitant with earthquakes.

This observation made Bunjiro Koto think that earthquake was the result of dislocation on a fault (Koto, 1893). The controversy at that time was to know if faults were the origin or a consequence of earthquake. The final proof came from geodetic observations after the 1906 San Francisco earthquake by Harry Fielding Reid (1859-1944). He showed that the rupture was not only superficial but also happened in depth. This led to the generally accepted faulting origin of earthquakes. Reid gave the five statements of his elastic rebound theory in 1911 (Segall, 2010):

1. The fracture of the rock, which causes a tectonic earthquake, is the result of elastic strains, greater than the strength of the rock can withstand, produced by the relative displacements of neighbouring portions of the earth crust.
2. These relative displacements are not produced suddenly at the time of the fracture, but attain their maximum amounts gradually during a more or less long period of time.
3. The only mass movements that occur at the time of the earthquake are the sudden elastic rebounds off the sides of the fracture towards position of no elastic strain; and these movements extend to distances of only a few miles from the fracture.
4. The earthquake vibrations originate in the surface of fracture; the surface from which they start has at first a very small area, which may quickly become very large, but at a rate not greater than the velocity of compressional elastic waves in the rock.
5. The energy liberated at the time of an earthquake was, immediately before the rupture, in the form of energy of elastic strain of the rock. (Reid 1911, p. 436)

These statements lay the foundations for the understanding of faulting origin of earthquake. The next major theoretical advance came with the application of elastic dislocation theory to the study of earthquakes (Segall, 2010). Dislocation theory dates to the Italian mathematicians Vito Volterra and Carlo Somigliana in the early part of the twentieth century; however, it was J. A. Steketee who first suggested that elastic dislocations could be used to model deformation due to faulting and was the first to use Volterra's formula for this application. Steketee was also the first to derive the displacements due to a point-source representation of a fault (Steketee, 1958). It is worth noting that dislocation theory requires the user to prescribe the amount by which each sides of the fault slid past each other. If known well then it would let us calculate the resulting deformation of the region around the fault. How the fault decided on that amount of slip required one to know 'how strongly were the two sides being loaded' and 'what was the resistance offered by the two sides'. Luckily, the plate tectonics revolution of the 1960's solved the one of the final puzzles on the origin of elastic strains in the crust, i. e. loading, and associated them to the relative motion of lithospheric plates (Romanet, 2017). The 1960's also brought along pioneering rock mechanicians into the realm of earthquake mechanics via studies

on rock friction i. e. the resistance offered by sliding surfaces. William F. Brace at MIT along with James Byerlee of Stanford University realised that the stick-slip friction events observed in the laboratory could be used to understand ruptures occurring at much larger scale during destructive earthquakes (Brace & Byerlee, 1966; Byerlee, 1967). In their famous experiment they showed that creating new fractures was not the only model that can explain earthquake faulting. They saw-cut a sample rock and loaded it at both ends with a confining pressure. They observed that the sliding between the two pieces of rocks was not smooth but rather in boom and bust motion. This was really the beginning of the well accepted theory of frictionally controlled earthquakes. These early works established frictional instability as a possible mechanism for repetitive stick-slip failure and the seismic cycle (Marone, 1998).

One of the final pieces of the puzzle was fit by the arrival of fracture mechanics like B. Kostrov, J. Eshelby, J. R. Rice, R. Madariaga, S. Das, L. Freund, J. Rudnicki among many others, into the subject. By developing an analogy between earthquakes and cracks, the question of how the fault decided on the amount of slip was fulfilled.

Starting from the classical theoretical work by Kostrov (Kostrov, 1964; Kostrov, 1966) and Eshelby (Eshelby, 1969), very soon it became clear that friction also played a fundamental role in the initiation, development of rupture and the healing of faults. The classical Amonton-Coulomb model of a sudden drop in friction from a static to a kinematic coefficient led to an impasse however. It predicted infinite stress singularities at the crack-tip and many other physical problems. The reason is that this model lacks an essential length scale needed to define a finite energy release rate near the rupture front (Madariaga, 2012).

Through these scientific feats of success, along with several missteps and misunderstandings, over several centuries we thus arrive at the following set of statements that describes the modern view of earthquakes and earthquake cycles.

*The motion of tectonic plates is resisted along the faults, by friction, leading to a buildup of strain energy. The sudden release of this energy manifests itself as an earthquake that ruptures the fault and radiates elastic waves through the entire earth. Once this energy is dissipated, the buildup of energy continues leading up to the next earthquake.*

## 1.2 Supershear Earthquake Ruptures

With the acceptance of dynamic fracture mechanics as the correct modelling framework for earthquakes, the notion of rupture speed, or fracture speed or rupture velocity, became firmly associated with each individual earthquake. In an excellent introduction Prof. S. Das traces the history of rupture speed estimation for early earthquakes.

But more importantly, seismologists estimated the average rupture speed for several earthquakes by studying the directivity effects and spectra of seismic waves. The first was for the 1952 Ms 7.6 Kern County, California earthquake. Benioff (1955) concluded that “the progression speed is in the neighbourhood of speed of Rayleigh waves” using body wave studies.

– Das (2015)

The earliest mathematical solutions for a dynamic shear crack were developed over a half century ago. An original solution for a steady state semi-infinite crack, subjected to combined mode I and mode II loading, was given by Craggs (1960). This was followed by a self-similar solution for a propagating mode II shear crack given by Kostrov (1964). Each of these solutions was characterised by a singular crack front, with surrounding elastic fields, which decayed as the inverse square-root of the radial distance from the crack front. Craggs (1960) realised that stable crack growth can only result if energy for the surrounding linear elastic field is drawn into the singular crack tip. Such a condition can only arise if the rupture propagates at speeds,  $v_r$ , below the Rayleigh wave speed of the surrounding medium i.e. ( $v_r < c_R$ ). Kostrov (1964) recognised that energy will be radiated out from the crack tip if the rupture speed lies between the Rayleigh and shear wave speeds of the surrounding linear elastic medium, i.e. ( $c_R < v_r < c_s$ ). The latter scenario is rejected on physical grounds leading to the conclusion that a mode II shear crack will tend to propagate in the sub-Rayleigh rupture speed regime ( $v_r < c_R$ ).

While the rupture speed of most earthquakes is limited by the speed of the Rayleigh waves,  $c_R$ ,<sup>2</sup> earthquakes can occasionally transition to higher speeds and exceed the shear wave speed,  $c_s$ . Such events are known as Supershear Earthquakes.

<sup>2</sup> In homogeneous elastic solids,  $c_R < c_s < c_p$ . Typically, for the upper crust of the earth,  $c_p \approx 5\text{km/s}$ ,  $c_s \approx 3.5\text{km/s}$  and  $c_R \approx 0.92c_s = 3.2\text{km/s}$

Whether supershear ruptures exist in nature has been a matter of debate for a long time. One of the earliest theoretical models was proposed by Weertman (1969) who treated the crack as smeared-out dislocations along a surface following a dynamic friction law. He showed that such dislocations can travel at supersonic velocities (faster than the P-wave speed,  $c_p$ ). Crucially, he claimed that supershear velocity,  $c_s < v_r < c_p$ , is *forbidden*. The earliest known laboratory evidence dates back to the experiments of Wu et al. (1972). He had one experiment, with the highest stress drop, where he concluded that the rupture velocity was about  $1.1c_s$ . Unfortunately, interpreting the experiments based on Weertman (1969) work, Wu did not make a conclusive observation that his experiments indeed demonstrated the supershear phenomenon.

Burridge (1973) was the first to propose conditions under which a plain-strain, self-similar mode II crack can bypass the forbidden rupture speed regime ( $c_R < v_r < c_s$ ) and propagate within the supershear rupture speed regime ( $c_s \leq v_r \leq c_p$ ), where ( $c_p$ ) represents the dilatational wave speed. A simple Coulomb friction relation was assumed to model the interfacial shear strength ahead of the primary (sub-Rayleigh) crack front. The ap-

proach assured that stresses would remain bounded at the primary crack front but failed to account for the effects of inelastic (cohesive) energy losses at the singular crack tip. In spite of this limitation, the analysis identified the presence of a peak in the shear stress field, which propagates ahead of the primary crack front at the shear wave speed. This was a key finding, which revealed a natural mechanism for nucleating a secondary (supershear) rupture ahead of the primary crack front in the event that the magnitude of the peak shear stress exceeded the intrinsic fault strength. The analysis concluded that the supershear crack speed would rapidly approach the dilatational wave speed ( $c_p$ ) of the surrounding medium.

Andrews (1976) produced the very first numerical finite difference calculations, which successfully simulated a sub-Rayleigh to supershear rupture transition. The model featured a linear slip weakening failure criterion, which defined the loss of frictional strength with increased slip over a characteristic length along the fault plane. The implementation of a finite slip weakening distance eliminated the crack tip singularity and provided an energy dissipation mechanism, which was lacking in the earlier analysis by Burridge (1973). Numerical trails revealed the peak shear stress positioned just ahead of the primary (sub-Rayleigh) crack front, as noted by Burridge (1973), which nucleated a secondary crack in cases where the local fault strength was exceeded. The trailing edge of a newly spawned secondary shear crack was observed to rapidly merge with the primary (trailing) sub-Rayleigh rupture, while the leading edge raced ahead as an supershear crack front. A key outcome of this study was the identification of a mechanically stable portion of the supershear rupture speed regime  $\sqrt{2}c_s < v_r \leq c_p$ , which we henceforth refer to as the supershear rupture speed domain. It is worth noting here, as it has been long forgotten, that Das & Aki (1977) also showed that shear ruptures could attain supershear speeds. Also, crucially, Das introduced the  $S$ -ratio<sup>3</sup>, a non-dimensional measure of the strength of a fault, and established the link between  $S$ -ratio and rupture velocity. For 2D ruptures they showed that for  $S \leq 1.77$  ruptures tend to transition to supershear speed.<sup>4</sup>

Burridge et al. (1979) revisited the problem of admissible rupture speeds by conducting a rigorous stability analysis of a steady-state shear crack, which was driven by a point load maintained at a constant distance behind the crack tip. Energy dissipation was accounted for in the analysis through a Dugdale-type cohesive traction relation confined to a small region around the crack tip. Conclusions regarding the stability of supershear ruptures were in general agreement with the numerically based findings of Andrews (1976). Specifically, (1) the supershear velocity regime  $\sqrt{2}c_s \leq v_r \leq c_p$  was identified to be stable with a unique local minima within this velocity domain and (2) the supershear velocity regime  $c_s \leq v_r < \sqrt{2}c_s$  was deemed as unstable. Conclusions regarding the stability of sub-shear crack propagation were also consistent with the earlier findings by Craggs (1960) and Kostrov (1964). Most notably, (1) the velocity domain  $c_R < v_r < c_s$  was deemed to be strictly forbidden, since the crack tip would otherwise act as a source of energy if allowed to propagate at these speeds, and (2) sub-shear

<sup>3</sup>  $S \equiv (\tau_p - \tau_0)/(\tau_0 - \tau_r)$  where  $\tau_p$  is the peak frictional resistance of the fault,  $\tau_r$  is the residual resistance and  $\tau_0$  is the initial traction on the fault

<sup>4</sup> Dunham (2007) showed that for 3D unbounded faults,  $S \leq 1.19$ .

cracks will be generally confined to the sub-Rayleigh velocity regime, i.e.,  $v_r < c_R$ . A crack confined within this velocity domain will tend to asymptotically approach the Rayleigh wave speed.

Closed form analytical solutions for the singular elastic stress and particle velocity fields radiated by a 2D steady state shear crack were given in the seminal work by Freund (1979). Sub-Rayleigh and supershear crack field solutions were given for the shear stress ( $\sigma_{12}$ ) and fault-parallel velocity component ( $\dot{u}_1$ ). The resulting field expressions are modulated by a velocity-dependent “dynamic stress intensity factor”, which characterises the intrinsic strength of the fracture plane.

The stability of sub-shear crack propagation was considered by examining the relationship between the normalised stress intensity factor and the crack tip speed. Results were consistent with those of Burridge et al. (1979), along with a more recent stability analysis by Fossum & Freund (1975), which considered the energy flux into a dynamic shear crack. The stability of supershear ruptures was speculated upon but no similar analysis was provided.

Even though theoretical models, and one laboratory experiment, provided evidence that supershear ruptures are feasible, it was not until the  $M_w$  6.5 Imperial Valley earthquake (California, 1979) that a supershear rupture was inferred in nature for the first time by Archuleta (1984) and Spudich & Cranswick (1984). This was not universally accepted and the scale tipped in the favour of supershear skeptics for more than 25 years (Das, 2015).

Pioneering laboratory experiments by Rosakis et al. (1999) and Xia et al. (2004) together with observations from the  $M_w$  7.4 1999 Izmit and the  $M_w$  7.2 1999 Düzce earthquakes in Turkey by Bouchon et al. (2001), then conclusively confirmed that supershear ruptures are in fact much more common than previously expected. Bouchon conclusively showed that to best reproduce the observation of a near-fault accelerogram, for the Izmit earthquake, the rupture had to propagate at supershear speed. The 2002  $M_w$  7.9 Denali earthquake was an exceptionally well-characterised event due to an array of well-positioned, near field ground motion stations located along the Alaskan pipeline. In particular, the ground motion records acquired at Pump Station 10 (PS10), positioned  $\approx 3km$  north of the Denali strike-slip fault, are arguably the finest near source records of a supershear rupture that have ever been recorded. The pioneering works of Dunham & Archuleta (2004) and Ellsworth et al. (2004a) on PS10 ground motion records provided multiple, independent evidence that the earthquake could clearly be classified as supershear. The pioneering experiments of Passelègue et al. (2013), on a saw-cut granite under crustal stress conditions, landed the last nail in the coffin of supershear skeptics<sup>5</sup>.

Supershear ruptures have now been inferred<sup>6</sup> for several, albeit rare, events: the  $M_w$  7.5 2013 Craig (Alaska) earthquake (Yue et al., 2013), the  $M_w$  6.7 2013 Okhotsk (Kamchatka) earthquake (Zhan et al., 2014), and

<sup>5</sup> A few still roam conference halls whispering their skepticisms, with the fervour of a cult acolyte, supposedly based on gut feelings. Clearly, their collective guts haven't been to a physics class

<sup>6</sup> In fact, not unlike Elvis sightings, supershear earthquakes are now observed everywhere by some researchers

most recently the  $M_w$  7.5 2018 Palu (Indonesia) earthquake (Amlani et al., 2020; Bao et al., 2019; Socquet et al., 2019).

I would like to conclude this chapter with a note of caution. Typically, earthquake rupture speeds are inferred from recordings done at teleseismic distances by quantifying the directivity effects of the radiated waves. Nowadays, Back-Projection methods are used to quantify the same. The latter is also inferred using recordings done at teleseismic distances. Neither of these methods are satisfactory enough to conclusively make an argument for supershear earthquake.<sup>7</sup> At such distances, the best technique to identify supershear earthquakes was developed by Vallée & Dunham (2012). They showed that on the Mach cone, band-passed surface wave seismograms from a large supershear rupture will be identical to those from much smaller events with similar focal mechanisms and will have an amplitude ratio equal to the ratio of the seismic moments of the two events. If the latter technique provides an almost conclusive hint of a supershear earthquake then one should exploit the unique signatures of a supershear earthquake that can manifest itself in near-source accelerometers, GPS stations, aftershock distribution and even tsunamis (Amlani et al., 2020; Bhat et al., 2007; Dunham & Bhat, 2008; Jara et al., 2020; Mello et al., 2014, 2016; Passelègue et al., 2013).

This thesis is focussed on expounding these unique signatures of a supershear earthquake that are derived from theoretical models, verified in controlled laboratory experiments and then further validated with observations made for natural earthquakes.

<sup>7</sup> At the end of the day, these methods infer speed by determining the slope of a distance-time curve. Most of the data is so scattered that trying to fit them on a straight line is as futile as herding cats.



# 2

## THEORY

### 2.1 Classification and Stability of Ruptures

A mode II rupture, or a shear rupture, is classified as sub-Rayleigh if it propagates with a rupture speed  $v_r < c_R$  with the rupture speed tending to approach the Rayleigh wave speed,  $c_R$ , (Broberg, 1999; Burridge et al., 1979; Rosakis, 2002). Natural earthquakes result from mode II crustal ruptures, which typically propagate at sub-Rayleigh speeds. In plane strain/stress, the rupture speed regime  $c_R < v_r < c_s$  is strictly forbidden since a rupture in this speed regime would otherwise become a source rather than a sink of fracture energy (Broberg, 1989, 1996; Burridge et al., 1979; Freund, 1979; Kostrov, 1964; Rosakis, 2002).

A mode II rupture is classified as supershear if it propagates with a rupture speed such that  $c_s \leq v_r \leq c_p$ , where  $c_s$ ,  $c_p$  are the respective shear and dilatational wave speeds within the local surrounding medium. Rupture speed stability analyses have been performed within the context of either self-similar crack growth by Broberg (1989), Burridge et al. (1979), and Obrezanova & Willis (2003), or steady-state, cohesive zone models by Dunham & Archuleta (2004, 2005), Rosakis (2002), and Samudrala et al. (2002a,b) under uniform background stress and fault strength conditions. Once a rupture front has transitioned into the supershear domain it will tend to favor a stable rupture speed regime  $v_0 \leq v_r < c_p$  with  $v_r \rightarrow c_p$ , given a sufficient rupture propagation distance in the case of self-similar growth. The domain  $c_s < v_r < v_0$  is regarded as the unstable portion of the supershear rupture speed regime. The lower bound  $v_0$  is a function of the fault strength and may also depend upon other system parameters, such as rate of velocity weakening and background stress. The minimum value that  $v_0$  can assume is  $v_0 = \sqrt{2}c_s$ , in the case of infinite fault strength, in which case the maximum extent of the stable rupture speed regime becomes  $\sqrt{2}c_s \leq v_r \leq c_p$ . We exclusively denote the latter speed domain as the “supershear rupture regime” in order to distinguish it from the general supershear domain.

The superposition of shear wavelets emitted by a steady-state, supershear rupture front leads to the formation of a shear Mach cone, which stems from the advancing rupture tip and envelopes the surrounding medium along either side of the fault. The resulting Mach cone half-angle, measured with respect to the fault plane, is given by the familiar relation,

$$\theta = \sin^{-1}(c_s/v_r) \quad (2.1)$$

Inspection of Eqs.2.1 reveals that the Mach angle domain

$$\sin^{-1}(c_s/c_p) \leq \theta \leq \pi/4$$

corresponds to the maximum stable (supershear) rupture speed regime

$$\sqrt{2}c_s \leq v_r \leq c_p$$

while  $\pi/4 < \theta \leq \pi/2$  corresponds to the unstable rupture speed domain  $c_s \leq v_r < \sqrt{2}c_s$ . Special cases of interest that set a lower bound for  $\theta_{min} = \sin^{-1}(c_s/c_p)$  (as  $v_r \rightarrow c_p$ ) are (1)  $c_p = \sqrt{3}c_s$ , often a good approximation for crustal rock, in which case supershear Mach angles are restricted to  $\sin^{-1}(1/\sqrt{3}) \leq \theta \leq \pi/4$ , and (2)  $c_p \approx 2c_s$ , applicable to H-100 laboratory earthquake test specimens, in which case the supershear Mach angles are restricted to  $\pi/6 \leq \theta \leq \pi/4$ .

## 2.2 2D Steady State Singular Elastic Model

### Overview of the 2D Steady State, Singular Elastic Solution for a Dynamic Shear Crack : Sub-Rayleigh Rupture Speed Regime

Freund (1979, 1990) rigorously solved the 2D plane strain problem of a steady state dynamic (mode II) shear crack in a linear elastic half-space. The problem was posed under the assumption of plane strain, with the crack front oriented parallel to the  $x_3$  axis of a Cartesian coordinate frame. The crack was assumed to propagate strictly along the  $x_1$  direction with crack-tip coordinates given by  $(x_1 = l(t), 0)$ , where  $l(t)$  is a continuous function of time. The instantaneous crack-tip speed is then given by  $v_r(t) = \dot{l}(t)$ . A local coordinate system  $(\xi_1, \xi_2)$  was then introduced with the origin selected to coincide with the crack tip, such that  $\xi_1 = x_1 - l(t)$  and  $\xi_2 = x_2$ . A local polar coordinate system  $(r, \theta)$  was also introduced, whereby  $r = \sqrt{\xi_1^2 + \xi_2^2}$  and  $\theta = \tan^{-1}(\xi_2/\xi_1)$ . The governing wave equations for the dilatational displacement potential  $\phi$  and shear displacement potential  $\psi$  become two-dimensional in  $\xi = x - v_r t$  and  $\xi_2 = y$  under a Galilean coordinate transformation. The derivation leads to a standard Hilbert problem in analytic function theory which is then solved subject to the prescribed traction-free boundary conditions on the crack surfaces. This then leads to the 2D asymptotic stress and particle velocity field solutions for a propagating mode II shear crack. The physical assumptions and derivations in Freund (1990) are well-posed and accurately presented leading up through the formulation of the stress field solutions. Unfortunately, the expressions for the particle velocity components are not accurately expressed in Freund

(1990), most likely due to typographical errors, which resulted during publication of the manuscript. The singular elastic (asymptotic) solutions for the sub-Rayleigh (in-plane) particle velocity field components  $\dot{u}_1(r, \theta)$  and  $\dot{u}_2(r, \theta)$  of a mode II shear crack are given by

$$\dot{u}_1 = \frac{v_r \alpha_s K_{II}(t)}{\mu D \sqrt{2\pi r}} \left[ 2 \frac{\sin \frac{1}{2} \theta_d}{\sqrt{\gamma_d}} - (1 + \alpha_s^2) \frac{\sin \frac{1}{2} \theta_s}{\sqrt{\gamma_s}} \right] \quad (2.2)$$

and

$$\dot{u}_2 = -\frac{v_r K_{II}(t)}{\mu D \sqrt{2\pi r}} \left[ 2 \alpha_d \alpha_s \frac{\cos \frac{1}{2} \theta_d}{\sqrt{\gamma_d}} - (1 + \alpha_s^2) \frac{\cos \frac{1}{2} \theta_s}{\sqrt{\gamma_s}} \right]. \quad (2.3)$$

Here,  $K_{II}(t)$  is the instantaneous mode II dynamic stress intensity factor,  $\mu$  represents the shear modulus and the factors  $\alpha_s, \alpha_d, \gamma_s, \gamma_d, \theta_s$ , and  $\theta_d$  are given by

$$\theta_s = \tan^{-1}(\alpha_s \tan \theta) ; \theta_d = \tan^{-1}(\alpha_d \tan \theta) \quad (2.4)$$

$$\gamma_s = \sqrt{1 - (v_r \sin \theta / c_s)^2} ; \gamma_d = \sqrt{1 - (v_r \sin \theta / c_p)^2} \quad (2.5)$$

$$\alpha_s = \sqrt{1 - (v_r / c_s)^2} ; \alpha_d = \sqrt{1 - (v_r / c_p)^2}. \quad (2.6)$$

The factor  $D$  in the denominator of Eqs. 2.2, 2.3 is the Rayleigh wave function given by

$$D = 4\alpha_s \alpha_d - (1 + \alpha_s^2)^2. \quad (2.7)$$

The root of Eqs.2.7 corresponds to the Rayleigh wave speed over a homogeneous, linear elastic half-space Graff(1991). Careful examination of Eq. 2.7 reveals that  $D \rightarrow 0$  as  $v_r \rightarrow c_R$ , while  $D > 0$  corresponds to admissible sub-Rayleigh rupture speeds  $v_r < c_R$ , and  $D < 0$ , corresponds to the forbidden rupture speed domain  $c_R < v_r < c_s$ . We note as well, how  $D < 0$  implies that the sign of each motion component given by Eqs. 2.2, 2.3 would both reverse if the forbidden rupture speeds  $c_R < v_r < c_s$  were admissible.

### Spatio-temporal Properties of a Sub-Rayleigh Shear Crack Velocity Field: 2D Steady State, Singular Elastic Solution

The 2D particle velocity vector field plot, normalized attenuation curve, and synthetic particle velocity waveforms depicted in Figure 2.1 were all obtained from the the particle velocity field expressions given by Eqs. 2.2,2.3. The plots were generated using a convenient and arbitrary choice of values for the material constants corresponding to  $K_{II}/\mu = 0.19mm^{1/2}$ ,  $c_s = 1.3mm/\mu s$ , and  $c_p/c_s = \sqrt{3}$ .

Figure 2.1(a) represents the particle velocity vector field  $\vec{\dot{u}}(\xi_1, \xi_2)$  corresponding to a right-lateral/right-traveling, dynamic shear crack propagating at  $v_r = 0.9c_s$ . The colors displayed by the plot legend correspond to the magnitude of the particle velocity ( $|\dot{\vec{u}}| = \sqrt{\dot{u}_1^2 + \dot{u}_2^2}$ ) while the white arrows of constant length constitute a streak plot, which indicates the sense of particle motion. The velocity field is characterized by a dominant FN particle motion component ( $\dot{u}_2$ ), as revealed by the steeply inclined streak plot vectors within the half-space  $\xi_1 > 0$ .

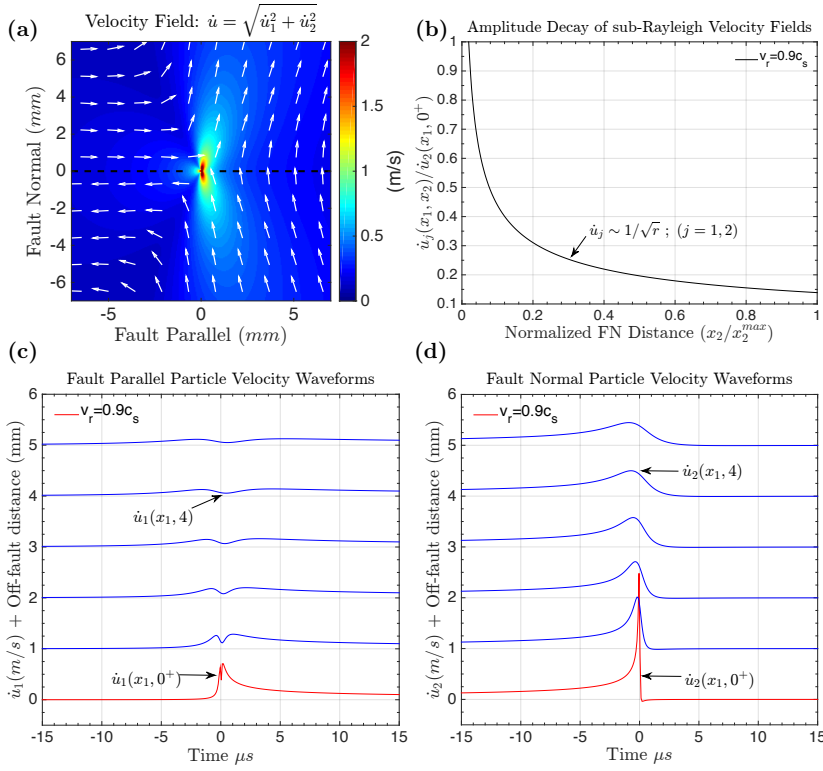


Figure 2.1: (a) Sub-Rayleigh velocity field plot for a dynamic shear crack as predicted by the steady-state singular elastic solution. (b) Normalized attenuation curve of the FN and FP velocity components. (c) Synthetic FP velocity waveforms at incremented distances from the fault. (d) Synthetic FN velocity waveforms at incremented distances from the fault.

The curve in Figure 2.1(b) depicts how each particle velocity component is predicted to decay with increased FN distance ( $\xi_2$ ) from the crack plane. The plot was generated by computing the ratio

$$\delta \dot{u}_2^{max}(\xi_1, \xi_2) / \delta \dot{u}_2^{max}(\xi_1, 0^+)$$

where  $\delta \dot{u}_2^{max}(\xi_1, \xi_2)$  is the numerically calculated amplitude of the velocity swing at an off-fault field point  $(\xi_1, \xi_2)$ , and  $\delta \dot{u}_2^{max}(\xi_1, 0^+)$  is the corresponding velocity jump at a “near-fault” point  $(\xi_1, 0^+)$ , which was carefully selected in order to avoid the crack tip singularity. In the current example  $\xi_2 \rightarrow 0^+$  represents a point lying at  $\xi_2 = 0.2mm$  within the arbitrarily imposed length scale. The horizontal axis is normalized with respect to the maximum value of the  $\xi_2$ -axis. The normalized attenuation curve demonstrates how rapidly particle velocity components are expected to decay in accordance with the  $r^{-1/2}$  amplitude factor in Eqs. 2.2,2.3.

Figures 2.1(c,d) represent synthetic particle velocity waveforms corresponding to the FP ( $\dot{u}_1$ ) and FN ( $\dot{u}_2$ ) motion components, computed at various distances from the fault plane. Line plots extracted from the spatial field description given by Eqs. 2.2,2.3 were reflected with respect to the vertical axis  $x_1 = 0$  of Figure 2.1(a) and replotted with with an equivalent time axis ( $t = \xi_1/v_r$ ) in accordance with the steady state assumption. The curves plotted in red highlight the “near-fault” velocity waveforms while the blue curves correspond to particle velocity waveforms plotted in FN increments of  $\Delta \xi_2 = 1mm$ , out to a distance  $\xi_2 = 5mm$ . within the arbitrarily defined length scale. Two distinct and fundamental spatiotemporal properties of a steady state (sub-Rayleigh) shear dislocation are revealed: (1) the parti-

cle velocity waveforms are characterized by a prominent FN component, as previously noted, which clearly dominates in magnitude over the FP component, and (2) sharp velocity waveforms recorded close to the fault plane are very quickly stripped of their high frequency content and undergo a rapid amplitude decay with increased FN distance ( $\xi_2$ ), as described by the normalized attenuation plot in Figure 2.1(b).

### Overview of the 2D Steady State, Singular Elastic Solution for a Dynamic Shear Crack : Supershear Rupture Speed Regime

Freund (1979, 1990) also considered the problem for the stress and particle velocity fields radiated by a steady-state shear crack propagating in the supershear rupture speed domain ( $c_s \leq v_r \leq c_p$ ). The problem was posed under the assumption of plane strain with traction-free boundary conditions imposed on the crack faces. The crack was assumed to propagate along the  $x_1$  direction with the crack front oriented parallel to the  $x_3$  axis of a global Cartesian coordinate frame. A Cartesian coordinate frame ( $\xi_1, \xi_2$ ) was introduced, with its origin at the crack tip, which is equivalently expressed in polar form  $(r, \theta)$ , whereby  $r = \sqrt{\xi_1^2 + \xi_2^2}$  and  $\theta = \tan^{-1}(\xi_2/\xi_1)$ . The governing wave equations for the dilatational displacement potential  $\phi$  and shear displacement potential  $\psi$  are uniquely transformed under the Galilean coordinate transformation  $\xi = x_1 - v_r t$  and  $\xi = x_2$ , subject to the restriction that  $v_r \geq c_s$ . The governing PDE for the dilatational displacement potential  $\phi$  is transformed into a scaled Laplacian equation while the shear displacement potential  $\psi$  remains governed by a wave equation. The derivation leads to a standard Hilbert problem in analytic function theory which is then solved for the in-plane stress and particle velocity fields, subject to the prescribed traction-free boundary conditions on the crack surfaces.

The solution for the particle velocity field components  $\dot{u}_1$  and  $\dot{u}_2$  is conveniently expressed as the superposition of the dilatational and shear field contributions

$$\dot{u}_j = A v_r (\dot{u}_j^s + \dot{u}_j^d); \quad j = 1, 2 \quad (2.8)$$

where  $A = K_{II}/\mu$  represents an effective dynamic stress intensity factor, as previously defined, and  $v_r$  is the rupture speed ( $c_s \leq v_r \leq c_p$ ).

The shear field contributions of Eqs. 2.8 are given by

$$\dot{u}_1^s = -sgn(\xi_2) \frac{\beta_s (2 - \frac{v_r^2}{c_s^2}) \sin(\pi q)}{2(-\xi_1 - \beta_s |\xi_2|)^q} H(-\xi_1 - \beta_s |\xi_2|) \quad (2.9)$$

and

$$\dot{u}_2^s = \frac{(2 - \frac{v_r^2}{c_s^2}) \sin(\pi q)}{2\beta_s (-\xi_1 - \beta_s |\xi_2|)^q} H(-\xi_1 - \beta_s |\xi_2|) \quad (2.10)$$

where the variables  $\beta_s$  and  $q$  are given by

$$\beta_s = \sqrt{(v_r/c_s)^2 - 1} \quad (2.11)$$

$$q = \frac{1}{\pi} \tan^{-1} \left[ \frac{4\alpha_d \beta_s}{(2 - v_r^2/c_s^2)^2} \right] \quad (2.12)$$

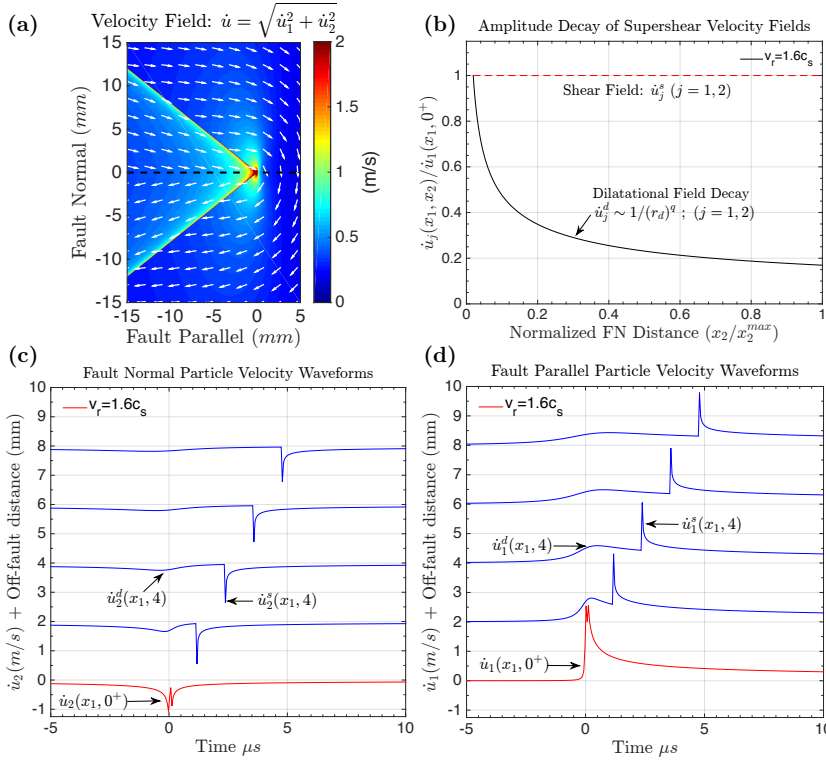


Figure 2.2: (a) Supershear velocity field plot for a dynamic shear crack as predicted by the steady-state singular elastic solution. (b) Normalized attenuation curve of the dilatational velocity field components. (c) Synthetic FP velocity waveforms at incremented distances from the fault. (d) Synthetic FN velocity waveforms at incremented distances from the fault.

and  $sgn(\xi_2)$  represents the sign function, which is equal to +1 for  $\xi_2 > 0$  and  $-1$  for  $\xi_2 < 0$ . Eqs.2.9, 2.10 collectively describe the motion components along shear Mach fronts which extend from the rupture tip and envelope the radiated shear field.

The dilatational velocity field contributions in Eqs. 2.8 are given by

$$\dot{u}_1^d = \frac{\sin(q\theta_d)}{r_d^q} ; \dot{u}_2^d = -\alpha_d \frac{\cos(q\theta_d)}{r_d^q} \quad (2.13)$$

where the variables  $r_d$  is given by

$$r_d = \sqrt{\xi_1^2 + (\alpha_d \xi_2)^2} \quad (2.14)$$

with  $\theta_d$  and  $\alpha_d$  previously given by Eqs. 2.4 and Eqs. 2.6, respectively.

Examination of Eqs. 2.12 reveals that that  $0 < q < 1/2$ . A maximum value  $q = 1/2$  is approached as  $v_r \rightarrow \sqrt{2}c_s$  whereas  $q \rightarrow 0$  as  $V \rightarrow c_s$  or  $v_r \rightarrow c_p$ . The singularity  $r_d^{-q}$  is thus generally weaker than the  $r^{-1/2}$  singularity, which implies that the dilatational field will tend to decay more slowly compared to the fields radiated by a sub-Rayleigh rupture field. Interestingly, the  $r^{-1/2}$  singularity reemerges only in the limiting case  $v_r \rightarrow \sqrt{2}c_s$ , corresponding to the lowest bound of the supershear rupture speed regime.

### Spatiotemporal Properties of a Supershear Crack Velocity Field : 2D Steady State, Singular Elastic Solution ( $\sqrt{2}c_s \leq v_r < c_p$ )

The particle velocity field, attenuation curve, and synthetic waveforms depicted in Figure 2.2 were generated by plotting the singular elastic solutions for an supershear, mode II shear crack given by Eqs. 2.8. The plots were generated using a convenient and arbitrary choice of values for the material constants corresponding to  $A = 0.45mm^{1/2}$ ,  $c_s = 1.3mm/\mu s$ , and  $c_p/c_s = \sqrt{3}$ .

Figure 2.2(a) displays the particle velocity field  $\vec{u}(\xi_1, \xi_2)$  of a right-lateral / right-traveling dynamic shear crack rupture propagating at  $v_r = 1.6c_s$ . The plot legend colors correspond to the magnitude of the particle velocity ( $|\dot{u}| = \sqrt{\dot{u}_1^2 + \dot{u}_2^2}$ ) and the white arrows of constant length constitute a streak plot, indicating the sense of particle motion throughout the field. The concentrated supershear rupture tip is surrounded by an elliptically-shaped field lobe and flanked by prominent shear Mach fronts, which bounds the radiated shear field. The velocity vector field plot is characterized by a dominant FP particle velocity component ( $\dot{u}_1$ ) as revealed by the manner in which the streak plot vectors are predominantly oriented along the horizontal direction in the half-space  $\xi_1 > 0$ .

Figure 2.2(b) depicts the predicted amplitude decay of the radiated dilatational field components ( $\dot{u}_1^d$ ) and ( $\dot{u}_2^d$ ) as a function of the FN distance  $\xi_2$ . The normalized attenuation curve predicts a very rapid decay of the dilatational field components in accordance with the  $r_d^{-q}$  amplitude factor in Eq. 2.13. The analysis conveniently avoided the singularity at  $\xi = 0$  by computing the ratio

$$\max(\dot{u}_1^d(\xi_1, \xi_2)) / \max(\dot{u}_1^d(\xi_1, 0^+))$$

between the magnitude of the velocity swing at the off-fault point ( $\xi_1, \xi_2$ ), and the amplitude of the velocity swing at a “near-fault” point ( $\xi_1, 0^+$ ), where ( $\xi_2 = 0^+$ ) corresponds to a FN distance  $\xi_2 = 0.2mm$  within the arbitrarily imposed length scale.

The dashed horizontal red line in Figure 2.2(b) is included to represent the fact that the shear field velocity components are not predicted to decay within the framework of the 2D steady state singular elastic solution.

Figures 2.2(c,d) represent synthetic supershear particle velocity waveforms corresponding to the FP ( $\dot{u}_1$ ) and FN ( $\dot{u}_2$ ) motion components. The curves are velocity field line plots, which have been reflected with respect to the  $\xi_2$ -axis and replotted with an equivalent time axis ( $t = \xi_1/v_r$ ) in accordance with the steady state assumption. The curves plotted in red highlight the “near-fault” velocity waveforms while the blue curves correspond to particle velocity waveforms plotted in FN increments of  $\Delta\xi_2 = 2mm$  out to a distance  $\xi_2 = 8mm$ , within the arbitrarily defined length scale.

There is considerable structure within the synthetic supershear waveforms displayed in Figures 2.2(c,d). The most prominent features are the

sharp, step-like velocity jumps within each waveform, which are attributed to the “arrival” of the shear Mach front. The ratio between these noted velocity jumps remains constant at any point along the shear Mach front and is given by

$$\frac{\delta \dot{u}_1^s}{\delta \dot{u}_2^s} = -\beta_s \operatorname{sgn}(\xi_2). \quad (2.15)$$

Eq.2.15 is readily verified by inspecting the ratio between Eqs. 2.9, 2.10. We note that Eq.2.15 is applicable to the motion components along the shear Mach front of a right-lateral / right-traveling supershear rupture. Examination of the factor  $\beta_s$  (Eqs. 2.11), reveals that  $\delta \dot{u}_1^s / \dot{u}_2^s \geq 1$  when  $\sqrt{2}c_s \leq v_r \leq c_p$ . The motion propagated by shear Mach front is thus generally characterized by a pronounced FP velocity jump, which dominates in magnitude over the corresponding FN velocity jump.

The magnitude of the particle velocity jump at the fault plane results from the superposition of the dilatational and shear field contributions. The radiated shear and dilatational fields naturally propagate away at their respective, characteristic elastic wave speeds and proceed to physically separate with increased FN distance ( $\xi_2$ ) as displayed in Figures 2.2(c,d). The effect is a direct consequence of the fact that space and time are virtually synonymous in the steady-state solution and that the observed separation in time is equivalent to the increased spatial separation between the shear Mach front and the concentrated dilatational field lobe as displayed by the velocity vector field plot of Figure 2.2(a).

The off-fault particle velocity waveforms in Figures 2.2(c,d) are distinctly characterized by a broad pulse-like feature attributed to the concentrated dilatational field, which is registered in advance of the shear Mach front. The FP component of the dilatational field disturbance exhibits a positive velocity swing ( $\delta \dot{u}_1^d$ ) that dominates in magnitude over the corresponding (negative) velocity swing ( $\delta \dot{u}_2^d$ ) exhibited by the FN component. The sign of each dilatational field component in the waveforms is naturally consistent with the sense of motion depicted by the streak plot vectors in Figure 2.2(a). The amplitude of the dilatational field contribution tends to rapidly decay with increased FN distance ( $\xi_2$ ) in stark comparison to the velocity jumps propagated by the shear Mach front, which remain unattenuated out to infinity. Any subtle differences in the magnitude of the velocity jumps along the shear Mach front in Figures 2.2(c,d) are a numerical artifact related to the density of grid points used to generate the field plot. In experimental section of the present paper we demonstrate how the particle velocity waveforms obtained from a variety of LEQ experiments reveal strikingly similar features and always correlate directly with same predicted sense of motion.

### Predicted Sense of Particle Motion for Right-Lateral and Left-Lateral Supershear Rupture Velocity Fields

The diagrams in Figure 2.3 enable quick determination of the expected sense of particle motion of the dilatational field lobe and shear Mach fronts of a left-bilateral or right-bilateral supershear rupture propagating in the stable

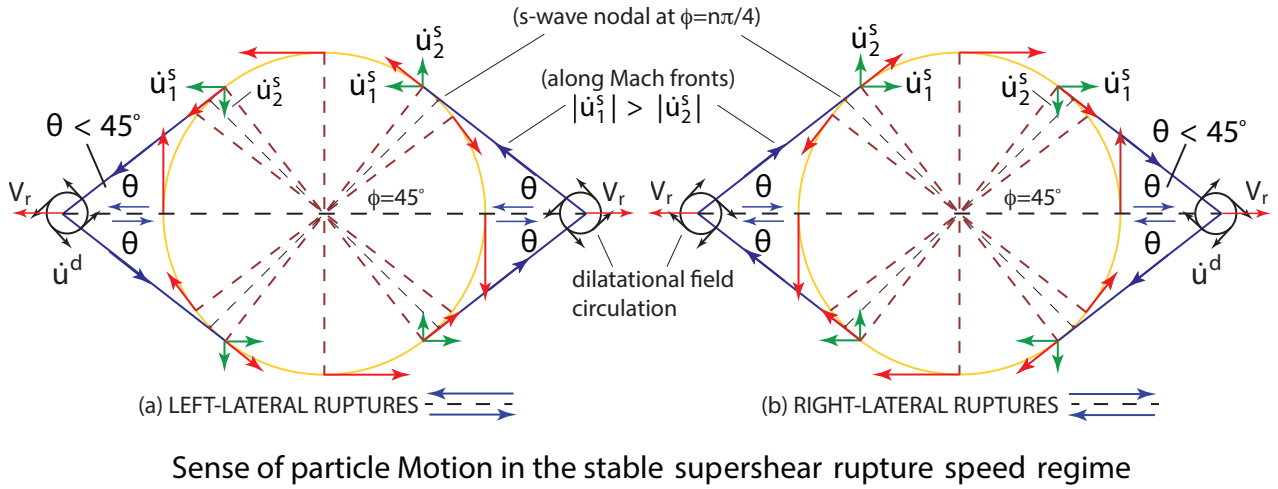


Figure 2.3: (a) Sense of particle motion for (stable) left-lateral supershear rupture (b) Sense of particle displacement for (stable) left-lateral supershear rupture

rupture speed regime  $\sqrt{2}c_s \leq v_r \leq c_p$ .

The large circle in each diagram represents a hypothetical S wavelet emitted by the rupture tip at an earlier time. The dashed black lines oriented at  $\phi = \pm 45^\circ$  with respect to the fault plane intersect the S-wavefronts at the nodal points where  $\dot{u}^s = 0$  and the sense of particle motion reverses. The shear Mach fronts arise from the constructive superposition of a continuum of S-wave fronts emitted by the propagating rupture at earlier times. The blue lines stemming from the crack tips and oriented at an angle  $\theta$  with respect to the fault depict represent the shear Mach fronts. As previously noted,  $\sin^{-1}(c_s/c_p) \leq \theta \leq \pi/4$  in the case of a stable supershear rupture. A shear Mach front must therefore lie tangent to the expanding S-wave front at a point located within the angular domain  $\pi/4 \geq \phi \leq \pi/2 - \sin^{-1}(c_s/c_p)$ , as depicted in Figure 2.3. The point of tangency is simply dictated by the rupture speed  $v_r$  in accordance with Eqs. 2.1. The red arrows lying tangent to the circular S-wave front indicate the sense of particle motion at the point of tangency in accordance with the far-field S-wave radiation pattern produced by a shear dislocation (Aki & Richards, 2002).

The velocity fields predicted by Eqns. 2.9,2.10 describe a right-lateral right-traveling rupture and thus correspond to the right-half of the diagram in Figure 2.3(b). The magnitude and sense of particle motion along a shear Mach front is decomposed into FP and FN particle velocity components ( $\dot{u}_1^s$  and  $\dot{u}_2^s$ ), which are represented by the green arrows in Figure 2.3.

The black circles with tangent vectors, which are centered around the hypothetical rupture tips in each diagram indicate the sense of particle motion of the dilatational velocity field ( $\dot{u}^d$ ), which circulates around the rupture tip in accordance with the kinematic condition  $\nabla u^d = 0$ . Careful examination of the sense of motion corresponding to the right-lateral/right-traveling rupture in Figure 2.3(b) shows it to be in full agreement with the the velocity field plot and synthetic waveforms depicted in Figure 2.2. We

will appeal to this diagram at a later stage when examining and interpreting particle velocity waveforms obtained in supershear rupture experiments.

Finally, we note that the signs of the velocity components given by Eqns. 2.9, 2.10 are readily adjusted in order to describe the remaining 3 cases portrayed in Figure 2.3, i.e., (1) the right-lateral /left-traveling rupture corresponding to the left-half of the diagram in Figure 2.3(b), (2) the left-lateral / right-traveling rupture corresponding to the right-half of the diagram in in 2.3(b), and (3) the left-lateral /left-traveling rupture corresponding to the left-half of Figure 2.3(a).

### Vanishing of the S-wave field at $v_r = \sqrt{2}c_s$

A curious observation was made by Eshelby (1949) when he was studying the motion of dislocations. He showed that at a speed exactly equal to  $\sqrt{2}c_s$  the shear wave contribution (also the Mach front) vanishes.

As the rupture speed  $v_r \rightarrow \sqrt{2}c_s$ , the Mach angle approaches  $\theta = \pi/4$  in accordance with Eq. 2.1. The shear Mach front must therefore vanish at this rupture speed since it is formed along a locus of nodal points positioned at  $\phi = \pi/4$  on the radiated S-waves. This is a fundamental wavefront superposition property, which must occur as  $v_r \rightarrow \sqrt{2}c_s$ , irrespective of whatever dynamic rupture model is invoked. Indeed, the vanishing Mach front condition naturally emerges from the 2D steady state singular elastic solutions given by Eq. 2.8. Figure 2.4 depicts velocity field, which results in the limiting case when  $v_r = \sqrt{2}c_s$ . The dilatational field is now prominently displayed, with the shear Mach fronts conspicuously absent at this rupture speed. Note that the amplitude of the dilatational field is now characterized by a square root singularity ( $r_d^{-1/2}$ ) at this rupture speed since  $q = 1/2$  in accordance with Eq. 2.12 when  $v_r = \sqrt{2}c_s$ .

The prediction that S-wave radiation should vanish at  $v_r = \sqrt{2}c_s$  is consistent with the observations made by (Broberg, 1989) in his analysis of supershear velocities in the case of a mode II rupture. A continuum mechanics based treatment of the significance of the rupture speed  $v_r = \sqrt{2}c_s$  in isotropic, steady-state elastodynamics problems is also found in Liu et al. (1995) and Gao et al. (1999). In particular, the paper by Liu et al. (1995) uses continuum mechanics to show that a shear Mach front features jumps in shear stress and particle velocity. These jumps are shown to disappear when the rupture speed reaches  $v_r = \sqrt{2}c_s$ . Consistent with the above discussion, the work of Gao et al. (1999) uses a continuum mechanics approach to identify radiation-free stress states for various steady-state, linear elastodynamics problems including dislocations and cracks. Dunham & Archuleta (2005) conducted numerical simulations using a linear distance weakening relation in a 2D steady slip pulse model order to examine how energy is partitioned between radiated S-waves and fracture, and assess how this relationship is modulated by the ratio between the cohesive zone ( $R$ ) and slip pulse length ( $L$ ). The analysis concluded that "most of the energy is radiated, with the exception of a small range of velocities surrounding

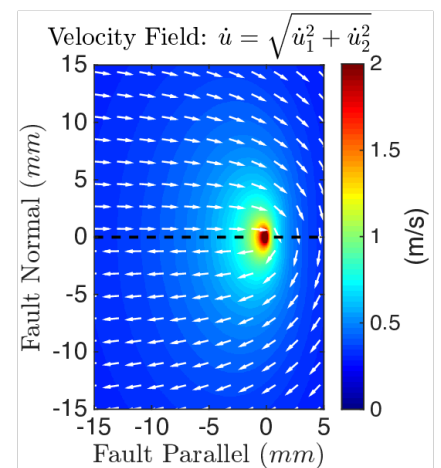


Figure 2.4: Supershear rupture velocity field at  $v_r = \sqrt{2}c_s$ .

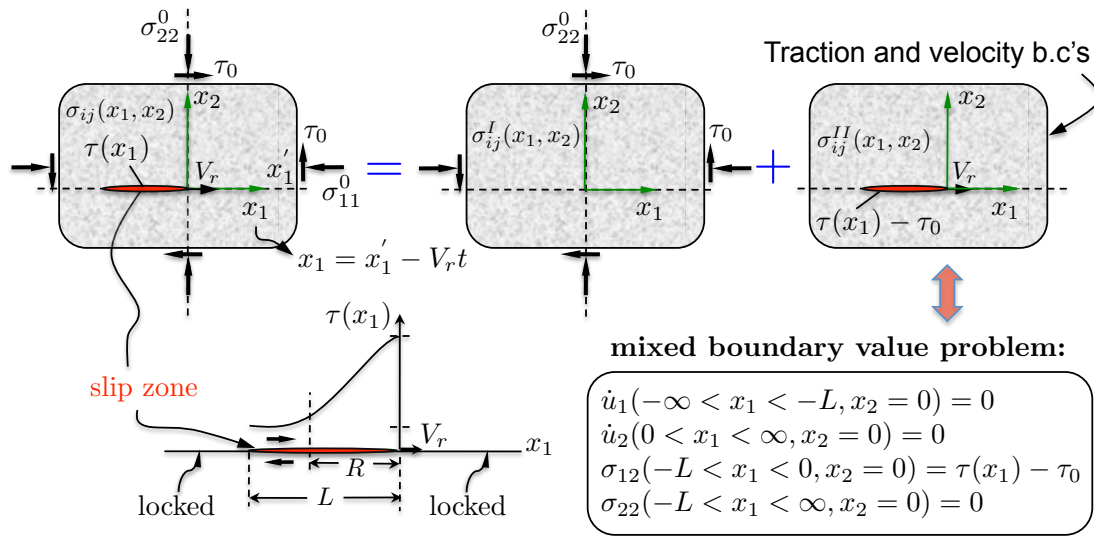


Figure 2.5: Mixed boundary value problem: 2D steady state sliding pulse subject to a cohesive zone  $\tau(x_1)$ .

$\sqrt{2}c_s$ , since no S waves are excited at this speed.” (Dunham & Archuleta, 2005). In this context, the 2D steady state singular elastic dynamic shear crack model by Freund (1979) corresponds to the limiting case  $R/L \rightarrow 0$ , whereby no energy is consumed by fracture at any rupture speed other than at  $v_r = \sqrt{2}c_s$ , where no S-waves are radiated.

## 2.3 2D Steady State Cohesive Zone Models

### Steady State Cohesive Zone Models

The underlying assumption in the singular elastic crack models is that rupture process is assumed to occur at a mathematically singular crack tip. A major weakness of this type of model is that it fails to account for a finite process zone and a cohesive strength which varies along the length of the rupture zone. Non-singular, slip-weakening models for shear, or Mode II cracks, incorporate a description of the shear tractions within a finite breakdown zone (Barenblatt, 1962; Ida, 1972; Palmer & Rice, 1973). The shear traction is generally characterized by a peak strength just ahead of the crack tip, which decreases with increased distance behind the crack tip and then levels off to a residual shear strength level. The incorporation of a cohesive zone in these models introduces a characteristic length scale into the analysis, which is distinctly missing in the singular elastic models. The resulting length scale is proportional to the size of the breakdown zone. Non-singular models such as these and others, which have followed, generally feature 2D steady-state solutions that depend on the real and imaginary parts of the following integral (Broberg, 1978, 1989, 1999; Muskhelishvili, 1953)

$$N(z_{p/s}) = c_1 [\Omega(z_{p/s})]^q \int_{\Gamma} \frac{\tau(w)}{[\Omega_+(w)]^q (w - z_{p/s})} dw, \quad (2.16)$$

where  $\Omega$  is an analytic function with branch cuts along the crack (or pulse),  $\Gamma$ ,  $c_1$  depends on the rupture speed, and  $q$  is the rupture speed dependent

exponent given by Eqs. 2.12.  $\tau(x)$  is either prescribed *a priori* (e.g. a slip-weakening model), or is obtained for slip-velocity-weakening models by solving a singular integral equation (Samudrala et al., 2002a,b). This integral is evaluated in the Cauchy Principal Value sense and has analytical closed-form solutions for certain forms of  $\tau(x)$  and sub-Rayleigh rupture velocities. For supershear cases the closed-form solution exists only for constant  $\tau(x)$ , i.e.,  $\tau(x) = \tau_p$ .

## 2D steady-state Supershear Slip-Pulse with Prescribed Shear Traction within a Finite Slip Zone

Bhat et al. (2007) and Dunham & Archuleta (2005) extended an earlier solution given by Broberg (1989), to obtain non-singular analytical solutions for the stress and particle velocity fields radiated by a 2D steady-state supershear slip-pulse with an arbitrarily prescribed shear traction within a finite slip zone. The mixed boundary value problem (bvp) along with a description of the superposition principles invoked in the solution are summarized in Figure 2.5. A right-lateral supershear slip pulse is assumed to propagate in the positive  $x_1'$  direction, along the fault plane adjoining two identical, isotropic, and linear elastic half-spaces. A local coordinate system  $(x_1, x_2)$  is introduced at the leading edge of the slip pulse, which translates with the slip pulse at the steady-state rupture speed  $v_r$ . The material making up each elastic half-space is characterized by a shear modulus  $\mu$ , shear wave speed  $c_s$ , and dilatational wave speed  $c_p$ . Far field stresses  $\sigma_{11}^0, \sigma_{22}^0$ , and  $\sigma_{12}^0 = \tau_0$  are exerted on the fault plane as shown. The slip zone, which spans the region  $-L \geq x \leq 0$ , is subjected to a prescribed shear traction  $\tau(x_1)$ , while regions of the fault plane to the right and left of the slip zone remain locked. The shear traction relation  $\tau(x_1)$  emulates a breakdown zone of length  $R$  over which the sliding resistance degrades smoothly and monotonically before settling to a residual strength level. The solution to the mixed bvp problem is approached by invoking linear superposition as depicted in Figure 2.5. The figure to the left of the equality symbol represents the full mixed bvp. The first figure to the right of the equality symbol represents the trivial solution corresponding to the constant far field stresses  $\sigma_{ij}^I(x_1, x_2) = \sigma_{11}^0 + \sigma_{22}^0 + \tau_0$ , which are imposed upon the fault at all times. The second figure to the right of the equality symbol represents the local stress field problem, which must be solved, subject to the prescribed traction  $\tau(x_1) - \tau_0$  across the slip zone. The complete state of stress is obtained by superimposing the two solutions.

The solution path adopted invoked the Poisson representation for the displacement field  $\vec{u} = \vec{u}^d + \vec{u}^s$  where  $\vec{u}^d, \vec{u}^s$  represent the dilatational and shear field contributions, respectively. Displacement field components are subject to the conditions  $\nabla \cdot \vec{u}^s = 0$  and  $\nabla \times \vec{u} = 0$  and are each governed by a wave equation and a characteristic elastic wave speed in the time domain. A Galilean coordinate transformation  $x_1 = x_1' - v_r t$  is imposed, which transforms the wave equations in the time domain to equivalent steady-state forms in the spatial domain. Restriction of the rupture speeds to the supershear rupture speed domain ( $c_s \leq v_r \leq c_p$ ) leads to the following

partial differential equations, which govern the dilatational and shear displacement fields.

$$\left( \frac{\partial^2}{\partial x_1^2} + \frac{\partial^2}{\partial (\alpha_d^2 x_2^2)} \right) u_i^d(x_1, x_2) = 0 \quad (2.17)$$

$$\left( \frac{\partial^2}{\partial x_1^2} - \frac{1}{\beta_s^2} \frac{\partial^2}{\partial x_2^2} \right) u_i^s(x_1, x_2) = 0 \quad (2.18)$$

The dilatational field term is now governed by a scaled Laplacian equation while the shear field contribution is still governed by a wave equation, but with the factor  $\beta_s$  now serving as the characteristic “wave speed”. The problem is solved by determining the analytic function  $N(z)$ , which satisfies Eqs.2.17 subject to the shear and normal stress boundary conditions summarized in Figure 2.5. The derivation ultimately leads to a standard Hilbert problem in analytic function theory, which is then solved subject to the prescribed traction-free boundary conditions on the crack surfaces. Solutions for the stress and particle velocity fields are obtained in terms of a single integral expression for  $\tau(x_1)$  over the slip zone, weighted by a singular kernel. The fault-parallel ( $\dot{u}_1$ ) and fault-normal ( $\dot{u}_2$ ) particle velocity components for the case of a right-traveling, right-lateral slip pulse are given by

$$\dot{u}_1 = -\frac{v_r}{\mu} \left[ \frac{1}{2\alpha_d} \Im N(z_d) + \frac{\beta_s^2 - 1}{4\alpha_d} \Im N(z_s) \right] \quad (2.19)$$

$$\dot{u}_2 = -\frac{v_r}{\mu} \left[ \frac{1}{2} \Re N(z_d) - \text{sgn}(x_2) \frac{\beta_s^2 - 1}{4\alpha_d \beta_s} \Im N(z_s) \right] \quad (2.20)$$

where the variables  $z_d, z_s$  are given by

$$z_d = x_1 \pm i\alpha_d x_2 ; \quad z_s = x_1 + \beta_s x_2 \quad (2.21)$$

and

$$N(z) = -\frac{\sin(\pi q)}{\pi} z^{1-q} (z + L)^q \int_{-L}^0 \frac{\tau(w) - \tau_0}{(-w)^{1-q} (w + L)^q (w - z)} dw \quad (2.22)$$

represents a complex integral solution of the Hilbert problem corresponding to a specific case of the general form given by Eqs.2.16.  $N(z)$  is analytic everywhere except along the branch cut ( $-L < x_1 < 0$ ) corresponding to the slip zone. The analytic function  $N(z)$  provides the connection between the shear traction  $\tau(x)$  within the slip zone and the explicit form of the stress and particle velocity fields radiated by a 2D steady state supershear slip pulse. In the case of a sliding mode II rupture,  $\tau(x)$  represents the frictional resistance (cohesion), which stems from a governing friction law. Numerical solutions for Eqs.2.19 and Eqs.2.20 were obtained by Dunham & Archuleta (2005) using a linear-distance weakening model for  $\tau(x)$ , originally formulated by Palmer & Rice (1973).

The general expression for  $N(z)$  is given here and briefly interpreted largely for the sake of completeness. We will soon establish unique kinematic and spatiotemporal properties, which arise from Eqs.2.19,2.20, which do not require an explicit solution for  $N(z)$  and are thus independent of the shear traction within the slip zone and any underlying friction law. The

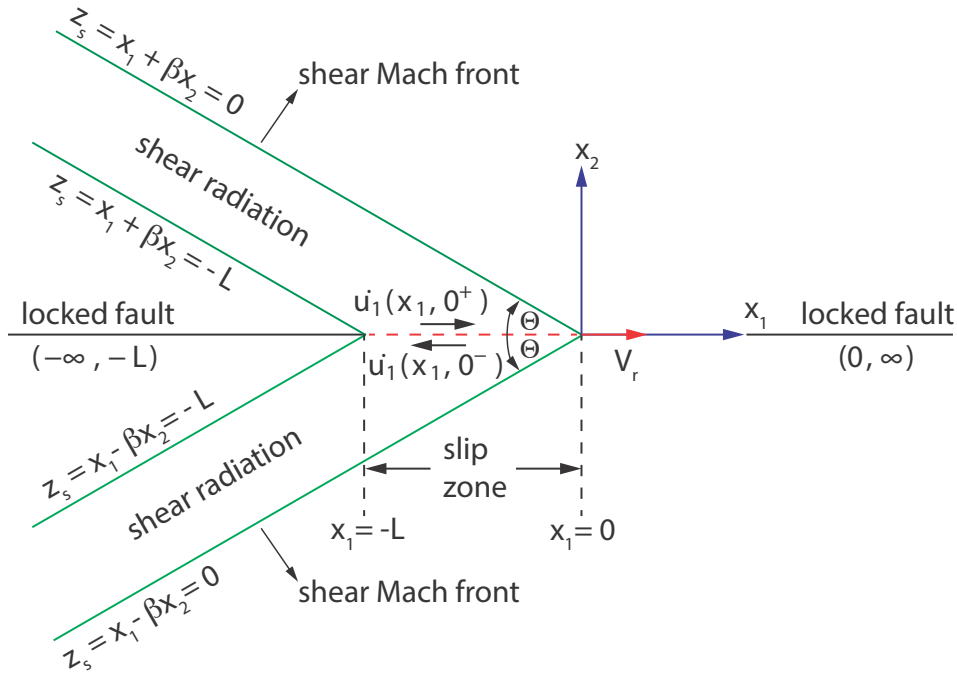


Figure 2.6: S-wave radiation field emitted from the slip zone

anti-symmetric property of the analytic function  $N(z)$ , i.e.,  $\Im N(z) = -\Im N^-(\bar{z})$ , is exploited in order to glean these fundamental relationships from the 2D steady state slip pulse solutions.

A careful examination of Eqs. 2.22 at points very close to the fault (letting  $z_I \rightarrow 0$ ) reveals that  $N(z)$  is a complex function only within the interval  $(-L < x_1 < 0)$ , corresponding to the slip zone. This implies that S-wave radiation is confined within a region of space bounded by pairs of leading and trailing characteristics  $z_s = x_1 \pm \beta_s x_2 = c$ , corresponding to the shear Mach fronts, which stem from the points  $x_1 = 0$  and  $x_1 = -L$ , as depicted in Figure 2.6. In the case of a right-lateral/right-traveling slip pulse, the characteristic defined by  $z_s = x_1 + \beta_s x_2 = 0$  describes the leading, negatively-sloped shear Mach front within the upper half-space ( $x_2 > 0$ ), while the characteristic  $z_s = x_1 - \beta_s x_2 = 0$  corresponds to the leading positively-sloped shear Mach front within the lower half-space ( $x_2 < 0$ ). The “sign function”  $sgn(x_2)$  in Eqs.2.20 accommodates for the anti-symmetry of  $\Im N(z_s)$  with respect to the fault plane and extends the solution into the lower half-space ( $x_2 < 0$ ). The FN velocity component would otherwise abruptly reverse sign cross the fault, which is prohibited in the case of a mode II rupture.

The dilatational and shear field contributions are each uniquely represented by separate terms in the solutions given by Eqs.2.19 and Eqs.2.20. The first term in each equation corresponds to the dilatational field contribution, expressed in terms of the real and imaginary parts of  $N(z_d)$  and is evaluated at points  $z_d = x_1 + i\alpha_d x_2$  in the complex plane, i.e.,  $\Im N(z_d)$  in Eqs.2.19 and  $\Re N(z_d)$  in Eqs.2.20. The shear field terms are both functions of  $\Im N(z_s)$ , and are evaluated exclusively along the family of characteristics defined by  $z_s = x_1 \pm \beta_s x_2 = c$ , where  $c$  is a constant.

Due to the finite crack-tip stresses and finite width of the process zone ( $R$ ) (Figure 2.5), the resulting particle velocity waveforms are of finite width and magnitude, unlike the waveforms, which emerge from the singular elastic solution. Indeed, as previously mentioned, the singular elastic solution given by Freund (1979) emerges as a special case of the 2D steady state slip pulse model in the limit ( $R/L \rightarrow 0$ ). Also, in stark contrast to the singular models, the crack-tip energy flux is non-zero and finite in the supershear regime (Broberg, 1989; Rosakis et al., 2007; Samudrala et al., 2002a,b).

### Relationship Between the Slip Function and the Particle Velocity Field Propagated by the Shear Mach Front

The slip function along the fault ( $x_2 = 0$ ) is defined as

$$\Delta \dot{u}_1(x_1, 0) = \dot{u}_1(x_1, 0^+) - \dot{u}_1(x_1, 0^-) \quad (2.23)$$

where  $\dot{u}_1(x_1, 0^+)$  and  $\dot{u}_1(x_1, 0^-)$  represent the FP velocity components at two infinitesimally separated points positioned just above and below the fault. We note that since  $z_d = z_s = x_1^+$  as  $x_2 \rightarrow 0^+$ , Eqn. 2.19 then assumes the form

$$\dot{u}_1(x_1, 0^+) = -\frac{v_r}{\mu} \left[ \frac{1}{2\alpha_d} \mathfrak{I}N^+(x_1) + \frac{\beta_s^2 - 1}{4\alpha_d} \mathfrak{I}N^+(x_1) \right] \quad (2.24)$$

where

$$N^+(x_1) = \lim_{x_2 \rightarrow 0^+} N(z) = \frac{\sin(\pi q)}{\pi} e^{-i\pi q} \left[ (-x_1)^{1-q} (x_1 + L)^q \times \int_{-L}^0 \frac{\tau(w) - \tau_0}{(-w)^{1-q} (w + L)^q (w - x_1)} dw + i\pi[\tau(x_1) - \tau_0] \right] \quad (2.25)$$

is a complex expression containing a real integral, which is evaluated within the slip zone ( $-L < x_1 < 0$ ). We note the presence of the familiar rupture speed dependent factor  $q$  given by Eqs.2.12, which continues to govern the rate at which the field strength decays with increased distance from the fault plane. Invoking mode II anti-symmetry of the fault-parallel component, i.e.,  $\Delta \dot{u}_1(x_1, 0) = 2\dot{u}_1(x_1, 0^+)$ , in combination with Eqs.2.24, leads to an alternate expression for the slip function given by

$$\Delta \dot{u}_1(x_1, 0) = -2 \frac{v_r}{\mu} \left( \frac{\beta_s^2 + 1}{4\alpha_d} \right) \mathfrak{I}N^+(x_1). \quad (2.26)$$

Similarly, since  $\Delta \dot{u}_1(x_1, 0) = -2\dot{u}_1(x_1, 0^-)$  and since

$$\mathfrak{I}N^+(x_1) = -\mathfrak{I}N^-(x_1)$$

(mode II antisymmetry), it follows that

$$\Delta \dot{u}_1(x_1, 0) = 2 \frac{v_r}{\mu} \left( \frac{\beta_s^2 + 1}{4\alpha_d} \right) \mathfrak{I}N^-(x_1). \quad (2.27)$$

and thus,

$$\Delta \dot{u}_1(x_1, 0) = \mp 2 \frac{v_r}{\mu} \left( \frac{\beta_s^2 + 1}{4\alpha_d} \right) \mathfrak{I}N^\pm(x_1) \quad (2.28)$$

The somewhat ambiguous form given by Eqs. 2.28 can be recast into a more compact expression by invoking  $\Delta\dot{u}_1(x_1, 0) = \Delta\dot{u}_1(z_s)$  and  $\Im N^+(x_1) = \Im N(z_s)$ , where  $z_s = x_1 \pm \beta_s x_2 = c$  defines the characteristics (shear Mach fronts), which extend to infinity within each respective half-space. We may then write

$$\Delta\dot{u}_1(z_s) = -sgn(x_2) \frac{2v_r}{\mu} \left( \frac{\beta_s^2 + 1}{4\alpha_d} \right) \Im N(z_s) \quad (2.29)$$

where the function  $sgn(x_2)$  acts to preserve the sign of  $\Delta\dot{u}_1(z_s)$  regardless of which characteristic is assumed. Substitution of Eqs.2.29 into Eqs.2.19 and Eqs.2.20 leads to alternative forms for the particle velocity field components given by

$$\dot{u}_1(z) = -\frac{v_r}{\mu} \left[ \frac{1}{2\alpha_d} \Im N(z_d) \right] + sgn(x_2) \frac{\beta_s^2 - 1}{2(\beta_s^2 + 1)} \Delta\dot{u}_{x_1}(z_s) \quad (2.30)$$

$$\dot{u}_2(z) = \left[ -\frac{v_r}{\mu} \frac{1}{2} \Re N(z_d) - \frac{1}{2\beta_s} \frac{\beta_s^2 - 1}{\beta_s^2 + 1} \Delta\dot{u}_{x_1}(z_s) \right] \quad (2.31)$$

Eqs.2.30 and Eqs.2.31 reveal that a shear Mach front carries an unattenuated, scaled replica of the slip function deep into the far field Dunham & Archuleta (2005). This unique feature of supershear S-wave radiation fields is in stark contrast to the nature of S-wave radiation fields arising from a sub-Rayleigh ruptures, which are stripped of high-frequency content and attenuate rapidly with off-fault distance Dunham & Archuleta (2005) and Mello et al. (2010).

Finally, we may consider the limiting case, where the dilatational field contribution has decayed away, leaving only the unattenuated FP and FN shear field velocity components given by

$$\dot{u}_1(z_s) \approx sgn(x_2) \frac{1}{2} \frac{\beta_s^2 - 1}{\beta_s^2 + 1} \Delta\dot{u}_1(z_s) \quad (2.32)$$

$$\dot{u}_2(z_s) \approx -\frac{1}{2\beta_s} \frac{\beta_s^2 - 1}{\beta_s^2 + 1} \Delta\dot{u}_1(z_s). \quad (2.33)$$

The sign of the FP and FN motion components propagated along the shear Mach front are thus determined by the corresponding sign of the slip function  $\Delta\dot{u}_1$  at the fault plane.

Dividing Eqs.2.32 by Eqs.2.33 recovers the previously noted relationship given by Eqs.2.15 for the ratio between the FP and FN motion components. The relationship is now expressed in terms of the characteristic variable  $z_s = x_1 \pm \beta_s x_2$  and given by

$$\frac{\delta\dot{u}_1(z_s)}{\delta\dot{u}_2(z_s)} = -sgn(x_2)\beta_s; \text{ (right-lateral/right-traveling)}. \quad (2.34)$$

The forms given by Eqs.2.15 and Eqs.2.34 apply exclusively to a right-lateral/right-traveling rupture. The result must be adjusted in order to for the case of a right-lateral/left-traveling supershear rupture, in which case, the ratio between the FP and FN motion components propagated by the shear Mach

fronts is given by

$$\frac{\delta \dot{u}_1(z_s)}{\delta \dot{u}_2(z_s)} = \text{sgn}(x_2)\beta_s; \text{ (right-lateral/left-traveling)}. \quad (2.35)$$

The forms expressed by Eqs.2.34 and Eqs.2.35 are consistent with the predicted sense of the motion along the shear Mach fronts of a right-lateral rupture as displayed in Figure 2.3. Similar modifications are readily implemented for the case of left-lateral ruptures.

### Partitioning Relationship Between the Frictional Fault Sliding Speed and the FP Components of the Dilatational Field and Shear Mach Front

We now recast the 2D steady-state particle velocity field expressions into alternative forms, which will prove very useful at a later stage in the analysis and interpretation of the on-fault and off-fault particle velocity waveforms obtained in LEQ supershear experiments. Recall the expression for the frictional fault sliding speed  $\dot{u}_1(x_1, 0^+) = \lim_{x_2 \rightarrow 0^+} \dot{u}_1(z)$ , given by Eqs.2.24.

Experimental estimates of the frictional fault sliding speed are obtained in laboratory earthquake experiments by focusing a laser vibrometer beam at nearly grazing incidence, onto a point positioned within  $200\mu m$  above frictional fault plane. Details of the vibrometer probe configuration are described in the experimental methods section. Note that obtaining a temporally resolved “on-fault” record of  $\dot{u}_1(x_1, 0^+, t)$  is equivalent to measuring  $\mathcal{J}N^+(x_1, t)$ , when interpreted in the context of Eqs.2.24. Substituting for  $\mathcal{J}N^+(x_1)$  in Eqs.2.24, using the slip function relation given by Eqs.2.26, and invoking anti-symmetric slip function relation  $\dot{u}_1(x_1, 0^+) = \frac{1}{2}\Delta\dot{u}_1(x_1, 0)$  leads to

$$\dot{u}_1(x_1, 0^+) = \left(\frac{2}{\beta_s^2 + 1}\right)\dot{u}_1(x_1, 0^+) + \left(\frac{\beta_s^2 - 1}{\beta_s^2 + 1}\right)\dot{u}_1(x_1, 0^+) \quad (2.36)$$

We note that the first and second terms to the right of the equality symbol must still represent the dilatational and shear field contributions, respectively. Eqs.2.36 thus reveals how the frictional fault sliding speed  $\dot{u}_1(x_1, 0^+)$ , is partitioned between the dilatational and shear field radiation terms in accordance with the rupture speed dependent amplitude scaling factors appearing in parentheses.

Hence we may define,

$$r_d = \frac{\dot{u}_1^d(x_1, 0^+)}{\dot{u}_1(x_1, 0^+)} = \frac{2}{\beta_s^2 + 1} \quad (2.37)$$

as the FP amplitude scaling factor that dictates how much of the frictional fault sliding speed  $\dot{u}_1(x_1, 0^+)$  is converted into the FP component of the dilatational field and subsequently radiated away.

A second FP amplitude scaling factor given by

$$r_s = \frac{\dot{u}_1^s(x_1, 0^+)}{\dot{u}_1(x_1, 0^+)} = \frac{\beta_s^2 - 1}{\beta_s^2 + 1} \quad (2.38)$$

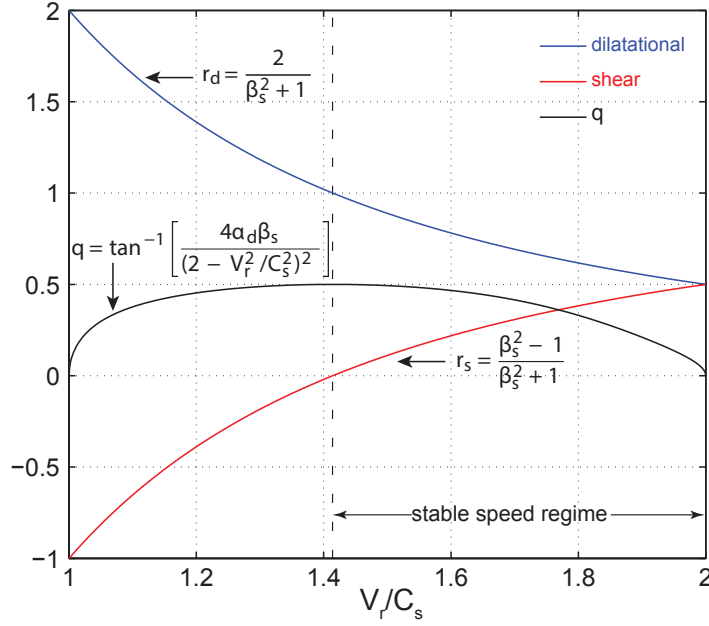


Figure 2.7: Partitioning of the Frictional Fault Sliding Speed Between the FP Velocity Components of the Dilatational Field and Shear Mach Front

is similarly defined, which governs how what portion of the frictional fault sliding speed  $\dot{u}_1(x_1, 0^+)$  is converted into the FP component of the shear field  $\dot{u}_1^s(z_s)$  and subsequently propagated out into the far field along a shear Mach front.

Eqs.2.37 and Eqs.2.38 represents a 2D steady-state, non-singular, scaling relationship between the sliding component induced by the supershear rupture at the fault plane and the FP component propagated by the the shear Mach front. A similar relation naturally applies on the opposite side of the fault plane, between the frictional fault sliding speed  $\dot{u}_1^d(x_1, 0^-)$ , and the shear field velocity component  $\dot{u}_1^s(z_s)$ , where  $z_s = x_1 - \beta_s x_2$  corresponds to the shear Mach front within the lower half-space  $x_2 < 0$ .

Alternative and simplified forms for  $r_s$  and  $r_d$ , given by

$$r_d = 2 \frac{c_s^2}{v_r^2} ; r_s = 1 - 2 \frac{c_s^2}{v_r^2} \quad (2.39)$$

are obtained by substituting for  $\beta_s$  through Eqn. 2.11, where  $r_s + r_p = 1$  is naturally observed.

Figure 2.7 depicts the graphical relationship between the amplitude scaling factors  $r_d$ ,  $r_s$  given by Eqs.2.37 and Eqs.2.38 and the normalized rupture speed  $v_r/c_s$ . A plot of the rupture speed dependent factor  $q$ , given by Eqs.2.12 is also included in the figure. The vertical dashed line at  $v_r/c_s = \sqrt{2}$  denotes the boundary between the unstable and stable rupture speed domains.

The maximum normalized rupture speed  $v_r/c_s = 2$  in Figure 2.7 corresponds to the limit  $v_r \rightarrow c_p$ , for a material with  $c_p = 2c_s$  such as the H-100 material used in LEQ experiments. The dilatational partitioning fac-

tor is bounded between  $0.5 \leq r_d \leq 1$  within the stable rupture speed regime, reaching a maximum value  $r_d = 1$  when  $v_r/c_s = \sqrt{2}$  and decreasing with increased rupture speed toward a minimum value of  $r_d = 0.5$  as  $v_r \rightarrow c_p$ . The shear field partitioning factor ( $r_s = 1 - r_d$ ) is bounded between  $0 \leq r_s \leq 0.5$  within the stable rupture speed regime, and ranges from a minimum value  $r_s = 0$  when  $v_r/c_s = \sqrt{2}$  to a maximum value  $r_s = 0.5$  as  $v_r \rightarrow c_p$ .

The fact that  $r_s \rightarrow 0$  as  $v_r/c_s \rightarrow \sqrt{2}$ , further implies that the shear Mach front must vanish altogether at this rupture speed in light of Eqs. 2.34. This prediction is consistent with the heuristic argument given earlier that the shear Mach front must vanish as  $v_r/c_s \rightarrow \sqrt{2}$  since it is formed by the locus of nodal points of the shear wavelets radiated by the rupture front at earlier times. A more rigorous treatment of energy partitioning between the shear and dilatational fields reveals that the energy, which would otherwise be radiated as shear waves is instead consumed by fracture at this rupture speed (Dunham & Archuleta, 2005).

Indeed there are no S-waves radiated at this rupture speed and so the heuristic argument based upon the nodal point condition, while true, is a weaker condition, which is superseded by energy partitioning between the shear and dilatational fields. We also note that  $q = 1/2$  at  $v_r/c_s \rightarrow \sqrt{2}$  thus revealing that the dilatational field will tend to decay as fast as a sub-Rayleigh rupture in accordance with Eqs. 2.13 at this unique rupture speed.

The portion of the curves corresponding to the unstable rupture speed regime ( $c_s \leq v_r < \sqrt{2}c_s$ ) appears somewhat odd and confusing at first glance, since  $-1 \leq r_s < 0$  and  $1 < r_d \leq 2$  within this domain. The situation is best understood by referring back to Figure 2.3 and noting that the shear Mach front will be tangent to the S-wavelets along points corresponding to  $(0 < \phi \leq \pi/4)$  when  $c_s \leq v_r < \sqrt{2}c_s$ . The FN component is now directed upward and dominates in magnitude over the FP component, which is directed opposite to the assumed direction of slip. Thus  $\dot{u}_1^s(z_s) < 0$  even though the sliding speed  $\dot{u}_1(x_1, 0^+)$  is positive. The negative range of values exhibited by  $r_s$  simply reflects the fact that  $\dot{u}_1^s(z_s) < 0$  when  $c_s \leq v_r < \sqrt{2}c_s$ . The corresponding positive range of values  $1 < r_d \leq 2$  for the dilatational field contribution  $\dot{u}_1^d(z_s)$  offset the negative contribution of the shear field so as to satisfy  $r_s + r_d = 1$  within the unstable rupture speed domain.

Finally we note that there is also no known counterpart of Eqs. 2.36, which applies to sub-Rayleigh rupture field components, nor is there an analogous partitioning relationship, which applies to the FN component ( $\dot{u}_2(x_2, 0^+)$ ) of a supershear rupture. The presence of  $\Re N(z_d)$  in the dilatational field term and  $\Im N(z_s)$  in the shear field term of Eqs. 2.20 (and no anti-symmetry relation for  $\dot{u}_2$ ) prohibits the types of substitutions and algebraic manipulations that were adopted in the case of the fault-parallel component ( $\dot{u}_1$ ). That Eqs. 2.36 represents a unique scaling relationship, which emerges from the 2D state slip pulse solution and only strictly applies to the FP velocity

(and normal stress  $\sigma_{11}$ ) component of a supershear rupture field.

### Off-fault Stress Field due to a Supershear Slip Pulse

Following the work of Poliakov et al. (2002), Rice et al. (2005) calculated the stress field near an elastodynamic slip pulse of length  $L$  propagating in steady state at the rupture speed  $v_r$  (the speed of the pulse) when  $v_r$  was in the sub-Rayleigh wave speed regime. They used a non-singular slip-weakening model in a special simplified form in which stress is assumed to vary linearly with spatial position. Weakening begins when shear stress on the fault,  $\tau$ , first reaches a finite peak strength  $\tau_p$  on an unslipped part of the fault. When slip begins,  $\tau$  decreases with slip, approaching  $\tau_r$  at large slip; the simplified model assumes linear degradation of strength with distance over the slip-weakening zone length,  $R$ , and then a constant strength value over the remaining part of the pulse. The decrease of  $\tau$  with slip  $\delta$  is then not linear in  $\delta$ , but is moderately different from linear and, in the sub-Rayleigh range, it is independent of  $v_r$  for a given  $R/L$ , and is only weakly dependent on  $R/L$  (Rice et al., 2005). We show later here that a similar feature holds for the supershear range, but with a small dependence on  $v_r$ . The peak strength  $\tau_p$  is generally assumed to be proportional to the compressive normal stress acting on the fault and is set equal to  $-f_s(\sigma_{yy})$ . We take the static friction coefficient  $f_s = 0.6$  based on lab values for typical rocks. The residual strength  $\tau_r = -f_d(\sigma_{yy})$  is determined by the dynamic coefficient of friction,  $f_d$ . We choose  $f_d/f_s = \tau_r/\tau_p = 0.2$  as in Poliakov et al. (2002) and Rice et al. (2005) but note that this number cannot be ascertained precisely. However, some results with appropriately scaled measures of stress changes (scaled with  $\tau_0 - \tau_r$  or  $\tau_p - \tau_r$ ) do not depend on  $\tau_r/\tau_p$ .

Let the total stress tensor during the propagation of the slip-pulse be given by  $\sigma_{ij} = \sigma_{ij}^0 + \Delta\sigma_{ij}$  where  $\sigma_{ij}^0$  and  $\Delta\sigma_{ij}$  are, respectively, the tensors of pre-stress and perturbation of stress. The perturbation of the stress field in a homogeneous, isotropic, elastic medium due to a slip pulse propagating at supershear speeds (under plane strain conditions in an unbounded solid) must have a form in terms of a single analytic function  $N(z)$  (see eqn. 2.22), such that the stress perturbations are given by

$$\begin{aligned}\Delta\sigma_{xx} &= \frac{1 + \beta_s^2 + 2\alpha_d^2}{2\alpha_d} \Im N(z_d) + \frac{\beta_s^2 - 1}{2\alpha_d} \Im N(z_s) \\ \Delta\sigma_{xy} &= \Re N(z_d) + \frac{(\beta_s^2 - 1)^2}{4\alpha_d\beta_s} \Im N(z_s) \\ \Delta\sigma_{yy} &= \frac{\beta_s^2 - 1}{2\alpha_d} \Im [N(z_d) - N(z_s)] \\ \Delta\sigma_{zz} &= \nu(\Delta\sigma_{xx} + \Delta\sigma_{yy})\end{aligned}\tag{2.40}$$

where  $\beta_s = \sqrt{v_r^2/c_s^2 - 1}$ ;  $\alpha_d = \sqrt{1 - v_r^2/c_d^2}$ ;  $z_s = x - v_r t + \hat{\alpha}_s |y|$  and  $z_d = x - v_r t + i\alpha_d y$ ;  $i = \sqrt{-1}$ ; we show results here at time  $t = 0$ .  $\nu$  is the Poisson ratio for the medium and is chosen later to be 0.25, so that  $c_d = \sqrt{3}c_s$ , in our numerical evaluations.  $c_d$  and  $c_s$  are the P (dilatational) and S (shear) wave speeds of the medium respectively.  $N(z)$ , with different arguments, expresses the contributions of the P (dilatational) and the S (shear) waves

propagating through the medium; it must be chosen so that the stresses follow the linear strength degradation boundary conditions. A condition for such a solution to exist, giving bounded stresses at the leading and trailing edges of the pulse, is that  $N(z) \rightarrow 0$  as  $|z| \rightarrow \infty$  (Muskhelishvili, 1953). This results in a constraint equation on the shear pre-stress level which is consistent with a given  $R/L$  and  $v_r$ . That can be determined as follows.

Define

$$\sigma_{drop} = \frac{\tau_0 - \tau_r}{\tau_p - \tau_r} \quad (2.41)$$

Then

$$\sigma_{drop} = \frac{I_1}{I_2} \quad (2.42)$$

where

$$I_1 = \int_0^1 \frac{(1-t)dt}{(t)^{1-q}(L/R-t)^q}; I_2 = \int_0^1 \frac{dt}{(t)^{1-q}(1-t)^q}$$

in non-dimensionalized form. Note that since  $q = q(v_r)$  is involved, the scaled dynamic stress drop,  $(\tau_0 - \tau_r)/(\tau_p - \tau_r)$  depends on both  $R/L$  and  $v_r/c_s$  (Figure 2), unlike for its sub-Rayleigh analogue in which case the dependence was only on  $R/L$ . Similarly  $N(z)$  can be non-dimensionalized as follows

$$\frac{N(\hat{z})}{\tau_0 - \tau_r} = -\frac{\sin(\pi q)}{\pi} \hat{z}^{1-q} \left( \hat{z} + \frac{L}{R} \right)^q \times \left[ \frac{R}{L} I_3 - \left( \frac{\tau_p - \tau_r}{\tau_0 - \tau_r} \right) I_4 \right] \quad (2.43)$$

where

$$I_3 = \int_0^1 \frac{dt}{(t)^{1-q}(1-t)^q(t + \hat{z}\frac{R}{L})};$$

$$I_4 = \int_0^1 \frac{(1-t)dt}{(t)^{1-q}(\frac{L}{R}-t)^q(t + \hat{z})} \text{ and } \hat{z} = \frac{z}{R}$$

### Non-dimensional Parameters in the Model

We now have the perturbation  $\Delta\sigma_{ij}$  from the pre-stress field, if normalized by the dynamic stress drop  $\tau_0 - \tau_r$ , or by the strength drop  $\tau_p - \tau_r$ , expressed in terms of non-dimensionalized parameters, namely  $z/R$ ,  $R/L$  and  $v_r/c_s$ . The in-plane pre-stress is characterized by a non-dimensional parameter,  $\sigma_{xx}^0/\sigma_{yy}^0$  which is a proxy for the angle of inclination of the maximum in-plane principal stress (compressive) with the slip-pulse,  $\Psi$ , measured clockwise from the top of the slip pulse. The in-plane stress components are then given by

$$\frac{\sigma_{yy}^0}{\tau_0 - \tau_r} = \frac{-1/f_s}{\sigma_{drop}(1 - f_d/f_s)}$$

$$\frac{\tau_0}{\tau_0 - \tau_r} = 1 + \frac{f_d/f_s}{\sigma_{drop}(1 - f_d/f_s)} \quad (2.44)$$

To examine out-of-plane failure modes (reverse or normal faults) we must also assign a value for  $\sigma_{zz}^0/\sigma_{yy}^0$ . We choose various values for  $\sigma_{zz}^0$  lying

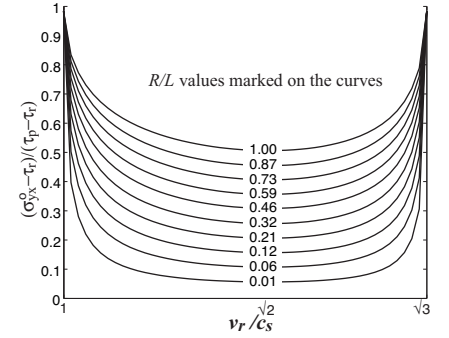


Figure 2.8: Variation of scaled dynamic stress drop  $(\tau_0 - \tau_r)/(\tau_p - \tau_r)$  with rupture speed  $v_r$  and  $R/L$  where  $R$  and  $L$  are the size of the slip weakening zone and the length of the slip pulse respectively.  $\tau_p$  and  $\tau_r$  are the peak and residual strengths respectively and  $\tau_0$  is the initial shear stress.

between, or equal to one of, the maximum ( $\sigma_3$ ) and minimum ( $\sigma_1$ ) in-plane compressive principal stresses, determined from the initial in-plane stresses. That is, we consider pre-stress states which are at least as favorable to strike-slip as to normal or to thrust failure.

Thus the model has six non-dimensional parameters that need to be declared *a priori* (if the total stress tensor is to be evaluated), namely  $v_r/c_s$ ,  $R/L$ ,  $f_s$ ,  $f_d/f_s$ ,  $\sigma_{xx}^0/\sigma_{yy}^0$  and  $\sigma_{zz}^0/\sigma_{yy}^0$ . On this list,  $\sigma_{drop}$  can replace  $R/L$ .

### Off-fault Stressing due to a Supershear Slip Pulse

Supershear ruptures differ from their sub-Rayleigh analogues in many different ways. The stressing due to the P and the S waves in the medium is almost decoupled. The S wave field stresses the region only behind the Mach-front emanating from the rupture front. In case of a slip pulse, as studied here, two Mach fronts develop at the leading and the trailing edge of the slip pulse and the band between these fronts defines the S wave stressing region (Figure 1). Within the band, the stress field is non-attenuating with distance and is constant (neglecting the modest, attenuating, contributions of the P wave field) along lines parallel to the leading Mach front. The non-attenuation feature in the band is a unique signature of supershear pulses which could potentially lead to damage at distances far away from the slip pulse. The three-dimensional nature of the actual problem presumably restricts this distance to be of the order of the depth of the seismogenic zone (once the rupture saturates in depth the dominant length scale in the problem is related to this depth and 3D effects can no longer be ignored), usually around 10-15 km. However this distance is still substantial and of the order of a few tens of kilometers.

Outside the Mach band, the stressing is only due to the P waves and attenuates with distance. However, as the rupture speed approaches the upper limiting speed, i.e., the P wave speed of the surrounding medium, the Lorentz-like contraction of the stressing region in the fault parallel direction (with a corresponding extension in the fault normal direction) also increases significantly leading to a greater extent of the P wave stressing region in the medium hosting the slip pulse. Once again we notice a greater spatial influence by supershear ruptures compared to sub-Rayleigh ruptures. Figure 2.9 showing the perturbation in  $\Delta\sigma_{xx}$  illustrates the non-attenuating and Lorentz-like contraction features of supershear ruptures.

To characterize the off-fault stressing induced by a supershear slip pulse, we should look at the change of Coulomb stress on fault structures with assumed orientations, and also on structures which are optimally oriented for Coulomb failure based on the total stress tensor. Note that in calculating dynamic Coulomb stress changes on optimally oriented structures and in the evaluation of off-fault failure, all the six non-dimensional parameters are to be specified. However, when evaluating the change in the dynamic Coulomb stress on fault structures with assumed orientations, only three non-dimensional parameters need to be specified (if stresses are normalized

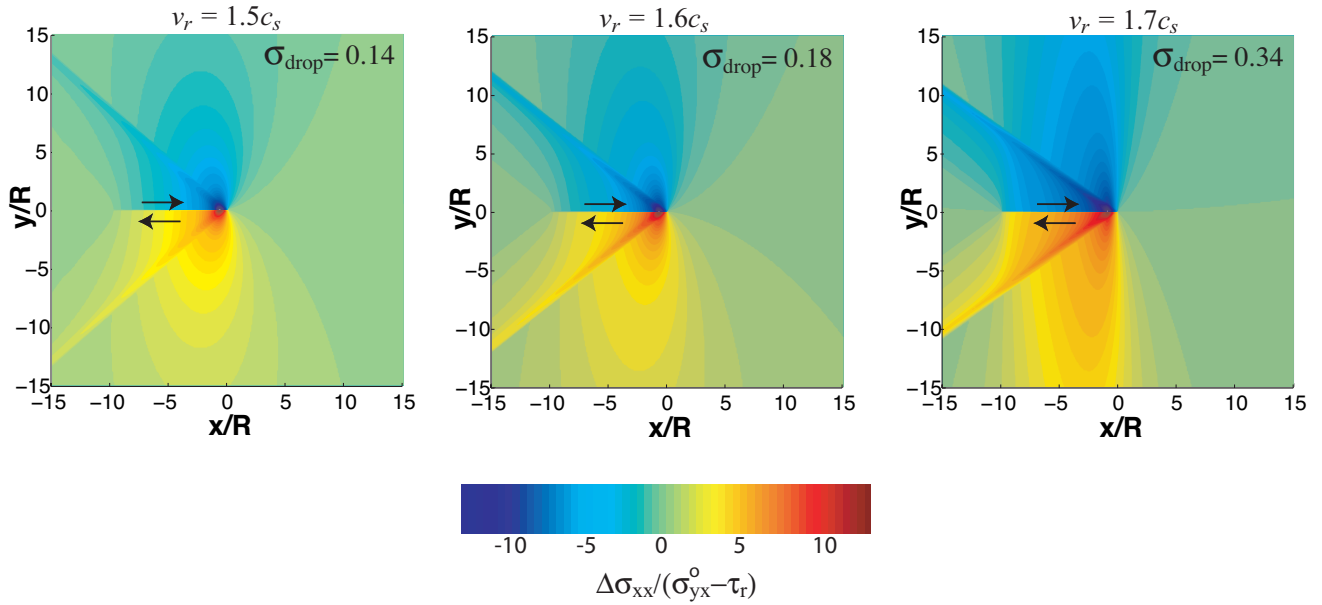


Figure 2.9: Perturbation in fault parallel stress,  $\Delta\sigma_{xx}/(\tau_0 - \tau_r)$  normalized by dynamic stress drop due to a supershear slip pulse propagating steadily at various rupture speeds,  $v_r$ . All results are for  $R/L = 0.1$  where  $R$  and  $L$  are the size of the slip weakening zone and the length of the slip pulse respectively and  $\sigma_{drop} = (\tau_0 - \tau_r)/(\tau_p - \tau_r)$ .

by the dynamic stress drop) *a priori*, namely,  $v_r/c_s$ ,  $R/L$  and  $f_s$ .

### Energy Balance and Estimates

As explained in Dunham & Archuleta (2005), the proper energy balance for a supershear slip pulse is given by  $\tau_0\delta = \tau_r\delta + G_{frac} + G_{rad}$ , where  $\tau_0$  is the far field shear stress,  $\tau_r$  is the residual strength of the fault,  $\delta$  is the locked-in slip left in the wake of the slip pulse. Here  $\tau_r\delta$  is the dissipation at the residual strength level,  $G_{frac}$  is the dissipation at stresses excess of the residual which defines the fracture energy, and  $G_{rad}$  is the energy flow away from the slip pulse associated with the S waves.

The locked-in slip  $\delta$  is given by the expression,

$$\frac{\delta}{R} = \frac{1}{v_r} \int_0^{L/R} V(\xi) d\xi \quad (2.45)$$

where  $V$  is the slip velocity distribution which depends on  $R/L$  and  $v_r/c_s$  and is given by  $V(\xi) = -2v_r[(\beta_s^2 + 1)/4\mu\alpha_d]\mathfrak{JN}(\xi)$  when approaching the fault from  $y > 0$  and  $\xi$  denotes  $x/R$ .  $G_{frac}$  is given by

$$\frac{\mu G_{frac}}{(\tau_p - \tau_r)^2 R} = \int_0^1 V^*(\xi)(1 - \xi) d\xi \quad (2.46)$$

where  $V^*(\xi) = \mu V(\xi)/[(\tau_p - \tau_r)v_r] = -2\{(\beta_s^2 + 1)/[4\alpha_d(\tau_p - \tau_r)]\}\mathfrak{JN}(\xi)$ .  $G_{rad}$  is then evaluated from the energy balance equation. The energy flux associated with  $G_{rad}$  extends all the way to infinity and vanishes when the rupture velocity is  $\sqrt{2}c_s$ . We non-dimensionalize energy in our model, following Rice et al. (2005), with seismically observable parameters, as  $\hat{G} = \pi LG/\mu\delta^2 = F(v_r/c_s, R/L)$  where  $\mu$  is the shear modulus of the medium hosting the slip pulse. The non-dimensional function,  $F$  cannot be reduced to a simple analytical expression, as in the sub-Rayleigh case, but has to be

numerically determined. Also, unlike the sub-Rayleigh case, the dependence of  $F$  on rupture speed and  $R/L$  are no longer separable. Figure 2.10 shows the variation of  $G_{frac}$  and  $G_{rad}$  with rupture velocity for a fixed ratio of dynamic stress drop to strength drop,  $(\tau_0 - \tau_r)/(\tau_p - \tau_r) = 0.3$ . The total energy,  $G_{frac} + G_{rad}$ , decreases monotonically with increasing fracture energy. Since this ratio is dependent on both the rupture speed and the size of the process zone with respect to the length of the slip pulse we have to vary  $R/L$  with rupture velocity to obtain the energy values at fixed stress drop.

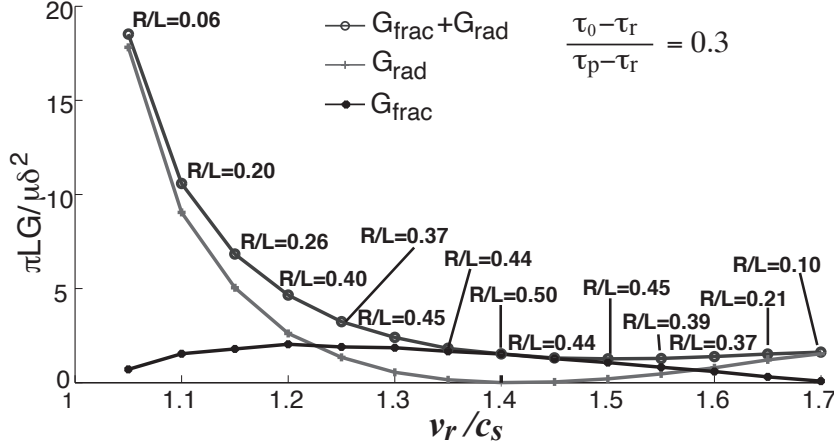


Figure 2.10: Scaled fracture energy release rate,  $G_{frac}$ , energy radiated by S-wave,  $G_{rad}$  and the total energy as a function of rupture speed,  $v_r$  for  $(\tau_0 - \tau_r)/(\tau_p - \tau_r) = 0.3$ .

One can also use the energy balance equation to evaluate how the size of the slip-weakening zone,  $R$ , varies with  $R/L$  and  $v_r/c_s$ . We scale this value of  $R$  with the size of the process zone at static limit for a semi-infinite crack,  $R_0^*$  as in Rice *et al.* [2005] where

$$R_0^* = \frac{9\pi}{16(1-\nu)} \frac{\mu G_{frac}}{(\tau_p - \tau_r)^2} \quad (2.47)$$

Here  $\nu$  is the Poisson ratio of the medium, set at 0.25 in our model, and  $G_{frac}$  is the fracture energy release rate. Using this with the above equation we get  $R/R_0^*$ .

Figure 2.11 shows the variation of  $R/R_0^*$  for the complete range of admissible speeds for a dynamic shear crack. The expression for  $R/R_0^*$  for the sub-Rayleigh range was obtained from Rice *et al.* (2005) equation 14.  $R/R_0^*$  undergoes Lorentz-like contraction in the sub-Rayleigh regime, diminishing to zero at the Rayleigh wave speed,  $c_R$ . The speed range between  $c_R$  and  $c_s$ , the S wave speed, is inadmissible on energetic grounds for a steady shear crack. Beyond  $c_s$ ,  $R/R_0^*$  monotonically diminishes to zero again as the rupture speed approaches the P wave speed. For the supershear speed range inferred from various earthquakes, between  $1.5-1.7c_s$ ,  $R/R_0^*$  lies between 0.3 and 0.6. Estimates of  $R_0^*$  by Rice *et al.* (2005), for the Heaton (1990) event set, varies between 1.3-36 m (with an uncertainty of factor of two since this value depended on  $R/L$ ). This was obtained under the assumption of high peak strength and low residual strength implying  $(\tau_p - \tau_r) \approx \tau_p = f_s \bar{\sigma}_n$  where  $f_s = 0.6$  and  $\bar{\sigma}_n$  is the effective normal pressure calculated at median depth for each of the earthquakes in the set. For low strength drop

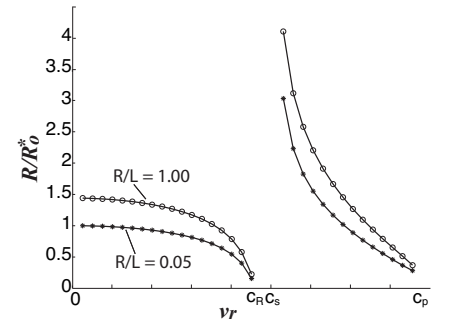


Figure 2.11: Variation in the scaled size of the process zone,  $R/R_0^*$ , with rupture velocity,  $v_r$ .  $R_0^*$  is the size of the process zone at static limit for a semi-infinite shear crack.  $c_R$ ,  $c_s$  and  $c_p$  are the Rayleigh, S and P wave speeds of the medium respectively.

case, their estimates of  $R_0^*$  varied between 73m to 3.3 km.

We evaluate the spatial slip distribution,  $\Delta u(x)$ , on the fault by numerically integrating the expression for slip velocity,  $V = \partial \Delta u / \partial t = -v_r \partial \Delta u / \partial x$ . This spatial distribution of slip is then used along with the spatially linear failure criterion used in our model to determine the slip weakening law implied by our model. Figure 2.12 shows this slip-weakening behavior. There is little deviation from the linear slip-weakening law, that is often (but somewhat arbitrarily) assumed in numerical simulations of dynamic shear ruptures, regardless of the choice of  $R/L$ . There is also some sensitivity to rupture velocity in the slip-weakening curves unlike the sub-Rayleigh case but that too is modest.

## 2.4 Far Field Stresses Along Mach Fronts

In their study of an supershear slip pulse, propagating at steady state in a two dimensional homogeneous isotropic medium under plane strain conditions, Dunham & Archuleta (2005) have shown that the off-fault velocity fields trace out the exact slip velocity during the passage of the S-wave front. This means that a non-attenuating field, caused by the passage of the S-wave front, is traced out in the medium, through which the slip pulse passes, and extends, theoretically, to infinity. Nevertheless this observation points out that significant effects of the supershear slip pulse can be observed at large distances away from it unlike its sub-Rayleigh analogue where both the P wave and the S wave stress fields attenuate as  $1/r$  with distance from the source,  $r$ . In the following section we re-express the far field stress distribution in terms of the slip velocity distribution on the fault. Let  $V(x)$  be the slip rate along the rupture and  $\Delta u$  the slip, i.e.,

$$\begin{aligned}
 V(x) &= (\partial u_x / \partial t)^+ - (\partial u_x / \partial t)^- \\
 &= -v_r [(\partial u_x / \partial x)^+ - (\partial u_x / \partial x)^-] \\
 &= -2v_r (\partial u_x / \partial x)^+ = -2v_r \epsilon_{xx}^{fault} \\
 &= -2v_r \left[ \frac{1-\nu}{2\mu} \sigma_{xx}^{fault} \right] \\
 &= -[v_r (\beta_s^2 + 1) / (2\mu \alpha_d)] \Im S(z_s) \quad (2.48)
 \end{aligned}$$

using  $\nu = 0.25$  and equation 2.40.  $N(z_s)$  is given by equation 2.22, and  $z_s = x + i0^+$ , the limit as we approach the fault from  $y > 0$ , in order to get the sign of  $\Im N(z_s)$  correct. Solving for  $\Im N(z_s)$  and using this in equation 2.40 (ignoring the P wave contribution) with  $z_s = x + \beta_s |y|$ , the far field stress changes are

$$\begin{aligned}
 \Delta \sigma_{xx}^{far} &= -\mu (v_r^2 - 2c_s^2) V(z_s) \text{sign}(y) / v_r^3 \\
 \Delta \sigma_{yx}^{far} &= -\mu (v_r^2 - 2c_s^2)^2 V(z_s) / (2v_r^3 c_s^2 \beta_s) \\
 \Delta \sigma_{yy}^{far} &= -\Delta \sigma_{xx} \\
 \Delta \sigma_{zz}^{far} &= 0 \quad (2.49)
 \end{aligned}$$

Because  $V(x)$  is always positive in our cases,  $\Delta \sigma_{xx}^{far}$  and  $\Delta \sigma_{yy}^{far}$  change signs as  $v_r$  increases past  $\sqrt{2}c_s$ , but  $\Delta \sigma_{yx}^{far}$  is negative for all  $v_r$ , except for  $\sqrt{2}c_s$

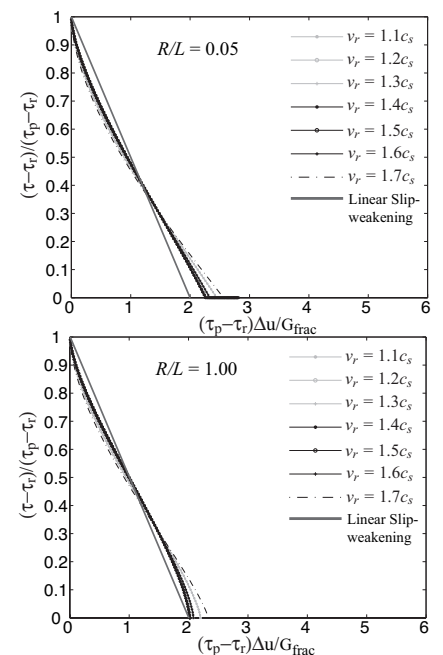


Figure 2.12: Slip weakening law implied by our analysis compared with the linear slip weakening law for  $R/L = 0.05$  and  $1.00$ .

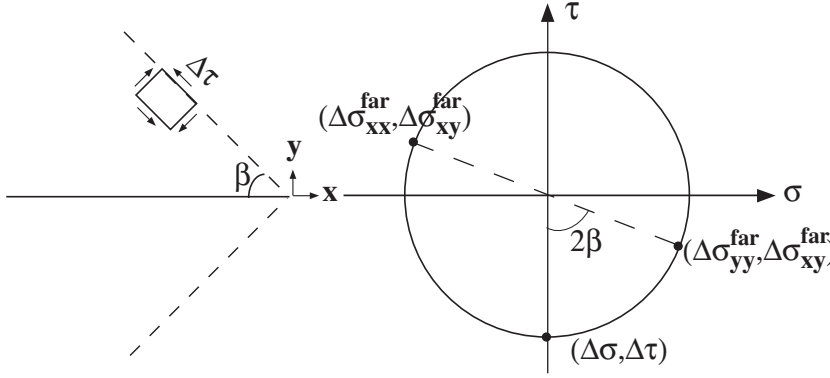


Figure 2.13: Stresses acting on an element aligned with the Mach-fronts and in the cartesian system.  $\Delta\tau$  is the shear stress acting on the element in that orientation and  $\Delta\sigma$  is the normal stress ( $= 0$ ).  $\beta$  is the inclination of the Mach-front with respect to the slip pulse.  $\Delta\sigma_{xy}^{far}$  and  $\Delta\sigma_{yy}^{far}$  are the shear and normal stress in the far-field measured with respect to the x-y co-ordinates. For the Mohr's circle we use tensile positive convention. Note that  $\Delta\tau > 0$  when  $v_r < \sqrt{2}c_s$  and changes sign at higher speeds crossing zero at  $v_r = \sqrt{2}c_s$ .

at which all the  $\Delta\sigma_{kl}^{far}$  vanish. The expressions predict that when  $v_r > \sqrt{2}c_s$ , the sign of the far-field  $\Delta\sigma_{xx}^{far}$  is the same as that along the rupture surface on the corresponding side of the fault, but that the sign is reversed when  $v_r < \sqrt{2}c_s$ . It can also be quite easily shown that the far-field stress perturbation,  $\Delta\sigma_{xx}^{far} = 0.75(1 - 2\sin^2\beta)\Delta\sigma_{xx}^{on-fault}$  where  $\beta$  is the Mach angle,  $\sin\beta = c_s/v_r$ . Thus at velocities close to  $\sqrt{2}c_s$  the far-field stress perturbation is still a significant percentage of the same on the fault.

We note that an alternative way to derive the ratio of far-field shear to normal stresses is to employ Mohr's circle concepts. We know that for an element of material, in the medium in which a steady state supershear rupture is propagating, one of whose faces is aligned with the Mach front (in  $y > 0$  say), the stress component that jumps in value as the Mach front is crossed is the shear stress acting on it. The shear and normal stresses in the cartesian coordinate system for this element is then obtained by rotating it about the center by an angle  $\beta$ . This translates to a rotation in the Mohr's circle plane by an angle of  $2\beta$ . Thus, if  $\Delta\tau$  is the shear stress acting on the element aligned with the Mach front then  $\Delta\sigma_{yy}^{far} = \Delta\tau \sin(2\beta)$  and  $\Delta\sigma_{yx}^{far} = -\Delta\tau \cos(2\beta)$ . Thus  $\Delta\sigma_{yx}^{far}/\Delta\sigma_{yy}^{far} = -\cot(2\beta)$  [Figure 2.13]. Using the results above we can now make some estimates on far field stress perturbations left in the wake of an supershear slip pulse. Some assumptions need to be made before making estimates of the far field stress values. Firstly, we shall use the maximum slip velocities obtained from our model for small ( $R/L = 0.05$ ) and large ( $R/L = 1.0$ ) values of the process zone ( $R$ ) with respect to the length of the slip pulse ( $L$ ). Slip velocity,  $V$ , in our model is non-dimensionalized as  $\mu V/[(\sigma_{yx}^0 - \tau_r)c_s]$ , where  $\mu$  is the shear modulus of the medium,  $(\sigma_{yx}^0 - \tau_r)$  is the dynamic stress drop and  $c_s$  is the shear wave speed of the medium. We assume that  $\mu = 30\text{GPa}$ ,  $(\sigma_{yx}^0 - \tau_r) = 3\text{MPa}$  and  $c_s = 3\text{km/s}$ . This gives us maximum slip velocity values varying from 0.5m/s to 10.5m/s and increasing with increasing rupture velocity.

Using the above values of slip velocity one can now make reasonable estimates of far field stresses. This provides some interesting results. Firstly, the perturbation in the shear stress field  $\Delta\sigma_{xy}^{far}$  is always negative in the far field as expected earlier.  $\Delta\sigma_{xx}^{far}$  changes sign from being extensional ( $\Delta\sigma_{xx}^{far} > 0$ ) to compressional as one crosses the  $\sqrt{2}c_s$  rupture velocity

value. The magnitude of the stress perturbation is also quite high, varying between -17MPa and 8MPa (using the maximum value of slip velocity). Also, the changes in the far field stresses seem to be very sensitive to the rupture velocity. For example,  $\Delta\sigma_{xx}^{far}$  increases from 1MPa to 3MPa as the rupture velocity changes from  $1.45c_s$  to  $1.5c_s$ . Ofcourse, the slip velocity also changes here as the rupture velocity changes. Hence it is useful to know the change in the stress field for fixed value of peak slip velocity and slightly different values of rupture velocity. Taking  $V = 5\text{m/s}$  as representative of the faster slip velocities we get the rough estimates for  $v_r = 1.51c_s$  to  $1.61c_s$  (on the compressional side of the fault),

$$\begin{aligned}\Delta\sigma_{xx}^{far} &= -(4.0 \text{ to } 7.0 \text{ MPa}) \text{sign}(y) \\ \Delta\sigma_{yx}^{far} &= -(0.4 \text{ to } 1.5 \text{ MPa}) \\ \Delta\sigma_{yy}^{far} &= +(4.0 \text{ to } 7.0 \text{ MPa}) \text{sign}(y)\end{aligned}\quad (2.50)$$

Those are large normal stress changes, 40 bars at  $1.51c_s$ , 70 bars at  $1.61c_s$ , especially given that they do not attenuate with distance until 3D effects enter the model. For  $v_r = 1.21$  to  $1.31c_s$ , the normal stress changes have the same magnitude range but reverse sign from those above. The estimates are peak stress values; average stress changes, if  $V_{average}$  is about 1m/s, would be a fifth as large, but still significant at about 10 bars.

## 2.5 2D Spontaneous Rupture Models

Space and time are essentially equivalent in 2D steady-state rupture models. Such models implicitly assume that the rupture has existed for all time and thus cannot account for the rupture history and dynamic mechanisms that lead to the emergence of the supershear rupture in the first place. Various supershear rupture transition mechanisms have been proposed through self-similar analytical models and numerical simulations. Such models typically rely upon an initial sub-Rayleigh rupture, which spontaneously nucleates and spawns an supershear “daughter-crack” as a consequence of a critical dynamic stress condition, which is reached. In the original Burridge-Andrews model (Andrews, 1976; Burridge, 1973; Burridge et al., 1979), a peak in the S-wave field positioned just ahead of the sub-Rayleigh rupture front steadily increases in magnitude until it overcomes the frictional fault strength. Once this occurs a so-called “daughter crack” is formed, which is momentarily dissociated from the original ruptured portion of the fault. The leading front of the daughter crack begins as an unstable supershear rupture, which then rapidly accelerates and transitions into a stable supershear rupture.

Alternative and equally plausible models for the nucleation of supershear ruptures consider the dynamic interaction of the sub-Rayleigh rupture with an inclusion or a local patch of higher strength along the frictional fault. The presence of these features can also directly lead to dynamic stress concentrations and localized instabilities, which can give rise to a supershear rupture (Dunham & Archuleta, 2004; Dunham et al., 2003; Liu & Lapusta, 2008). Both of the aforementioned supershear rupture transition

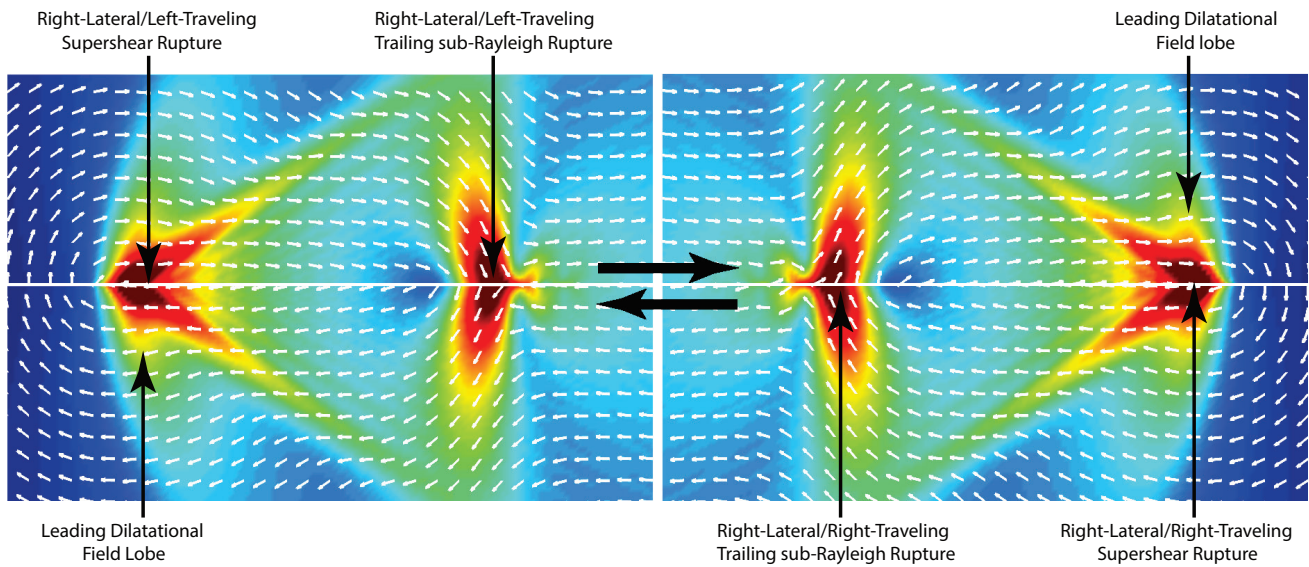


Figure 2.14: Contour and velocity vector field plots corresponding to right-lateral/left traveling and right-right-traveling supershear ruptures. Field plots were generated by the finite element code ABAQUS, using a slip-weakening friction law in a numerical simulation of the Burridge-Andrews mechanism. Contour plot colors scale with the magnitude of the velocity field, while the streak plot vectors reveal the sense of particle motion throughout the field.

mechanisms have been experimentally investigated and observed in LEQ experiments (Mello et al., 2014). The graphical illustration in Figure 2.14 depicts the velocity fields and sense of particle motion in the immediate region surrounding a pair of left- and right-traveling (right-lateral) supershear ruptures. The field plots were generated by assuming a slip-weakening friction law in a numerical simulation of the Burridge-Andrews mechanism (Andrews, 1976). The analysis was conducted using the commercial Finite Element code, ABAQUS. The left panel in Figure 2.14 corresponds to the velocity field of a right-lateral/left-traveling supershear rupture while the panel on the right represents a right-lateral/right-traveling supershear rupture velocity field. The colors of the contour plot scale with the magnitude of the velocity field, while the streak plot vectors reveal the sense of particle motion throughout the field, which is perfectly consistent with the sense of motion depicted in Figure 2.3(b).

The velocity vector field plots in Figure 2.14 depict a leading and concentrated supershear slip zone corresponding to the deepest shade of red at the vertex formed by the prominent shear Mach fronts which extend back and bound the shear radiation field emitted by each rupture. Pronounced dilatational field lobes envelope and circulate each supershear rupture zone and extend out beyond the shear Mach fronts. The FP component is clearly the dominant velocity field component, as expected, in the immediate vicinity of the supershear slip zone and along the shear Mach fronts. The influence of the dilatational field lobe on the magnitude of the velocity field along the shear Mach fronts decays with increased FN distance until a constant value is approached in the far-field, as represented by the light green shade.

Another notable feature appearing in the left and right panels of Figure 2.14, which is otherwise unaccounted for in 2D steady-state analytical rep-

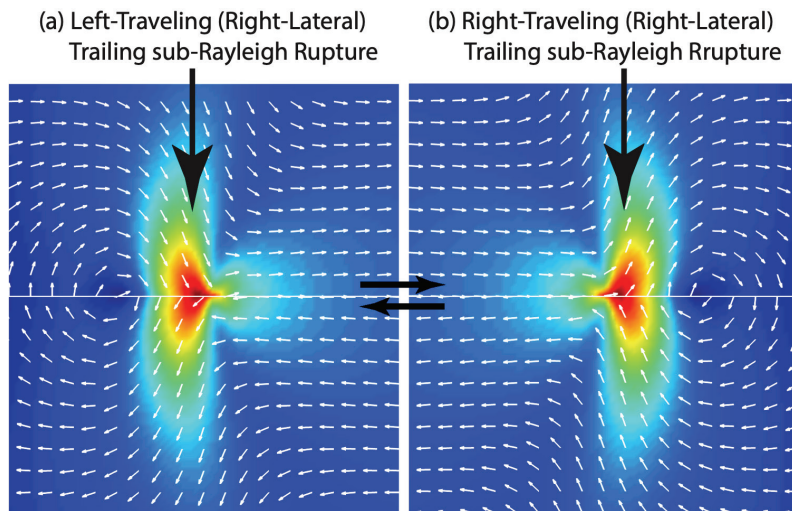


Figure 2.15: Sense of particle motion for a spontaneous right-lateral left-traveling (a) and right-traveling (b) sub-Rayleigh rupture. The contour plot shows the magnitude of the velocity field while the streak plot vectors reveal the sense of motion.

representations, are the concentrated secondary rupture zones, corresponding to the deepest shades of red, which trail in the wake of each supershear rupture. The sense of particle motion and the obvious dominance of the FN motion component within each secondary rupture zone is perfectly consistent with the kinematic signatures of left- and right-traveling (right-lateral) sub-Rayleigh ruptures. We thus recognize and henceforth denote this secondary disturbance as a trailing sub-Rayleigh rupture, corresponding to what remains of the original spontaneous sub-Rayleigh rupture, which spawned the supershear rupture. Close scrutiny of the entire class of self-similar analytical solutions for supershear ruptures (Broberg, 1994; Burridge, 1973) reveals that the secondary rupture travels behind the main crack tip at speeds approaching the Rayleigh wave speed. Furthermore, depending on the governing friction law, both the main rupture and the trailing Rayleigh rupture can be pulses in the strictest sense of the word (i.e., the fault is locked from slipping in their wake) or they could both be crack-like ruptures or be a combination of crack-like and pulse-like rupture.

Secondary trailing sub-Rayleigh ruptures are commonly observed in LEQ experiments and always seen trailing in the wake of the supershear ruptures. There has also been at least one confirmed recording of a trailing sub-Rayleigh rupture pulse during a supershear earthquake as revealed by the celebrated

“Pump Station 10” ground motion records obtained during the 2002  $M_w$  7.9 Denali fault earthquake rupture (Dunham & Archuleta, 2004; Mello et al., 2014). We will appeal to the supershear velocity vector field plots in Figures 2.14 when analyzing and interpreting particle velocity records obtained in supershear LEQ experiments.

Figure 2.15 depicts a pair of right-lateral sub-Rayleigh rupture velocity field plots that were generated through a similar set of finite element simulations. In this case the normal stress was reduced so as to prevent a sub-Rayleigh to supershear transition from occurring in the numerical simula-

tion. 2.15(a) depicts the velocity field corresponding to a right-lateral/left-traveling sub-Rayleigh rupture and 2.15(b) represents the velocity field corresponding to a right-lateral/right-traveling sub-Rayleigh rupture. The direction of particle motion revealed by the streak plot vectors exposes the dominant FN motion component exhibited by the sub-Rayleigh rupture fields. The particle motion is consistent with the predicted sense of motion of a right-lateral sub-Rayleigh rupture as previously discussed. Indeed, the right-traveling sub-Rayleigh rupture in Figure 2.15(b) is also in agreement with the general sense of particle motion exhibited by the sub-Rayleigh shear crack field plot in Figure 2.1(a).

We note as well how the direction of the velocity vector field within the primary rupture zone of the right-traveling rupture is directed upwards as it crosses the fault plane. The FN component cannot change sign across the fault plane since no crack opening is allowed in the case of a mode II rupture. The particle velocity vector field then proceeds to circulate clockwise just out ahead of the main rupture as shown. The opposite sense of motion is observed for the left-traveling sub-Rayleigh rupture depicted in Figure 2.15(a). The direction of the velocity vector field within the primary rupture zone is now directed downwards as it crosses the fault plane and then proceeds to circulate clockwise just out ahead of the of the main rupture. We will appeal to the the sub-Rayleigh velocity vector field plots in Figure 2.15 when analyzing and interpreting particle velocity records obtained in sub-Rayleigh LEQ experiments.

## 2.6 3D Steady State Cohesive Zone Model

The velocity at which a rupture propagates influences the amplitude and character of the radiated ground motion and stresses. A distinct manifestation of this occurs when ruptures exceed the S-wave speed and generate shear Mach waves that efficiently transmit ground motion and stresses away from the fault. Supershear speeds are also super-Rayleigh ones, and in an elastic half-space we also expect Rayleigh Mach waves. Slip alters the component of normal stress parallel to the rupture front; for vertical strike-slip faults, negation of these stresses on the free surface generates Rayleigh waves. The Rayleigh Mach front originates near the intersection of the rupture front with the free surface, and as one moves away from the fault along the free surface, the Rayleigh Mach front lags behind the shear Mach front. The objective of the current work is to quantify how the amplitude of radiated ground motion, specifically that of the Mach waves, diminishes with distance from the fault. We further compare fields from supershear ruptures to those of sub-Rayleigh ruptures with the aim of contrasting the rate at which amplitudes decay with distance from the fault for both classes of ruptures.

We build on a number of previous studies that have examined the influence of rupture speed on near-source ground motion. Ben-Menahem & Singh (1987) studied the acceleration field generated by a point velocity dislocation (a singularity moving along a line and leaving in its wake a fixed

moment per unit length) that travels a finite distance at a supershear speed before stopping. In addition to starting and stopping phases, shear Mach waves were implicated as carriers of large-amplitude accelerations. Their results further demonstrate how Mach waves pass only through a particular region surrounding the fault. By only considering propagation of a point source along a line, their analysis applies only to observation points sufficiently removed from the fault (i.e., at distances much greater than the fault width). A number of other researchers have focused on the wavefield in the immediate vicinity of the fault (extending out to distances comparable to the fault width, but not much beyond that). By examining a sequence of kinematic models with various rupture speeds, Aagaard & Heaton (2004) demonstrated how the well-known velocity waveform of sub-Rayleigh ruptures (the two-sided fault-normal “directivity pulse” that has been of primary concern in seismic hazard (Somerville et al., 1997)) vanishes when ruptures exceed the S-wave speed. Instead, the largest amplitudes now occur at the Mach fronts. Bernard & Baumont (2005) combined kinematic models of supershear ruptures together with an asymptotic isochrone based analysis of fields near the Mach fronts to explore features of Mach waves from supershear ruptures. Their asymptotic analysis, which did not include any corrections for a finite fault width, showed that for straight rupture fronts, field amplitudes at the Mach fronts remain undiminished with distance from the fault; rupture-front curvature leads to an inverse square-root decay of amplitudes with distance due to a loss of coherence at the Mach front.

The starting point for our analysis is the two-dimensional (2D) steady-state slip-pulse model developed by Rice et al. (2005) to examine stress fields near the rupture front of sub-Rayleigh ruptures. This model was extended to supershear speeds by Dunham & Archuleta (2005) and Bhat et al. (2007). Dunham & Archuleta (2005) focused on ground motion (specifically, velocity records) from slip pulses in the context of models of the Denali fault event (Dunham & Archuleta, 2004; Ellsworth et al., 2004a). Bhat et al. (2007) studied the off-fault damage pattern due to supershear ruptures and hypothesized that anomalous ground cracking observed at a few tens of kilometers from the fault during the 2001 Kokoxili (Kunlun) event resulted from the high stresses at the Mach front emanating from a supershear rupture. This observation raises the possibility that radiated stresses from a large supershear event might trigger slip on adjacent faults of the proper orientation. One objective of the current work is to quantify how the amplitude of Coulomb stresses on pre-existing structures is influenced by rupture speed and the finite fault width.

The most distinctive features of the 2D supershear slip-pulse models are the shear Mach waves. The combined assumptions of two dimensions (i.e., an infinite extent of the slipping region parallel to the rupture front), steady-state propagation, and a homogeneous linear elastic medium cause the Mach waves to extend infinitely far from the fault and for the amplitude of fields at the Mach fronts to remain undiminished with distance from the fault. This study addresses the first of these assumptions by considering ruptures

in three dimensions (3D), specifically right-lateral strike-slip ruptures on a finite-width vertical fault breaking the surface of an elastic half-space. The focus is on the wavefield after the rupture has propagated many times further than the fault width. In addition to the shear Mach waves found in 2D models, we also expect Rayleigh Mach waves emanating from the rupture front out along the free surface. The 2D plane-strain models feature large changes in the normal stress parallel to the rupture front. These changes appear only in the vicinity of the fault and not further away at the shear Mach front since fields there are nondilatational. When considering ruptures on vertical faults in a half-space, the component of normal stress parallel to the rupture front is also normal to the free surface, and must be negated there to satisfy the traction-free boundary condition. This can be accomplished by the superposition of normal loads on the free surface that negate the moving vertical-normal-stress pattern. These moving loads, which propagate at a super-Rayleigh speed, will then excite Rayleigh Mach waves (Georgiadis & Lykotrafitis, 2001; Lansing, 1966).

To understand the effect of bounding the vertical extent of the slipping region, consider two limiting cases of rupture on a vertical surface-breaking fault of width  $W$  and half-length  $L$  (Figure 2.6a). At locations close to the fault and away from both its edges and the free surface (specifically, at locations much closer than  $W$ ), the fault width is unimportant and 2D plane-strain models provide an accurate description of the fields, at least if the length of the slip-weakening zone,  $R$ , is much less than  $W$ . In this extremely near-source region, the shear Mach front assumes the form of a wedge (Figure 2.6b) and Mach-wave amplitudes will not diminish with distance from the fault. Of course, this region is further complicated by the presence of dilatational fields of comparable amplitude. At the opposite extreme, consider points far removed from the fault (specifically, at distances greatly exceeding  $W$ ). From these distant points, the fault appears as a line source, and S-wave radiation now forms a Mach cone (Figure 2.6c). Since the cross-section of the cone is a circle, geometrical spreading dictates that Mach-wave amplitudes will decrease with the inverse square-root of radial distance from the fault. (And it is not clear if the amplitude of Rayleigh Mach waves would attenuate at all, at least in the ideally elastic material considered.) It is of critical importance to hazard calculations to understand exactly how the transition between these two extremes occurs, and to explore how Rayleigh Mach waves influence the wavefield. Specifically, to what distances are large ground motion and stresses transported for realistic fault geometries? Bhat et al. (2007) hypothesized that the transition between the two limits occurs at distances comparable to  $W$ , and our results confirm this hypothesis, although the Rayleigh Mach waves also contribute to the fields.

### Model Geometry

We model ruptures on a vertical right-lateral strike-slip fault that intersects the free surface

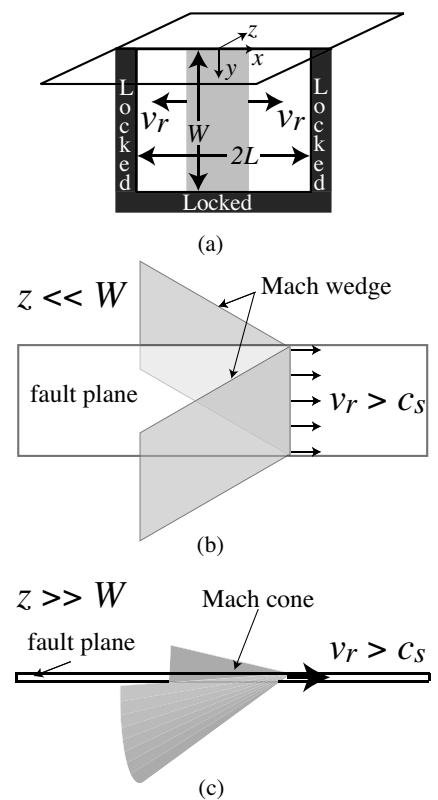


Figure 2.16: (a) Rupture on a fault of width  $W$  and half-length  $L$  that expands bilaterally at speed  $v_r$ . (b) Mach wedge from a supershear rupture in 2D, which approximates S-wave radiation from slip on a finite-width fault at locations close to the fault ( $z \ll W$ ) and away from the fault edges. (c) Mach cone emitted by supershear point source moving along a line, which approximates radiation from slip on a finite-width fault when viewed from afar ( $z \gg W$ ).

(Figure 2.6a). We study three representative rupture speeds,  $v_r$ :  $0.8c_s$ ,  $1.3c_s$ , and  $1.6c_s$ , where  $c_s$  is the S-wave speed. The sub-Rayleigh speed,  $0.8c_s$ , lies in the middle of the typical speed range ( $0.7 - 0.9c_s$ ) inferred for most earthquakes. Two speeds are necessary within the intersonic range, since the sign of the radiated shear fields changes as the Eshelby speed,  $\sqrt{2}c_s$ , (at which no S-waves are generated) (Eshelby, 1949) is crossed (Dunham & Archuleta, 2005). Stability considerations (Burrige et al., 1979; Obrezanova & Willis, 2003) suggest ruptures should only propagate above  $\sqrt{2}c_s$ , and most of the previously mentioned inversions have found speeds in this range. Consequently we focus primarily on  $v_r = 1.6c_s$  within the supershear regime, but also present results for  $v_r = 1.3c_s$ , which lies on the opposite side of the Eshelby speed. For simplicity, we keep  $v_r$  fixed (rather than considering a more natural transition from sub-Rayleigh to supershear speeds, which would generate a more complicated set of waveforms) and consider symmetrically expanding bilateral ruptures that propagate a distance  $L$  in each direction. We also wish to work in the context of a dynamic model, in the sense that we specify a constant stress drop,  $\Delta\sigma$ , within the rupture. In this sense, our models are closely related to self-similar singular crack models in 2D. In our work, we prevent a stress singularity at the rupture front by employing a cohesive zone model that can be interpreted in the context of the commonly used slip-weakening friction law. The parameters of this model are the peak and residual strengths,  $\tau_p$  and  $\tau_r$ , and the distance,  $R$ , over which strength drops from  $\tau_p$  to  $\tau_r$ . As discussed by Dunham & Archuleta (2005) and Bhat et al. (2007), the extent of the slip-weakening zone (relative to the length of the rupture) plays a large role in determining the maximum amplitude of fields at the Mach front.

The specific, simplified, procedure we use to force ruptures with the desired properties was originally employed by Andrews (1985). The shear strength of the fault,  $\tau_{str}$ , weakens linearly with distance (with weakening rate  $A$ ) behind the rupture front:

$$\tau_{str}(x, t) = \max\{\tau_r, \tau_p + A(|x| - v_r t)\}. \quad (2.51)$$

The fault is locked until stress reaches the fault strength,  $\tau_p$  (which is not specified *a priori* in this approach, but depends on  $\tau_r$  and  $A$ , and varies moderately with the position of the rupture tip), at which time slip commences and weakening occurs in such a way as to ensure that stress always equals strength during sliding. This is illustrated in Figure 2.17. In this model, both  $\tau_p$  and  $R$  evolve as the rupture expands in order to provide a solution with nonsingular and continuous stress at the tip. An associated energy release rate, or fracture energy  $G$ , can then be inferred as the area under the resulting plot of  $\tau - \tau_r$  versus slip. In 2D self-similar crack models,  $G$  increases linearly with propagation distance; the procedure we use, if applied in this context, results in an increase of both  $\tau_p$  and  $R$  to accommodate the increasing energy flux into the slip-weakening zone.

We note several other important quantities that will be of interest to us. The first is the seismic  $S$  ratio [ $S = (\tau_p - \sigma_{zx}^0)/(\sigma_{zx}^0 - \tau_r)$ ], a measure of the initial load,  $\sigma_{zx}^0$ , relative to the peak and residual strengths. The stress

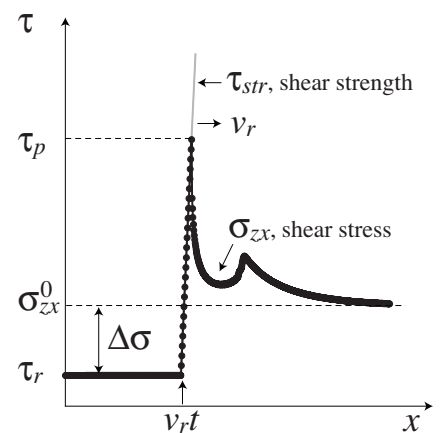


Figure 2.17: Fracture criterion used to force a rupture at speed  $v_r$  with stress drop  $\Delta\sigma$ . Fault strength,  $\tau_{str}$ , increases linearly from  $|x| = v_r t$  (grey line). When shear stress on the fault (black line and points from our numerical model at  $v_r = 0.8c_s$ ) reaches the strength, slip commences.

field, scale (units)	Low	Moderate	Large
	$\Delta\sigma$	$\Delta\sigma$	$\Delta\sigma$
stress, $\Delta\sigma$ (MPa)	0.3	3	30
velocity, $\Delta\sigma c_s/\mu$ (m/s)	0.03	0.3	3
displacement, $\Delta\sigma W/\mu$ (m)	0.1	1	10
fracture energy, $\Delta\sigma^2 W/\mu$ (MJ/m <sup>2</sup> )	0.03	3	300

Table 2.1: Representative dimensionalizing factors by which nondimensional values reported in this study may be converted to physical values; a range exists due to uncertainty in  $\Delta\sigma$ . Other parameters employed in these relations are  $\mu = 30$  GPa,  $c_s = 3$  km/s, and  $W = 10$  km.

drop is  $\Delta\sigma = \sigma_{zz}^0 - \tau_r$  and the strength drop is  $\tau_p - \tau_r$ . The fracture energy,  $G$ , may be calculated for each point on the fault as

$$G = \int [\tau(t) - \tau_r] V(t) dt = \int [\tau(\delta) - \tau_r] d\delta, \quad (2.52)$$

in which  $V$  is the slip velocity and the integrals are taken over all time  $t$  or all slip  $\delta$ . Finally, we define an equivalent slip-weakening distance  $D_c$  via the relation

$$G = \frac{1}{2}(\tau_p - \tau_r) D_c, \quad (2.53)$$

which proves useful when interpreting our results in the context of the commonly used linear slip-weakening law (Andrews, 1976).

We next nondimensionalize the model by scaling all distances by  $W$  and time by  $W/c_s$ . Stress is scaled with  $\Delta\sigma$ , particle and slip velocities by  $\Delta\sigma c_s/\mu$ , and displacements and slip by  $\Delta\sigma W/\mu$ ;  $\mu$  is the shear modulus. When considering physical values of these parameters, we take  $\mu = 30$  GPa,  $c_s = 3$  km/s, and  $W = 10$  km. We consider a Poisson material (i.e., one for which the P- and Rayleigh-wave speeds are  $c_p = \sqrt{3}c_s$  and  $c_R \approx 0.9194c_s$ ), and choose  $\tau_r$  to yield a dynamic coefficient of friction of 0.2 (but note that the actual value of normal stress,  $\sigma_{zz}^0$ , is unimportant since normal stress on the fault remains unaltered by slip on vertical strike-slip faults in a homogeneous medium). Estimates of stress drop vary widely, and to encompass this range we consider three representative values of  $\Delta\sigma$ : 0.3 MPa, 3 MPa, and 30 MPa. We report nondimensional values (denoted by a superscript \*) in our figures, and these may easily be converted to physical values by the scaling factors described above and summarized for reference in Table 2.1.

We numerically solve our problem with a staggered grid finite difference code (Favreau et al., 2002) with fault boundary conditions implemented using the staggered-grid split-node (SGSN) method of Dalgner & Day (2007). Rake rotation is permitted, in that the slip vector rotates so as to be aligned with the shear traction vector. The degree of rake rotation depends on the change in stress relative to the initial level of stress in the medium. In our simulations,  $\sigma_{zz}^0/(\sigma_{zz}^0 - \tau_r) = 1.2$  and we apply no transverse shear loads (i.e.,  $\sigma_{zy}^0 = 0$ ). The method is fourth order in space and second order in time for wave propagation in the body, but the spatial order is reduced to second order at the fault. We implement the free-surface boundary condition using the fourth-order W-AFDA scheme proposed by Kristek et al. (2002) (which collocates the free surface with the grid points for vertical

velocity and normal stresses), and place perfectly matching layer (PML) absorbing boundaries on the remaining sides (Marcinkovich & Olsen, 2003). Ruptures propagate for  $15W$  in each direction before reaching the end of the fault (we lock the fault beyond this), but the computational domain extends in this direction out to  $\pm 20W$  to permit an examination of stopping phases. The fault-normal extent of the computational domain on each side of the fault is  $15W$ . We run each simulation for a duration that permits the S-wave stopping phase from the fault ends to reach  $15W$  in the fault-normal direction for any  $x$ . We discretize the medium with a uniform grid spacing of  $h^* = 0.02$  (i.e., a grid spacing of  $h = 200$  m for  $W = 10$  km, which is far larger than desired if the estimates of slip-weakening-zone sizes,  $R$ , of a few tens of meters at mid-seismogenic depths by Rice et al. (2005) are accurate). Numerical resolution is discussed below, but we note here that the resolution is determined by the choice of  $A^*$ ; larger  $A$  implies smaller  $R$ .

The 2D case provides a convenient starting point to calibrate the numerical method, and it further provides reference solutions to which we can compare our 3D results to isolate the effects of the finite fault width. The immediately arising question is which parameters should be held fixed when comparing sub-Rayleigh and supershear ruptures. For expanding ruptures on homogeneous faults, the seismic  $S$  ratio determines whether or not ruptures will achieve supershear speeds (Andrews, 1976). While this parameter has less importance in the context of our constant-speed models, this knowledge motivates our method of comparing sub-Rayleigh and supershear ruptures.

Consider the case that both  $G$  and  $\tau_p - \tau_r$  are intrinsic properties of the fault, which immediately implies a particular  $D_c$  as defined above. Then what determines whether or not a rupture propagates at a supershear speed is the stress drop,  $\Delta\sigma$ , relative to  $\tau_p - \tau_r$ . From this perspective, we wish to hold  $G$ ,  $\tau_p - \tau_r$ , and  $D_c$  fixed while varying  $v_r$  and  $\Delta\sigma$ . However, the former quantities all vary with propagation distance in our model. In the 2D self-similar case,  $G$  increases linearly with distance (Broberg, 1960, 1999; Freund, 1990). Upon introducing a slip-weakening zone with characteristic size  $\Delta\sigma/A$ , self-similarity is lost and both  $\tau_p - \tau_r$  and  $D_c$  become increasing functions of distance. A strictly self-similar model—which would feature a constant  $\tau_p - \tau_r$  and a  $D_c$  that increased linearly with time or propagation distance—could be achieved by making  $A$  inversely proportional to time, but we do not follow this approach. Instead, we simply select a distance  $x^* = 8$  and match  $G$  and  $\tau_p - \tau_r$  at this location. Matching  $G$  at any location suffices to match  $G$  for all locations in this 2D model, but this is not the case for  $\tau_p - \tau_r$  and  $D_c$  as discussed above.

The single tunable parameter in our models is  $A^*$ , and we first examined the sub-Rayleigh case ( $v_r = 0.8c_s$ ) with an eye on numerical resolution. Choosing  $A^* = 7.00$  places a minimum of  $(\Delta\sigma/A)/h \approx 7$  grid points within the slip-weakening zone; this number increases as the rupture expands (see Figure 2.17 for an example of our resolution). By gathering data from ruptures with various  $A^*$  at the two supershear values of  $v_r$ , we iden-

$v_r/c_s$	$S$	$A^*$	$G^*$	$D_c^*$	$\Delta\sigma$ (MPa)	$A$ (MPa/km)	$R$ (km)
0.8	2.03	7.00	3.19	2.10	3.00	2.10	4.33
1.3	1.28	2.71	1.80	1.58	3.99	1.08	8.42
1.6	0.53	3.72	0.82	1.06	5.92	1.93	4.71

Table 2.2: Model parameters, reported as both nondimensional values and when dimensionalized in the case that  $\Delta\sigma = 3$  MPa for  $v_r = 0.8c_s$  (see Table 2.1 and text for further discussion of the dimensionalization method). Parameters which are independent of  $v_r$  are  $G = 9.57$  MJ/m<sup>2</sup>,  $\tau_p - \tau_r = 9.09$  MPa, and  $D_c = 2.10$  m. Note that  $G$ ,  $\tau_p - \tau_r$ ,  $D_c$ , and  $S$  increase with propagation distance in our model; the values reported here are measured at  $x = 8W$  in the 2D geometry.

tified the model parameters listed in Table 2.2.

We further need to explore how the particular choice of  $A$  (and hence  $\tau_p - \tau_r$  and  $D_c$ ) influences field amplitudes. There is considerable uncertainty in the appropriate values of  $\tau_p - \tau_r$  and  $D_c$ . From the perspective of seismic inversions, here are two primary reasons for this. First, slip inversions are limited in bandwidth, and Guatteri & Spudich (2000) and Spudich & Guatteri (2004) have shown that a strong trade-off exists between strength drop and slip-weakening distance for sub-Rayleigh ruptures. Second, Dunham & Archuleta (2005) have pointed out that, at least for 2D steady-state ruptures, the wavefield of sub-Rayleigh ruptures consists entirely of evanescent waves. This implies that a given frequency component of the wavefield decays exponentially with distance from the fault over a scale that is inversely proportional to the frequency. This also occurs for the dilatational component of fields from supershear ruptures. In contrast to this, the frequency content of the shear component of the wavefield (in the form of Mach waves) is preserved with increasing distance from the fault. To explore this issue in the context of our 3D rupture model, we conduct an additional two runs for  $v_r = 0.8$  and  $1.6c_s$ , increasing  $A$  first by a factor of two and then by a factor of four.

## Results

We proceed by propagating ruptures using the model parameters listed in Table 2.2 for both the 2D and 3D geometries. Prior to examining the off-fault fields, it is appropriate to examine the pattern of wavefronts generated by an expanding supershear rupture that stops. Only a certain region—a trapezoid on each side of the fault—experiences the passage of Mach waves (Figure 2.18), and it is within this region that the largest amplitudes are expected. In the 2D case, after the rupture has stopped, amplitudes at the planar Mach fronts remain undiminished as they radiate from the fault.

Figure 2.19 shows snapshots of particle velocities from our 3D ruptures. The wavefronts illustrated in Figure 2.18 are clearly seen. As previous studies have revealed, the dominant component of motion changes from the fault-normal to the fault-parallel direction as the rupture exceeds the S-wave speed (Agaard & Heaton, 2004; Dunham & Archuleta, 2005). The two-sided fault-normal pulse dominates the ground motion from sub-Rayleigh ruptures, but the largest amplitudes are concentrated within a distance  $\sim$

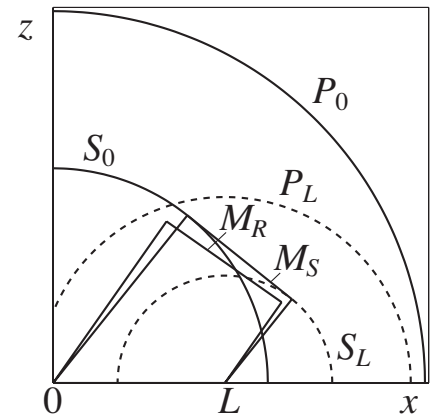


Figure 2.18: Wavefronts from an expanding supershear rupture that stops after propagating a distance  $L$ . The starting phases are marked as  $P_0$  and  $S_0$ , the stopping phases as  $P_L$  and  $S_L$ , and the Rayleigh and shear Mach fronts as  $M_R$  and  $M_S$ . Only points within the trapezoidal regions have experienced the passage of the respective Mach waves. A number of other wavefronts—such as head waves, Rayleigh waves on the fault, and Rayleigh-wave diffractions—are not shown.

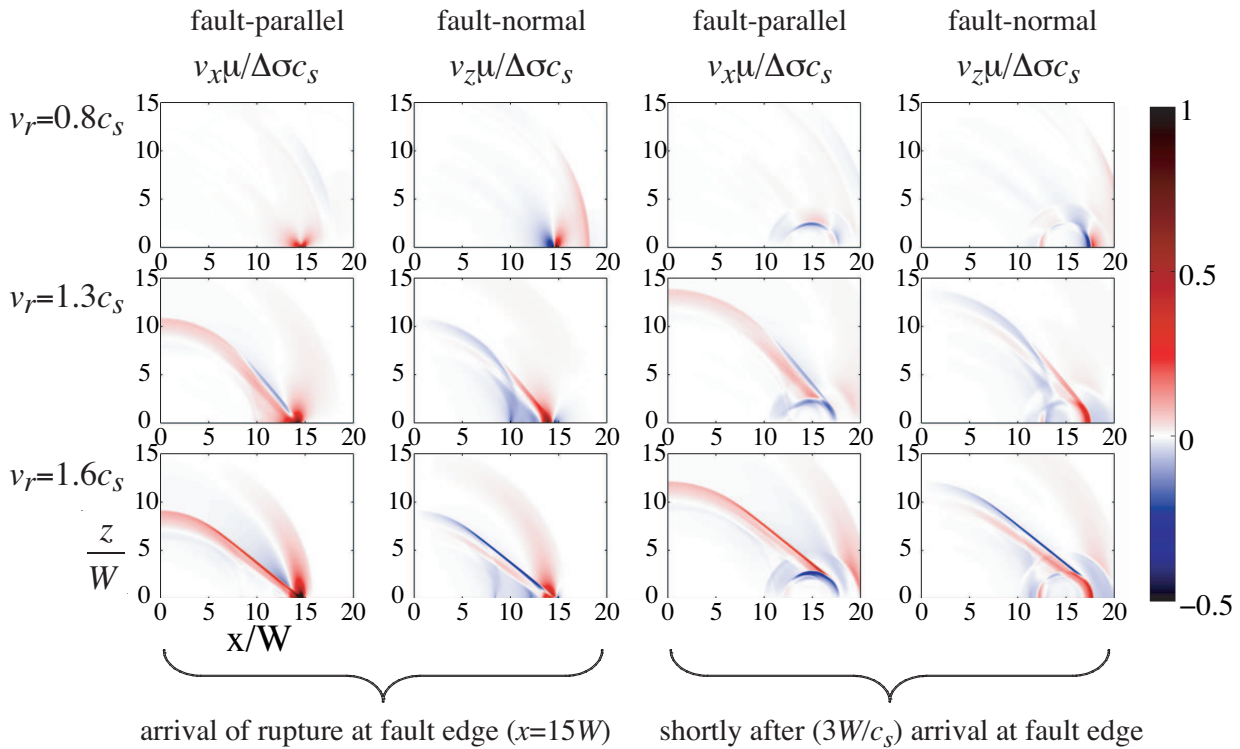


Figure 2.19: Snapshots of the free-surface velocity field for various rupture speeds at two times: just as the rupture arrives the edge of the fault and at a slightly later time (an additional  $3W/c_s$  after the arrival) to emphasize the stopping phases. Ruptures have identical  $G$ ,  $\tau_p - \tau_r$ , and  $D_c$  but different  $\Delta\sigma$ . Note that the value of  $\Delta\sigma$  used to nondimensionalize the velocities is different for each rupture speed (see Table 2.1). The color scale is saturated for positive values to emphasize field amplitudes away from the rupture front. The closely coincident shear and Rayleigh Mach fronts can most clearly be seen in the fault-normal component for  $v_r = 1.6c_s$  since the sign of this component is opposite for the two fronts.

$W$  from the fault. Large amplitudes are also present in the region beyond the end of the fault; these are carried by S-wave stopping phases. For supershear ruptures, the largest amplitudes, aside from those in the immediate vicinity of the rupture front, occur along the closely coincident Rayleigh and shear Mach fronts, which extend from the fault out to a distance determined by how far the rupture has propagated.

To further explore the ground motion histories, we plot seismograms at  $x = 10W$  for various distances from the fault (Figure 2.20). The location  $x = 10W$  is chosen because the rupture is well developed at this point (in the sense that the effects of the fault width are established), but the effects of the stopping phases are relatively minor. In addition to the velocity traces, we mark the arrival times of the P- and S-wave starting and stopping phases and, for stations within the Mach region for supershear ruptures, the arrival time of the shear Mach front. For example, the S-wave stopping phase arrives at

$$t = \frac{L}{v_r} + \frac{\sqrt{(L-x)^2 + z^2}}{c_s}. \quad (2.54)$$

The shear Mach front arrives at

$$t = \frac{x + z\sqrt{v_r^2/c_s^2 - 1}}{v_r}, \quad (2.55)$$

and the Rayleigh Mach front arrives at

$$t = \frac{x + z\sqrt{v_r^2/c_R^2 - 1}}{v_r}. \quad (2.56)$$

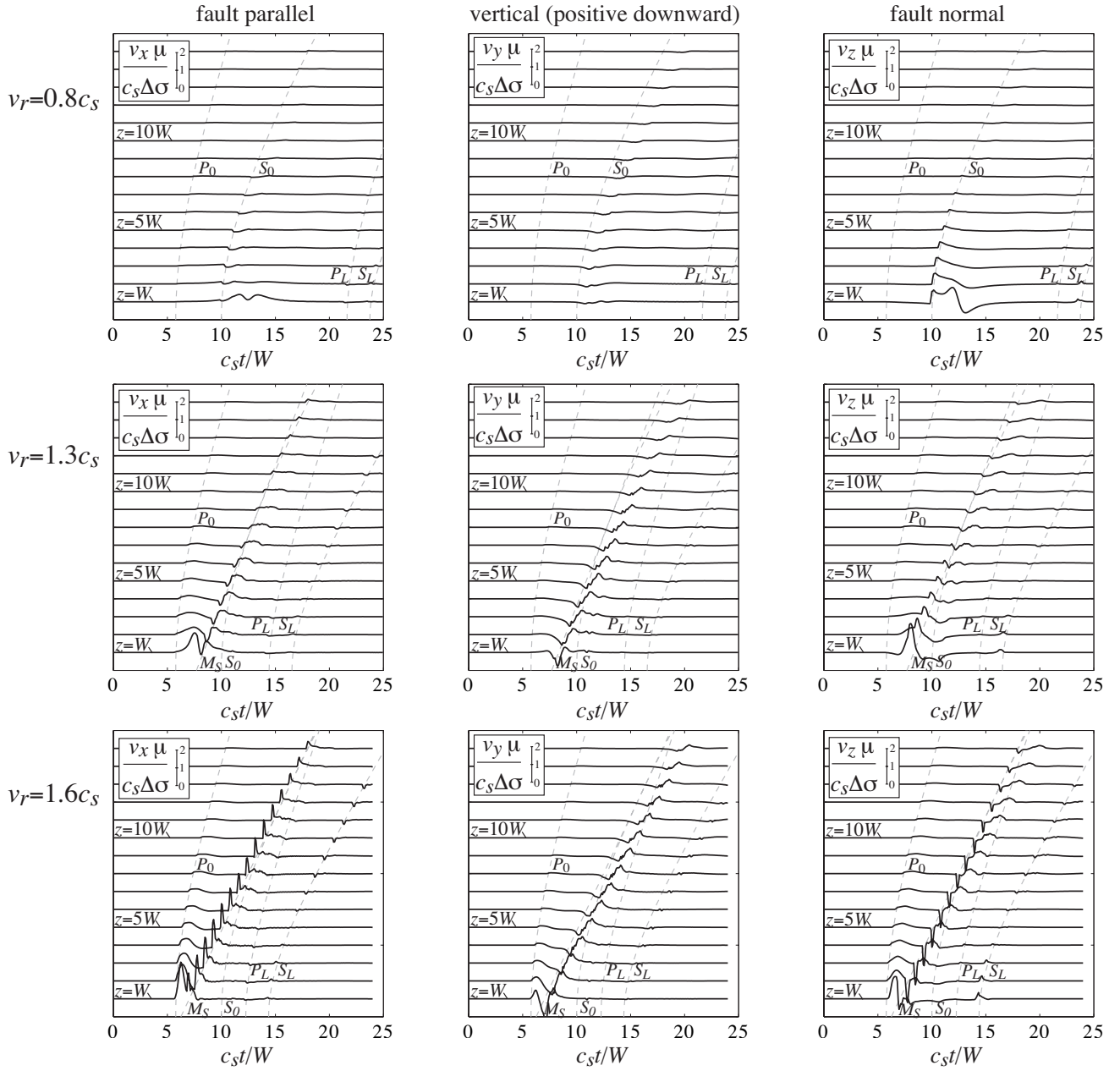


Figure 2.20: Velocity seismograms at  $x = 10W$  for various distances from the fault. Major wavefront arrivals illustrate in Figure 2.18 are marked. Ruptures have identical  $G$ ,  $\tau_p - \tau_r$ , and  $D_c$  but different  $\Delta\sigma$ . Note that the value of  $\Delta\sigma$  used to nondimensionalize the velocities is different for each rupture speed (see Table 2.1).

Using these seismograms as a reference, we are now in a position to determine the influence of the slip-weakening-zone size on ground-motion amplitudes. To illustrate the main results, we compare velocity seismograms from supershear ruptures with three values of  $A$  (Figure 2.21). For supershear ruptures, as  $A$  is increased (corresponding to more rapid weakening with a larger  $\tau_p - \tau_r$  and smaller  $D_c$  but fixed  $G$ ), amplitudes rise accordingly, but only at the Mach fronts. This is clearly evident when comparing the amplitudes of the dilatational waveform that precedes the Mach fronts; these amplitudes are completely insensitive to how rapidly the fault weakens. It further follows that the entire wavefield (both dilatational and shear components) of sub-Rayleigh ruptures will be rather insensitive to details of the weakening process at the rupture front, and our simulations

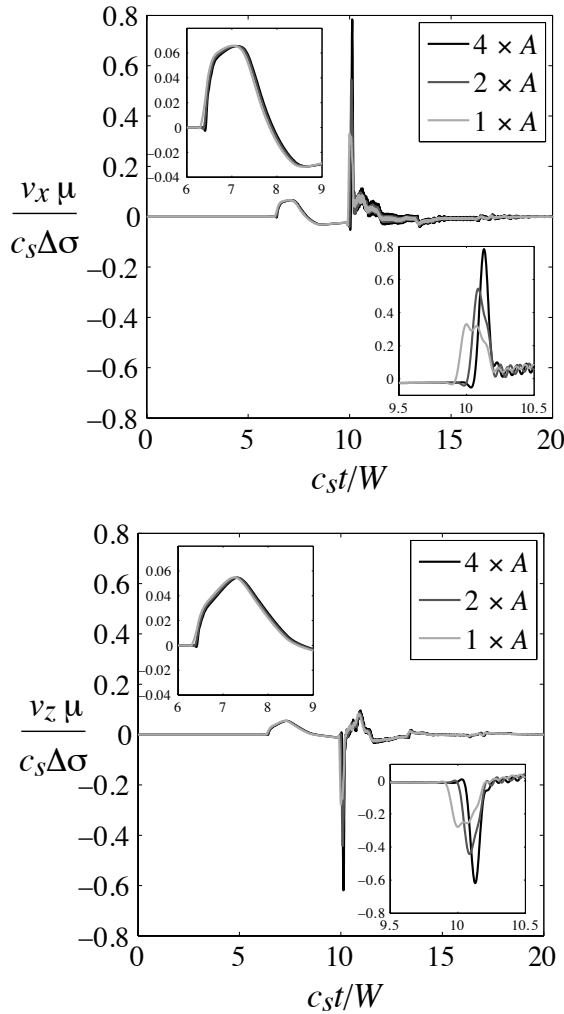


Figure 2.21: Velocity seismograms at  $x = 10W$  and  $z = 5W$  for a supershear rupture ( $v_r = 1.6c_s$ ) illustrating the effect of increasing  $A$ , the rate of weakening with distance from the rupture front [ $A = (\tau_p - \tau_r)/R$ ] by simultaneously decreasing the slip-weakening-zone size  $R$  and increasing the strength drop  $\tau_p - \tau_r$ . The two insets show close-up views of the dilatational waveform (upper left), which is insensitive to  $A$ , and the Mach fronts (lower right), which are highly sensitive to  $A$ . Seismograms at the same location from a sub-Rayleigh rupture with  $v_r = 0.8c_s$  (not shown), like the dilatational waveform of the supershear rupture, are insensitive to  $A$ . Due to the limited numerical resolution in our simulations, we are unable to use the realistic values of  $R$  predicted by Rice et al. (2005), and are consequently unable to separate the effects of the shear and Rayleigh Mach waves.

(not shown) confirm this. A possible exception to this might occur when the rupture process is highly unsteady. In this case, the wavefield would consist of both evanescent and radiating waves; the radiating waves will transport high-frequency signals away from the fault.

Our next step is to quantify the ground motion in our simulations by plotting the maximum peak-to-peak velocity experienced at each point on the free surface (Figure 2.22). In all cases, the largest ground motion occurs in the immediate vicinity of the fault. For sub-Rayleigh ruptures, the region beyond the fault end in the propagation direction also experiences strong shaking; this is carried by the S-wave stopping phase. For supershear ruptures, locations within the Mach region also experience large amplitudes; this is most evident for  $v_r = 1.6c_s$ . As discussed above, the peak amplitudes transmitted along the Mach front are quite sensitive to the particular details of the weakening process at the rupture front. As  $A$  is increased, the amplitudes within the Mach region also increase and eventually dominate any peak-to-peak motion generated by stopping phases.

The final step in our analysis is to plot maximum peak-to-peak ampli-

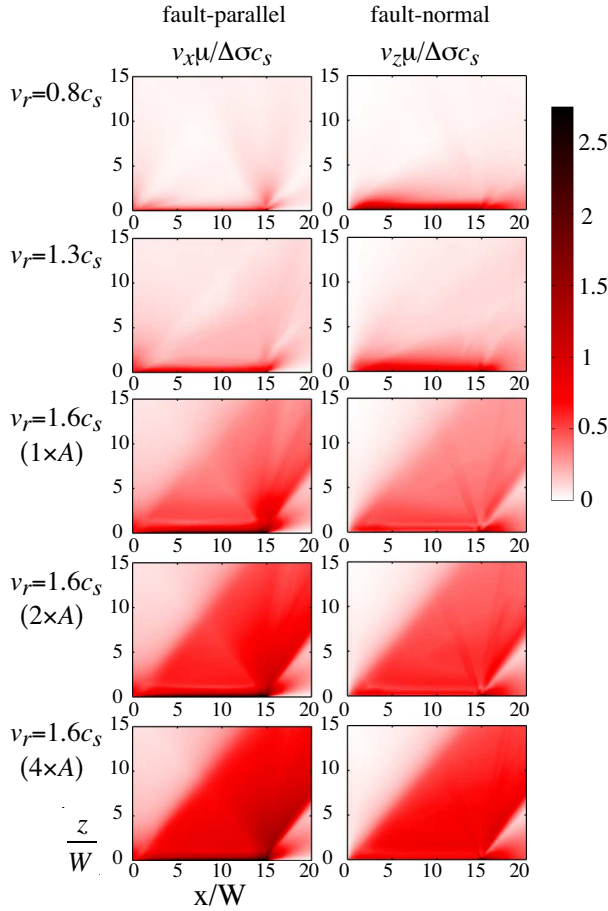


Figure 2.22: Maximum peak-to-peak amplitude of the free-surface velocity field. The top three rows compare ruptures with different speeds; these ruptures have identical  $G$ ,  $\tau_p - \tau_r$ , and  $D_c$  but different  $\Delta\sigma$ . The bottom three rows illustrate the effect of increasing the weakening rate,  $A$ , at the rupture front. Fracture energy is preserved, so increasing  $A$  increases  $\tau_p - \tau_r$  and decreases  $D_c$ . Note that the value of  $\Delta\sigma$  used to nondimensionalize the velocities is different for each rupture speed (see Table 2.1). The color scale covers the entire range of amplitudes for the top three rows, but is saturated for the bottom two rows.

tudes on the free surface along a line normal to the fault at  $x = 10W$  (Figure 2.23). Amplitudes from the supershear rupture with  $v_r = 1.6c_s$  are almost always the largest, except that fault-normal motion close to the fault is largest from sub-Rayleigh ruptures. The contrast between supershear and sub-Rayleigh ruptures is quite prominent at distances exceeding  $W$ . The nonmonotonic decrease of amplitude with increasing distance that appears for supershear ruptures (e.g., around  $x = 2W$  for  $v_r = 1.6c_s$  on the fault-parallel component) stems from the fact that close to the fault, peak amplitudes occur not at the Mach fronts but within the dilatational waveform preceding it. At a distance of about  $2W$ , the Mach waves, which decay at a more gradual rate than the dilatational field components, become the carriers of the peak amplitudes. This can be seen by examining the seismograms in Figure 2.20.

We also show a similar plot for supershear ruptures ( $v_r = 1.6c_s$ ) with larger values of  $A$  (corresponding to larger  $\tau_p - \tau_r$  and smaller  $D_c$  and  $R$ ) in Figure 2.24. As  $A$  is increased, the Mach fronts become more concentrated and exhibit larger amplitudes. As discussed previously, fields from sub-Rayleigh ruptures become progressively more insensitive to  $A$  away from the fault. This means that larger values of  $A$  will result in an increase in peak-to-peak amplitudes far from the fault for supershear ruptures (as evidenced by Figure 2.24). On the other hand, sub-Rayleigh ruptures will have

amplitudes only as large as those shown in Figure 2.23 regardless of the extent of the slip-weakening zone.

As stated earlier, one objective of this project is to evaluate the validity of using the 2D steady-state slip-pulse model of Dunham & Archuleta (2005) and Bhat et al. (2007) to predict fields around propagating ruptures. We consider only the case of  $v_r = 1.6c_s$ , since we are primarily interested in how rapidly amplitudes at the Mach fronts decay with distance from the fault (which we expect to be influenced by the finite fault width). The parameters of the slip-pulse model are the rupture speed  $v_r$ , the strength drop  $\tau_p - \tau_r$ , the extent of the slip-weakening zone  $R$ , and the length of the slip pulse. We assign these parameters by comparison to our 3D results at the free surface when the rupture front reaches  $x = 10W$ . This is shown in Figure 2.25. Then, by evaluating the expressions given in Dunham & Archuleta (2005), we obtain plots of the maximum peak-to-peak amplitudes in the 2D model as a function of distance from the fault; these are compared to our 3D results, calculated not over all time as before, but now from the wavefield present in the medium at the time that the rupture front reaches  $x = 10W$ . This appears in Figure 2.26. The 2D model provides an accurate prediction of the fields in the immediate vicinity of the fault, especially on the fault-parallel component. The fault-normal component is not precisely matched; this is likely because of free surface effects (since the agreement between the two models increases if the station is situated below the free surface). The 2D approximation breaks down at distances larger than  $W$ , where an inverse square-root decay of amplitudes at the shear Mach fronts diminishes amplitudes below that in the 2D model. Furthermore, Rayleigh Mach waves are completely absent in the 2D model, and at great distances from faults in 3D, these are expected to carry the largest amplitudes.

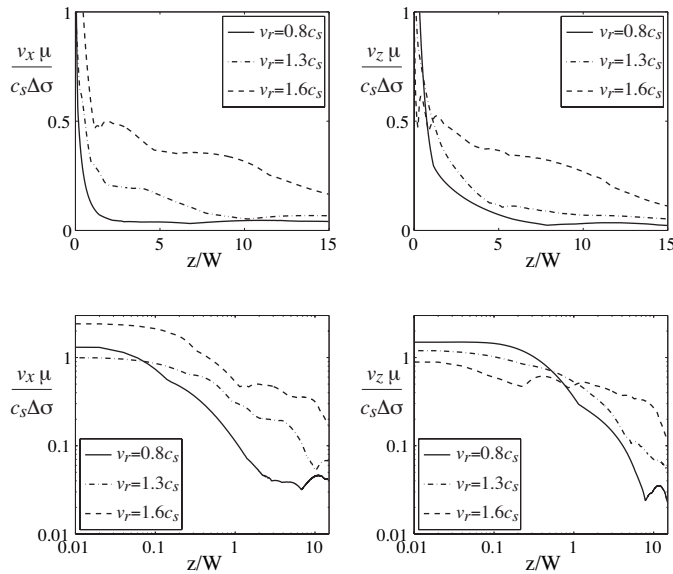


Figure 2.23: Maximum peak-to-peak amplitude of fields at  $x = 10W$  as a function of fault-normal distance (shown on both linear and log-log scales). Ruptures have identical  $G$ ,  $\tau_p - \tau_r$ , and  $D_c$ , but different  $\Delta\sigma$ . Note that the value of  $\Delta\sigma$  used to nondimensionalize the velocities is different for each rupture speed (see Table 2.1).

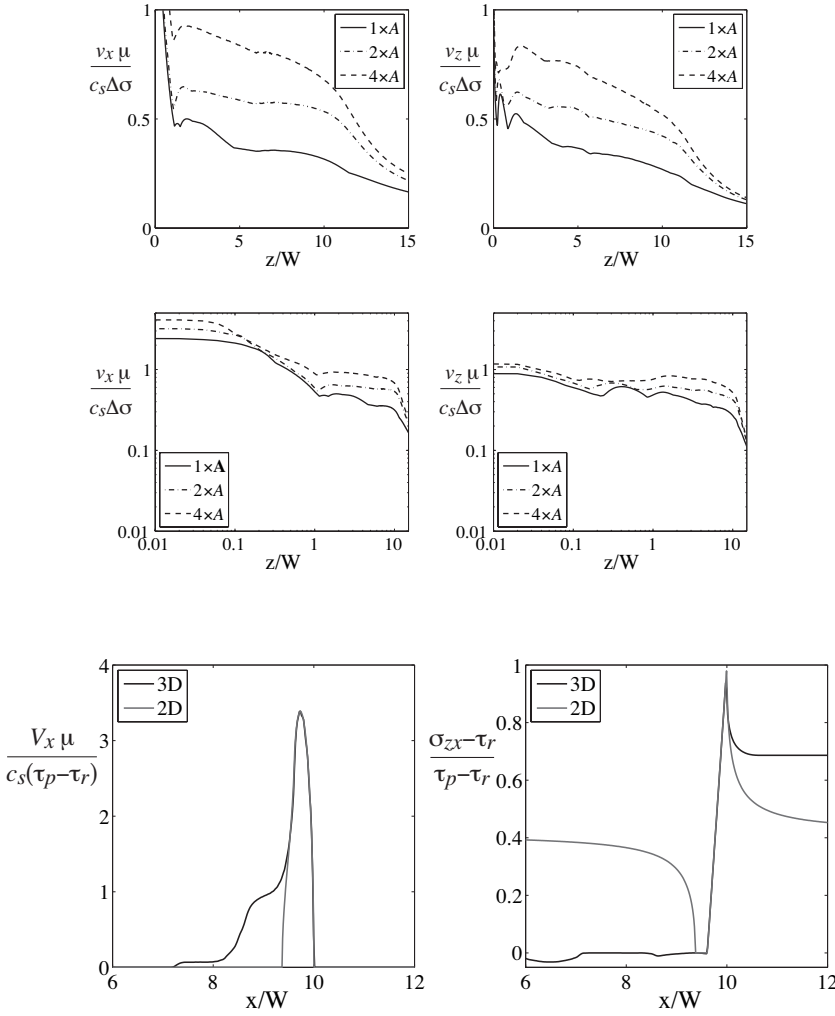


Figure 2.24: Maximum peak-to-peak amplitude of fields from a supershear rupture ( $v_r = 1.6c_s$ ) at  $x = 10W$  as a function of fault-normal distance (shown on both linear and log-log scales). The weakening rate at the rupture front,  $A$ , is increased by a factor of two and then by a factor of four. Fracture energy is preserved, so increasing  $A$  increases  $\tau_p - \tau_r$  and decreases  $D_c$  and  $R$ .

Figure 2.25: Slip velocity and shear stress for a 3D supershear rupture ( $v_r = 1.6c_s$ ) and its approximation by a two-dimensional steady-state slip pulse. Parameters are matched to the solution on the fault at the free surface when the rupture reaches  $x = 10W$ .

### Numerical Evidence for Rayleigh-Wave Mach Fronts from Supershear Ruptures

The most distinctive features of the 2D supershear slip-pulse models are the shear Mach waves. In 3D calculations incorporating a free surface, we also expect Mach fronts from Rayleigh waves that are generated by the interaction of the rupture with the surface. As a rupture propagates through an elastic half-space it would, if constraints of plane strain in the  $x - z$  plane were imposed, perturb the out-of-plane stress component,  $\sigma_{yy}$ , near the free surface. Since there is nothing to supply such constraint,  $\sigma_{yy}$  must vanish on the free surface; this can be accomplished by applying moving normal loads on the surface to negate the otherwise nonzero  $\sigma_{yy}$  pattern. These loads, which propagate at a super-Rayleigh speed if the rupture speed is supershear, will then excite Rayleigh Mach waves (Georgiadis & Lykotrfitis, 2001; Lansing, 1966).

As our simulations reveal, supershear slip pulses emit both Rayleigh and shear Mach waves into Mach bands bounded by linear wavefronts extending from both the leading and trailing edges of the slipping region, though

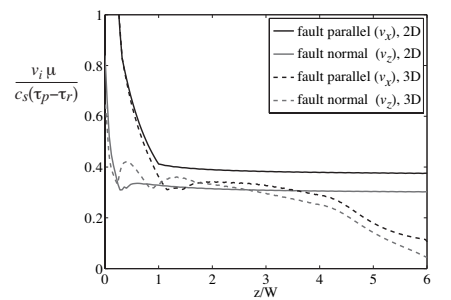


Figure 2.26: Maximum peak-to-peak amplitude of fields when the rupture reaches  $x = 10W$  as a function of fault-normal distance. The curves labeled “3D” are from our three-dimensional numerical simulations (stations on the free surface); these are compared with the two-dimensional steady-state slip-pulse model (labeled “2D”) of Dunham & Archuleta (2005) and Bhat et al. (2007).

the largest amplitudes occur in a narrower region corresponding to the portion of the slip pulse having the largest slip velocities (typically the size of the slip-weakening zone). The Rayleigh and shear Mach bands overlap close to the fault, but since the Rayleigh-wave speed is less than the S-wave speed, the two Mach bands eventually separate at sufficiently far distances from the fault. Denoting the length of the region emitting strong Mach waves as  $\tilde{R}$ , the two Mach bands separate at the fault-normal distance of

$$z = \tilde{R}/(\cot \beta_R - \cot \beta_s), \quad (2.57)$$

where  $\beta_R = \arcsin(c_R/v_r)$  and  $\beta_s = \arcsin(c_s/v_r)$  are the angles between the  $-x$ -axis and the Rayleigh and shear Mach fronts (or, equivalently, the half-angle of the Mach cones). The difficulty in clearly distinguishing the Rayleigh and shear Mach waves arises from the fact that the angle of the Rayleigh Mach fronts is only slightly smaller than that of the shear Mach fronts. For  $v_r = 1.6c_s$  and  $c_R \approx 0.9194c_s$  (assuming a Poisson material),  $\beta_s - \beta_R \approx 3.6^\circ$  and the separation distance is  $z \approx 5.7\tilde{R}$ .

The Rayleigh and shear Mach bands overlap over the entire computational domain in our simulations, but this may be an artifact of the extremely large slip-weakening zones (several kilometers when dimensionalized) that we had to assume to make our simulations numerically feasible. This is vastly larger than the estimate by Rice et al. (2005) of a few tens of meters. If their estimates are indeed correct, then the Rayleigh and shear Mach bands will separate at a fault-normal distance much smaller than  $W$ .

Since the orientation of the two Mach bands is so similar, we confirm the existence of Rayleigh Mach waves by exploiting certain properties of the particle velocities and stresses. First, we separate the dilatational and shear components of the fault-parallel and fault-normal velocities. To isolate the dilatational component, we take the divergence of the velocity vector. This filters out the shear component of the velocity (though it only approximately removes all S waves since S waves impinging on the free surface can generate both P and Rayleigh waves). The resulting Mach band associated with this filtered field is parallel to the expected orientation of the Rayleigh Mach front. To isolate the shear contribution to the velocity field, we take its curl and approximately filter out P waves and the dilatational component of Rayleigh waves. The resulting Mach band of the filtered field is parallel to the shear Mach front orientation. The filtered fields are shown in Figure. 2.27.

Second, the surface velocity vector associated with shear Mach waves should be parallel to the shear Mach front, and the velocity vector associated with Rayleigh Mach waves should be perpendicular to the Rayleigh Mach front. Thus, examining just the component of velocity parallel to the Rayleigh Mach front should emphasize the shear Mach band, and viewing just the component of velocity normal to the shear Mach front should emphasize the Rayleigh Mach band. Figure. 2.27 also shows this. In general we notice that the Rayleigh Mach waves are largest toward the trailing edge of the Mach band and that the shear Mach waves are largest toward the

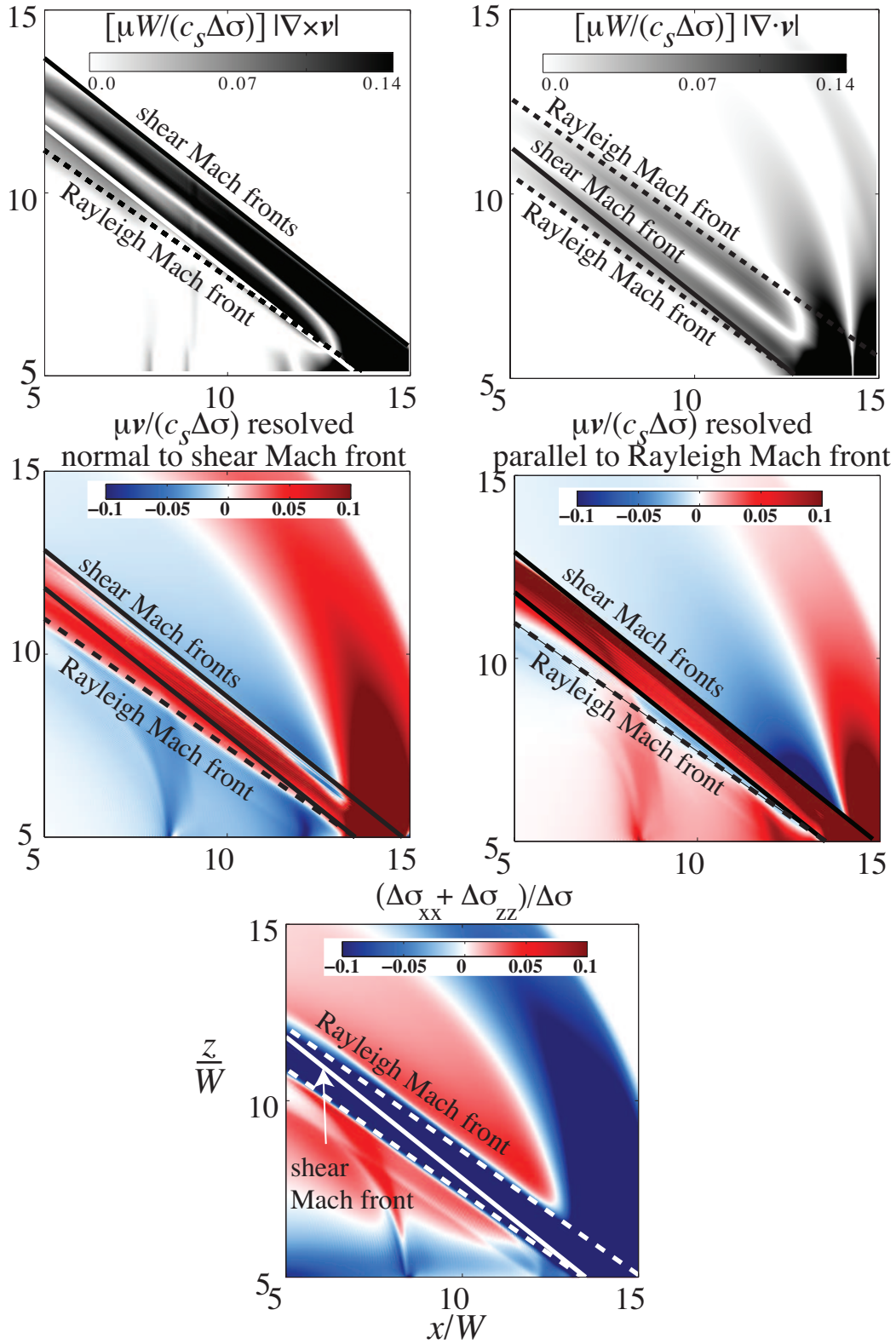


Figure 2.27: Various filtering techniques adopted to separate the Rayleigh and shear Mach fronts on the free surface. The solid lines are the shear Mach fronts and the dashed lines are the Rayleigh Mach fronts.  $\nabla \cdot \mathbf{v}$  filters out shear contributions, and  $\nabla \times \mathbf{v}$  filters out dilatational contributions (note that Rayleigh waves are comprised of both shear and dilatational fields).  $\mathbf{v}$  resolved normal to shear Mach front isolates Rayleigh Mach waves, and  $\mathbf{v}$  resolved parallel to Rayleigh Mach front isolates shear Mach waves.  $\Delta \sigma_{xx} + \Delta \sigma_{zz}$  (which is the trace of  $\sigma$  since  $\sigma_{yy} = 0$ ) is zero in the shear Mach band, but will be non-zero within Rayleigh Mach band.

leading edge.

A third way to illustrate the existence of Rayleigh Mach waves is to look at the volumetric part of the stress field. For 2D plane-strain supershear ruptures, the Mach waves are entirely comprised of S waves. This means that the volumetric part of the stress tensor (i.e., the trace,  $\Delta\sigma_{xx} + \Delta\sigma_{yy} + \Delta\sigma_{zz}$ ) vanishes within the Mach band. In 3D, if the Mach band is comprised mainly of S waves, then the same condition should be true. We check for this feature in our 3D results on the free surface (where  $\Delta\sigma_{yy} = 0$ ), and as Figure 2.27 demonstrates, this is clearly not the case. In fact we see large compressive stressing in the Mach band, which is consistent with the expected sense of stressing due to a Rayleigh wave that exerts compressional stresses in both the fault-parallel and fault-normal directions on the compressional side of the fault. Furthermore, the Mach band revealed in this filtered field is cleanly delimited by the Rayleigh Mach fronts.

We have thus shown that unlike the 2D supershear slip-pulse models of Dunham & Archuleta (2005) and Bhat et al. (2007), in which the Mach bands were comprised solely of S waves, supershear ruptures in a 3D elastic half-space also generate Rayleigh Mach waves. This leads to a more complex stress and velocity field within the Mach bands. Most importantly, since Rayleigh waves are confined to the free surface, they experience less attenuation from geometrical spreading than do body waves. In fact, for the ideally elastic medium we consider here, Rayleigh Mach waves suffer no attenuation with distance from the fault. This leads us to expect that even in 3D, supershear ruptures are capable of transmitting significant ground motion and stresses far from the fault.

### Off-fault Stressing and Activation of Secondary Faults

We next turn our attention to the off-fault stress fields, in particular to explore the hypothesis that the large stresses carried by the shear and Rayleigh Mach waves of supershear ruptures could activate secondary faulting on nearby faults. The observation of triggered faulting in the 2002 Denali fault earthquake (Eberhart-Phillips et al., 2003) prompted studies of whether or not something similar could occur in southern California. Our work builds on the latter study, though we do not explicitly model slip on secondary faults. Instead, we look at Coulomb stress changes,  $\Delta CS$ , on pre-existing fault structures of a given orientation (Figure 2.28). We specifically focus on two fault orientations, motivated by potential rupture of the southern San Andreas fault. The first is a thrust fault with a dip of  $30^\circ$  that strikes at  $30^\circ$  with respect to the main fault; this provides a rough approximation to thrust features like the Sierra Madre fault north of the Los Angeles basin. The second is a vertical strike-slip fault that strikes at  $150^\circ$  with respect to the main fault. This orientation is inspired by the San Jacinto fault; like the main fault, it is right-lateral. Note that we do not specify any spatial dimensions of the faults as we are only interested in resolving shear and normal stresses onto structures of a particular orientation. To briefly summarize the procedure, we calculate the shear stress change in the direction of slip,

$\Delta\tau$ , and the normal stress change,  $\Delta\sigma_n$  (positive in tension), and then evaluate  $\Delta CS = \Delta\tau + f_s\Delta\sigma_n$  for a static friction coefficient of  $f_s = 0.6$ . Finally, it is important to keep in mind that these estimates are surely affected by our large slip-weakening zone sizes, which cause the high-stress shear and Rayleigh Mach fronts to remain overlapped in the region studied (they do not seem to have reinforcing effects on Coulomb stress in general, but rather seem to have somewhat opposing effects).

Figures 2.29 and 2.30 show snapshots of  $\Delta CS$  from our 3D simulations, evaluated at mid-seismogenic depth ( $y = 0.5W$ ) at two times: just as the rupture arrives the edge of the fault and at a slightly later time (an additional  $3W/c_s$  after the arrival) to emphasize the stopping phases. Stress fields are evaluated at every point on the free surface, and only the regions of positive Coulomb stress change ( $\Delta CS > 0$ ) are shown. While Bhat et al. (2007) have obtained simple expressions for the far-field stress perturbations along the shear Mach bands of 2D supershear slip pulses, any comparison of their results with the 3D calculations would be invalid as the dilatational part of the stress field in the Mach bands is non-negligible. A possible exception might occur at distances sufficiently removed from the fault that shear and Rayleigh Mach bands do not overlap (such distances are probably unrealistically large in our simulations). Furthermore, we emphasize that the figures would likely look notably different if calculations could be done with small enough slip-weakening zones that the shear and Rayleigh Mach bands did not overlap so substantially as in the present work.

We evaluate the temporal evolution of Coulomb stress change, akin to the synthetic seismogram plots in Figure 2.20, on the above structures, along a line extending perpendicularly away from the fault at  $x = 10W$  at mid-seismogenic depth ( $y = 0.5W$ ). This is shown in Figures 2.31 and 2.32. We also calculate the maximum positive Coulomb stress change,  $\Delta CS_{\max}$ , experienced over all times, and study how this quantity decreases with distance from the fault in Figure 2.33.

Figure 2.29 shows  $\Delta CS$  for Sierra Madre-like structures due to a rupture propagating at various speeds and propagation directions on the San Andreas-like fault. In general, these thrust structures are favorably oriented for activation by stresses within the Mach bands of supershear ruptures ( $v_r > \sqrt{2}c_s$ ) propagating from the northwest (NW) to the southeast (SE) on San Andreas. The fault structures strike almost parallel to the Mach fronts for this direction of propagation. For SE to NW propagation, Sierra Madre-like structures are also favorably stressed for activation (for both  $v_r = 0.8c_s$  and  $1.6c_s$ ), but these stress changes are smaller than those from supershear ruptures propagating NW to SE. The influence of propagation direction is far more pronounced for San Jacinto-like structures, as illustrated in Figure 2.30. For all speeds, the favorable propagation direction for activation of these strike-slip structures is from the NW to the SE. In this case, the fault structures strike almost perpendicular to the Mach fronts.

It is interesting to note that the radiated stress field from stopping a su-

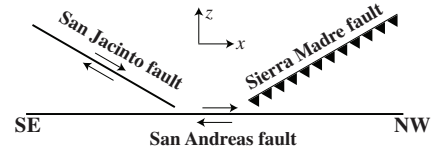


Figure 2.28: Geometry of faults on which Coulomb stress change,  $\Delta CS$ , is calculated. The right-lateral vertical strike-slip (San Jacinto-like) and thrust (Sierra Madre-like) faults strike at  $150^\circ$  and  $30^\circ$ , respectively, with respect to the main (San Andreas-like) fault. The Sierra Madre-like fault dips at  $30^\circ$ . Note that only the fault-plane orientations are required to calculate  $\Delta CS$ ; hence, the location and dimensions of the faults are for illustrative purposes only.

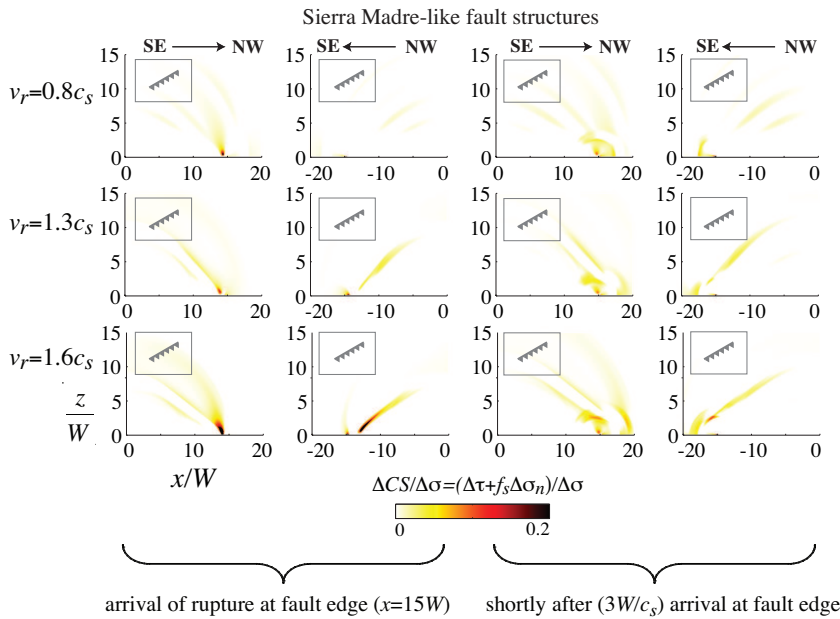


Figure 2.29: Snapshots of Coulomb stress change,  $\Delta CS$ , on Sierra Madre-like thrust structures at mid-seismogenic depth ( $y = 0.5W$ ) for various rupture speeds at two times: just as the rupture arrives the edge of the fault and at a slightly later time (an additional  $3W/c_s$  after the arrival) to emphasize the stopping phases. Ruptures have identical  $G$ ,  $\tau_p - \tau_r$ , and  $D_c$  but different  $\Delta\sigma$ . Note that the value of  $\Delta\sigma$  used to non-dimensionalize the velocities is different for each rupture speed (see Table 2.1).

pershear rupture at  $v_r = 1.6c_s$  is only slightly larger than that from stopping a sub-Rayleigh rupture. This is due to the fact that as the rupture approaches the P-wave speed, the dilatational field undergoes a Lorentz-like contraction parallel to the propagation direction. Furthermore, we see that the amplitude of Coulomb stress changes at the Mach fronts is generally comparable to stress changes in the immediate vicinity of the fault from a stopping sub-Rayleigh rupture. For a stress drop of 3 MPa, the Coulomb stress perturbation carried by the Mach front for  $v_r = 1.6c_s$  is about 0.3 MPa at a distance of  $3W$ . This estimate will only increase with decreasing slip-weakening-zone size.

Harris et al. (1991), Harris et al. (1991), and Fliss et al. (2005) suggest that stopping-phase stress fields might activate slip on adjacent, but unconnected, fault segments. However, while the large stress perturbation experienced in the near-fault-end region (for both sub-Rayleigh and supershear ruptures) is a permanent feature (at least until altered by postseismic or interseismic processes), the Mach-front stress perturbations are transient. The duration of these features can be seen in the Coulomb stress “seismograms” in Figures. 2.31 and 2.32. The typical duration of these features (for the probably too-large slip-weakening-zone sizes in our simulations) at a distance of  $5W$  is about  $0.5W/c_s$ , which translates to about 1.7 seconds for representative values of  $W$  and  $c_s$ . It is not yet established whether or not stress perturbations of such short duration (but large amplitude) can nucleate ruptures on secondary faults.

Figure. 2.33 shows the maximum positive Coulomb stress change,  $\Delta CS_{\max}$ , experienced at locations along a line extending from the fault at  $x = 10W$  and  $y = 0.5W$ . The direction of propagation for sub-Rayleigh ruptures barely changes  $\Delta CS_{\max}$  experienced by our two secondary fault orientations at distances  $z \gg W$ . For supershear ruptures, the propagation di-

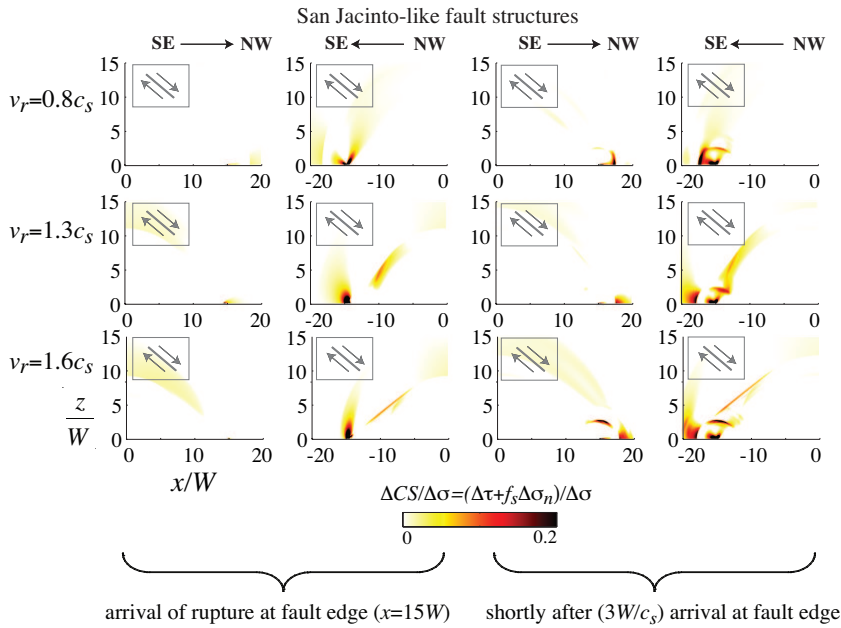


Figure 2.30: Same as Figure. 2.29 but for San Jacinto-like strike-slip structures.

rection that favors activation of San Jacinto-like and Sierra Madre-like ruptures is clear. A NW to SE supershear rupture transmits stresses along the Mach front out to distances as large as our computational domain ( $15W$ ) that might activate San Jacinto-like faults. For Sierra Madre-like thrust features, SE to NW propagation produces the largest stresses, though propagation in the opposite direction also generates significant stresses. Finally, these estimates of stress changes from supershear ruptures are highly sensitive to details of the weakening process at the rupture front, as discussed earlier in the context of the velocity field. The estimates given here should be interpreted as a lower bound, since we are constrained to the most gradual of physically likely weakening rates by numerical constraints. When parameterized by the slip-weakening distance, a reduction of  $D_c$  from about 2 m (as used in the calculations shown here) to 0.5 m (with a corresponding increase in the strength drop) would increase amplitudes at the Mach fronts by a factor of four. Furthermore, the overlapping Mach bands are sometimes partly self-canceling as regards contributions to  $\Delta CS$ , a feature that would not be present when they do not overlap.

To conclude, we have explored the influence of rupture speed on the character and amplitude of ground motion and radiated stresses from ruptures on a vertical finite-width fault breaking the free surface of a half-space. This extends our previous work on supershear dynamic ruptures in two dimensions (Bhat et al., 2007; Dunham & Archuleta, 2005). In those 2D steady-state models, shear Mach waves transport velocities and stress comparable to those experienced on the fault out to infinity. Without a source of waves below the bottom edge of the fault, field amplitudes of body waves in our 3D model must diminish beyond a distance that scales with the fault width,  $W$ . As Ben-Menahem & Singh (1987) pointed out, the decay rate of shear Mach waves will be governed by the geometrical spreading of the Mach cone, causing amplitudes to decrease with the inverse square-root of

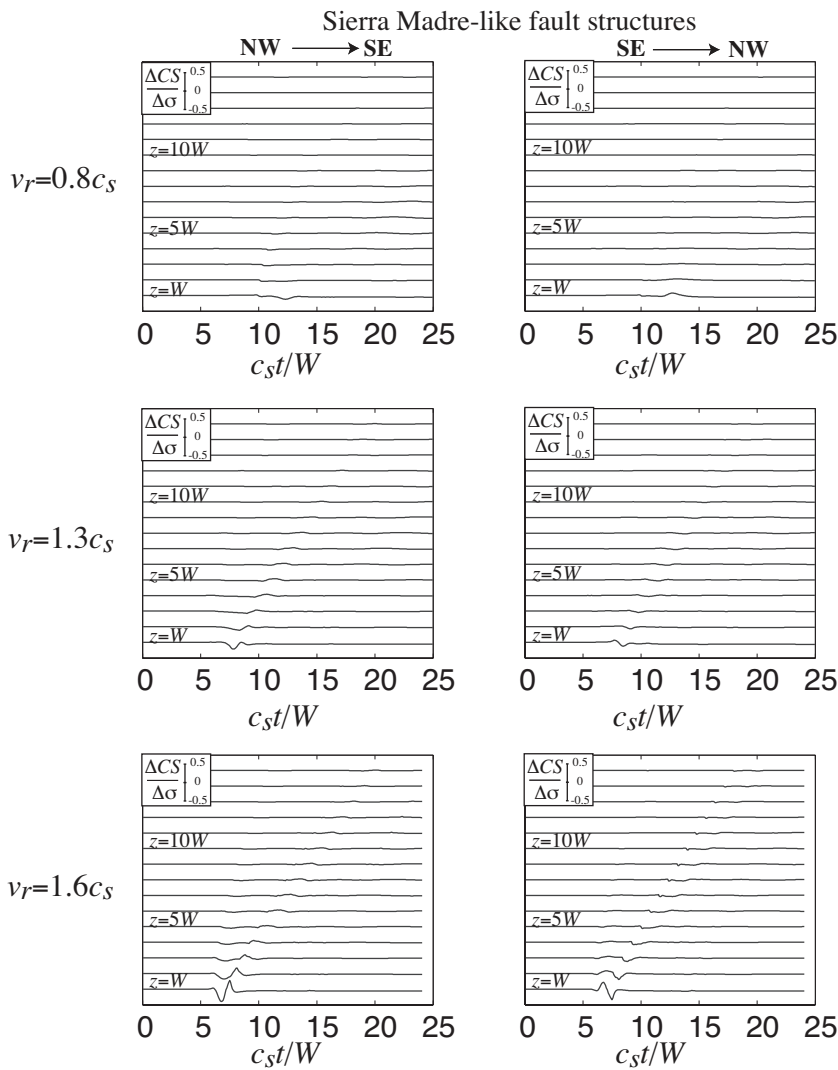


Figure 2.31: Temporal evolution of  $\Delta CS$  on Sierra Madre-like fault structures at various fault-normal distances at  $x = 10W$  at mid-seismogenic depth ( $y = 0.5W$ ).

distance from the fault. In addition to producing the shear Mach waves seen previously in 2D models, 3D supershear ruptures in a half-space also generate Rayleigh Mach waves. The Rayleigh and shear Mach bands overlap near the fault, but eventually separate due to the slight difference in wave speeds. The interference of the two Mach bands in the overlap region leads to more complex velocity and stress fields. Perhaps most importantly, geometrical spreading considerations suggest no attenuation of Rayleigh Mach waves.

We have not modeled two important factors that will influence field amplitudes: incoherence of the rupture process, and scattering and attenuation along the path of radiating waves. The former has been examined by Bernard & Baumont (2005) in the context of rupture-front curvature. At distances much closer than  $W$ , an extra factor proportional the inverse square-root of distance to the fault must be added. Ben-Menahem & Singh (1987) accounted for attenuation in the form of a constant quality factor in their study of propagating supershear dislocations, finding the precise manner

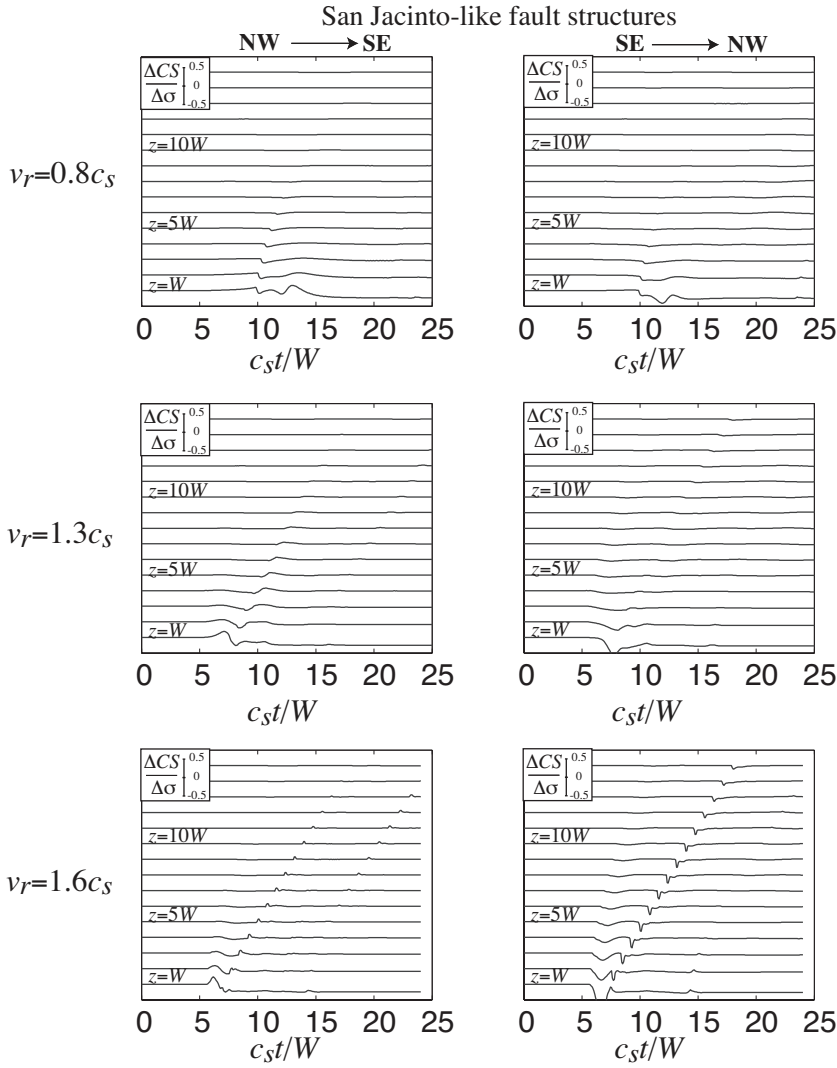


Figure 2.32: Same as Figure. 2.31 but for San Jacinto-like strike-slip structures.

in which attenuation bounds otherwise infinite accelerations (arising from their choice of a delta-function source time function).

As our 2D models suggested, there are significant differences between the radiated wavefields of sub-Rayleigh and supershear ruptures. Off-fault fields not in the immediate vicinity of the fault are only sensitive to details of the weakening process at the rupture front within the Mach bands of supershear ruptures. Increasing the weakening rate (by simultaneously decreasing the extent of the slip-weakening zone and increasing the strength drop) increases the amplitude of the Mach waves. This furthermore decreases the fault-normal distance required for separation of the Rayleigh and shear Mach bands. In general, we find that supershear ruptures produce larger velocities and stresses far from faults than do sub-Rayleigh ruptures. At a distance of  $x = 10W$ , supershear ( $v_r = 1.6c_s$ ) ruptures produces velocities that are five to ten times higher than those of sub-Rayleigh ruptures. The differences are not quite as pronounced for stress changes, but stresses at  $x = 10W$  from supershear ruptures are several times larger

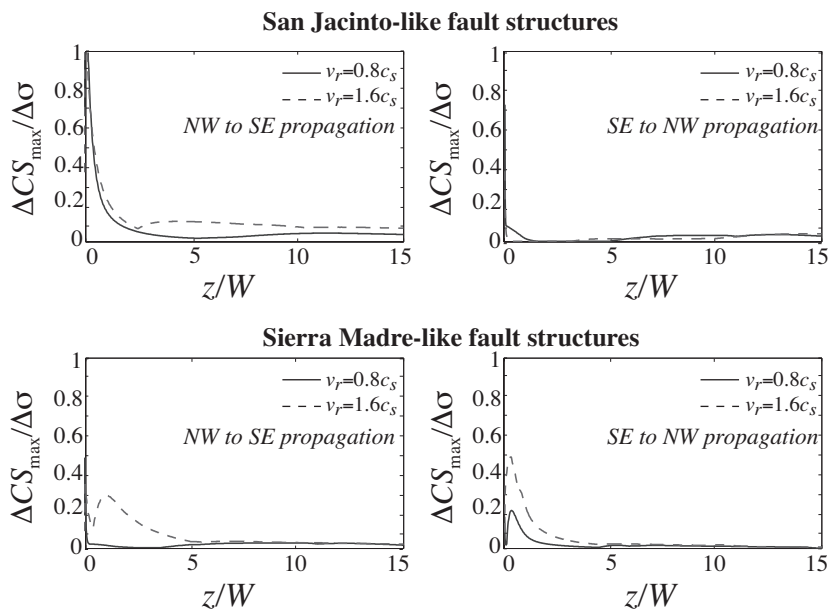


Figure 2.33: Evolution of maximum positive Coulomb stress change,  $\Delta CS_{\max}$ , on San Jacinto-like and Sierra Madre-like fault structures with fault-normal distance.  $\Delta CS_{\max}$  is evaluated at  $x = 10W$  at mid-seismogenic depth ( $y = 0.5W$ ).

than those from sub-Rayleigh ones. Quite importantly, both velocity and stress amplitudes from supershear ruptures depend highly on the extent of the slip-weakening zone. The estimates given above lie at the least conservative end of physically likely values, since much smaller slip-weakening distances — which would generate much higher velocities and stresses — have been suggested from a combination of laboratory constraints and seismic observations (Rice et al., 2005). When decreasing the slip-weakening-zone size by some factor, the peak velocities and stresses at the Mach fronts are increased by approximately that same factor. This sensitivity to the slip-weakening-zone size is not present for sub-Rayleigh ruptures.

Our results raise the possibility that stresses from a supershear rupture might initiate slip on faults adjacent to the one hosting the supershear rupture. As a hypothetical example, we consider what might occur if the southern San Andreas fault fails at supershear speeds. Activation of San Jacinto-like structures is favored if the rupture propagates from the northwest to the southeast, but receives almost negligible positive stressing for ruptures propagating in the opposite direction. The sensitivity of Sierra Madre-like thrust structures to propagation direction is less pronounced, though activation is again favored by ruptures propagating from the northwest to southeast. Our least conservative, but computationally most feasible, parameter choice involves overlap of the two Mach bands at all distances investigated, a condition which usually leads to some partial cancellation of Coulomb stress changes. This would not be present for more conservative choices, for which the bands would not overlap except quite near the fault.

## 2.7 Transition to Supershear Speed

As discussed before the rupture speed regime between the Rayleigh and shear wave speeds is energetically inadmissible, under idealised 2D conditions. Thus transition from a sub-Rayleigh to a supershear speed requires a jump in rupture velocity. This conundrum was first solved by Burridge and Andrews and the mechanism they proposed is called Mother-Daughter transition. It is also referred to as the Burridge-Andrews mechanism (Andrews, 1976; Burridge, 1973; Burridge et al., 1979). It was proposed that a peak in the S-wave field positioned just ahead of the sub-Rayleigh rupture front steadily increases in magnitude until it overcomes the frictional fault strength. Once this occurs a so-called “daughter crack” is formed, which is momentarily dissociated from the original ruptured portion of the fault and, by definition, is supershear. The leading front of the daughter crack begins as a unstable supershear rupture, which then rapidly accelerates and transitions into a stable supershear rupture. The trailing front rapidly merges with the “Mother” crack making the entire crack supershear. Liu et al. (2014) further refined this picture and showed that for relatively weaker faults, the rupture speed always passes smoothly and continuously through the range of speeds between the Rayleigh and shear wave speeds in a very short time.

Alternative and equally plausible models for the nucleation of supershear ruptures consider the dynamic interaction of the sub-Rayleigh rupture with an inclusion or a local patch of higher strength along the frictional fault. The presence of these features can also directly lead to dynamic stress concentrations and localized instabilities, which can give rise to a supershear rupture (Dunham & Archuleta, 2004; Dunham et al., 2003; Liu & Lapusta, 2008). Both of the aforementioned supershear rupture transition mechanisms have been experimentally investigated and observed in LEQ experiments (Mello et al., 2014).

The methods used to infer supershear ruptures in nature, in most cases, are designed to reveal *a posteriori* which segment of the rupture propagated at supershear velocities. However, these methods often ignore the details of the transition to supershear rupture speed as they usually focus on the analysis of full-grown supershear ruptures. The location of the transition from sub- to supershear speeds is often inferred as follows. Once the regions of fully-developed ruptures are mapped, guided by seismological and geodetic inversions, the supershear transition is presumed to have occurred in-between the subshear and supershear segments, leading to an imprecise and ad hoc location of this transition. Moreover, it remains difficult to assign the location of this transition to specific features of the rupture path, as the conditions for supershear transitions in nature are still poorly understood, despite numerical efforts to characterise the mechanics of the transition process (Bhat et al., 2007; Bruhat et al., 2016; Liu et al., 2014; Liu & Lapusta, 2008).

However, under idealised conditions of planar fault with uniform fric-

tion and traction conditions it has been shown by Andrews (1976, 1985) that two conditions need to be met for supershear transition. One relates to the relative strength of the fault and states that the  $S$  ratio needs to be below the critical value,  $S_c$ .  $S_c$  is 1.77 in 2D and 1.19 in 3D (Dunham, 2007). The other states that the length of the fault has to be larger than  $L$ , the distance taken by a sub-Rayleigh rupture to eventually attain supershear speeds.

$$L = \frac{39.2}{\pi(1-\nu)} \frac{1}{(S_c - S)^3} \frac{\mu G}{(\tau_0 - \tau_r)^2} \quad (2.58)$$

Here  $\nu$  is the Poisson's ratio,  $\mu$  is the shear modulus and  $G$  is the fracture energy. As laboratory earthquake experiments come close to the ideal conditions, one can quite confidently use the above two guidelines to design supershear experiments.

In nature, unfortunately it's not true anymore. Thus, being able to locate precisely the supershear transition would therefore greatly help at identifying the mechanical reasons for such rupture process.

We first develop an approximation to understand how the velocity grows during a seismic rupture using the Linear Elastic Fracture Mechanics approach. In a 2D homogeneous isotropic linear-elastic body, we consider a semi-infinite plain-strain crack of length  $L$ , and  $(r, \theta)$  polar coordinates centred at the crack tip. Let  $\sigma_{\alpha\beta}^0$  represent the initial stress state of the medium. The static near-tip stress (positive in tension)  $\sigma_{\alpha\beta}$  field is given by

$$\sigma_{\alpha\beta}(r, \theta) = \sigma_{\alpha\beta}^0 + \frac{K_{II}}{\sqrt{2\pi r}} f_{\alpha\beta}^{II}(\theta) \quad (2.59)$$

where  $K_{II}$  is the static stress intensity factor and  $f_{\alpha\beta}^{II}$  are universal angular functions (Freund, 1979; Williams, 1957). The static stress intensity factor varies with the crack length such that

$$K_{II} = \phi(\sigma, \tau) \sqrt{\pi L} \quad (2.60)$$

where  $\phi(\sigma, \tau)$  depends on the applied normal  $\sigma$  and shear  $\tau$  stress. The stress at the rupture tip increases with the crack length.

Now consider that the crack tip that moves at a speed  $v \leq c_R$ , where  $c_R$  is the Rayleigh wave speed. The near-tip stresses now depend on a the rupture speed  $v$  as follows

$$\sigma_{\alpha\beta}(r, \theta, v) = \sigma_{\alpha\beta}^0 + \frac{K_{II}^{dyn}(v)}{\sqrt{2\pi r}} f_{\alpha\beta}^{II}(\theta, v) \quad (2.61)$$

where  $K_{II}^{dyn}$  is the dynamic stress intensity factor. This solution is entirely analogous to the static problem. However, due to the moving coordinate system, all the fields undergo a Lorentz-like contraction, affecting both the stress intensity factor and the angular distribution. The dynamic stress intensity factor can be approximated as Freund, 1972

$$K_{II}^{dyn} \approx \frac{1 - v/c_R}{\sqrt{1 - v/c_P}} K_{II} \quad (2.62)$$

where  $c_P$  is the limiting speed for a mode II crack, being  $c_P$  the P-wave speed. Also  $K_{II} = \phi(\sigma, \tau) \sqrt{\pi L(t)}$  where the crack length is given by  $L(t) = \int_0^t v(t) dt$ .

Using the expressions above, we will compute the extent of the ‘yield’ region in the off-fault medium. To generalize and illustrate the state of stress, we represent normal and shear stress using invariants

$$\sigma = \frac{\sigma_{kk}}{3} \quad \text{and} \quad \tau = \sqrt{\frac{1}{2} s_{ij} s_{ji}} \quad \text{with} \quad s_{ij} = \sigma_{ij} - \sigma \delta_{ij} \quad (2.63)$$

Solutions from linear elastic fracture mechanics give the state of stress at the crack tip for a mode II crack:

$$\sigma_{11} + \sigma_{22} = \sigma_{11}^0 + \sigma_{22}^0 + \frac{K_{II}}{\sqrt{2\pi r}} \left( -2 \sin \frac{\theta}{2} \right). \quad (2.64)$$

Since  $\sigma_{33} = \nu(\sigma_{11} + \sigma_{22})$  in plane strain, where  $\nu$  Poisson’s ratio, we can compute  $\sigma$ :

$$\sigma = \sigma^0 - \frac{2(1+\nu)}{3} \frac{K_{II}}{\sqrt{2\pi r}} \sin \frac{\theta}{2}. \quad (2.65)$$

Likewise, we compute  $s_{12}$ :

$$s_{12} = \sigma_{12}^0 + \sigma_{12} \quad (2.66)$$

$$= \sigma_{12}^0 + \frac{K_{II}}{\sqrt{2\pi r}} \left[ \cos \frac{\theta}{2} \left( 1 - \sin \frac{\theta}{2} \sin \frac{3\theta}{2} \right) \right] \quad (2.67)$$

The bracketed term is designated as  $A(\theta)$ . Thus we can compute  $\tau$ ,

$$\tau = \sqrt{\frac{1}{2} s_{12}^2} \quad (2.68)$$

The Drucker-Prager failure criterion,  $F$ , with a friction coefficient  $f$  is defined as,

$$F(r, \theta, L, \phi, v/c_R, \sigma_{ij}^0) \equiv \tau - f\sigma = 0, \quad (2.69)$$

For a fixed initial stress state,  $\sigma_{ij}^0$ , and a rupture velocity history,  $v(t)$ , one can then calculate the furthest distance from the fault,  $r_{DP}$ , where the Drucker-Prager yield criterion is violated.

When an earthquake rupture transitions to a supershear regime, the rupture has to first accelerate to the Rayleigh wave speed. As the rupture approaches the supershear transition,  $K_{II}^{dyn}$  monotonically decreases to zero, strongly reducing the stress concentration at the rupture tip. A Lorentz-like contraction of the stress field occurs around the rupture tip as the rupture speed approaches its limiting speed,  $c_R$  (Freund, 1972). This contraction has already been observed and verified experimentally (Svetlizky & Fineberg, 2014). Thus the off-fault domain affected by this stress concentration will also shrink. We illustrate this effect by calculating the extent of the region where the stress state goes beyond the limits defined by a Drucker-Prager failure criterion (Figures. 2.34a and 2.34b). This domain, which

describes the theoretical extent of coseismic off-fault deformation, such as fracture damage and aftershocks, will be directly affected by stress changes. We show that the extent of the coseismic off-fault deformation results from a combined effect of the increase in the rupture length and the decrease of the term

$$(1 - v/c_R)/\sqrt{1 - v/c_P}$$

with increasing speed  $v$  (see Methods Section for details of the demonstration). As the rupture approaches the Rayleigh wave speed, with uniform (Figure. 2.34a) or non-uniform (Figure. 2.34b) rupture velocity, the stress concentration at the rupture tip ultimately collapses, limiting the spatial extent of possible off-fault damage and consequent aftershocks during the transition from the sub-Rayleigh to the supershear regime.

This theoretical demonstration is then validated through two different numerical models that account for dynamic evolution of coseismic damage (Okubo et al., 2019; Thomas et al., 2017; Thomas & Bhat, 2018). In these models, unlike the theoretical development presented above, the rupture is spontaneous and there is a feedback between off-fault damage and on-fault rupture. Both models produce in-plane dynamic simulations of an earthquake rupture on a 1D right-lateral planar fault embedded in a 2D medium. A slip-weakening friction law is used to model the earthquake rupture and damage only occurs on the tensional side of the fault (bottom side of the fault on Figure. 2.34c and d, see Methods Section and Supporting Information for further details).

The first model employs novel numerical algorithms for earthquake rupture allowing for spontaneous activation of off-fault fracture networks (Okubo et al., 2019), HOSSedu, developed by the Los Alamos National Laboratory (LANL) (Rougier et al., 2016). The numerical algorithms behind this tool are based on the combined Finite-Discrete Element Method (FDEM) to produce dynamically activated off-fault fracture networks. One of the key FDEM is to allow each individual interface between the finite elements describing the off-fault medium to have their own tensional and shear cohesion. Furthermore, these interfaces can break under appropriate stress conditions. Each broken interface is then assimilated to a damage fracture. When the rupture propagates, this allows for a live build-up of the damage patterns (Klinger et al., 2018; Okubo et al., 2019).

Closeness to failure is derived using the invariant form of the Mohr-Coulomb yield criterion:

$$F_{MC} \equiv \tau R_{MC} - \sigma \tan \phi - C_{II}^p \quad (2.70)$$

where  $\tan \phi = f_s$  is initial static friction coefficient and  $C_{II}^p$  is initial peak shear cohesion. Failure occurs when  $F_{MC} \geq 0$ . Note that when  $R_{MC} = 1$ , the above become the Drucker-Prager yield criterion.

Here,

$$R_{MC} = \frac{1}{\sqrt{3} \cos \phi} \sin \left( \Theta + \frac{\pi}{3} \right) + \frac{1}{3} \cos \left( \Theta + \frac{\pi}{3} \right) \tan \phi \quad (2.71)$$

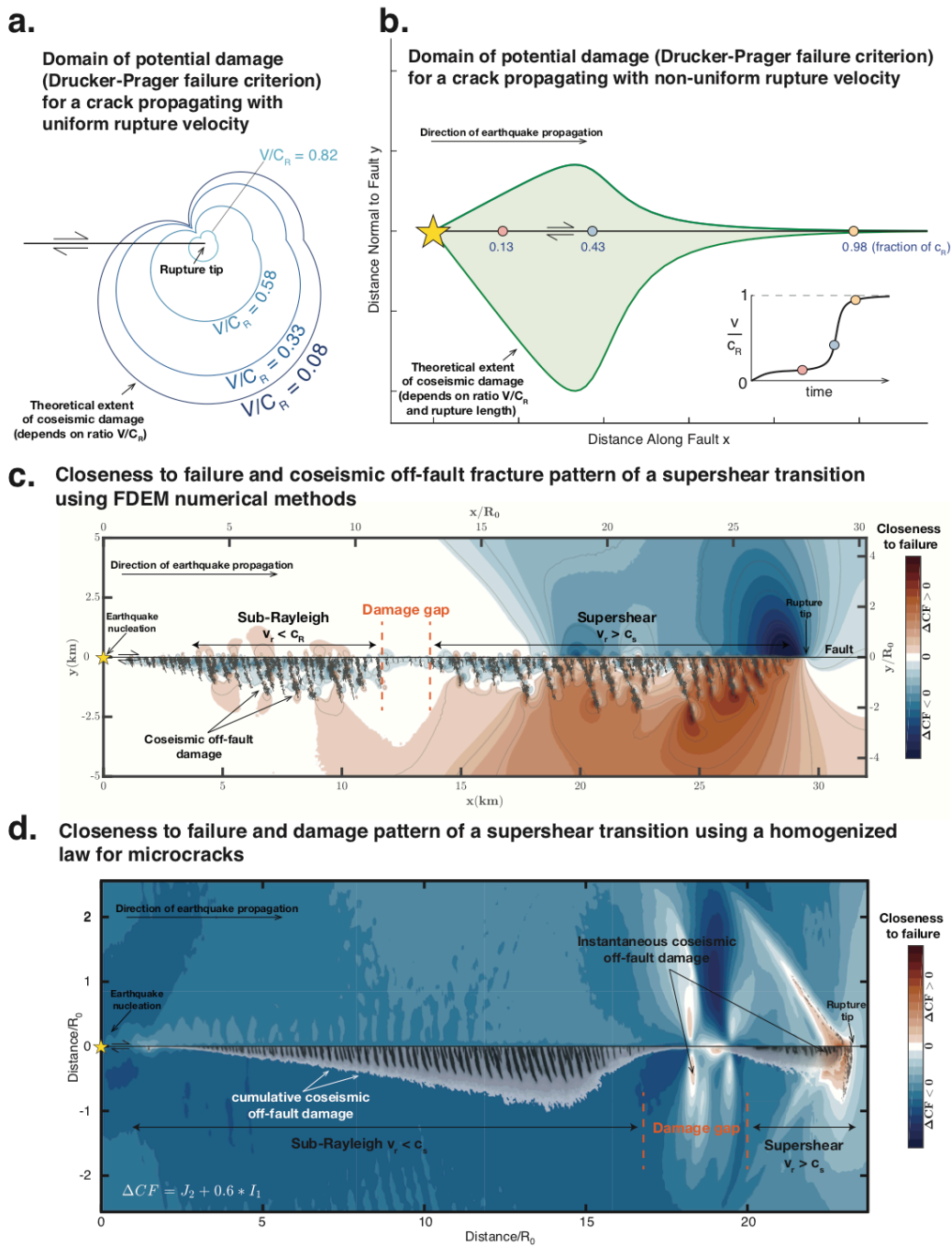


Figure 2.34: **Theoretical and Numerical Evidence of Supershear Transition Signature.** **a.** & **b.** Domain that exceeds Drucker-Prager failure criterion for a crack of uniform rupture velocity **(a)** and for a crack of non-uniform rupture velocity **(b)**. Both cases show that the region of potential damage shrinks as the rupture velocity  $v$  approaches the Rayleigh wave speed  $c_R$ . **c.** Changes in closeness to failure associated with Drucker-Prager failure criterion, computed using 2D FDEM dynamic simulation including coseismic off-fault damage generated by the rupture propagation (Okubo et al., 2019). **d.** Same as **(c)** but using an effective medium theory (Thomas & Bhat, 2018). The grey regions map the spatial distribution of damage density that occurs during the entire event while the black field record the damage that takes place at the time at which the Drucker-Prager failure criterion was computed. In both cases **(c** & **d)**, regions of positive change are more likely to host fracture damage and trigger future aftershocks. The transition from the sub-Rayleigh to the supershear regime is clearly denoted by a more localised and weaker stress perturbation and a consequent gap in damage.

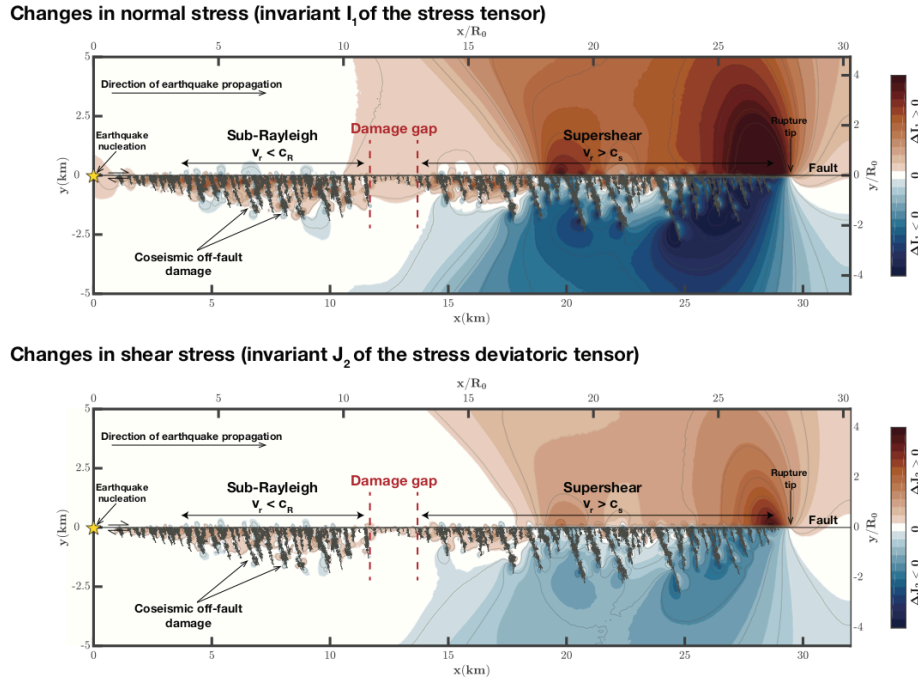


Figure 2.35: Changes in the normal stress (the first invariant of the stress tensor,  $I_1$ , is shown in the top panel) and shear stress (the second invariant of the deviatoric stress tensor,  $J_2$ , is shown in the bottom panel), obtained from a 2D FDEM dynamic rupture simulation including coseismic off-fault damage generated by the rupture propagation. Sub-Rayleigh and Supershear domains are denoted by black arrows with their respective rupture velocities, while the damage gap is the region between the red dashed lines. The earthquake is nucleated on the left of the each figure and symbolized by a yellow star. Coseismic off-fault damage is indicated by the black lines located south of the fault.

where  $r_s = \left( \frac{9}{2} s_{ij} s_{jk} s_{ki} \right)^{\frac{1}{3}}$  and  $\Theta = \frac{1}{3} \cos^{-1} \left( \frac{r_s}{\tau} \right)^3$ .

The closeness to failure yields

$$\Delta CF(\mathbf{x}, t) = \frac{F_{MC}(\mathbf{x}, t)}{F_{MC}^0(\mathbf{x}, t)} - 1. \quad (2.72)$$

Here  $F_{MC}^0$  is the Mohr-Coulomb yield function for the initial, uniform, state of stress. Failure is more likely to occur when  $\Delta CF > 0$ . (See Table S1 for all the parameters used in the simulations).

During the supershear transition, the intensity and spatial extent of off-fault damage drops (Figure. 2.34). In fact, while both the sub-Rayleigh and the supershear segments present high fluctuations of the stress invariants  $\sigma$  and  $\tau$ , the transitional region is clearly depleted in stress changes (Figures. 2.35, 2.36).

This has been observed in experiments as well (Rosakis, 2002). Once the rupture is over, we evaluate the damage pattern and the spatial variation of closeness to failure ( $\Delta CF$ ) resulting from the rupture. Regions with positive values of  $\Delta CF$  are more likely to host fracture damage and trigger future aftershocks. We see that the regions experiencing sub-Rayleigh and full blown supershear regimes manifest high local stress fluctuations (Figure. 2.34c). However, when the rupture is transitioning to supershear speed,  $\Delta CF \sim 0$ , and the spatial extent of the off-fault damage zone drops dramatically.

The second numerical model accounts for off-fault damage using a micro-mechanics based effective constitutive law (Bhat et al., 2012; Thomas & Bhat, 2018). This method reflects the micro-physics of damage evolution

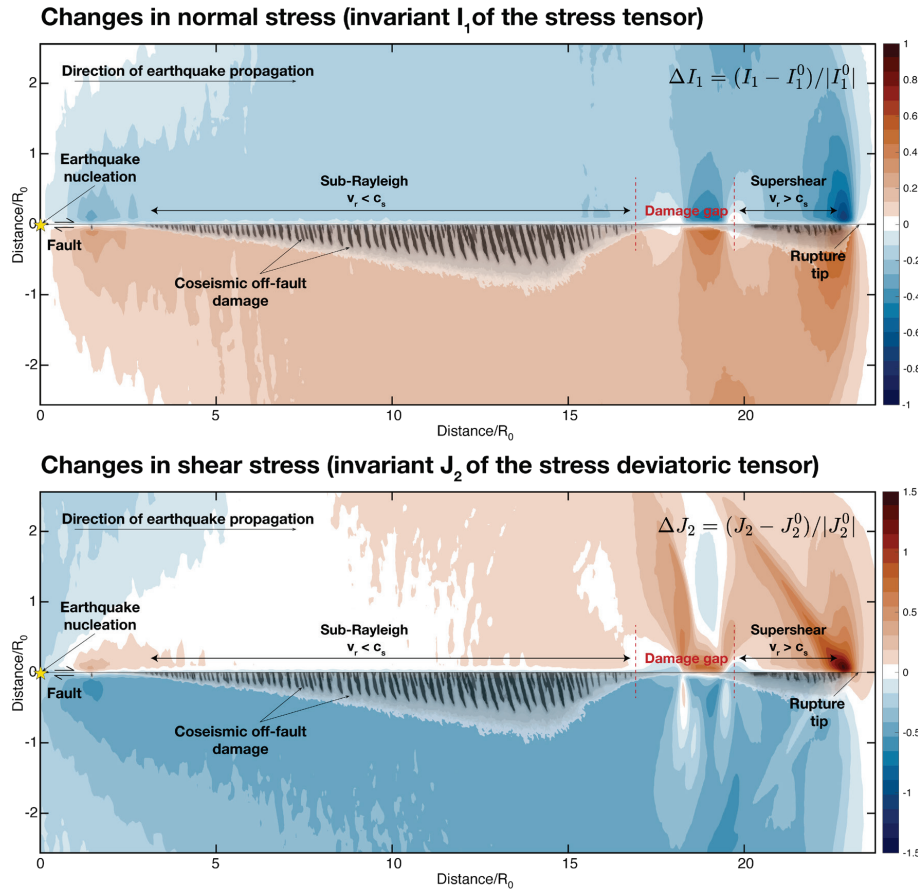


Figure 2.36: The same as previous except using effective medium theory.

by relating damage density to the near-tip stress state and by computing the corresponding dynamic changes of elastic properties in the medium due to the presence of newly formed cracks.

Here, closeness to failure  $\Delta CF$  is simply derived using the Drucker-Prager yield criterion:

$$\Delta CF(\mathbf{x}, t) = \frac{F_{MC}(\mathbf{x}, t)}{F_{MC}^0(\mathbf{x}, t)} - 1 \quad \text{with} \quad F_{MC} \equiv \tau - \sigma \tan \phi, \quad (2.73)$$

where  $\tan \phi = f_s = 0.6$  is initial static friction coefficient. Failure is more likely to occur when  $\Delta CF > 0$ .

The resulting off-fault damage density, which is directly affected by the near-tip stress state, as illustrated by the  $\Delta CF$ , is also characterised by a sudden shrinkage of the damage zone (Figure. 2.34d) during the supershear transition.

We can thus confidently conclude that, irrespective of the constitutive model to capture off-fault damage, one should expect a dramatic reduction in the spatial extent of the off-fault damage around supershear transition. This is due to the fundamental physical property, the so-called Lorentz contraction of the stress field, of a dynamic rupture approaching its limiting speed.

## 2.8 Scaling Relationship for Laboratory Earthquakes

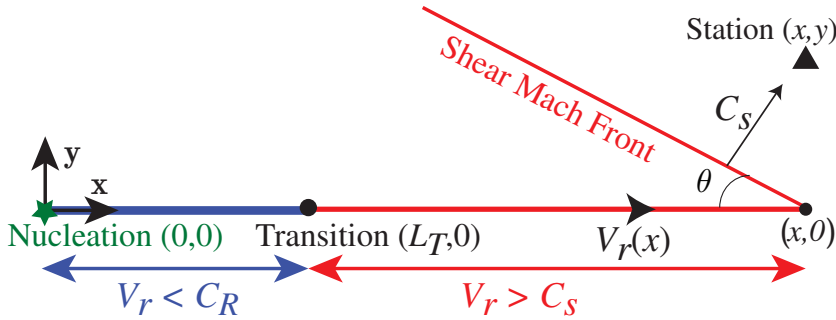


Figure 2.37: Problem Geometry

Consider the problem geometry shown in Fig. 2.37. We have a fault (horizontal straight line) where the rupture nucleates at the origin and transitions to supershear speed at  $x = L_T$ . The station is located at  $(x, y)$ . Let  $v_r(x)$  be the rupture velocity history on the fault where  $v_r(x) < c_R$ , the Rayleigh wave speed, for  $x < L_T$  and  $v_r(x) > c_s$ , the shear wave speed, for  $x \geq L_T$ . Then the time taken for the rupture to arrive at  $(x, 0)$  is simply:

$$\int_0^{L_T} \frac{dx}{v_{r,SR}(x)} + \int_{L_T}^x \frac{dx}{v_{r,SS}(x)} \quad (2.74)$$

We have intentionally written the integral in the above form so that the sub-Rayleigh (SR) and the supershear (SS) parts of the rupture are separated.

By the time the rupture arrives at  $(x, 0)$  it is already supershear and has a Mach front associated with it. Assuming that the rupture speed is constant after transition, the Mach front is straight and the speed of the normal to the Mach front is the shear wave speed,  $c_s$  (see figure above). As an aside, note that if the rupture front accelerates or decelerates the Mach front is convex or concave respectively and the speed of the normal to the local tangent of the Mach front is still the shear wave speed. Thus the time taken for the Mach front to reach the station is simply  $y \cos \theta / c_s$  where  $\sin \theta = c_s / v_{r,SS}$ . Thus the time taken for the main rupture information to reach the station,  $t_{SS}$ , is given by

$$t_{SS} = \int_0^{L_T} \frac{dx}{v_{r,SR}(x)} + \frac{x - L_T}{v_{r,SS}} + \frac{y \cos \theta}{c_s} \quad (2.75)$$

Lets now consider the time taken for the trailing Rayleigh pulse of a supershear rupture to arrive at the station. We can imagine that this pulse existed from the nucleation site and traveled at the speed of the main rupture until transition point. From here on this pulse travelled exactly at the Rayleigh wave speed,  $c_R$ . Also, lets assume that if the station is close to the fault then the pulse arrives at  $(x, 0)$  and the station  $(x, y)$  simultaneously i.e. the time taken for this pulse to arrive at the station  $(x, y)$  is equal to the time taken for it to propagate along the fault to a location that corresponds to the projection of the station on the fault plane,  $(x, 0)$ . Thus the time taken for this pulse to reach the station  $(x, y)$ ,  $t_R$ , is,

$$t_R = \int_0^{L_T} \frac{dx}{v_{r,SR}(x)} + \int_{L_T}^x \frac{dx}{c_R} = \int_0^{L_T} \frac{dx}{v_{r,SR}(x)} + \frac{x - L_T}{c_R} \quad (2.76)$$

Hence, the difference in the rupture arrival time and the Rayleigh pulse arrival time,  $\Delta t_{SS,R} = t_R - t_{SS}$ , is given by

$$\Delta t_{SS,R} = \frac{x - L_T}{c_R} - \frac{x - L_T}{v_{r,SS}} - \frac{y}{c_s} \sqrt{1 - \frac{c_s^2}{v_{r,SS}^2}} \quad (2.77)$$

where  $\cos \theta = \sqrt{1 - c_s^2/v_{r,SS}^2}$ . From here on we will drop the subscript  $SS$  and simply denote the supershear rupture velocity by  $v_r$ . Solving for  $x$  we obtain,

$$x = L_T + c_s \Delta t_{SS,R} + y \sqrt{1 - \frac{c_s^2}{v_r^2} \left( \frac{c_s}{c_R} - \frac{c_s}{v_r} \right)^{-1}} \quad (2.78)$$

Define the following quantities,

$$\begin{aligned} \tan \beta &= \left( \frac{c_s}{c_R} - \frac{c_s}{v_r} \right) \left( 1 - \frac{c_s^2}{v_r^2} \right)^{-1/2} \\ L_* &= (L_T + c_s \Delta t_{SS,R}) \tan \beta \end{aligned} \quad (2.79)$$

Rearranging eqn. (2.78) and using eqn. (2.79) we get a linear relationship between  $x$  and  $y$  which is the locus of stations that give the same  $\Delta t_{SS,R}$  given by

$$y = x \tan \beta - L_* \quad (2.80)$$

This locus consists of a pair of straight lines inclined at an angle  $\pm\beta$  and

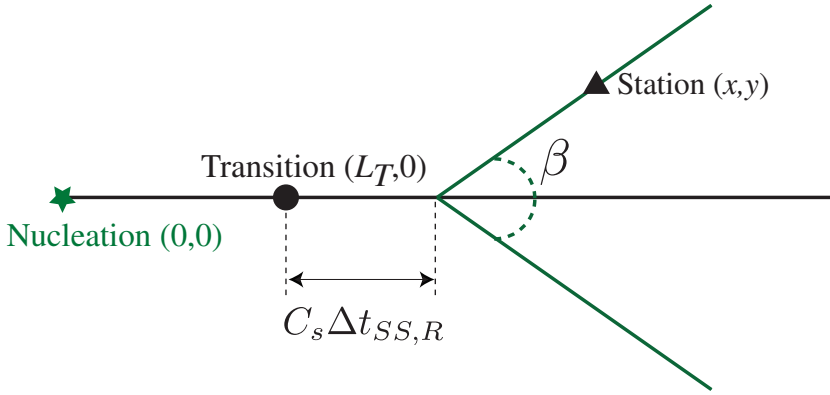


Figure 2.38: Locus of stations with the same  $\Delta t_{SS,R}$  assuming a fixed transition length and constant supershear rupture velocity.  $\beta$  is defined in eqn. (2.79).

intersecting the fault at  $L_T + c_s \Delta t_{SS,R}$  (See Fig. 2.38). To further constrain the above solutions we impose that geometric scaling is retained. It is assumed that in both cases, Laboratory and Denali, the ratio of the fault normal co-ordinate of the station,  $y$ , to the fault parallel distance relative to the supershear transition location,  $(x - L_T)$ , remain the same. That is

$$\frac{y^D}{(x^D - L_T^D)} = \frac{3 \text{ km}}{18 \text{ km}} = \frac{y^L}{(x^L - L_T^L)} = S_L \quad (2.81)$$

Here the superscripts  $D$  and  $L$  correspond to the Denali Pump Station 10 (PS10) and the Laboratory Station respectively. Solving the above equation with the equation for the locus, eqn. (2.80), we get the co-ordinates for the experimental station.

$$x^L = \frac{L_*^L - L_T^L S_L}{\tan \beta^L - S_L} ; \quad y^L = S_L (x^L - L_T^L) \quad (2.82)$$

where

$$\begin{aligned} L_*^L &= (L_T^L + c_s^L \Delta t_{SS,R}^L) \tan \beta^L \\ \tan \beta^L &= \left( \frac{c_s^L}{c_R^L} - \frac{c_s^L}{v_r^L} \right) \left[ 1 - \left( \frac{c_s^L}{v_r^L} \right)^2 \right]^{-1} \end{aligned} \quad (2.83)$$

To be very precise the above expressions determine a geometrically equivalent station, in terms of the arrival times of the rupture and the trailing Rayleigh, in a medium with different elastic properties than typical rock. One needs to know, *a priori*, the transition length,  $L_T^L$ , for the experiment (often set by a far field load level or by seeding transition by a stress perturbation) and the difference in the arrival time,  $\Delta t_{SS,R}^L$ .

The transition length in the laboratory is known as it is constructed by design. To determine  $\Delta t_{SS,R}^L$  we make the following temporal scaling argument. We start from the Denali PS10 record which provides the equivalent time difference,  $\Delta t_{SS,R}^D$ . This is now scaled temporally by ensuring that the trailing Rayleigh signature in the laboratory experiment would match the same in the Denali PS10 record when multiplied by an appropriate temporal scaling factor. This requires some confidence in the constancy of the temporal width of the trailing Rayleigh signature,  $\Delta t_R^L$ , in the experiments. We determine  $\Delta t_R^L$  to be  $17.8 \mu s$  based on a series of past experiments which indeed show trailing Rayleigh pulses of a remarkably consistent width at near fault distances. Figure 3F of the main text indeed confirms a trailing Rayleigh pulse (shaded in blue) width of  $17.8 \mu s$  as stated above. The corresponding value for Denali PS10 record,  $\Delta t_R^D$  is  $6.9 s$ . Thus the temporal scaling factor,  $S_T$ , is

$$S_T = \frac{\Delta t_R^D}{\Delta t_R^L} = \frac{6.9 s}{17.8 \mu s} = 3.87 \times 10^5 \quad (2.84)$$

We can now use this temporal scaling factor to determine  $\Delta t_{SS,R}^L$  based on the corresponding value for Denali PS10 i.e.  $\Delta t_{SS,R}^L = \Delta t_{SS,R}^D / S_T$ . Substituting this into first equation of eqn. (2.83) one now obtains,

$$L_*^L = \left( L_T^L + \frac{c_s^L \Delta t_{SS,R}^D}{S_T} \right) \tan \beta^L \quad (2.85)$$

Substituting this into eqn. (2.82) along with  $L_T^L = 39 \text{mm}$ ,  $c_s^L = 1.28 \text{km/s}$ ,  $c_R^L = 0.92 c_s^L$  and  $v_r^L = 1.7 c_s$  one obtains  $(x^L, y^L) = (57, 3) \text{mm}$ . Once the experimental records are obtained they are then subjected to temporal scaling using the relation,  $t^{scaled} = t^L \times S_T$ .

## 2.9 Mach Envelopes for Arbitrary Ruptures

Consider a family of curves represented in the form

$$G(x, y, c) = 0 \quad (2.86)$$

For example  $G \equiv (x-c)^2 + y^2 = a^2$  represents a family of circles of radius  $a$  whose center is offset from the origin by an amount  $c$ . Our goal is to find an

envelope  $\mathbb{E}(x, y)$  such that at each point of  $\mathbb{E}$ , say  $(x, y)$ , there is a member of the family  $G$  that touches  $\mathbb{E}$  tangentially. In other words, for each point  $\mathbb{E}(x_0, y_0)$  there is a value of  $c = c_0$  (say) such that

$$G(x_0, y_0, c_0) = 0 \quad (2.87)$$

This means that the envelope can be represented parametrically as  $\mathbb{E}[x(c), y(c)]$ . Differentiating eqn. 2.86 with respect to  $c$  we get

$$\left(\frac{\partial G}{\partial x}\right)\left(\frac{\partial x}{\partial c}\right) + \left(\frac{\partial G}{\partial y}\right)\left(\frac{\partial y}{\partial c}\right) + \left(\frac{\partial G}{\partial c}\right) = 0 \quad (2.88)$$

For a particular curve in the family  $G$ , the parameter  $c$  is a constant. Differentiating eqn. 2.86 with respect to  $x$  we get

$$\left(\frac{\partial G}{\partial x}\right) + \left(\frac{\partial G}{\partial y}\right)\left(\frac{\partial y}{\partial x}\right) \Bigg|_{c=c_0} = 0 \quad (2.89)$$

For the envelope  $\mathbb{E}$ ,

$$\frac{\partial y}{\partial x} = \frac{\left(\frac{\partial y}{\partial c}\right)}{\left(\frac{\partial x}{\partial c}\right)} \quad (2.90)$$

At the point of tangency, the envelope and the corresponding curve of the family have the same slope. Therefore combining eqns. 2.89 and 2.90 we get

$$\left(\frac{\partial G}{\partial x}\right)\left(\frac{\partial x}{\partial c}\right) + \left(\frac{\partial G}{\partial y}\right)\left(\frac{\partial y}{\partial c}\right) = 0 \quad (2.91)$$

Compare this with eqn. 2.88. We immediately conclude that

$$\frac{\partial G}{\partial c} = 0 \quad (2.92)$$

Thus the equation of the envelope,  $\mathbb{E}[x(c), y(c)]$ , is given by simultaneously solving

$$\frac{\partial G}{\partial c} = 0 \text{ and } G(x, y, c) = 0 \quad (2.93)$$

for  $x$  and  $y$  as a function of  $c$ .

For example, let  $G(x, y, c) \equiv (x - v_r t)^2 + y^2 - (c_s t)^2 = 0; t \in (0, \infty]$ . This is the case of a particle moving at a speed  $v_r$  along the positive  $x$  axis and this particle emits a signal at speed  $c_s$  into the medium. Then  $\partial G / \partial t = 0 \Rightarrow x - v_r t = -c_s^2 t / v_r$ . Plugging this into  $G(x, y, c) = 0$  we get  $y^2 = c_s^2 t^2 (1 - c_s^2 / v_r^2)$ .

Clearly, when  $v_r < c_s$  the equation has only imaginary solutions. In other words there is no envelope. When  $v_r \geq c_s$  we have  $y = \pm c_s t \sqrt{1 - c_s^2 / v_r^2}$ ;  $x = v_r t (1 - c_s^2 / v_r^2)$ . If we set  $c_s / v_r = \sin \theta$ , where  $\theta$  is the Mach angle, then the co-ordinates of the Mach envelope at any given time  $t^* > 0$  is given by  $(x, y) \equiv (v_r t \cos^2 \theta, \pm c_s t \cos \theta)$ ;  $t \in (0, t^*]$ .

# 3

## EXPERIMENTS

### 3.1 Caltech Laboratory Earthquake Experiment

The first recorded high speed images of a supershear rupture were reported by Lambros & Rosakis (1995) following a series of dynamic shear impact experiments conducted on PMMA/4340 steel-edge cracked bimaterial plates. Coherent gradient sensor (CGS) interference patterns revealed an interfacial shear crack propagating with very high crack-tip speeds approaching  $1.5C_R^{PMMA}$ . The technique was continuously refined and applied to numerous dynamic shear impact investigations of homogeneous and bimaterial systems (Coker & Rosakis, 2001; Coker et al., 2003; Kavaturu et al., 1998; Rosakis et al., 1998, 1999; Samudrala & Rosakis, 2003; Singh et al., 1997).

Research efforts subsequently shifted from dynamic shear impact studies to the investigation of spontaneously-nucleated mode II ruptures in an effort to emulate natural earthquake ruptures. This in turn prompted the development of the "laboratory earthquake" experiment (LEQ) by Xia et al. (2004, 2005b).

The traditional LEQ experiment features a transparent,  $150mm \times 150mm$  square test specimen formed by two statically compressed,  $10mm$  thick, quadrilateral sections of Homalite-100, a linear elastic, and stress birefringent polymer. The mating surfaces are each initially polished to a flat, and nearly optical-grade surface finish in order to remove all machining induced surface defects. The surfaces are then uniformly roughened to nominal rms surface roughness of  $1.5\mu m$  using a prescribed and repeatable micro-bead blasting procedure. The frictional interface inclined by an angle ( $\alpha$ ), which is formed by the mated surfaces of the statically-compressed test sections, is designed to mimic a tectonic fault within the Earth's crust.

The H-100 LEQ test specimen is initially subjected to a static, compressive "far-field" stress  $\sigma_0$  using a hydraulic mechanical press such as the one

pictured in Figure 3.1. The applied static compressive load ( $\sigma_0$ ) translates into a normal traction

$$\sigma_{22}^0 = \sigma_0 \cos^2 \alpha \quad (3.1)$$

and resolved shear traction

$$\sigma_{21}^0 = \sigma_0 \sin \alpha \cos \alpha \quad (3.2)$$

along the inclined frictional fault plane. Interfacial sliding is initially prevented by virtue of the fact that the resolved shear stress does not exceed the peak (static) frictional strength  $\tau_p = f_s \sigma_{22}^0$  of the interface, where  $f_s$  represents the static coefficient of friction.

The rupture nucleation procedure relies upon the rapid ablation of a thin NiCr wire filament (diameter  $\approx 80\mu m$ ). The wire filament is fed through a small hole formed by two mating semicircular cylindrical cavities, which are machined into the mating surfaces and aligned with the thickness direction. A spontaneous, mode II, bilateral rupture is nucleated by discharging a capacitor bank and directing a surge of current to pass through the NiCr wire filament. The resulting plasma discharge induces a momentary reduction of the local normal traction  $\sigma_{22}^0$  while ejected material spreads out across a characteristic patch length ranging in size from 1cm - 1.5 cm. After a short nucleation time on the order of  $4.4\mu s$ , the applied shear traction  $\sigma_{21}^0$  overcomes the local static frictional strength and a mode II bilateral rupture is nucleated. The relative orientation of the frictional fault plane (i.e., whether  $\alpha > 0$  or  $\alpha < 0$ ) determines whether a right-bilateral or left-bilateral rupture is nucleated.

Figure 3.1 depicts a recent configuration of the LEQ experiment. A well collimated and expanded laser is passed through the H-100 LEQ specimen as shown. The transmitted light beam is processed by a dark field photoelastic polariscope configuration to yield photoelastic fringe patterns, which are imaged by a pair of ultra-high speed gated intensified cameras. The recorded interference fringes correspond isocontours of  $\sigma_1 - \sigma_2 = C$ , where  $\sigma_1$  is the maximum principal stress and  $\sigma_2$  corresponds to the minimum principal stress under the assumption of plane stress. Fringes may be equivalently interpreted as contour maps of the maximum shear stress field, i.e.,  $2\tau_{max} = C$ . Spatially-resolved images of the propagating rupture tip and its surrounding stress field are revealed.

A unique advantage of the LEQ experiment is the flexibility it offers to spontaneously nucleate sub-Rayleigh or supershear ruptures depending upon the initial static compressive load ( $\sigma_0$ ), frictional fault angle ( $\alpha$ ), and other properties such as the rms surface roughness and cohesion of the fault surfaces.

The photoelastic image in Figure 3.2(a) depicts two sub-Rayleigh ruptures; a right-lateral/left-traveling rupture and a right-lateral/ right traveling rupture, both of which emerged from the spontaneous nucleation of a right-bilateral rupture at (0, 0). The dark shadow cast by an electrical "alligator clip" and connecting lead wire is visible at the nucleation site. The

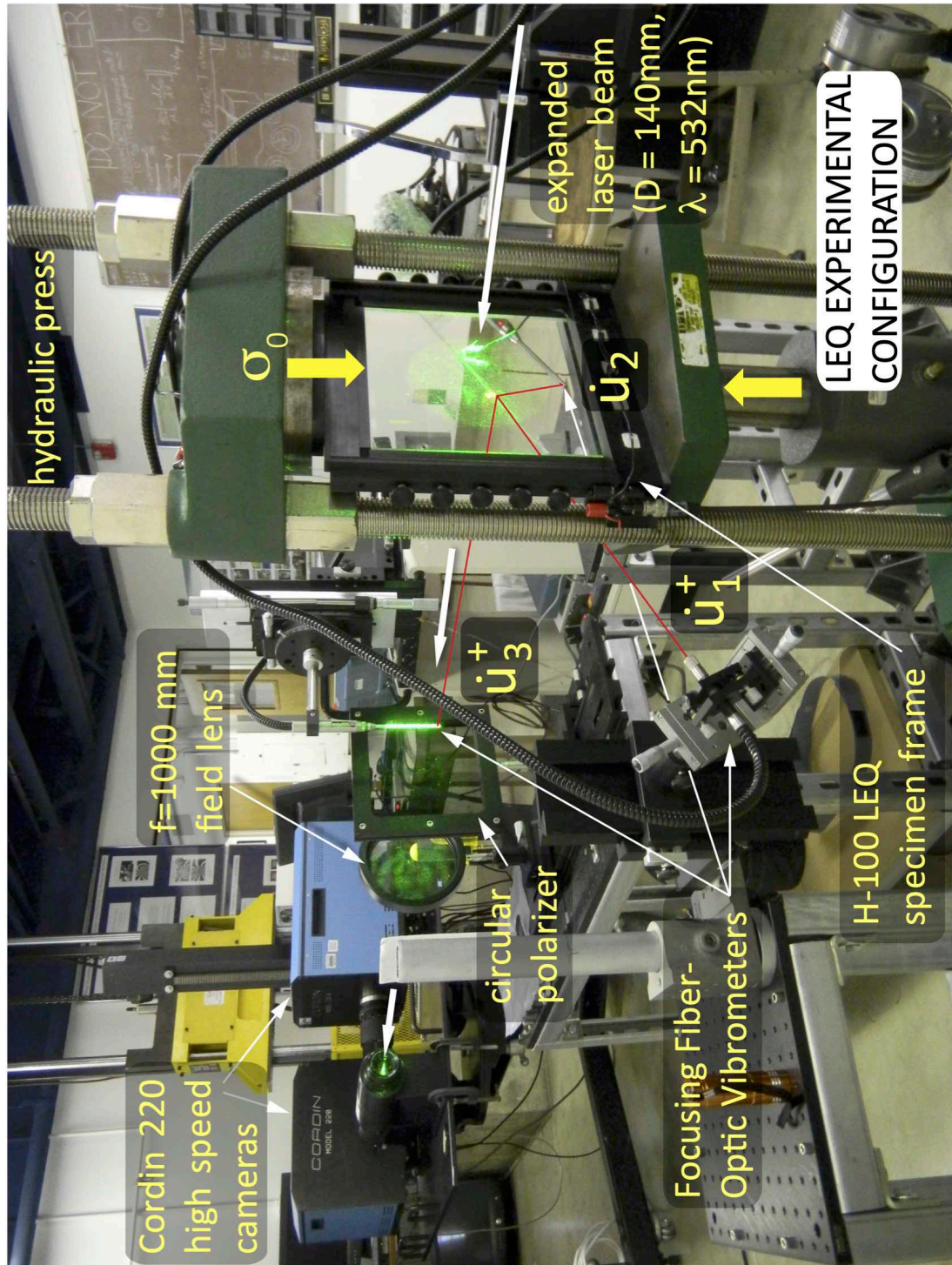


Figure 3.1: Laboratory earthquake (LEQ) experimental configuration featuring high-speed gated intensified cameras with integrated dark field polariscope for full-field visualization of photoelastic interference patterns. Three fiber-optic laser vibrometers enable simultaneous monitoring of the in-plane and out-of-plane surface velocity components ( $\dot{u}_1$ ,  $\dot{u}_2$ ,  $\dot{u}_3$ ) at fixed locations on the surface of the H-100 test specimen.

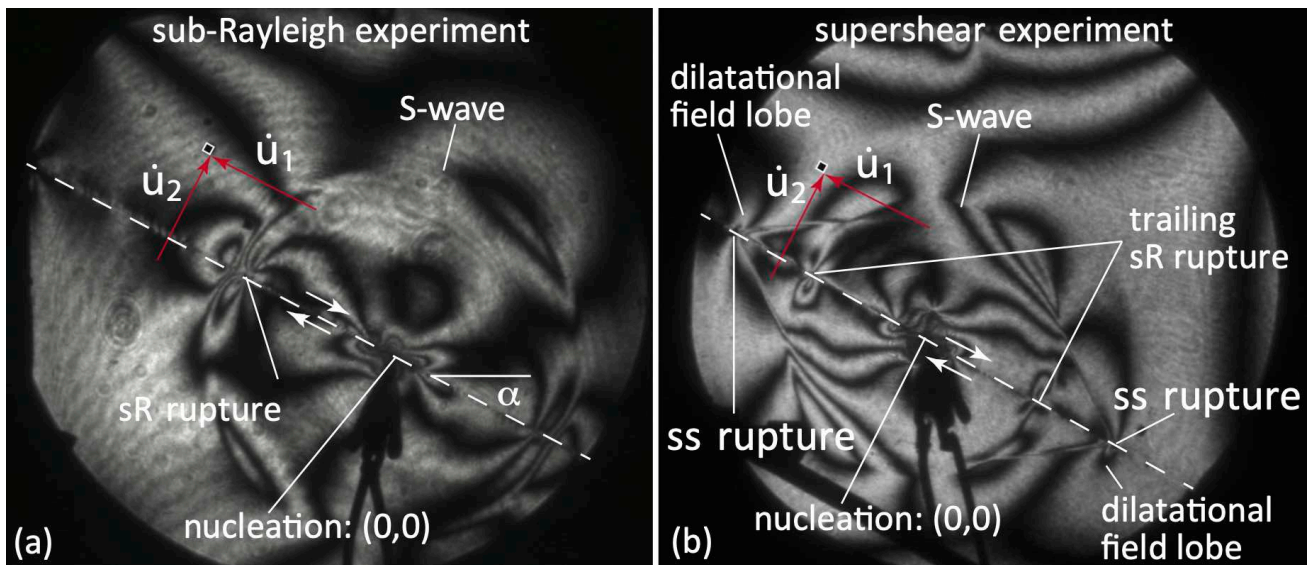


Figure 3.2: (a) High-speed photoelastic image of a right-bilateral sub-Rayleigh rupture and expanding s-wave front resulting from the right-lateral rupture of an H-100 laboratory earthquake specimen. (b) Right-bilateral supershear rupture characterized by prominent shear Mach fronts. The trailing sub-Rayleigh ruptures are also visible in the wake of each supershear rupture.

photoelastic fringe pattern reveals the concentrated sub-Rayleigh rupture tips and stress field lobes, which extend to either side of the fault plane. The circular arc of a nucleated S-wavefront is also clearly visible and highlighted within the image.

The photoelastic image in Figure 3.2(b) depicts a pair of supershear ruptures; a right-lateral/left traveling rupture and a right-lateral/right traveling rupture, each of which spontaneously transitioned at an earlier time from the corresponding trailing sub-Rayleigh ruptures, which are noted in the image. The dark shadow cast by the electrical "alligator clip" and connecting lead wire is visible at the nucleation site, where the original right-bilateral rupture was nucleated. The supershear rupture tips, leading dilatational field lobes, shear Mach fronts, and trailing sub-Rayleigh ruptures are all clearly revealed and noted within the image along with the circular arc of a nucleated S-wavefront.

Xia et al. (2004) successfully applied the LEQ experiment in combination with dynamic photoelasticity to record the frame-by-frame evolution of a spontaneously nucleated sub-Rayleigh-to-supershear rupture transition for the very first time. This was followed by a detailed experimental characterization of the sub-Rayleigh-to-supershear transition distance ( $L$ ) and the establishment of an empirical relationship  $L \propto \sigma_0^{-3/2}$ , which was interpreted within the context of a critical crack length criterion and an assumed linear slip-weakening friction relation with a pressure dependent slip weakening distance ( $D_c$ ) (Rosakis et al., 2006, 2007; Xia et al., 2004, 2005a,b).

In the years which immediately followed, the LEQ experiment was applied to the investigation of supershear rupture propagation along bi-material interfaces and to studies on the effects of off-fault damage (Bhat et al., 2010; Biegel et al., 2010; Griffith et al., 2009).

Measurement diagnostics were later expanded to include focusing, fiber-optic laser vibrometers to record temporally-resolved waveforms of the in-plane particle velocity components at fixed points of interest on the surface of the test specimen. The application of laser vibrometers to the measurement of in-plane motion components was actually first applied by Lykotrafitis & Rosakis (2006a,b) and Lykotrafitis et al. (2006) to measure the interfacial sliding speed in the dynamic shear impact investigations of bimaterial frictional interfaces. Lu (2009) and Lu et al. (2007, 2010) subsequently applied the technique to LEQ investigations of sub-Rayleigh and supershear slip pulses in LEQ experiments.

The red arrows in Figure 3.2(a,b) depict how laser vibrometer beams are focused at an off-fault field point in order to record the in-plane particle velocity components ( $\dot{u}_1, \dot{u}_2$ ) as the propagating rupture field sweeps the measurement station. The fiber-optic laser vibrometers configuration depicted in Figure 3.1 were used in a more recent study in order to simultaneously record temporally-resolved waveforms of the in-plane particle velocity components ( $\dot{u}_1, \dot{u}_2$ ) and the out-of-plane motion ( $\dot{u}_3$ ) at fixed locations on the surface of the H-100 test specimen Mello et al. (2014).

New H-100 specimen frictional fault configurations have also been developed and implemented in recent years, which emulate partially locked strike-slip faults and normal thrust faults within the Earth's crust (Gabuchian et al., 2014, 2017; Mello et al., 2014). Recent work by Rubino et al. (2017) has led to the development of new high-speed imaging techniques such as 2D image correlation for the direct measurement of displacement, strain, and particle velocity fields in LEQ experiments. Constitutive relationships naturally lead to the full-field characterization of stress which should extend the applicability of the LEQ experiment to numerous, new, and challenging problems within the field of seismology.

### Laser Vibrometer Configurations in Current LEQ Experiments

The three primary laser vibrometer configurations, which were adopted in our investigations are depicted in Figure 3.3. Figure 3.3a depicts the FN:FP probe beam configuration used for simultaneous measurement of the FN and FP velocity components at a point. The red lines in each figure depict how the FN and FP laser vibrometer beams were directed at nearly grazing incidence to the specimen surface, and focused to a nominal spot size of  $\approx 150 \mu\text{m}$  at a field point, herein referred to as the “measurement station”. Figure 3.3b depicts the FN:FN configuration used for simultaneous measurement of FN velocity components at a pair of -on and off-fault field points. The probe beams are focused at two distinct points, which are vertically separated along the FN direction, as shown. Figure 3.3c depicts the FP:FP configuration used for simultaneous measurement of FP velocity components at a pair of -on and off-fault field points. The two probe beams are now focused at two distinct points, which are horizontally separated along the FP direction, as shown.

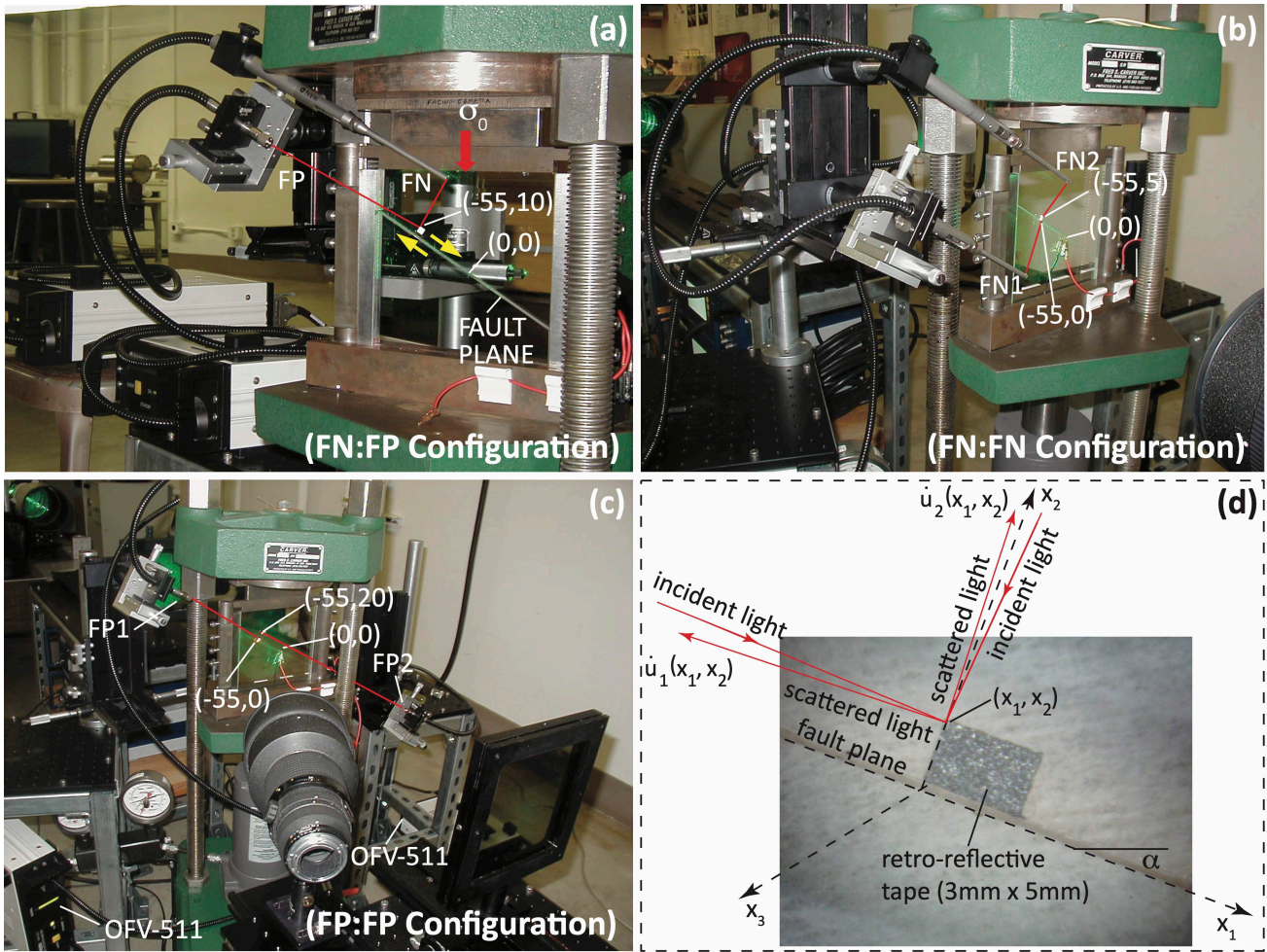


Figure 3.3d depicts how a small ( $3\text{mm} \times 4\text{mm}$ ) rectangular strip of retro-reflective tape (3M™ Scotchlite™), is adhered to the surface of the test specimen, with its upper left corner coincident with the field point  $(x_1, x_2)$ . Laser vibrometer beams are focused at a corner of the retro-reflective tape strip (along the edge), as shown. Focused laser light is efficiently scattered by the retro-reflective tape and collected by each respective fiber-optic probe. The collected light is directed by optical fiber to the Polytec model OFV-511 and model and OFV-551 heterodyne interferometers, which are visible in the lower left corner of Figure 3.3a.

Laser vibrometer beams are each initially focused and aligned in order to maximize the interference signal as reported by the Polytec model OFV-511 and model and OFV-551 heterodyne interferometer modules. Practical considerations require a small angle of incidence ( $\theta_i \approx 5^\circ - 10^\circ$ ), between the incident probe and beam and the plane of the specimen surface. Velocity measurement errors introduced by this slight departure from grazing incidence are negligible since the frequency content of the resulting interferometer signal scales with  $\cos \theta_i$ . Amplified photodetector signals from the OFV-511 and OFV-551 interferometer modules are then directed to a

Figure 3.3: Laser vibrometer configurations: (a) (FN:FP) for simultaneous measurement of FN and FP velocity components at a point. (b) (FN:FN) for simultaneous measurement of FN velocity components at a pair of -on and off-fault field points. (c) (FP:FP) for simultaneous measurement of FP velocity components at a pair of -on and off-fault field points. (d) Use of retro-reflective tape corner for efficient scattering of focused laser beam.

Polytec OFV-5000 modular controller (not depicted) where the interference signals are processed and converted into particle velocity waveforms. Continuous particle velocity records in the form of an analog voltage signal, are then output by a BNC cable to a Tektronix DPO3034, digital oscilloscope where the signals are acquired and displayed. The acquired voltage signals are then converted into the final particle velocity records through a linear scaling factor ( $1V = 1m/s$ ).

### High-Speed Configuration in Current LEQ Investigations

A 16-frame high-speed image sequence is obtained during each experiment by the pair of Cordin model 220 gated-intensified cameras depicted in Figure 3.1. The high-speed cameras are carefully aligned and focused so as to yield sharp images of the test specimen surface and the superimposed photoelastic interference pattern corresponding to the initial static compressive load. Cameras are typically set to record images at inter-frame times of  $1 - 4\mu s$ , with a fixed exposure time setting of  $50ns$ . A common electrical trigger derived from the rupture nucleation circuit ensures that the recorded image sequence is synchronized with the laser vibrometer waveforms recorded by the oscilloscope. Spatially-resolved images of dynamically evolving photoelastic fringe patterns reveal prominent features such as the propagating rupture zone, expanding P-wave and S-wave fronts, sub-Rayleigh field lobes, and supershear Mach fronts, as depicted in Figure 3.2a,b. Pronounced velocity changes at specific times in the recorded particle velocity waveforms are directly correlated to the arrival of these noted features at the measurement station.

### Investigation of Sub-Rayleigh and Supershear Rupture Velocity Waveform Signatures using using the (FN:FP) Laser Vibrometer Configuration

LEQ experiments depicted in Figure 3.4 conducted using  $150mm \times 150mm \times 10mm$  H-100 LEQ test specimens with a frictional fault plane inclined at an angle  $\alpha = -29^\circ$  with respect to the horizontal. The pair of high-speed images and corresponding particle velocity waveforms depicted in Figure 3.4 contrast the results obtained from two independent laboratory earthquake experiments, one of which yielded a sub-Rayleigh rupture and the other, which resulted in a supershear rupture. In each case, the rupture nucleation process resulted in a right-bilateral rupture at the point labeled  $(0, 0)$ . The expanded, illuminating laser beam was intentionally biased to favor the left side of the specimen in order to image the left-traveling rupture. The primary region of interest, located between the rupture nucleation site at  $(0, 0)mm$  and the measurement station at  $(-55, 10)mm$ , is well-centered within each FOV.

The FN and FP particle velocity waveforms in Figure 3.4 are both plotted out to  $t = 65 \mu s$ . The red triangles denote the time ( $t = 41\mu s$ ) at which the displayed photoelastic images were acquired. The dashed blue vertical lines

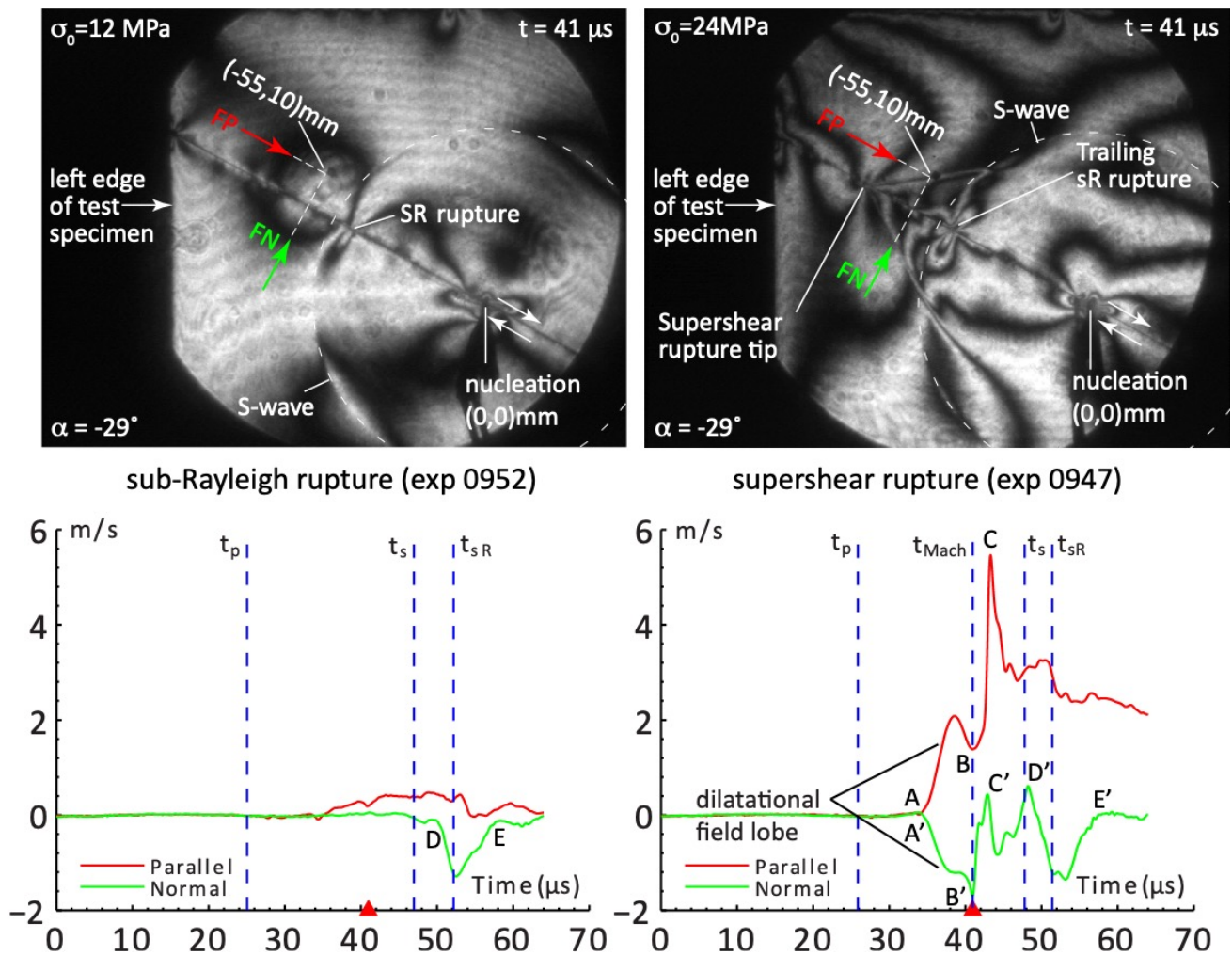


Figure 3.4: Sub-Rayleigh rupture experiment (exp 0952) with high-speed image and corresponding particle velocity waveforms (left), contrasted against a supershear rupture experiment (exp 0947) with high-speed image and corresponding particle velocity waveforms (right).

labeled  $t_p$  and  $t_s$  in the particle velocity plots mark the anticipated arrival times of the nucleated P-wave and S-wave fronts at the measurement station positioned at  $(-55, 10)mm$ . The dashed blue vertical lines labeled  $t_{sR}$  in each plot mark the anticipated arrival time of the sub-Rayleigh (sR) rupture in exp 0952 and the arrival time of the trailing sub-Rayleigh rupture in exp 0947. The dashed blue vertical line labeled  $t_{Mach}$  in the supershear particle velocity record marks the anticipated arrival of the shear Mach front at the off-fault measurement station  $(-55, 10)mm$ .

In the case of the sub-Rayleigh rupture experiment (exp 0952), the LEQ specimen was subjected to a static compressive load of  $\sigma_0 = 12MPa$ . The propagating sR rupture tip in exp 0952, coincides with a dark, concentrated caustic zone positioned just behind the faint circular outline of the expanding S-wave front. Prominent, symmetric field lobes radiate from the rupture tip and extend to either side of the fault.

A detailed examination of the photoelastic image sequence and the particle velocity records from the sub-Rayleigh rupture experiment (exp 0952) confirms that the segment  $D \rightarrow E$  in the FN wave form directly correlates

with the time during which the extended sub-Rayleigh rupture field lobe swept through the off-fault measurement station located at  $(-55, 10)$ mm. The FN component also dominates in magnitude over the FP velocity changed during this time interval, as expected for a sub-Rayleigh rupture. Furthermore, the sign of the velocity swings corresponding to the segment labeled  $D \rightarrow E$  are also consistent with the anticipated sense of particle motion induced by the upper field lobe of a right-lateral/left-traveling sub-Rayleigh rupture as it sweeps this location. The latter observation is readily verified by examining the FP and FN components of the streak plot vectors within the sub-Rayleigh field lobe of the left-traveling rupture in Figure 2.15.

In the case of the supershear experiment (exp 0947), the static, compressive load was doubled to  $P = 24$ MPa in order to initiate a sR to SS rupture transition along the fault segment  $(-55\text{mm} < x < 0\text{mm})$ . The supershear rupture tip in the right-hand image of Figure 3.4 is flanked by prominent shear Mach fronts, which extend to either side of the fault plane. An expanded view of the image also reveals a localized fringe concentration, positioned just ahead of the supershear rupture tip, which coincides with the leading dilatational field lobe. A trailing sub-Rayleigh rupture with extended field lobes is also clearly visible and labeled in the image along with the faint circular outline of an expanding S-wave front.

The corresponding particle velocity waveforms from exp 0947 resulted as the dilatational field lobe, shear Mach front, and the extended field lobe of the trailing sub-Rayleigh rupture swept past the measurement station located at  $(-55, 10)$ mm. A detailed examination of the photoelastic image sequence and the particle velocity waveforms from the supershear experiment confirms that the segment  $A \rightarrow B$  in the FP wave form and  $A' \rightarrow B'$  in the FN wave form correlate with the time during which the dilatational field lobe swept past the off-fault measurement station located at  $(-55, 10)$ mm. The observed positive swing in the FP wave form and corresponding negative swing of the FN wave form during this time interval are both consistent with the predicted sense of particle motion within the upper dilatational field lobe of a right-lateral/left-traveling supershear rupture. This is readily verified by carefully examining with the direction of the FP and FN components of the streak plot vectors within the light green shaded portions of the corresponding dilatational field lobe in Figure 2.14.

The segments labeled  $B \rightarrow C$  in the FP wave form and the segment labeled  $B' \rightarrow C'$  in the FN wave form correlate with the arrival of the shear Mach front at the off-fault measurement station located at  $(-55, 10)$ mm. The FP velocity jump clearly dominates in magnitude over the corresponding jump in FN velocity wave form, as predicted in the case of a stable supershear rupture. Moreover, the sharp, positively-sloped velocity jumps in the FP and FN waveforms during this time interval are also consistent with the predicted sense of motion along the shear Mach front from a right-lateral/left-traveling supershear rupture, on the extensional (upper left) side of the fault. This result is directly verified by appealing to Figure 2.3b or by direct comparison to the FP and FN components of the streak plot vectors

aligned along the corresponding shear Mach front in Figure 2.14.

We draw attention to the striking similarities between the synthetic FP waveforms depicted in Figure 2.2 and the experimental FP waveform in Figure 3.4. We note that the synthetic curves in Figure 2 represent the sense of motion resulting from a right-lateral/right-traveling rupture within the upper right (compressional) side of the frictional fault and that the experimental record pertains to a right-lateral/left-traveling rupture. Nonetheless, the visual comparison between the synthetic waveform signatures in Figure 2.2 and the velocity records obtained in exp 0947 remains valid since the same sense of particle motion is expected from the FP component of a left-traveling supershear rupture on the extensional (upper left) side of the fault. This is readily verified by appealing to Figure 2.3b or by examining the the velocity vector field plot for the left-traveling rupture portrayed in Figure 2.14. The sense of motion exhibited by the FN velocity component in exp 0947 is also reconciled in a similar manner.

We must also acknowledge that the scale of the axes between the synthetic and experimental waveforms cannot be correlated since the synthetic curves are derived from the singular elastic solution, which lacks an inherent physical length scale. Nonetheless, The FP waveform recorded in exp 0947 embodies the distinct and fundamental velocity waveform signatures, which are characteristic of a supershear dislocation field, i.e., the initial FP velocity swing induced by the leading dilatational field lobe and the sharp step-like velocity jump attributed to the shear Mach front which immediately follows. Indeed, these are universal features, which are embodied by all supershear velocity waveforms, which are always observed, regardless of the governing length scale and underlying frictional law.

Finally, the FP and FN velocity components in the supershear records exhibit a precipitous drop following the passage of the shear Mach front and remain quiescent for a short period until the arrival of the trailing Rayleigh rupture, which coincides segment  $D' \rightarrow E'$  in the FN waveform from. We note the strong resemblance between this segment of the supershear record and the segment labeled  $D \rightarrow E$  in the FN waveform of the sub-Rayleigh experiment (exp 0952), attributed to the sub-Rayleigh rupture as it swept the off-fault measurement station. The dominance of FN component over the FP component exhibited by segment  $D' \rightarrow E'$  in the supershear record and the observed sense of motion during this time interval is consistent with the predicted sense of particle motion induced by the upper field lobe of a right-lateral/left-traveling trailing sub-Rayleigh rupture at an off-fault station on the upper (extensional) side of the fault plane. This is readily confirmed by examining the vector field plots of the corresponding trailing sub-Rayleigh field lobe in Figure 2.14.

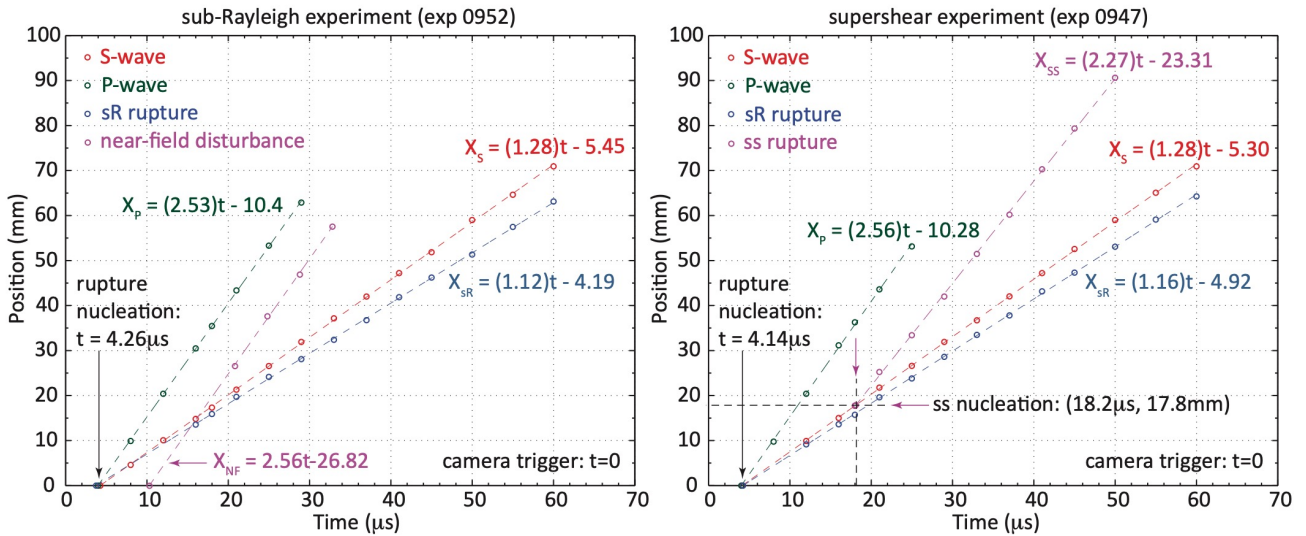


Figure 3.5: Displacement-time plots corresponding to the sub-Rayleigh and supershear experiments. Colored dots represent data points obtained from the analysis of photoelastic images. The intersection between the supershear rupture “best-fit line” and the S-wave “best-fit line” provides a precise estimate for the location and time of the sub-Rayleigh-to-supershear transition.

### Experimental Estimates of the Average Rupture Speeds and Elastic Wavespeeds in Sub-Rayleigh and Supershear Rupture Experiments

Figure 3.5 depicts distance-time plots corresponding to the elastic wave fronts and propagating ruptures observed in exp 0947 and exp 0952, which were contrasted in the previous section. Distance is taken to be positive in the plots for the sake of convenience even though the station was actually located at  $(-55, 10)mm$ . The colored circular symbols represent the actual data points obtained through a frame-by-frame analysis of the rupture tip and elastic wavefront positions using well-documented procedures as outlined in Mello et al. (2010). Dashed lines passing through the circle symbols represent a best linear curve fit to the raw data. A linear equation describing the best-fit line is displayed beside each respective curve. The excellent linear fit observed in each case reveals how steady the elastic-wave and rupture speeds remained throughout the duration of the experiments.

Analysis of the elastic wave speeds and rupture propagation speeds using the sub-Rayleigh high-speed images from exp 0952 yielded an estimated P-wave speed of  $c_p = 2.53mm/\mu s$  (slope of the dashed green line), S-wave speed  $c_s = 1.28mm/\mu s$  (slope of the dashed red line). An average sub-Rayleigh rupture speed  $\bar{v}_r = 1.12mm/\mu s$ , corresponding to  $\bar{v}_r/c_s = 0.875$ , is obtained from the slope of the best fit line (dashed blue line). The dashed violet line labeled “near-field” disturbance corresponds to a propagating front, which is observed to propagate at the dilatational wave speed and is often observed in photoelastic images as a faint, expanding circular front. Extrapolation of this curve back to the time axis reveals that it was released well after rupture nucleation, which suggests that it is very likely a relic of rupture nucleation related to the dilatational contraction of the cylindrical cavity, which surrounds the Nic Cr wire.

A similar analysis applied to the photoelastic image sequence correspond-

ing to the supershear experiment (exp 0947) yielded a P-wave speed estimate of  $c_p = 2.56\text{mm}/\mu\text{s}$ , (slope of the dashed green line), and an S-wave speed estimate of  $c_s = 1.28\text{mm}/\mu\text{s}$ , (slope of the dashed red line). An average sub-Rayleigh rupture speed  $\bar{v}_r = 1.16\text{mm}/\mu\text{s}$ , corresponding to  $\bar{v}_r/c_s = 0.903$ , is obtained from the slope of the best fit line (blue dashed

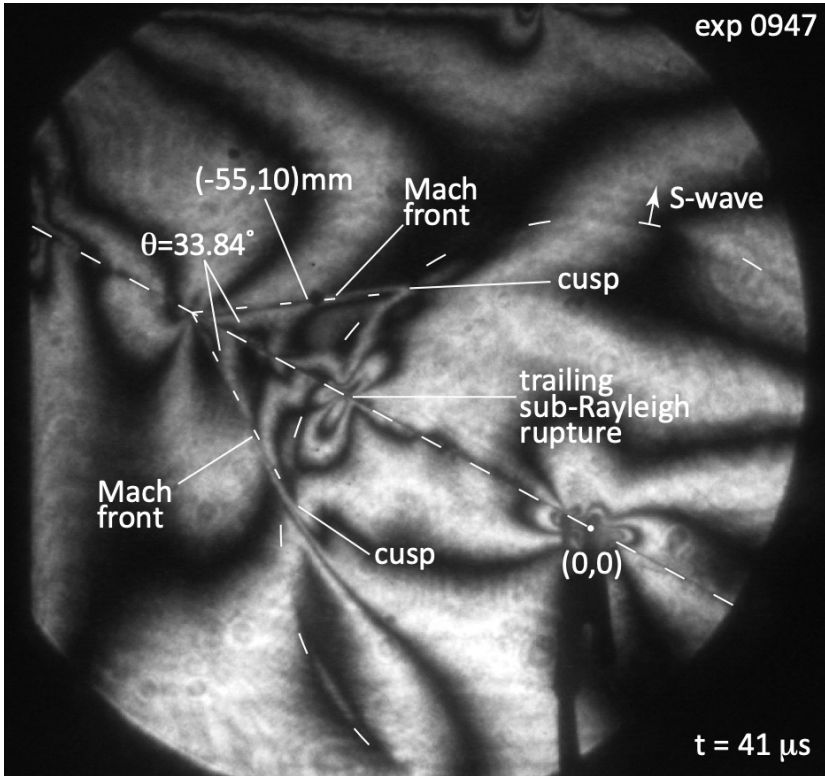


Figure 3.6: Expanded view of supershear rupture field with measured Mach front angles for determination of instantaneous supershear rupture speed.

blue line). We note the speed of the sub-Rayleigh rupture retained this value both before and after the supershear transition. An average supershear rupture speed of  $\bar{v}_{ss} = 2.27\text{mm}/\mu\text{s}$ , corresponding to  $\bar{v}_{ss}/c_s = 1.77$ , is directly inferred from the slope of the best-fit line (dashed violet line). The intersection of the S-wave curve and the supershear rupture curve at  $(17.8\text{mm}, 18.2\ \mu\text{s})$  provides a precise estimate for the location and time of the sub-Rayleigh-to-supershear transition.

The S-wave, P-wave, and sub-Rayleigh rupture curves in Figure 3.5 extrapolate back to a set of closely spaced points, which intercept the time axis. The time axis intercepts reveal an inherent rupture delay time between the instrumentation trigger ( $t = 0$ ) (when the oscilloscope and high-speed camera are triggered), and the time at which elastic waves were first emitted from the rupture nucleation site. The noted time delay is repeatedly observed in LEQ experiments and is related to the rupture nucleation process, as opposed to being an artifact of the electronic diagnostics. A slight difference between the S- and P-wave curve time axis intercepts is attributed to the increased measurement uncertainty of the P-wave measurements. The time axis intercept for the sub-Rayleigh rupture curve is not physically meaningful since the rupture tip is never located at the origin, but is instead initiated at a critical-crack-length distance located to the left and right of the

origin. The S-wave time axis intercept is thus regarded as the most trustworthy estimate of the rupture nucleation time. Measurements obtained from 49 independent laboratory earthquake experiments have yielded an average S-wave delay time of  $4.449 \mu s \pm 0.047 \mu s$ . The rupture delay time is determined in each experiment and taken into account when calculating the predicted P-wave and S-wave arrival times in relation to the rupture arrival times in the recorded particle velocity waveforms.

### Determination of the Instantaneous Supershear Rupture Speed from Mach Angle Measurements

Figure 3.6 corresponds to an expanded view of the photoelastic image acquired at time  $t = 41 \mu s$  during the supershear experiment (exp 0947). An independent estimate of the instantaneous supershear rupture speed is obtained by measuring the shear Mach angle and applying the familiar Mach cone half-angle relation Eq. 2.1, which is restated here for the sake of convenience.

$$\sin \theta = c_s / v_{ss} \quad (3.3)$$

Sharp cusps in the fringe pattern, such as those labeled in Figure 3.6 reveal the location of the steepest stress gradient and thus provide a natural fiducial for extending a line from the rupture tip when estimating the Mach angle. Lines were drawn from the supershear tip to each of the sharp cusps highlighted in Figure 3.6 in order to estimate the shear Mach angle. Mach angle measurements of  $\theta_1 = 33.75^\circ$  and  $\theta_2 = 33.97^\circ$ . A measurement uncertainty of  $\pm 0.25^\circ$  in the measurement of the Mach angle translates to an error bound of  $\pm 0.01$  in the normalized rupture speed estimate. Application of Eq. 3.3 to the average value of these two values yields an instantaneous normalized rupture speed estimate of  $v_{ss}/c_s = 1.79 \pm 0.01$ , ( $v_{ss} = 2.29 \pm 0.01 \text{ mm}/\mu s$ ), which is in excellent agreement with the average supershear rupture speed estimate  $(v_r/c_s)_{ave} = 1.77$  as determined from the slope of the best-fit line in Figure 3.5.

### Investigation of Crack-like and Pulse-like sub-Rayleigh Rupture Velocity Waveforms using using the (FN:FP) Laser Vibrometer Configuration

A series of sub-Rayleigh rupture experiments were conducted using the FP:FN fiber-optic probe configuration depicted in Figure 3.3a. Simultaneous FN and FP particle velocity records were obtained at various distances from the fault as a sub-Rayleigh rupture and its surrounding field swept past the measurement station. A synchronized, photoelastic image sequence of the event was also obtained using high-speed photography. The location of the sub-Rayleigh rupture tip and extended field lobes identified in high-speed images frames are correlated to the observed velocity swings exhibited by each particle velocity component.

We now present and contrast the results obtained from two independent sub-Rayleigh rupture experiments. The two experiments presented

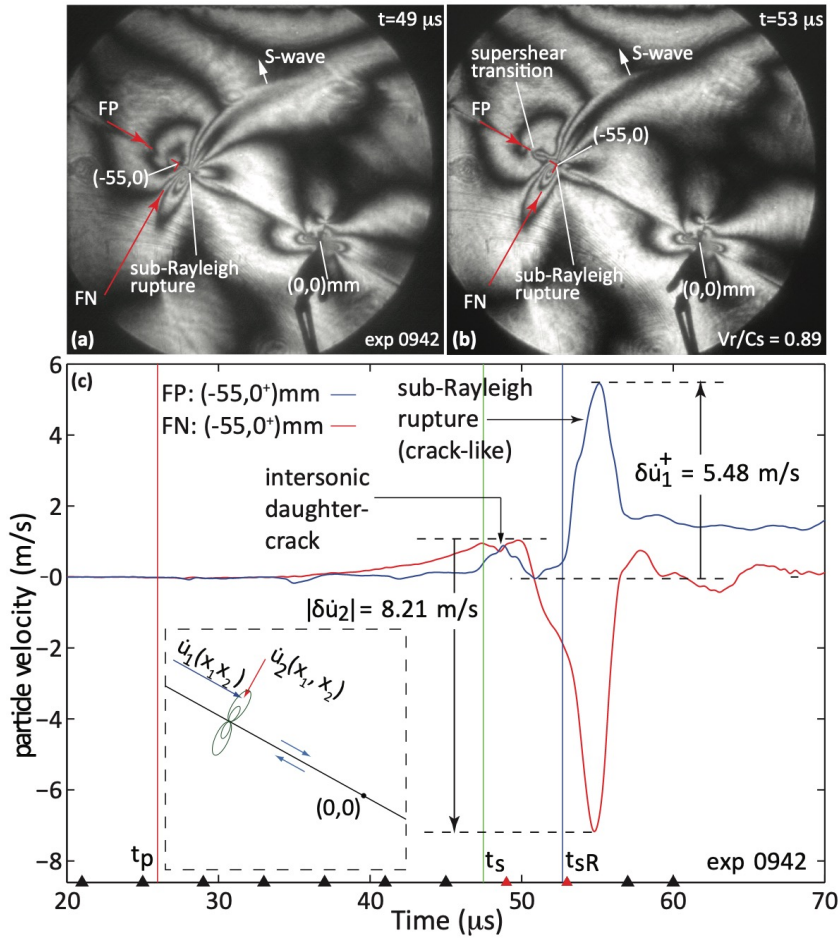


Figure 3.7: (a) Photoelastic image of a right-lateral/left-traveling sub-Rayleigh rupture approaching an on-fault particle velocity measurement station located at  $(-55, 0)$  mm. (b) Sub-Rayleigh rupture at  $t = 53 \mu\text{s}$  with emerging supershear secondary crack and the onset of a supershear transition. (c) Recorded particle velocity waveforms with leading disturbance attributed to the emergence of a secondary supershear crack trailed by the sub-Rayleigh segment characterized by a dominant FN component.

here resulted in uniquely different rupture profiles even though the same static compressive load of  $\sigma_0 = 19 \text{ MPa}$  was applied in each case. In the first experiment (exp 0942), the resulting particle velocity waveforms reveal the signature of a crack-like sub-Rayleigh rupture and the emergence of a secondary supershear (daughter) crack coincident with the location of the leading S-wave front. In the second experiment (exp 0943), the recorded velocity waveforms reveal the signature of a pulse-like sub-Rayleigh rupture with no evidence of a supershear transition.

The contrasting results between these two seemingly identical experiments were likely driven by slight variations in the curvature of the mated fault surfaces, which in turn lead to non-uniformities of the normal and shear stress distributions along the fault plane. Although not by design, the observed variability in the experimental results mimics the unpredictability and variability of natural earthquake events, which are often modulated by stress heterogeneities within natural crustal faults.

Figure 3.7 summarizes the key results obtained from the sub-Rayleigh rupture experiment (exp 0942). The rupture nucleation process resulted in a right-bilateral sub-Rayleigh rupture, which was accompanied by a stress drop of  $\Delta\sigma_0 = -3.4 \text{ MPa}$  in the far field load. Photoelastic images of the

left-traveling sub-Rayleigh rupture along with with particle velocity waveforms recorded at an on-fault station  $(-55, 0^+)mm$  are displayed in Figure 3.7.

Figure 3.7a, recorded to  $t = 49 \mu s$ , reveals a right-lateral/left-traveling sub-Rayleigh rupture as it approached an on-fault measurement station located at  $(-55, 0^+)mm$ . An expanded view of the image reveals a dark, concentrated caustic zone on the fault corresponding to the advancing rupture tip. Prominent field lobes radiate from the rupture tip and extending to either side of the fault. An expanding circular S-wave front, is clearly visible and labeled in the figure.

Figure 3.7b, recorded at  $t = 53 \mu s$ , reveals that the rupture tip after it had just cleared the measurement station. The discontinuity between the fringe, which protrudes out from the rupture tip and the arched looping fringe positioned just ahead of the sR rupture tip (at the point labeled “supershear transition”), reveals the emergence of an supershear rupture and onset of a sub-Rayleigh to supershear rupture transition.

The red lines in the images highlight the optical paths of the FP and FN fiber-optic probe beams, which were focused at nearly grazing incidence onto the lower-left corner of a retro-reflective strip of tape (also visible in an expanded view). Scattered laser light was collected and interfered to generate the continuous particle velocity records corresponding to  $\dot{u}_1(-55, 0^+)$  and  $\dot{u}_2(-55, 0^+)$  depicted in Figure 3.7c.

Figure 3.7c depicts the resulting on-fault particle velocity waveforms. The two red triangles mark the times at which the consecutive image frames were acquired. The blue vertical line positioned at  $t_{sR} = 52.9 \mu s$  marks the estimated rupture arrival time at the on-fault measurement station based upon an average rupture speed estimate of  $v_r = 0.89c_s$ . The anticipated rupture arrival time correlates very well with the sudden sharp velocity increase exhibited by the FP record. The sense of motion corresponding to the arrival of the sub-Rayleigh rupture in the particle velocity waveforms agrees with the anticipated sense of motion of a right-lateral/left-traveling sR rupture as predicted by the vector field plot in Figure 2.15a. The magnitudes of the corresponding FN and FP velocity swings are given by

$$|\delta\dot{u}_1^+| = |(\dot{u}_1^+)_{max} - (\dot{u}_1^+)_{min}| = 5.48m/s \quad (3.4)$$

$$|\delta\dot{u}_2^+| = |(\dot{u}_2^+)_{max} - (\dot{u}_2^+)_{min}| = 8.21m/s \quad (3.5)$$

and annotated in Figure 3.7c. The notation  $\delta u_1^+$  signifies that the FP particle velocity was measured on the extensional side of the fault at a point  $(x_2 \rightarrow 0^+)$  lying within  $200 \mu m$  of the interface.

The resulting particle velocity waveforms bear the signature of a “crack-like” sub-Rayleigh rupture, as revealed by the nearly constant sliding speed of  $\dot{u}_1^+ \sim 1.3 m/s$ , which was sustained well after the rupture had crossed the measurement station. The particle velocity waveforms are characterized

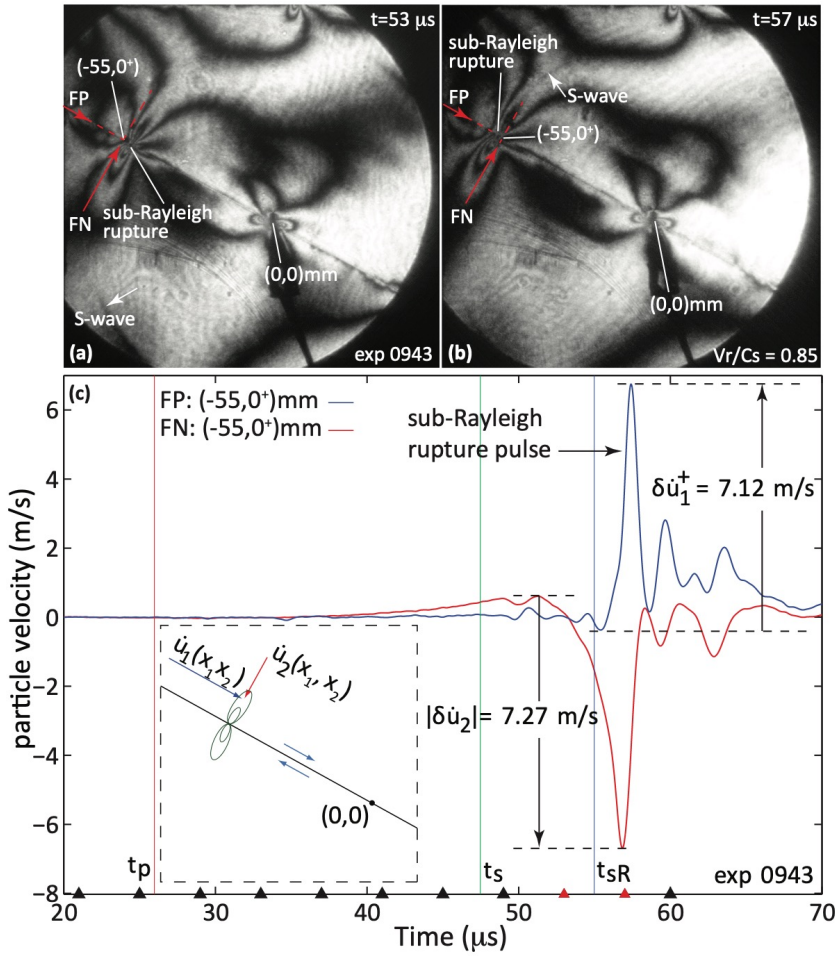


Figure 3.8: Consecutive image frames of a right-lateral and left-traveling sR rupture captured as it crossed an “on-fault” measurement station located at  $(-55, 0^+)mm$ . The red lines in the image highlight the optical paths of the FP and FN vibrometer beams, which simultaneously monitored the particle velocity at this location. The resulting particle velocity profiles reveal a “pulse-like” rupture characterized by a FN component, whose magnitude is only slightly greater than the magnitude of the FP component.

by a dominant FN component, as expected for a sR rupture, with the ratio between the noted velocity swings given by

$$|\delta\dot{u}_2^+|/|\delta\dot{u}_1^+| = 1.5$$

Finally, we draw attention to the small, pulse-like disturbances in the FN and FP records at time  $t = t_s$ , which correlate with the arrival of the supershear “daughter crack” and the onset of a sR to SS transition revealed in Figure 3.7b.

Figure 3.8 summarizes the key results obtained from the sub-Rayleigh rupture experiment (exp 0943). In this case the rupture nucleation process resulted in a right-bilateral sub-Rayleigh rupture accompanied by a stress drop of  $\Delta\sigma_0 = -2 MPa$  in the far field load, as noted at the conclusion of the experiment. Photoelastic images of the left-traveling sub-Rayleigh rupture along with with particle velocity waveforms recorded at an on-fault station  $(-55, 0^+)mm$  are displayed in Figure 3.8.

Figure 3.8a, recorded at  $t = 53 \mu s$ , depicts a right-lateral/left-traveling sub-Rayleigh rupture as it approached an on-fault measurement station located at  $(-55, 0^+)mm$ . As in the previous experiment, an expanded view

of the image reveals a dark, concentrated caustic zone on the fault corresponding to the advancing rupture tip. Prominent field lobes radiate from the rupture tip and extending to either side of the fault. A faint relic of the expanding circular S-wave front is also visible in the lower-left corner of the  $t = 53 \mu s$  image frame. Figure 3.8b, recorded at  $t = 57 \mu s$ , reveals the rupture just after it crossed the station. A faint relic of the expanding circular S-wave front is also visible in the upper-left corner of the  $t = 57 \mu s$  image frame.

The red lines in the images highlight the optical paths of the FP and FN fiber-optic probe beams, which were focused at nearly grazing incidence onto the lower-left corner of a retro-reflective strip of tape (also visible in an expanded view). Scattered laser light was collected and interfered to generate continuous particle velocity records corresponding to  $\dot{u}_1(-55, 0^+)$  and  $\dot{u}_2(-55, 0^+)$  depicted in Figure 3.8c.

The two red triangles on the time axis denote the times at which the consecutive image frames were acquired. The red and green vertical lines labeled  $t_p$  and  $t_s$  mark the anticipated arrival times of the leading P- and S-wave fronts at the measurement station. The blue vertical line positioned at  $t = 55 \mu s$  marks the rupture arrival time at the measurement station as determined by tracking the position of the rupture tip. The noted arrival time corresponds to an average rupture speed of  $v_r = 0.85c_s$  and correlates very well with the sudden sharp velocity increase exhibited by the FP record.

The resulting particle velocity profiles in Figure 3.8 reveal a sub-Rayleigh rupture pulse. The sense of motion exhibited by the “pulse-like” rupture waveforms agrees with the expected sense of motion for a right-lateral and left-traveling sR rupture as exhibited by the vector field plot in Figure 2.15a (i.e., a positive velocity swing in the FP component accompanied by a negative velocity swing in the FN component). The magnitudes of the FN and FP velocity swings, determined by

$$|\delta\dot{u}_1^+| = |(\dot{u}_1^+)_{max} - (\dot{u}_1^+)_{min}| = 7.12m/s \quad (3.6)$$

$$|\delta\dot{u}_2^+| = |(\dot{u}_2^+)_{max} - (\dot{u}_2^+)_{min}| = 7.27m/s \quad (3.7)$$

are each noted in Figure 3.8c. As previously noted, the notation  $\delta u_1^+$  signifies that the FP particle velocity was measured on the extensional side of the fault at a point ( $x_2 \rightarrow 0^+$ ) estimated to lie within  $200 \mu m$  of the interface. The resulting particle velocity profiles are thus characterized by a FN component, whose magnitude is only slightly greater than the magnitude of the FP component, i.e.,  $|\delta\dot{u}_2^+|/|\delta\dot{u}_1^+| = 1.02$ .

The results gathered in (exp 0942) and (exp 0943) are representative of a broad range of sub-Rayleigh rupture experiments, which were conducted using the (FN,FP) fiber-optic laser interferometer probe configuration. In all cases the magnitude of the FN component was observed to dominate over the magnitude of velocity swing exhibited by the corresponding FP component, i.e.  $|\delta\dot{u}_2^+|/|\delta\dot{u}_1^+| > 1$  without exception. In the few instances

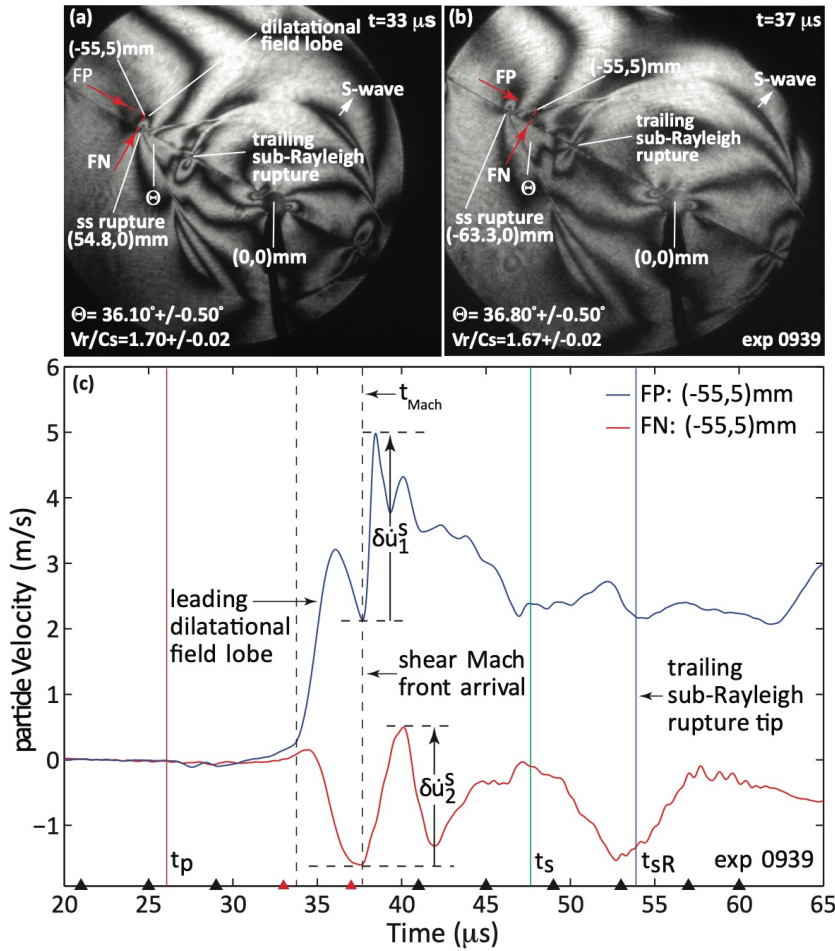


Figure 3.9: (a,b) Consecutive photoelastic image frames capture a shear Mach front crossing a particle velocity measurement station positioned at  $(-55, 5)\text{mm}$ . (c) Simultaneous FN and FP particle velocity waveforms recorded at the off-fault station reveal the velocity waveform signature of the leading dilatational field lobe followed by the sharp velocity jump associated with the arrival of the shear Mach front.

where a rupture pulse was recorded, the FN component remained dominant although the ratio is much closer to unity as noted in the case of exp 0943. Moreover, the observed sense of motion exhibited by sub-Rayleigh particle velocity waveforms is always found to be consistent with the sense of particle motion as predicted by theory.

### Investigation of the Velocity Component Ratio along a Shear Mach Front using the (FN:FP) Laser Vibrometer Configuration

A series of supershear rupture experiments were conducted using the (FP:FN) laser interferometer probe configuration depicted in Figure 3.3(a). Simultaneous particle velocity waveforms were recorded at various distances from the fault, and over a broad range of rupture speeds, as a supershear rupture and its surrounding field swept past the measurement station. The precise location of the supershear rupture tip, leading dilatational field lobe, and shear Mach fronts were all identified in the synchronized high-speed image frames and directly correlated to the velocity disturbances exhibited by the particle velocity waveforms.

Direct measurement of the particle velocity jumps  $\delta \dot{u}_1^s$  and  $\delta \dot{u}_2^s$  along the shear Mach front were obtained by taking advantage of the rapid separ-

ration between the leading dilatational field lobe and the shear Mach front, which results with increased FN distance from the fault plane. The ratio  $|\delta\dot{u}_1^s|/|\delta\dot{u}_2^s|$  was determined from 10 supershear experiments conducted over the broad range of supershear rupture speeds ( $\sqrt{2}c_s < v_r < c_p$ ). Results are plotted against the normalized rupture speed ( $v_r/c_s$ ), which was determined through direct measurement of the Mach front angle as previously outlined.

Figure 3.9 summarizes the key measurements obtained from a representative supershear rupture experiment (exp 0939). The LEQ specimen was subjected to an initial static compressive load of  $\sigma_0 = 24.8$  MPa. The rupture nucleation procedure resulted in a right-bilateral sub-Rayleigh rupture, which very quickly transitioned to a pair of right- and left-traveling supershear ruptures. Photoelastic images of the left-traveling supershear and trailing sub-Rayleigh ruptures, along with particle velocity waveforms recorded at an off-fault station  $(-55, 5)$  mm, are displayed in Figure 3.9(a,b).

The consecutive image frames in Figure 3.9(a,b) reveal the supershear rupture and its surrounding field as it approached and subsequently swept past the particle velocity measurement station located at  $(-55, 5)$  mm. Figure 3.9a, recorded at  $t = 33 \mu s$ , reveals the supershear rupture just as the dilatational field lobe begins to sweep the measurement station at  $(-55, 5)$  mm. Figure 3.9b, acquired at  $t = 37 \mu s$ , reveals the supershear rupture and its surrounding field just as the shear Mach front begins to cross the measurement station. The sharp outline of the expanding circular S-wave front is clearly visible in both images along with the sub-Rayleigh rupture and its extended field, which trails in the wake of the supershear rupture.

Figure 3.9c displays the FN and FP particle velocity records recorded at  $(-55, 5)$  mm. The red and green vertical lines at  $t = 26.1 \mu s$  and  $t = 47.7 \mu s$ , respectively, denote the anticipated arrival times of the leading P-wave and S-wave fronts at  $(-55, 5)$  mm. The blue line at  $t = 53.9 \mu s$  marks the anticipated arrival time of the trailing sub-Rayleigh rupture tip at  $(-55, 5)$  mm based upon a frame-by-frame analysis of the photoelastic image sequence. The two red triangles mark the times  $t = 33 \mu s$  and  $t = 37 \mu s$  when the consecutive image frames in Figure 3.9(a,b) were recorded. The dashed, black, vertical line at  $t = 33.6 \mu s$  marks the estimated arrival of the leading dilatational field lobe. The observed velocity jump correlates with the location of the leading dilatational field lobe relative to the off-fault station, in Figure 3.9a. The second, dashed, black, vertical line at  $t = 37.7 \mu s$  corresponds to the estimated arrival of the shear Mach front at  $(-55, 5)$  mm. The observed velocity jump, which commences at this time correlates very well with location of the shear Mach front relative to the off-fault station, as depicted in Figure 3.9b.

The pronounced velocity jumps  $\delta\dot{u}_1^s$  and  $\delta\dot{u}_2^s$  attributed to the arrival of the shear Mach front at  $(-55, 5)$  mm are annotated in Figure 3.9c. The positive increase exhibited by both motion components at this location are consistent with the anticipated sense of motion along the shear Mach front

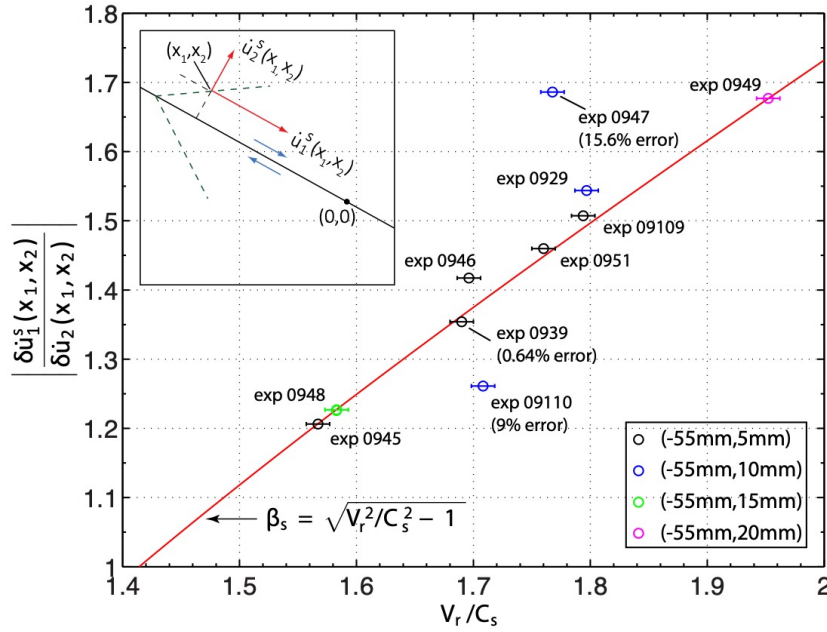


Figure 3.10: Measurements of  $\beta_s$  determined from supershear experiments plotted versus the normalized rupture speed. Excellent agreement between theory and experiment is demonstrated across a broad range of rupture speeds, which nearly span the entire domain of the supershear speed regime.

from a right-lateral/left traveling supershear rupture as confirmed by appealing to Figure 2.3(b) or Figure 2.14. A measured velocity jump of  $\delta u_1^s = 2.844 \text{ m/s}$  in the FP record and a corresponding velocity jump of  $\delta u_2^s = 2.101 \text{ m/s}$  exhibited by the FN signal leads to an experimental estimate of  $\beta_s^{meas} = \delta u_1^s / \delta u_2^s = 1.354$  for the ratio between the FP and FN jumps along the shear Mach front. The measured value for  $\beta_s$  may be compared to the theoretically predicted value given by Eq. 2.3, i.e.,

$$\beta_s = \frac{\delta u_1^s}{\delta u_2^s} = \sqrt{v_r^2/c_s^2 - 1} \quad (3.8)$$

assuming that the normalized supershear rupture speed is known.

The normalized rupture speed  $v_r/c_s = 1.69 \text{ m/s} \pm 0.01 \text{ m/s}$ , was estimated from the measurement of the shear Mach front angle. The measured normalized rupture speed corresponds to a theoretically predicted value of  $\beta_s = 1.362 \pm 0.03$  in accordance with Eq 2.11. The measured value of  $\beta_s^{meas} = 1.354$  is thus found to be within 1% of the theoretically predicted value.

The experiment (exp 0939) presented here is only one in a group of 10 similar supershear experiments conducted over a broad range of rupture speeds, which were analyzed in a similar manner. The solid red curve in the plot corresponds to the theoretical value given by  $\beta_s = \sqrt{v_r^2/c_s^2 - 1}$ . The individual data points are color coded according to the FN distance ( $x_2$ ) of the measurement station in the experiment. Estimates for  $\beta_s^{meas}$  obtained from each of these experiments are plotted against the corresponding (measured) normalized rupture speed in Figure 3.10. The horizontal error bars in Figure 3.10 correspond to the measurement uncertainty of  $\pm 0.01$  in the normalized rupture speed estimate.

Eight out of the ten supershear experiments represented in Figure 3.10

yielded a value for  $\beta_s^{meas}$  that was found to be within 3.44% of the theoretically predicted value. There are two noted “outliers”, in the plot corresponding to exp 09110 (9% error) and exp0939 (15.6% error). The primary difference between these two experiments is attributed to a “near-field disturbance”, which was superimposed with the supershear rupture field as the shear Mach front swept the off-fault station. The effect is very likely a relic of the rupture nucleation process and is attributed to the dilatational contraction of the cylindrical cavity, which surrounds the NiCr wire filament. Analysis of the near field disturbance reveals that it is initiated well after rupture nucleation and that it propagates at the dilatational wave speed ( $c_p$ ) (refer to Figure 3.5). The commonality between the eight “known good” experiments is that they all exhibited an early sR to SS rupture transition, which allowed the shear Mach front to sweep the measurement in advance of the near-field disturbance. This appears to be the only scenario whereby reliable shear Mach front measurements of the type considered here can be conducted when using the electrical rupture nucleation scheme.

Bearing all of these points and observations in mind, we may conclude that the experimental results summarized by the plot in Figure 3.10 demonstrate excellent agreement between theory and measurement. The results demonstrate that the observed ratio between the magnitudes of the FP and FN components along the shear Mach front is governed by the theoretical relationship given by Eq. 3.8 and preserved out to a considerable distance from the fault plane (note the data point obtained at  $x_2 = 20mm$ ).

### Attenuation Properties of sub-Rayleigh Rupture Fields: Experimental Investigations using the (FN:FN) Vibrometer Configuration

A series of sub-Rayleigh rupture experiments were conducted using the (FN:FN) laser vibrometer configuration depicted in Figure 3.3b. FN particle velocity waveforms were simultaneously recorded at an on-fault and an off-fault measurement station as the measurement stations were swept by the sub-Rayleigh rupture and its extended field. A synchronized, photoelastic image sequence of the event was also obtained using high-speed photography. The precise location of the sub-Rayleigh rupture was identified in high-speed image frames and directly correlated to the observed velocity swings in the recorded waveforms. The ratio between the measured velocity swings  $\delta\dot{u}_2(x_1, x_2)/\delta\dot{u}_2(x_1, 0^+)$  was obtained and plotted as a function of the normalized distance from the fault. The results from the experiments demonstrate how a sub-Rayleigh rupture field is rapidly stripped of its high frequency content and subject to a precipitous amplitude decay with increased distance from the fault plane Mello et al. (2010).

Figure 3.11 summarizes the key measurements obtained from a representative sub-Rayleigh rupture experiment (exp 0973). The rupture nucleation process resulted in a right-bilateral sub-Rayleigh rupture accompanied by a stress drop of  $\Delta\sigma_0 = -1 MPa$  in the far field load, as noted at the conclusion of the experiment. Photoelastic images of the left-traveling sub-Rayleigh rupture along with with particle velocity waveforms recorded

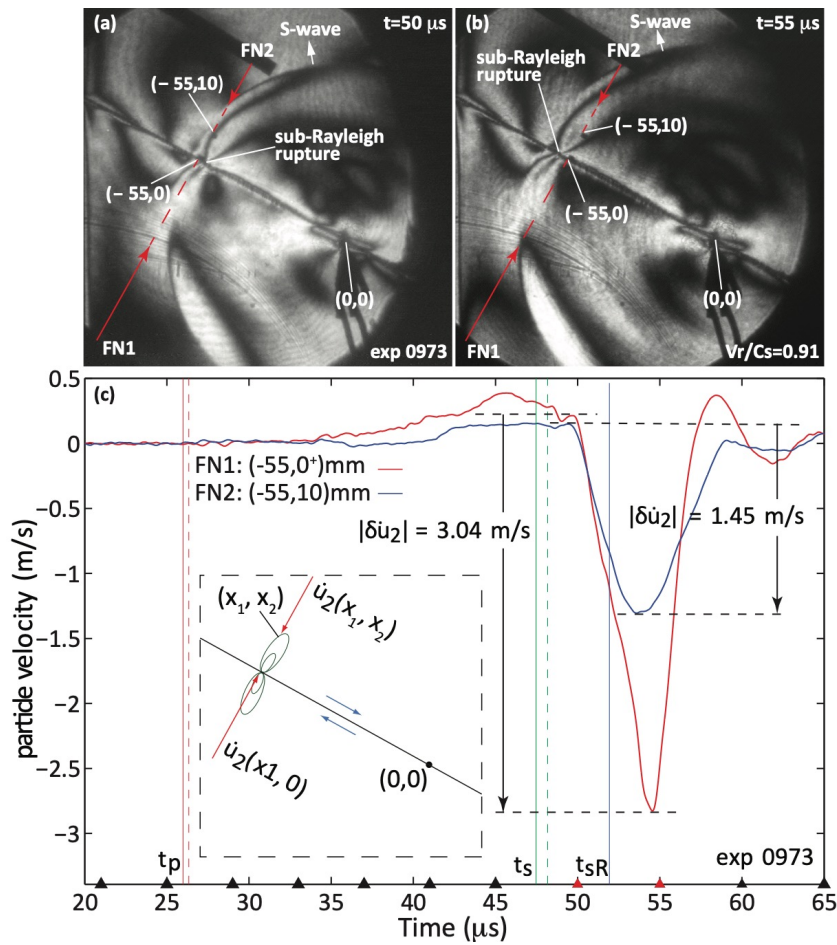


Figure 3.11: (a,b) Consecutive photoelastic image frames reveal the sub-Rayleigh rupture and its surrounding stress field lobes as they approach and subsequently cross the particle a pair of measurement stations located at  $(-55, 0)mm$  and  $(-55, 10)mm$ . (c) Paired FN particle velocity traces simultaneously recorded at the on-fault and off-fault stations. The FN record obtained at  $(-55, 10)mm$  exhibits a signal amplitude which has decayed to = 48% of its corresponding on-fault value.

at an on-fault station  $(-55, 0^+)mm$  and off-fault station  $(-55, 10)mm$  are displayed in Figure 3.11. The photoelastic image frames in Figures 3.11(a,b) reveal a sub-Rayleigh rupture and its extended field lobes as it crossed the two particle velocity measurement stations located at  $(-55, 0^+)mm$  and  $(-55, 10)mm$ . The red lines in the image highlight the optical paths of the two FN interferometer probe beams, which simultaneously monitored the particle velocity at these locations. The concentrated rupture tip, prominent field lobes, and the expanding circular S-wave fronts are clearly visible in each image frame. Figure 3.11a, acquired at  $t = 50 \mu\text{s}$ , depicts the sub-Rayleigh rupture tip approaching the on-fault measurement station  $(-55, 0^+)mm$ , while the Figure 3.11b, acquired at  $t = 55 \mu\text{s}$ , reveals the rupture just after it crossed the on-fault station. A rupture arrival time estimate of  $t = 51.88 \mu\text{s}$  was determined from a frame-by-frame analysis of the photoelastic image sequence. The images also reveal the leading edge of the upper field lobe reaching the off-fault station  $(-55, 10)mm$  at  $t = 50 \mu\text{s}$  and the trailing edge of the field lobe crossing the station at  $t = 55 \mu\text{s}$ .

Figure 3.11c depicts the resulting FN particle velocity waveforms recorded from (exp 0973). The two red triangles on the time axis correspond to the times at which the consecutive image frames in Figure 3.11 were acquired. The solid red and green vertical lines labeled  $t_p$  and  $t_s$  mark the anti-

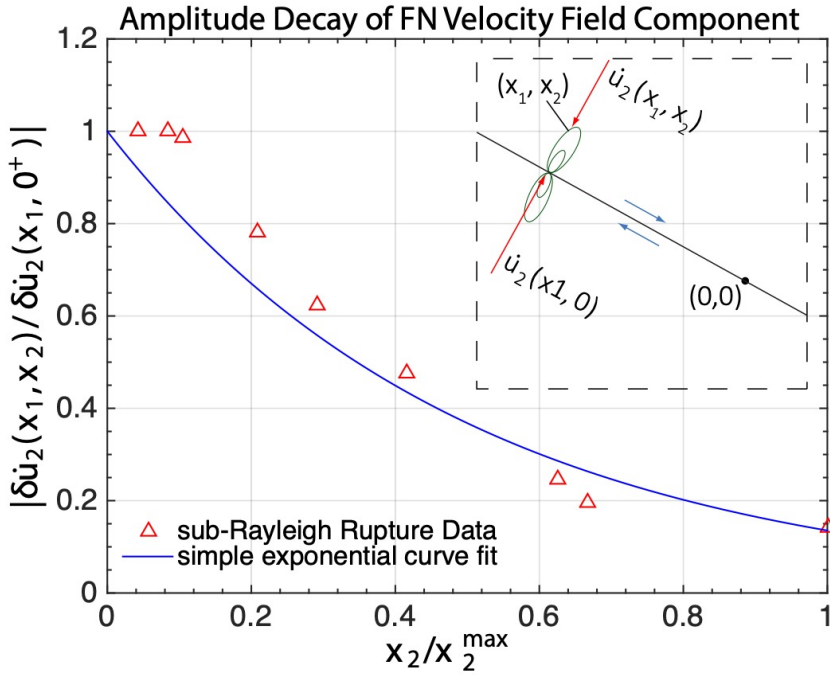


Figure 3.12: Decay of the FN signal amplitude represented by the  $|\dot{u}_y^{off-fault} / \dot{u}_y^{on-fault}|$  plotted versus the normalized FN distance. Results were obtained from 10 independent laboratory earthquake experiments using the paired FN laser interferometer probe configuration, as depicted in the inset.

pated arrival times of the leading P-wave and S-wave fronts at the on-fault measurement station  $(-55, 0^+)mm$ . The dashed red and green lines denote the anticipated P-wave and S-wave arrival times at the off-fault station  $(-55, 10)mm$ . The blue vertical line positioned at  $t = 51.88 \mu s$  marks the rupture arrival time estimate at the on-fault measurement station as determined from an analysis of the photoelastic image sequence. In this case the noted arrival time corresponds to an average rupture speed of  $v_r = 0.91c_s$ . The two symmetric particle velocity profiles displayed in Figure 3.11c correlate with the passage of the rupture tip and its extended field lobes at the two measurement stations. The observed sense of particle motion exhibited by the two curves is consistent with the predicted sense of motion for a right-lateral/left-traveling sub-Rayleigh rupture. This is readily verified by appealing to the vector velocity field plot in Figure 2.15a. The amplitude of the velocity swings recorded at each field point reveal how the FN velocity swing recorded at the on-fault station is stripped of high frequency content and decays to 48% of the FN velocity swing recorded at the off-fault station  $(-55, 10)mm$ .

The experiment (exp0973), which is examined here is only one in a group of 9 similar sub-Rayleigh rupture experiments conducted over a range of static compressive loads, which were all monitored and analyzed in a similar way. Figure 3.12 summarizes the results obtained from all of the sub-Rayleigh rupture experiments, which were monitored using the (FN:FN) laser vibrometer configuration.

The ratio  $|\dot{u}_2(x_1, x_2) / \dot{u}_2(x_1, 0^+)|$  is plotted versus the normalized FN distance  $(x_2/x_2^{\max})$ , where  $x_2^{\max} = 24mm$ .

The inset in the figure provides a simple reminder of the LEQ specimen fault orientation and laser vibrometer configuration that was used to record the FN velocity waveforms at each respective measurement station. The red triangles in the figure correspond to the measured ratios

$$|\dot{u}_2(x_1, x_2)/\dot{u}_2(x_1, 0^+)|$$

while the blue curve is a simple exponential curve fit. The cluster of data points corresponding to ( $1mm \leq x_2 \leq 2.5mm$ ) with a ratio near unity are a manifestation of the rupture process zone. The FN signal amplitude exhibits a rapid amplitude decay with increased FN distance ( $x_2$ ) from the rupture zone, as predicted, for a sub-Rayleigh particle velocity field.

### **Kinematic Partition Relationship Between the Rupture Sliding Speed and the FP Velocity Component Propagated by a Shear Mach Front: Experimental Investigations using the (FP:FP) Vibrometer Configuration**

A series of supershear rupture experiments were conducted using the (FP:FP) laser vibrometer configuration depicted in Figure 3.3c. The main objective of this series of experiments was to investigate the spatiotemporal property of supershear rupture fields, given by Eq. 2.36, which predicts how sliding speed at the fault plane  $\dot{u}_1(x_1, 0^+)$  is partitioned between the FP motion components of the radiated shear and dilatational fields.

The key to this particular series of experiments is the rapid separation, which occurs between the leading dilatational field lobe and the shear Mach front with increased FN distance ( $x_2$ ) from the frictional fault plane. Recall that the same principle was previously leveraged in order to investigate the ratio  $\delta\dot{u}_1^s(x_1, x_2)/\delta\dot{u}_2^s(x_1, x_2)$  between the FP and FN velocity jumps at an off-fault field point as it is swept by a shear Mach front. The ideal experiment to demonstrate this effect would require a set of simultaneous FP measurements conducted at different distances from the fault plane during a single supershear rupture experiment. Unfortunately, a limited number of laser vibrometers prohibited this approach and so separate experiments were conducted in order to demonstrate and visualize this effect. The particle velocity waveforms in Figure 3.13 were obtained from 5 independent supershear rupture experiments. In each case the vibrometer probe beam was focused at a different off-fault distance as indicated.

The lowest panel in Figure 3.13 corresponds to supershear experiment (exp 0913), which featured the simultaneous measurement of FP and FN particle velocity records at an on-fault station located at  $(-40, 0^+)mm$ . A sharp velocity jump commencing at  $t = 30 \mu s$  resulted from the dilatational and shear fields, which are superimposed at the fault plane and engulf the rupture zone. We note the second broader peak in the record at  $t = 44.6 \mu s$ , which corresponds to the peak sliding speed of the trailing Rayleigh rupture, which arrived at  $t = 40.4 \mu s$ . The FP record presented in the second panel from the bottom corresponds to the supershear experiment (exp 09039). The peak velocity attained by the dilatational and shear

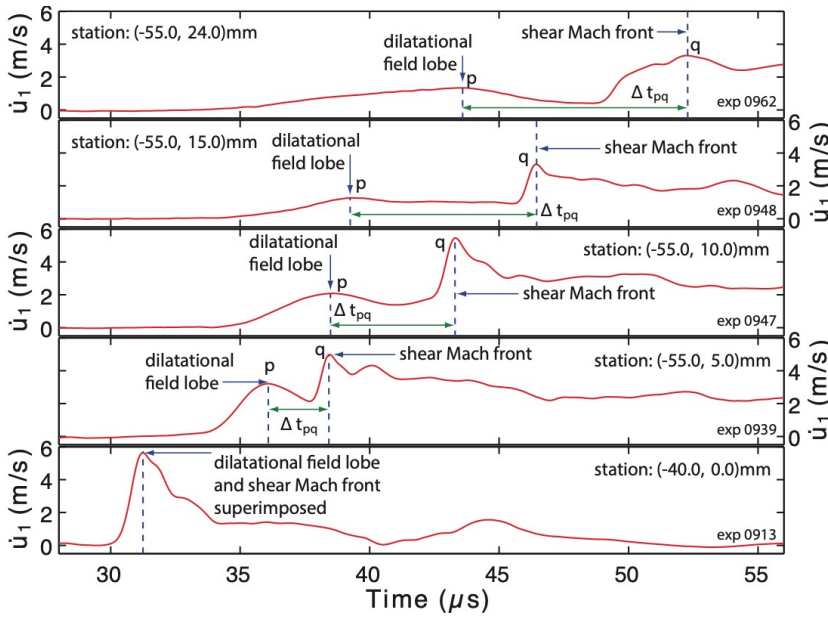


Figure 3.13: Series of FP particle velocity waveforms obtained in five separate supershear experiments showing the progressive separation between the leading dilatational field lobe and the shear Mach front with increased FN distance.

field portions of the waveform are labeled  $p$  and  $q$ , respectively. The noted separation  $\Delta t_{pq}$  reveals how rapidly the two fields begin to separate even at a modest FN distance of  $x_2 = 5\text{mm}$  from the fault plane. Indeed the separation between the two field contributions enabled a reliable estimate of  $\dot{u}_1^s$  and  $\dot{u}_2^s$  along the shear Mach front, as previously discussed.

The FP waveforms displayed in the remaining 3 panels were recorded at FN distances of  $x_2 = 10\text{mm}$ ,  $x_2 = 15\text{mm}$ , and  $x_2 = 24\text{mm}$ . The obvious and most striking feature of the curves in Figure 3.13 is the sustained amplitude of the FP velocity jump carried by the shear Mach front with increased FN distance ( $x_2$ ). Note as well the pronounced broadening and fairly rapid amplitude decay of the leading dilatational field lobe in comparison to the significantly sharper rise time and sustained amplitude associated with the motion propagated by the shear Mach front. In reality, the experiments exhibited varying stress drops, supershear transition distances, and rupture speeds and so the stacked plots are not equivalent to a single experiment based upon five simultaneous FP measurements. Nevertheless, the results clearly demonstrate the rapid spatiotemoral separation between the leading dilatational field lobe and the shear Mach front with increased FN distance ( $x_2$ ) from the specimen fault plane.

We now discuss and interpret the results obtained from a series of supershear experiments specifically designed to investigate the partitioning relationship given by given by Eq. 2.36, which governs the relationship between the sliding speed at the frictional fault plane  $\dot{u}_1(x_1, 0^+)$  and the FP velocity jump  $\dot{u}^s(x_1, x_2)$  propagated by the shear Mach front. The results from a supershear experiment (exp 0962) presented here are representative of a broader group of experiments that were conducted and analyzed in a similar manner using the (FP:FP) laser vibrometer configuration depicted in Figure 3.3c.

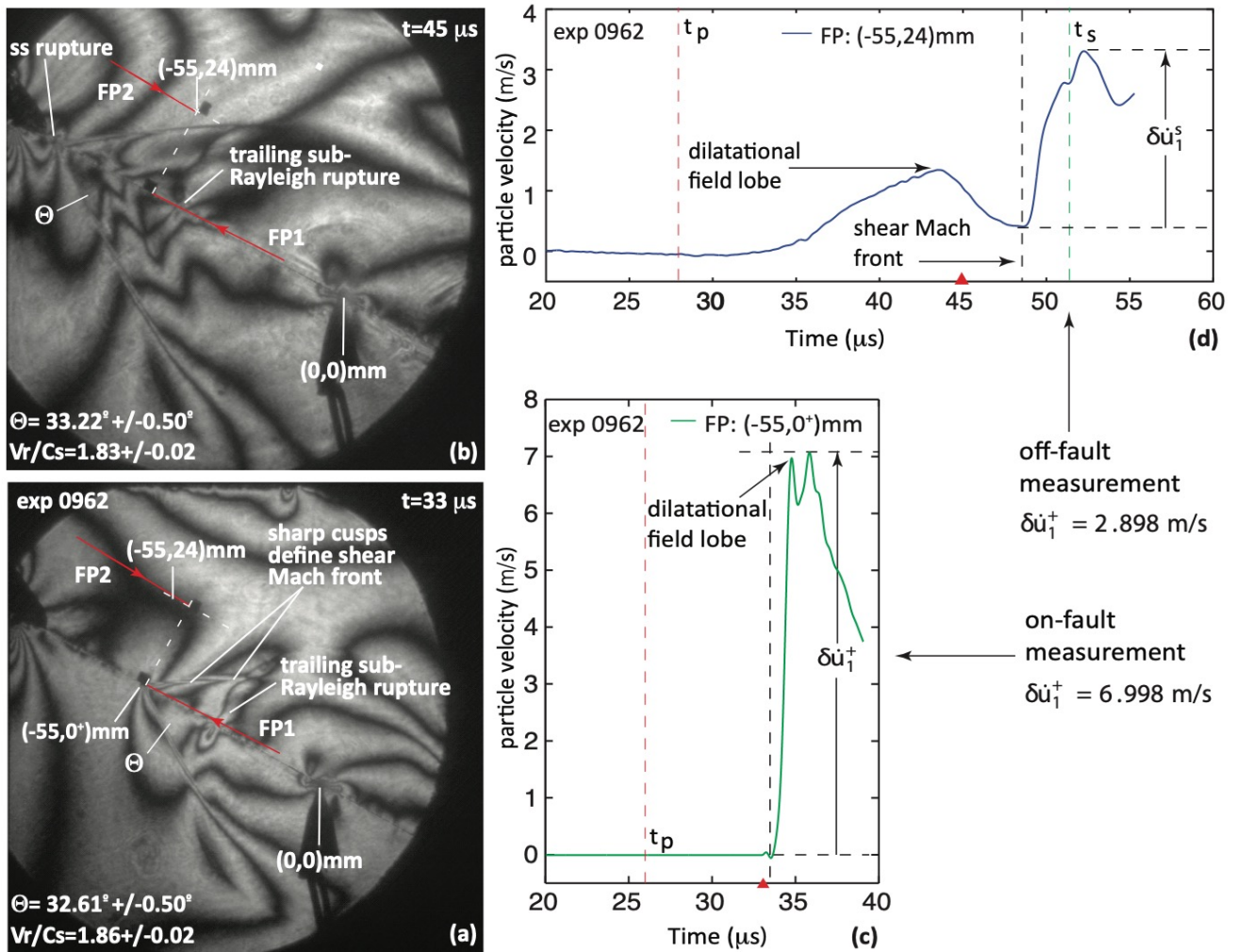


Figure 3.14 summarizes the key measurements obtained from the supershear rupture experiment (exp 0962). The rupture nucleation procedure resulted in a right-bilateral sub-Rayleigh rupture, which quickly transitioned to a pair of right-traveling and left-traveling supershear ruptures. Photoelastic images of the left-traveling supershear rupture along with particle velocity waveforms recorded at the off-fault station  $(-55, 24)mm$ , are displayed in Figure 3.14(a,b).

The consecutive high-speed images in Figures 3.14(a,b) display the supershear rupture field as the rupture tip and shear Mach front approached the on-fault station  $(-55, 0^+)mm$  and the off-fault measurement station  $(-55, 24)mm$ . Figure 3.9a, recorded at  $t = 33\mu s$ , reveals the supershear rupture just as the dilatational field lobe began to sweep the measurement station at  $(-55, 0^+)mm$ . Figure 3.9b, acquired at  $t = 37\mu s$ , reveals the upper shear Mach front on the extensional side of the fault as it approached the off-fault station. Mach angle measurements yielded a normalized rupture speed of  $v_r/c_s = 1.85$ , which was also consistent with the average rupture speed estimate obtained through a frame-by-frame analysis of the high-speed image sequence.

Figure 3.14: (a,b) Photoelastic image frames capture the supershear rupture field as the rupture tip and shear Mach front were about to cross the on- fault station  $(-55, 0^+)mm$  and the off-fault measurement station at  $(-55, 24)mm$ . (c,d) FP particle velocity records obtained the on- and off-fault measurement stations located at  $(-55, 0^+)mm$  and  $(-55, 24)mm$  during supershear experiment (exp 0962).

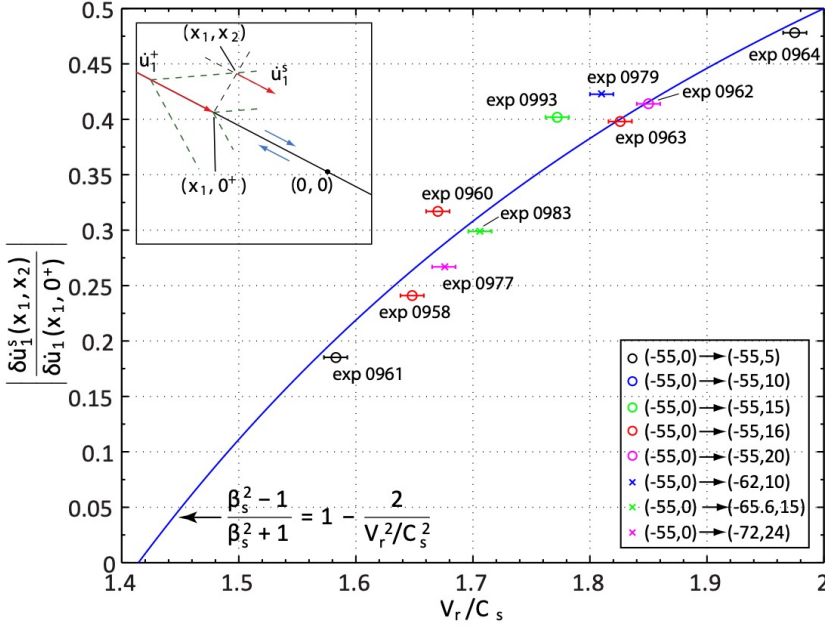


Figure 3.15: Plot of the measured ratio  $\dot{u}_x^s / \dot{u}_x(x, 0^+)$  obtained from 10 independent supershear experimental records plotted against the normalized wave speed  $v_r / c_s$ . Results compare quite favorably with theoretical partitioning relationship corresponding to the blue curve.

Figures 3.14(c,d) display the on-fault and off-fault FP particle velocity waveforms obtained in the experiment. Each waveform has been truncated in order to highlight the portion of the record attributed to the arrival of dilatational field and shear Mach front. The dashed red and green vertical lines labeled  $t_p$  and  $t_s$  represent the anticipated arrival times of the S- and P-waves at the measurement stations. The dashed black vertical line in Figures 3.14(c,d) denotes the arrival of the supershear rupture tip at the on-fault station  $(-55, 0^+)mm$ . The dashed black vertical line in Figure 3.14(d) marks the arrival of the shear Mach front at the off-fault station  $(-55, 24)mm$ .

The velocity jumps labeled  $\delta \dot{u}_1^+$  and  $\delta \dot{u}_1^s$  in Figure 3.14 correspond to

$$\delta \dot{u}_1^+ = \dot{u}_1^{max}(-55, 0^+) - \dot{u}_1^{min}(-55, 0^+) = 6.998 \text{ m/s} \quad (3.9)$$

$$\delta \dot{u}_1^s = [\dot{u}_1^s(-55, 24)]_{max} - [\dot{u}_1^s(-55, 24)]_{min} = 2.898 \text{ m/s} \quad (3.10)$$

The measured values of the on-fault and off-fault velocity jumps in exp 0962 correspond to a ratio  $(\delta \dot{u}_1^s)^{meas} / (\delta \dot{u}_1^+)^{meas} = 0.414$ . Application of Eq. 2.38 using a normalized rupture speed estimate of  $v_r / c_s = 1.85$  predicts a partitioning ratio of  $\delta \dot{u}_1^s / \delta \dot{u}_1^+ = 0.416$ . The measured value of 0.414 is thus found to be within 0.36% of the theoretically predicted value.

Figure 3.15 summarizes the results obtained from 10 independent supershear rupture experiments, which were analyzed in a similar manner. The inset in the upper left corner of the figure schematically depicts the (FP:FP) laser vibrometer configuration, which was applied to simultaneously monitor the FP velocity component at the on and off-fault field stations. The solid blue curve corresponds to a plot of the partitioning ratio ( $r_s$ ) versus

the stable portion of the normalized rupture speed ( $\sqrt{2} < v_r/c_s < 2$ ) in accordance with Eq. 2.38. The experimental data points corresponding to the measured ratios are plotted in the figure and are seen to span across a range of rupture speeds, which nearly spans the entire stable rupture speed regime. The symbol legend in the lower right corner provides a key to the coordinates of the on-fault and off-fault coordinates for each experiment. A very good match is observed between the measured ratios obtained from the experiments and the theoretical partitioning ratio given by Eq. 2.38. The largest error applies to exp 0993 and exp 0960, which deviate by 12% and 10.8% respectively, from the theoretical value. The larger deviation observed in these two experiments is attributed to superposition of the previously noted near-field disturbance. We also note the range of FN distances over which the tests were conducted and how the results appear to be independent of the FN distance ( $x_2$ ).

## Conclusions

Fundamental spatiotemporal field properties and particle velocity waveform signatures exhibited by sub-Rayleigh and supershear ruptures have been theoretically motivated and experimentally demonstrated. We have appealed to 2D dynamic rupture theory and identified specific kinematic relationships between the in-plane motion components, which are uniquely attributed to the velocity field of a propagating shear dislocation. Underlying kinematic properties are manifested in particle velocity records and experimentally verifiable using the LEQ experiment, which is quasi-2D by nature.

The original steady state singular elastic solution for the velocity field radiated by a dynamic shear crack Freund (1979) was reexamined and analyzed in detail. Vector field plots and synthetic waveforms reveal the defining spatiotemporal field properties and kinematic signatures of sub-Rayleigh shear cracks. The following properties of sub-Rayleigh rupture fields were identified and experimentally verified by LEQ experiments using the (FN:FP) and (FN:FN) vibrometer probe configuration: (1) Sub-Rayleigh shear cracks propagate with stable rupture speeds ( $v_r$ ), which asymptotically approach Rayleigh wave speed ( $c_R$ ), i.e.,  $v_r < c_R$ . (2) The particle velocity waveforms of a sub-Rayleigh rupture are distinguished by a FN component ( $\delta\dot{u}_2(t)$ ), which always dominates in magnitude over the FP component ( $\delta\dot{u}_1(t)$ ). (3) The shear and dilatational field contributions of the sub-Rayleigh rupture field are always superimposed and physically inseparable. (4) On-fault sub-Rayleigh velocity waveforms are rapidly stripped of their high frequency content and subject to a precipitous amplitude decay with increased FN distance from the frictional fault plane.

Spatiotemporal field properties and kinematic signatures of supershear rupture fields, which emerge from the singular elastic model, were identified and contrasted with sub-Rayleigh rupture field properties. The following properties of supershear rupture fields are predicted and verified by LEQ experiments: (1) The ratio between the particle velocity jumps propagated

by the shear Mach front was shown to observe the fundamental relationship  $\delta\dot{u}_1^s/\delta\dot{u}_2^s = -\beta_s \text{sgn}(\xi_2)$ , given by Eq. 2.15. (2) Motion propagated by the shear Mach front is characterized by a FP component ( $\dot{u}_1^s(t)$ ), which dominates in magnitude over the FN component ( $\dot{u}_2^s(t)$ ) in the stable rupture speed regime ( $\sqrt{2}c_s \leq v_r \leq c_p$ ). (3) the reverse situation applies in the unstable rupture speed domain ( $c_s \leq v_r < \sqrt{2}c_s$ ) (4) a peculiar circumstance arises when  $v_r = \sqrt{2}c_s$  whereby the shear field is predicted to vanish. (5) the shear and dilatational field contributions of a supershear rupture field are separable and predicted to rapidly separate with increased distance from the fault plane. (6) the portion of the on-fault velocity waveform attributed to the dilatational field term ( $\dot{u}^d$ ) tends to rapidly decay with increased FN distance, albeit more slowly than the rate of decay of a sub-Rayleigh rupture field. (7) the dilatational field circulates about the supershear rupture and extends out beyond the region bounded by the shear Mach fronts. This leads to a pulse-like a noted velocity disturbance in the FP and FN waveforms, characterized by a dominant FP component ( $\dot{u}_1^d$ ), which arrives in advance of the shear Mach front.

The non-singular analytical solution for a steady state supershear slip pulse (Dunham & Archuleta, 2005) was also presented and examined in considerable detail. Previously noted spatiotemporal field properties predicted by the singular elastic model are recovered by the non-singular model. The solution applies equally well to crack-like ruptures observed in LEQ experiments by considering the limiting case of a very long pulse length. New kinematic relationships are gleaned from the non-singular solution, which relate the sliding motion driven by the supershear rupture at the fault plane to the FP components of the radiated shear and dilatational fields. In particular, we have established a speed-dependent kinematic partitioning relationship given by

$$r_s = \dot{u}_1^s(x_1, 0^+)/\dot{u}_1(x_1, 0^+) = (\beta_s^2 - 1)/(\beta_s^2 + 1)$$

given by Eq. 2.38, which was also experimentally verified by LEQ experiments using the (FP:FP) vibrometer probe configuration.

### 3.2 ENS Laboratory Earthquake Experiment

The laboratory setup involves a tri-axial apparatus and a high-frequency acquisition system to record acoustic waves through piezo-ceramic sensors (Figure 3.16). The apparatus used here is a tri-axial oil medium loading cell ( $\sigma_1 > \sigma_2 = \sigma_3$ ). The apparatus can support a confining pressure of 100 MPa and up to 600 MPa in differential stress (for 40 mm sample diameter). The confining pressure ( $\sigma_2 = \sigma_3$ ) and the axial stress  $\sigma_1$  are servo-controlled independently. Experiments are conducted by imposing a constant strain rate, ranging from  $10^{-5} \text{ s}^{-1}$  to  $10^{-4} \text{ s}^{-1}$ . Displacement is measured externally by three gap sensors and then corrected from the machine stiffness. Stresses and strains are monitored at 10 Hz sampling rate. The piezo-ceramic sensors used consist of a PZT crystal (PI ceramic PI255, 5 mm in diameter and 0.5 mm in thickness) encapsulated within a brass casing. All the piezoelectric crystals are polarised in the same way and record

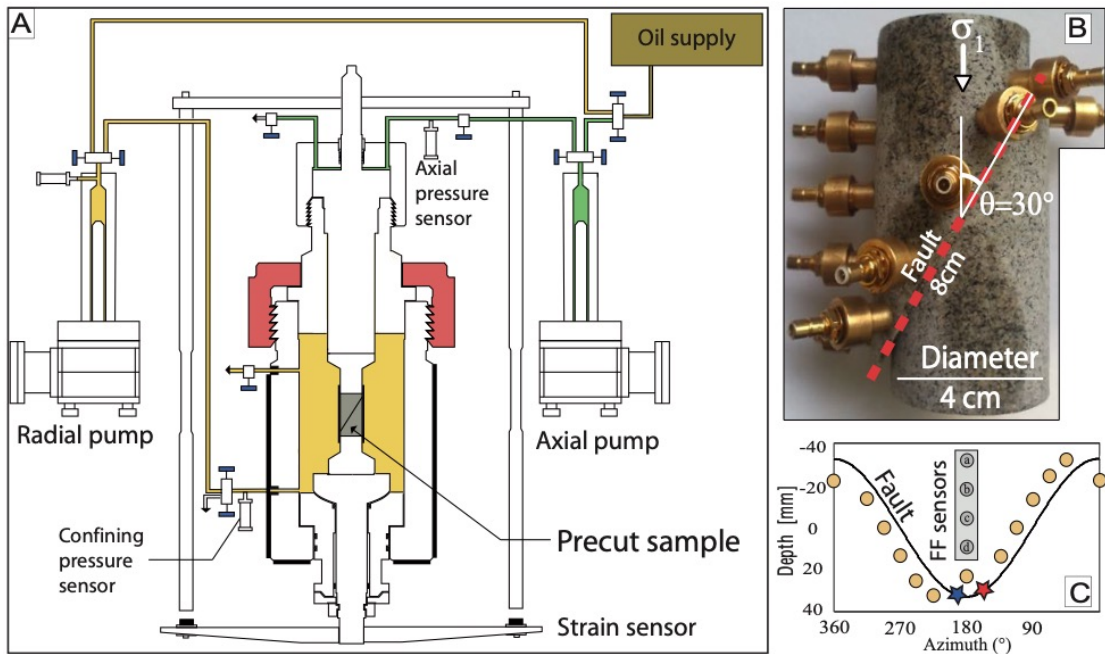


Figure 3.16: (A) Schematic of the triaxial apparatus. Axial and radial stresses are driven by two precision microvolumetric high pressure pumps. Axial deformation is measured by the mean of three displacement transducers. (B) The fault system is simulated using a saw cut Westerly granite sample. The fault is inclined at an angle  $\theta = 30^\circ$  to  $\sigma_1$  promoting mixed mode II and III ruptures. (C) Sensor arrays used to estimate the rupture velocity. Grey circles are sensors used to track the Mach cone (MFA). Yellow circles are Near-Field (NF) sensors used to estimate the rupture velocity.

preferentially compressional waves. The signal received on each sensor is unamplified and relayed to a 16 channel digital oscilloscope, at a sampling rate of 10 MHz. The waveforms recorded correspond to the variation of the particles acceleration during instability.

Stick-slip experiments were conducted on saw cut Westerly granite samples ( $c_p = 5800m/s$ ,  $c_s = 3500m/s$ ), which serve as proxies for crustal rocks, during triaxial loading. The fault length is 8cm. Stick-slip experiments and earthquake mechanisms are analogous in nature because they both result from rapid frictional sliding along pre-existing faults resulting in partial or total stress drop (Brace & Byerlee, 1966).

In our experiments, the stress conditions were typical of the upper crust, ranging from 10 to 150 MPa in normal stress acting on the pre-existing / saw-

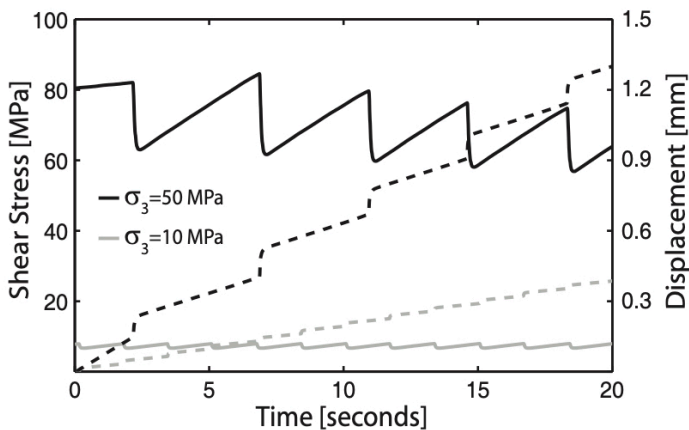


Figure 3.17: Evolutions of shear stress (solid lines) and displacement (dashed lines) during two stick-slip experiments at 10 MPa (A) and 50 MPa (B) confining pressure respectively.

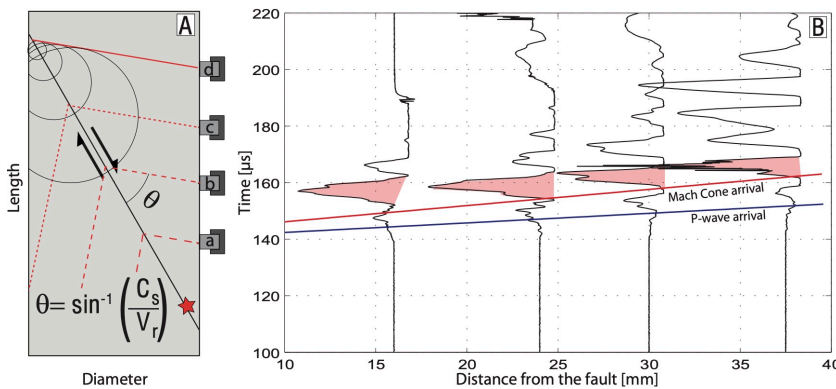


Figure 3.18: Evolutions of shear stress (solid lines) and displacement (dashed lines) during two stick-slip experiments at 10 MPa (A) and 50 MPa (B) confining pressure respectively.

cut fault. In total, more than 250 stick slip events were recorded (Figure 3.17). For each event, we inverted the rupture velocity directly from our experimental records using high frequency acoustics as a tracking tool.

We tracked the Mach wave front arrival using recorded accelerogram. Theoretical arrival time of the Mach wavefront radiated away from the rupture tip was predicted using: (i) the position of the rupture front determined from the inverted rupture velocity, (ii) the shear wave velocity and the distance between the Mach front antenna (MFA) sensors to the fault as defined in Figure 3.18A (Schubnel et al., 2011). Our calculation assumes that the rupture velocity is constant. Importantly, we looked for ruptures with velocity  $v_r$ , greater than the shear wave speed but different that  $\sqrt{2}c_s$ , for in this case no Mach cone is expected. We compared our calculation with waveforms recorded by the MFA array for a stick slip event during which a supershear rupture velocity was predicted by the inversion (Figure 3.18B). In agreement with theory outlined in the previous chapter, we first observed a weak P arrival, which corresponds to the continuous emission of P waves by the rupture tip as it propagates. However, the signal is dominated by the arrival of a large amplitude coherent wavefront just after the diffuse P wave arrival. The relative amplitude of this wavefront, when compared to the first P wave amplitude, increases with distance to the fault. This is expected because the geometric attenuation of a conic wavefront is smaller than that of spherical one. At each station, the arrival time of this wavefront is consistent with the predicted arrival time of the Mach wavefront.

To confirm our estimations of the rupture velocity, we conducted simulations using a 2D steady-state rupture model as explained before. We observe an excellent fit, both in relative amplitude and for the general waveform shape, when comparing the experimental waveforms recorded on the MFA sensors during a subshear event and the synthetics obtained by our numerical simulation (Figure 3.19B). We observed similar good correspondence between experimental waveforms and simulation of a supershear rupture (Figure 3.19C). In both cases, we obtained the best fit between analytical and experimental records by using the rupture velocity estimated experimentally, confirming that our experimental estimate of the rupture velocity is accurate. Furthermore, we show that dynamic rupture models that

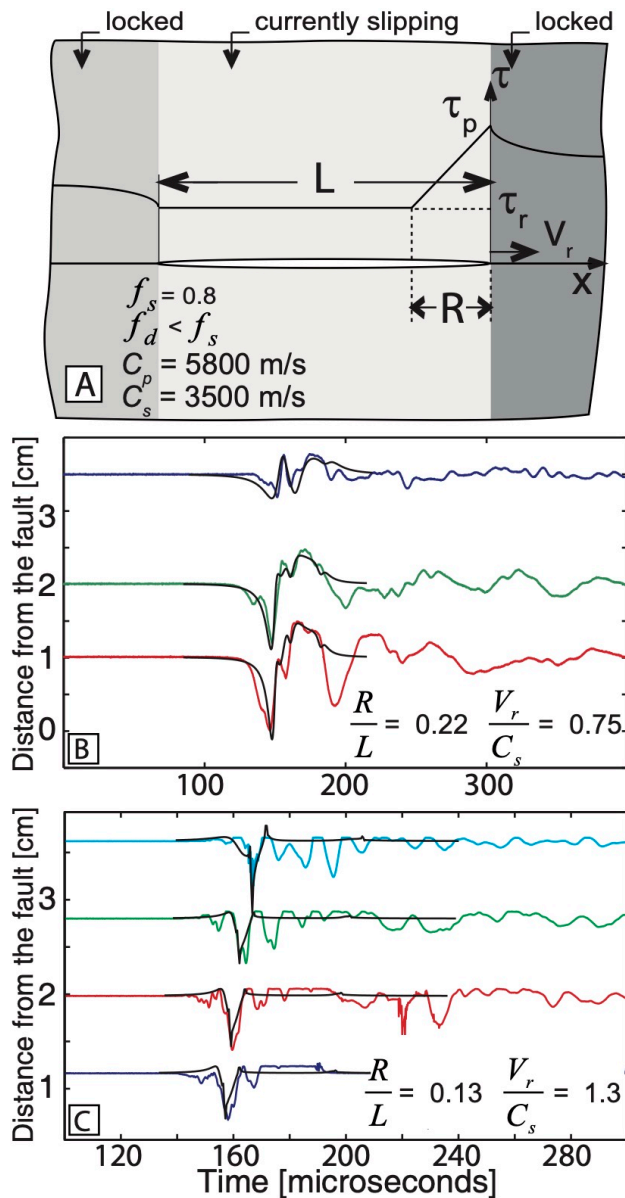


Figure 3.19: Comparison of experimental waveforms with synthetics. (A) Description of the distance weakening rupture model. Comparison of the analytical particle accelerations with the waveforms recorded during a sub-Rayleigh event (B) and during a supershear event (C) The best fit is obtained using the inverted rupture velocity.

can simulate accurately strong ground-motions on the kilometeric scale, can also simulate accelerations in the kHz range on centimetric sized samples. In other words, dynamic rupture propagation is truly a self-similar mechanism.

Our experimental results demonstrate that the ruptures were dominantly Mode-II. For this mode, the transition between sub-Rayleigh and supershear rupture has been extensively discussed in theoretical and experimental studies. We refer back to the chapter on theory. In our experiments, the initial stress on the fault,  $\tau_0$  was continuously measured (Figure 3.17). Taking the static and dynamic friction coefficients equal to  $f_s = 0.85$  and  $f_d = 0.1$  respectively, the seismic ratio,  $S$  could be estimated for each individual stick-slip. In our experiments one can attain supershear speeds if the length of the fault is clearly larger than the supershear transition length. We

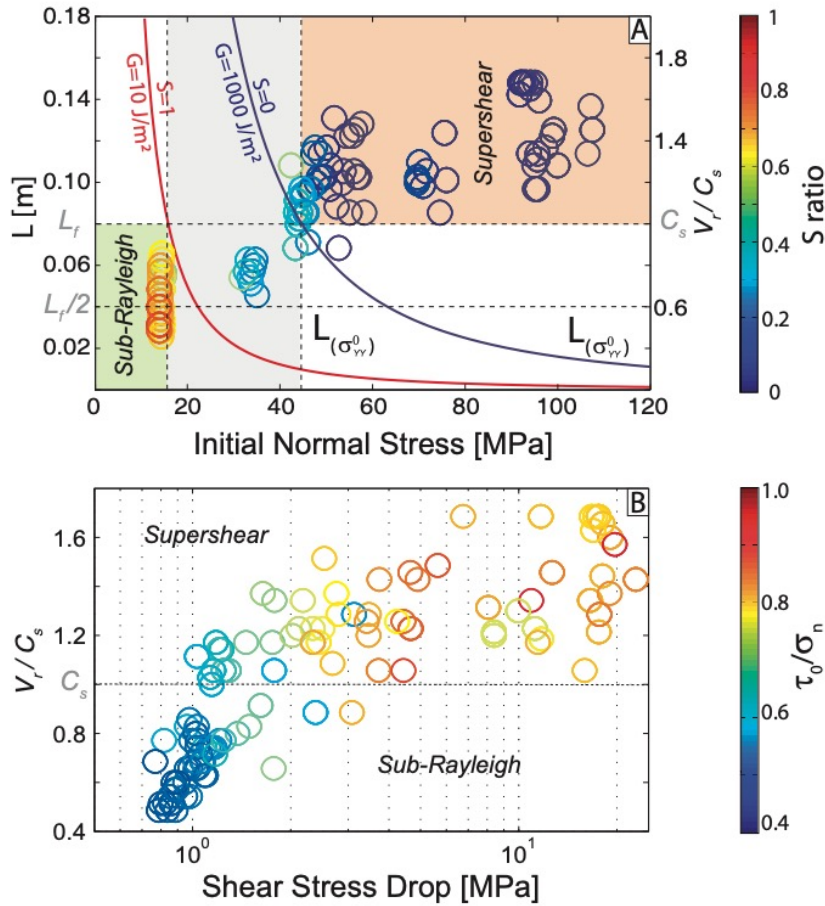


Figure 3.20: The transition to supershear ruptures. (A) Correlation between normal stress and rupture velocity. Color-coding corresponds to the value of  $S$ . Red and blue solid lines represent  $L$  as a function of normal stress assuming two combinations of  $S$  and  $G$ . (B) Correlation between rupture velocity and stress drop. Color-coding corresponds to the value  $\tau_0/\sigma_n$ .

remind the reader that fracture energy  $G$  is needed to compute this length.

In our experiments,  $G$  may range from the lower bound  $10 \text{ J/m}^2$  as given by single crystal fracture energy values and stick slip experiments performed at low normal stress (Ohnaka & Shen, 1999) to the upper bound  $104 \text{ J/m}^2$  measured for intact Westerly granite samples at high confining pressures (Wong, 1982). The transition length was calculated as a function of normal stress in two cases: (i)  $S = 1$  and  $G = 10 \text{ J/m}^2$ , (ii)  $S = 0$  and  $G = 1000 \text{ J/m}^2$  (Figure 3.20A). Experiments performed at the lowest normal stresses are compatible with  $G \approx 10 \text{ J/m}^2$ . However, experiments performed at intermediate normal stresses can only be explained using larger fracture energy ( $G = 1000 \text{ J/m}^2$ ). This is consistent with our observation of an intense production of fine gouge particles at intermediate and high normal stresses. Indeed, for spherical particles, the ratio between fracture energy  $G$  and surface energy of single crystals  $\gamma$  is  $G/\gamma \approx 3w/d$ , where  $w$  is the fault thickness and  $d$  is the average particle size. Our observation of gouge particles of  $1 \mu\text{m}$  diameter and smaller is consistent with a fault roughness of less than  $30 \mu\text{m}$ . The match between the measured rupture velocities and the prediction that the minimum transition length drops to a few centimeters (comparable to our sample size) at high normal stress, explains why in our experiments supershear rupture becomes a ‘normal’

phenomena for  $\sigma_n > 60 \text{ MPa}$ . It also explains why supershear was not observed in previous experimental studies on rocks conducted at low normal stress (most often in biaxial conditions) (Ohnaka & Shen, 1999; Okubo & Dieterich, 1984).

Finally, we observe a double correlation between the rupture velocity, the initial stress ratio  $\tau_0/\sigma_n$  and the final stress drop (Figure 3.20B). Subshear ruptures occurred for stress ratios  $\tau_0/\sigma_n < 0.6$  and resulted in stress drops generally lower than 1.5 MPa. Conversely, supershear ruptures occurred for stress ratios  $\tau_0/\sigma_n > 0.7$  and resulted in stress drops generally larger than 3 MPa. This not only makes sense physically but is also compatible with values previously observed on brittle polymers (Ben-David et al., 2010) and also with field observations for the Kunlun earthquake (Robinson et al., 2006a). Importantly, this is comparable to the average stress drops inferred by seismologists for most large crustal earthquakes.

Based on our experimental results, why then is there a paucity of supershear ruptures observed in nature? A first straightforward explanation is related to the difference in fault geometry between our experiments and seismogenic faults. Our experiments consisted of a perfectly planar fault geometry with very low initial roughness at high normal stress, leading to uniform and large stresses on the fault plane. Seismogenic faults, on the other hand, are most often non-planar and exhibit self-affine roughness (Candela et al., 2012). The occurrence of kinks and dilatational jogs could slow down or even arrest locally the propagation of seismic ruptures (Sibson, 1985). Indeed the few documented examples of supershear earthquakes are on very smooth, planar fault sections. In addition, the presence of a gouge layer along the fault interface may slow-down the propagation of the rupture, as well as thermo-hydro-mechanical coseismic processes within the breakdown zone — thermal pressurization, frictional melting, mineral reactions, off fault damage including pulverization — which dissipate part of the released strain energy available resulting in a deceleration of the rupture front. Alternatively, the paucity of supershear rupture observation in nature might also simply be due to limitations in instrumentation and/or spatial coverage. Nevertheless, the experimental values of transition length and stress drops reported here for a classical crustal lithology (Western granite) under upper crustal stress conditions ( $< 150 \text{ MPa}$ ) demonstrate that rupture velocity may exhibit important variations at the scale of small (centimetric) asperities, so that the seismological estimate of rupture velocities over long fault segments is an average that could well have little importance at the scale of an asperity. Our experimental results strongly suggest that, despite the scarcity of compelling measurements on natural earthquakes, supershear ruptures may frequently occur at the local scale of asperities for which the stress drop generally inferred is quite large. In turn, these sudden accelerations/decelerations of the rupture front should play an important role in generating high frequency radiation which will influence the total rupture energy budget.

# 4

## OBSERVATIONS

### 4.1 Ground Motion

#### 4.1.1 The 2002 $M_w$ 7.9 Denali Earthquake

The nature of near fault ground motion associated with a large strike-slip earthquake is of great interest to earthquake engineers and to earth scientists alike because there are few observations with which to constrain either empirical or theoretical models (Ellsworth et al., 2004a). The 2002 ( $M_w$ 7.9) Denali fault earthquake provided a unique ground motion record close to the source, at Pump Station 10 about 3 km away from the fault. Another unique feature was that this station recorded the passage of a supershear earthquake rupture (earthquake whose rupture speed exceeds the shear wave speed of the surrounding solid (Rosakis, 2002; Rosakis et al., 2007)) providing the only reliable near-source record of such an event. Supershear ruptures are expected to be more destructive since they manifest shear shock wave fronts (Mello et al., 2010; Rosakis, 2002). As a consequence the ground motion associated with supershear ruptures does not attenuate, with distance, as fast as that associated with sub-shear ruptures, sub-Rayleigh in 2D, (Das, 2007; Dunham & Archuleta, 2005; Dunham & Bhat, 2008; Mello et al., 2010; Rosakis, 2002; Rosakis et al., 2007). This doubly important nature of the 2002 Denali event recorded at Pump Station 10 has motivated the present study whose purpose was to recreate such a record in the laboratory earthquake setup (Mello et al., 2010; Rosakis et al., 2007; Xia et al., 2004), using carefully constructed scaling arguments. This opens up the potential to routinely generate near-source strong ground motion records in a controlled laboratory earthquake setting. In addition to its scientific value, this study has an important implication for the response and integrity of buildings near a major fault. For example, the probability of a major earthquake occurring on the southern San Andreas fault in the next 30 years is considered high, and its effect will be felt by large population centers in southern California (Field et al., 2009). This study provides a solid physical framework for generating realistic near-field ground motions.

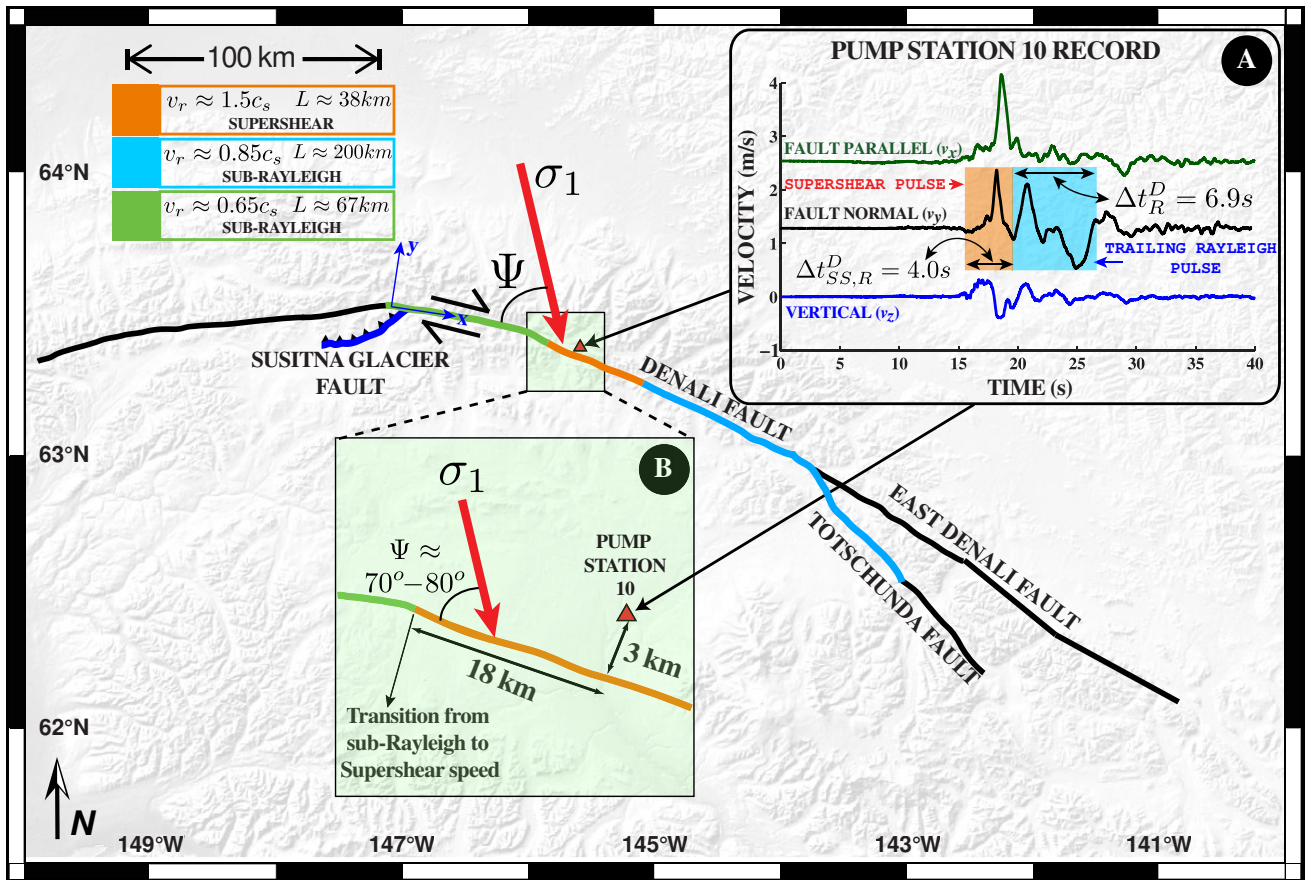


Figure 4.1: 2002  $M_w$  7.9 Denali Fault Earthquake surface rupture trace annotated with the kinematic inversion results from (Ellsworth et al., 2004a). Inset A shows the Pump Station 10 particle velocity records from (Ellsworth et al., 2004a) and Inset B shows the region of interest for this work.

The 2002 ( $M_w$  7.9) Denali fault earthquake was the largest strike-slip rupture to take place on the North American continent in over 150 years and was comparable in magnitude, if not rupture length, only to the 1906 ( $M_w$  7.8) San Francisco earthquake and the 1857 ( $M_w$  7.9) Fort Tejon earthquake. Its total rupture length of 334 km, average slip of 4.9 m, and maximum slip of 8.8 m, ranks it amongst the largest shallow-crust earthquakes recorded anywhere in the world throughout the past two centuries (Bouchon et al., 2010; Haeussler et al., 2004). Due to its remote location within south-central Alaska, there was very little damage to modern infrastructure and fortunately no loss of human life. Field evidence and ground motion data from this event have, however, provided seismologists with a rare and extraordinary opportunity to study a large, shallow crust, strike-slip earthquake, which is in many ways analogous to the major earthquakes which are known to occur along the San Andreas fault (Haeussler et al., 2004).

The Denali earthquake rupture initiated along a 40 km-long segment of the previously unknown Susitna Glacier thrust fault (Figure 4.1). The rupture then transferred to the Denali strike-slip fault system and propagated 218 km from west to east along the central Denali fault. The rupture eventually branched off the Denali fault and stepped over onto the Totschunda fault where it propagated for an additional 76 km before finally arresting (Haeussler et al., 2004).

The central Denali fault ruptured beneath the Trans-Alaska pipeline (TAP), which crosses the fault, and is located approximately 85 km east of the earthquake epicenter. Close to the TAP-Denali fault crossing a set of “celebrated” near-source ground motion records were obtained at Pump Station 10 (PS10) which is positioned at 63.424 N, 145.763 W along the TAP and is located just 3 km north of the fault. The accelerometer recording station at PS10 is part of the accelerograph network operated by the Alyeska Pipeline Service Company. Ellsworth et al. (2004a,b) conducted a thorough analysis and calibration of the PS10 instrumentation and re-processed the signals in order to recover the long-period ( $> 10$  s) ground motions. A set of instrument-corrected acceleration, velocity, and displacement time records were obtained and properly rotated into the fault normal ( $v_y$ ) and parallel ( $v_x$ ) directions. The fault parallel, fault normal, and vertical ( $v_z$ ) velocity records are depicted in Figure 4.1A.

Forward modeling of the instrument corrected ground motion records led Ellsworth et al. (2004a,b) to conclude that a supershear burst occurred along a 38 km segment of the fault, which was nearly centered about PS10. The ground motion records were best matched by their kinematic model if a normalized sub-Rayleigh rupture speed of  $v_r/c_s = 0.65$  was assumed over a 67 km stretch between the epicenter and the point of supershear transition. It also predicted that the normalized rupture speed jumped to  $v_r/c_s = 1.5$  beyond supershear transition and propagated for a distance of 38 km. This was followed by a decrease to a normalized sub-Rayleigh rupture speed of  $v_r/c_s = 0.85$  for points beyond the terminus of the supershear interval (i.e., distances  $> 20$  km east of PS10. See Figure 4.1). The synthetic records do a reasonable job in capturing the general profile of the leading portions of the FP, FN, and vertical (UP) records although the synthetic vertical curves tend to over-predict the peak vertical ground velocity. The biggest shortcoming of the kinematic model was its inability to capture the prominent secondary pulse in the FN ground motion record which is shaded in blue in Figure 4.1. Nevertheless, the careful processing of the instrument-corrected PS10 data and the interpretation of these remarkable ground motion records represent a major seismological finding and the most direct field evidence ever gathered for the existence of a supershear earthquake rupture. The existence of supershear ruptures was conclusively demonstrated in a physical setting in the laboratory earthquake experiments of Rosakis and his co-workers (Rosakis, 2002; Rosakis et al., 2007; Xia et al., 2004) but the Pump Station 10 observations provide one of the most reliable field evidence to their occurrence in the earth’s crust.

The numerical investigations of Dunham and Archuleta (Dunham & Archuleta, 2004) noted specific features in the PS10 ground motion records, which they identified as characteristic ground motion signatures of a supershear earthquake rupture. The first unique feature of note involves the existence of a fault parallel (FP) velocity pulse which is approximately  $1.5\times$  greater in magnitude than the corresponding fault normal (FN) velocity pulse. The second unique feature is the existence of pronounced velocity swings following the main rupture pulse in the FN record, which (Ellsworth

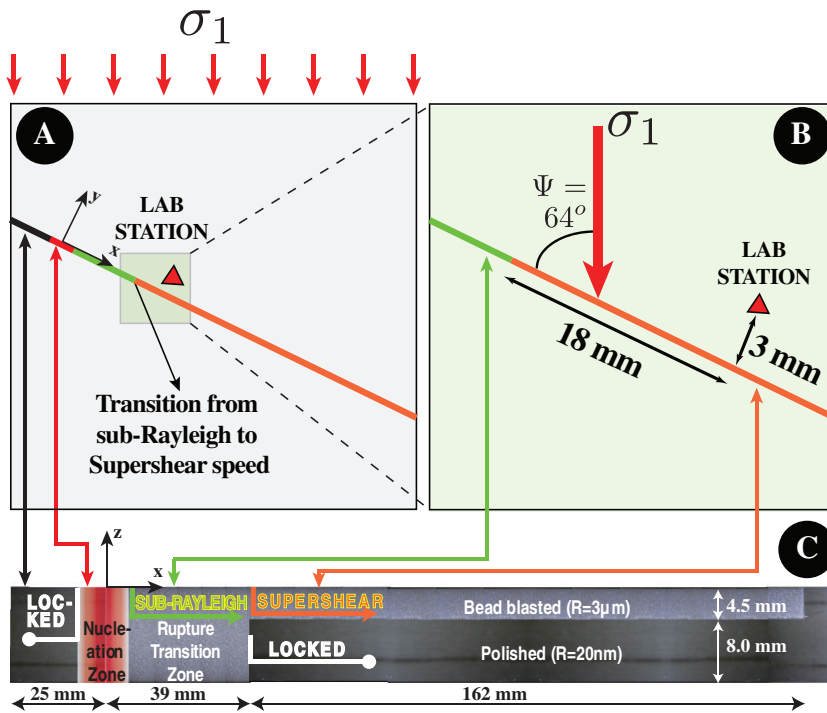


Figure 4.2: (A) Schematic of the 3D Laboratory specimen hosting a dynamic earthquake rupture along a fault. (B) The region of interest around laboratory station,  $(x^L, y^L)$ , corresponding to the region depicted in Figure 4.1B. (C) Mosaic image of the fault surface depicting the 3D fault geometry. The vertical scale is exaggerated.  $R$  corresponds to a root mean squared roughness measure of the bead blasted and polished regions.

et al., 2004a) was unable to replicate using a simple kinematic model. (Dunham & Archuleta, 2004) reasoned that the secondary pulses in the FN record resulted from rupture acceleration during the supershear transition and the release of Rayleigh waves during this phase which combine to produce a secondary slip-pulse. This pulse trails the primary supershear rupture and propagates at around the Rayleigh wave speed. We will henceforth call this secondary pulse the ‘Trailing Rayleigh Pulse’. Both these unique features were confirmed by them using a spontaneous dynamic rupture propagation model which incorporated a slip weakening friction law with a built-in healing mechanism (Nielsen & Carlson, 2000).

Motivated by the success of the dynamic simulations and the physically based interpretation of the secondary slip-pulse, an attempt was made to replicate the most striking features of the PS10 records using the laboratory earthquake arrangement (Mello et al., 2010; Rosakis et al., 2007; Xia et al., 2004). The region of interest that will be modeled experimentally is shown in Figure 4.1B. This is an ideal setting because, unlike spontaneous dynamic rupture models, the governing friction law of the interface is naturally ‘built-in’ and has been shown to have similar features as those for crustal rocks (Lu, 2009; Rosakis et al., 2007).

### Laboratory Earthquake Setup

Laboratory earthquake experiments were conducted using  $200 \times 200 \times 12.5$  mm (nominal thickness) Homalite-100 specimen assemblies featuring a 3D fault geometry and a fault oriented at  $\Psi = 64^\circ$  with respect to the direction of the compressive principal stress (Figure 4.2A,B). Figure 4.2C

shows specific details of the new 3D specimen fault geometry. This geometry is a 3D extension of the 2D geometry used in past laboratory earthquake studies (Rosakis et al., 2007; Xia et al., 2004). The fault segment to the left of the nucleation site corresponds to a  $25\text{ mm} \times 12.5\text{ mm}$  interface formed by two polished surfaces. The intent is to inhibit rupture propagation to the left through contact bonding of the flat polished surfaces of a short fault segment under the applied static compressive load. The  $39\text{ mm}$  roughened-fault-segment to the right of the polished section provides lower frictional resistance than the polished section and is referred to as the nucleation and rupture transition zone. A NiCr filament channel is milled within  $0.5\text{ mm}$  of the boundary between the short polished segment and the nucleation patch on the roughened side of the boundary. A sudden discharge of current through the wire, fluidizes it resulting in a local reduction of normal stress which leads to the nucleation and propagation of an unstable dynamic rupture (Rosakis et al., 2007; Xia et al., 2004). The coordinates  $(L_T, 0) = (39, 0)\text{ mm}$  correspond to a point on the surface of the specimen, at the end of the nucleation patch, where the roughened portion of the fault is abruptly reduced in width from  $12.5\text{ mm}$  to  $4.5\text{ mm}$  as depicted in Figure 4.2C. At the transition location,  $(L_T, 0)$ , a stress concentration develops, under applied load. This stress perturbation allows a sub-Rayleigh rupture to accelerate to supershear speed (Dunham et al., 2003; Liu & Lapusta, 2008). The polished part of the fault, situated below the roughened part, (width of  $8\text{ mm}$ ) has a higher frictional resistance and is expected to adhere under an applied static compressive load. The roughened frictional part (top) is meant to mimic the brittle upper crust where earthquakes are typically hosted. The polished bottom part represents the ductile part of the crust which remains essentially locked during an earthquake rupture.

A reflective tape strip used to enable the particle velocity measurements (Lu et al., 2007; Mello et al., 2010) was positioned with its lower-right corner at the scaled PS10 location  $(x^L, y^L)$ . The laboratory station coordinates, denoted by the superscript  $L$ , will be determined in the next section. The results from several experiments conducted in advance were also used to estimate that a critical load  $\sigma_1 > 30\text{ MPa}$  is required to trigger a supershear rupture at the desired location ( $x = L_T$ ).

The scaled PS10 supershear experiment was conducted under a static compressive load of  $\sigma_1 = 31\text{ MPa}$ . Three laser interferometer probe beams were focused on the measurement station at  $(x^L, y^L)$  in order to simultaneously monitor the fault parallel ( $v_x$ ), fault normal ( $v_y$ ), and vertical ( $v_z$ ) particle velocity components at this location. Synchronized, high-speed photoelastic images (where the fringes correspond to contours of maximum shear stress change in the medium), obtained every few microseconds, were simultaneously acquired in order to obtain a spatially resolved, full field view of the dynamic event (Mello et al., 2010; Xia et al., 2004).

### Development of a Scaling Relationship

To develop a reasonable scaling argument to reproduce the PS10 record we address the following three questions. One, what is the appropriate temporal scaling that will translate the laboratory station record (few 10's of micro-seconds in duration) to the PS10 records (few 10's of seconds in duration). Two, what is the corresponding location of the laboratory station that would ideally represent the spatial location of PS10 with respect to the Denali fault. Three, what is the appropriate amplitude scaling that would match at least the peak particle velocities of PS10 with the laboratory station. We refer the reader to the chapter on Theory for the mathematical development of the scaling relationship.

Once the observation station is set and experimental records are obtained they are then subjected to temporal scaling using the relation,  $t^{scaled} = t^L \times S_T$ . The spatial scaling and geometric constraint used to design the experiment automatically ensures that the arrival times of the supershear and trailing sub-Rayleigh ruptures in the scaled laboratory record will coincide with the arrival times of the equivalent features in the actual PS10 ground motion record.

As a final step, the particle velocity magnitudes are scaled by the peak to peak swing in the trailing Rayleigh pulse part of the record. Based on the steady-state slip-pulse models of (Dunham & Archuleta, 2005; Rice et al., 2005; Samudrala et al., 2002b) the proper non dimensionalized representation of the velocity field in a medium hosting a slip pulse of length  $L$  with a process zone of size  $R$  is given by

$$\mathbf{v} \left( \frac{x}{L}, \frac{y}{L} \right) = \hat{v}_o \mathbf{F} \left( \frac{x}{L}, \frac{y}{L}, \frac{R}{L}, \frac{v_r}{c_s} \right) \quad (4.1)$$

$$\text{where } \hat{v}_o = c_s \frac{(\tau_p - \tau_r)}{\mu}$$

where  $\mu$  is the shear modulus,  $\tau_p - \tau_r$  is the strength drop,  $c_s$  is the shear wave speed and  $\mathbf{v}$  is the in-plane particle velocity vector. This universal feature applies to all elastodynamic rupture models. For a class of models utilizing slip/distance weakening (Dunham & Archuleta, 2005; Rice et al., 2005) and velocity weakening (Samudrala et al., 2002b) the actual functional form of  $\mathbf{F}$  can be obtained analytically. A typical value for the shear modulus of crustal rock is 30 *GPa*, while the corresponding value for H-100 is 1.96 *GPa*. At mid-seismogenic depths (around 7 *km*) the normal stress  $\sigma$  is estimated to be of the order of 100 *MPa*. If a Coulomb-like friction relation is assumed ( $\tau = f\sigma$ , where  $f$  is the friction coefficient and  $\sigma$  is the normal stress), then assuming  $f_p = 0.6$  and  $f_r = 0.2$ , a strength drop on the order of 40 *MPa* is obtained for crustal rock. Assuming  $c_s$  for crustal rocks is 3.5 *km/s* the value of the velocity amplitude,  $\hat{v}_o$ , for rock is 4.67. A typical strength drop in laboratory earthquake experiments is about 7 *MPa* (assuming a principal stress magnitude of 31 *MPa*), giving a value of  $\hat{v}_o$  close to 4.57, while reasonably assuming  $R/L$  and  $v_r/c_s$  are similar for rupture in Homalite-100 and crustal rock. It stands to reason therefore, that the particle velocity records obtained in laboratory earthquake experiments

should be comparable to the magnitude of ground motion velocities measured in natural earthquakes and thus can be adjusted moderately to match the PS10 record. As stated earlier the actual adjustment is done by using the peak to peak swing of the trailing Rayleigh pulse part of the record.

### Experimental Results

The photoelastic image sequence in Figure 4.3 provides a spatially-resolved, frame-by-frame view of the scaled PS10 supershear experiment. The stationary dark, circular caustic zone at  $(39, 0)$  mm, indicated in Figures 4.3A and 4.3C-4.3E, corresponds to the stress concentration at the boundary between the roughened and polished (locked) fault segments. The long cylindrical shadow seen in each of the image frames was produced by the side exit probe, which was used to direct the vertical laser interferometer probe beam to the measurement station at  $(57, 3)$  mm. Figures 4.3A, B depict the sub-Rayleigh rupture as it encountered the boundary of the locked fault segment. The increased diameter of the caustic zone at  $(39, 0)$  mm reveals a stress build-up which occurred as the advancing sub-Rayleigh rupture field was superimposed upon the pre-existing static stress field at the boundary of the locked fault segment. A supershear transition was triggered by the locked fault segment, which acted as a high-strength barrier, or, alternatively, as a patch of higher pre-stress (Dunham et al., 2003). The observed supershear transition in the scaled PS10 experiment is notably different than the classical Burridge-Andrews (Rosakis, 2002; Rosakis et al., 2007) type transition mechanism since this transition is artificially induced. Well-formed shear Mach/Shock fronts are clearly visible in Figures 4.3D, E. The appearance of two shear Mach fronts indicates regions of high gradients in slip velocity traveling with the rupture tip. For a perfect slip pulse these two regions correspond to the leading and the healing edges of the slip pulse. The image frames also capture the trailing Rayleigh pulse, TR, rupture as it sweeps across the off-fault station at  $(57, 3)$  mm. The location of TR is indicated in Figures 4.3C-E.

The particle velocity records obtained from this experiment are shown in Figure 4.3F and Figure 4.4. The leading portions of all three of the particle velocity records are dominated by the fault parallel record, as expected to be generated by a supershear rupture front propagating at a speed in excess of  $\sqrt{2}c_s$  (Mello et al., 2010; Rosakis, 2002). Also, the fault parallel component features a pronounced double peak at about  $50 \mu s$ . The first velocity peak is attributed to the leading dilatational field lobe, which encircles the supershear rupture tip (Mello et al., 2010). The second velocity peak which follows immediately is accurately correlated to the arrival of the shear Mach front. The fault parallel signal eventually reaches a steady sliding value of around  $2 m/s$  resulting in a crack-like rupture unlike the Denali event. The fault normal signal also features a strong trailing Rayleigh pulse, shaded in blue in Figure 4.3F, which follows immediately after the passage of the shear mach cone peak. The arrival of this strong pulse is very well correlated with the visual evidence of the arrival of the trailing Rayleigh pulse fringe concentration at the measuring station (Figures 4.3D, E).

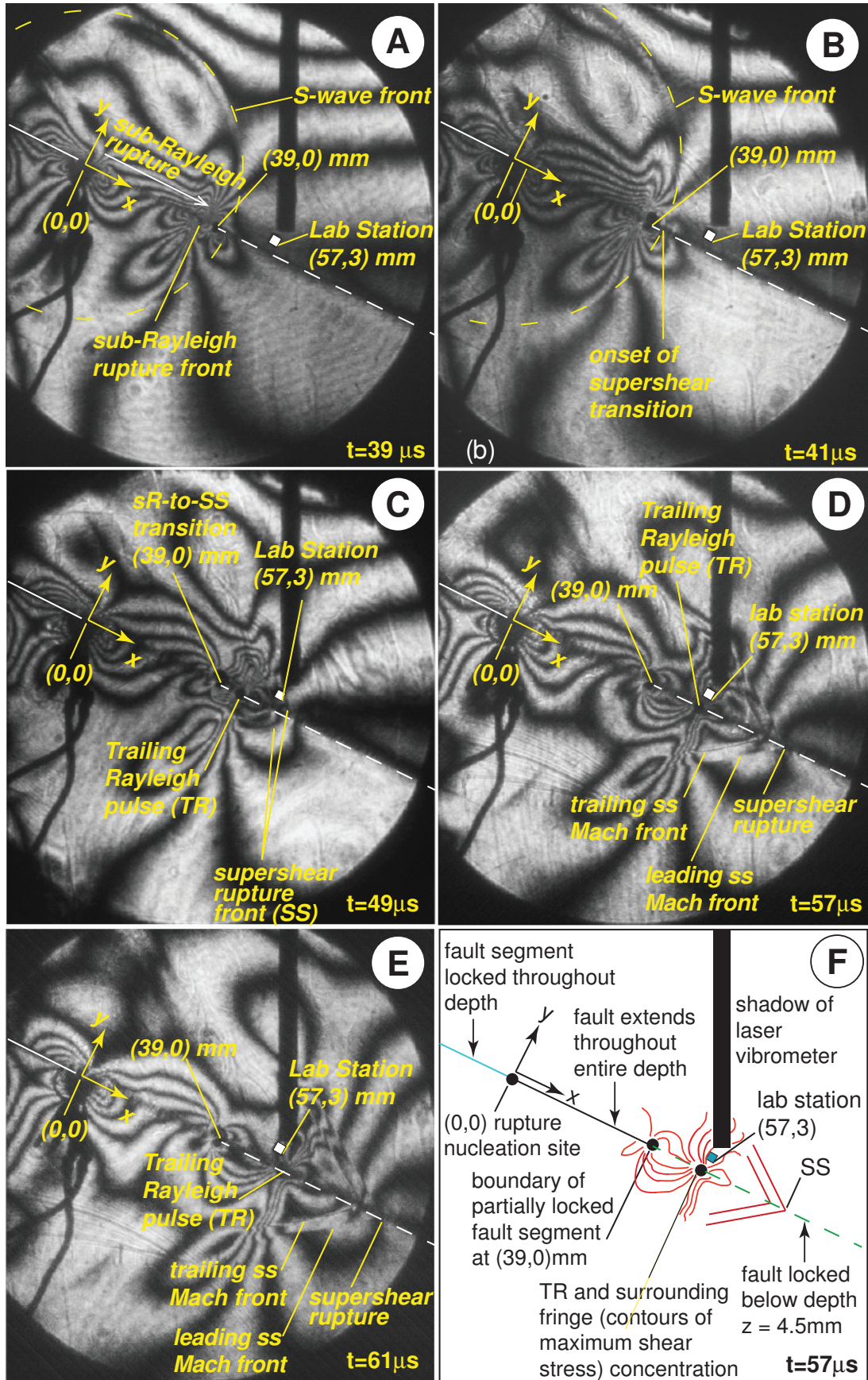


Figure 4.3: (A)-(E) Photoelastic images acquired at various stages of the experiment. (F) Schematic explanation of the Photoelastic images. SS stands for Supershear and TR for Trailing Rayleigh. The fringes in the photo elastic images correspond to contours of maximum shear stress induced by the propagating rupture.

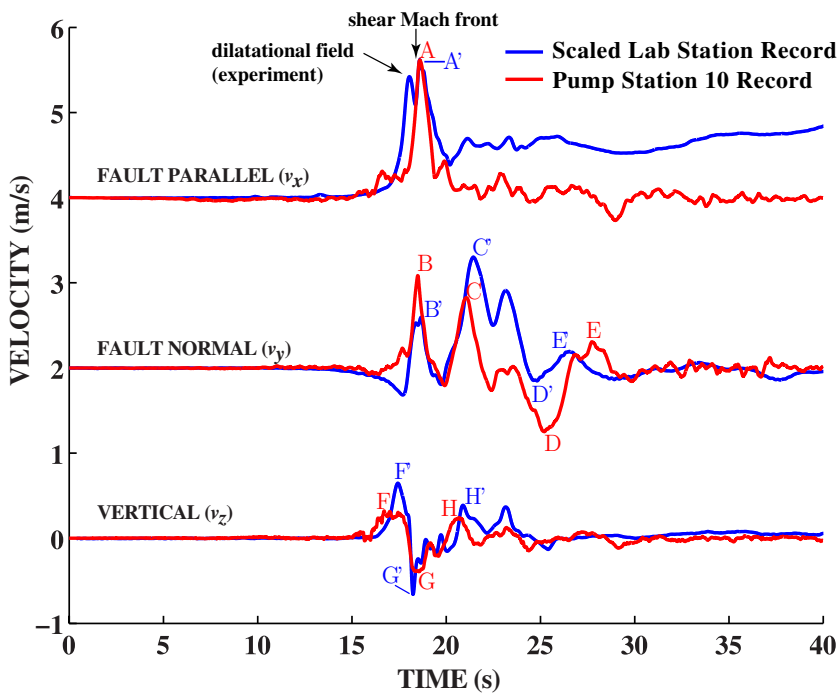


Figure 4.4: Scaled Laboratory Station records compared with the Denali Pump Station 10 record.

Figure 4.4 shows the comparison between the scaled laboratory ground motion records, using the scaling arguments developed earlier, and the actual Denali PS10 ground motion records. Each point labeled ( $A'$  -  $H'$ ) in the laboratory particle velocity records has a corresponding point ( $A$  -  $H$ ) in the PS10 ground motion records and vice versa. Apart from the fact that the experimental record is crack-like, the scaled records match up remarkably well with the PS10 ground motion records and capture all of the prominent signatures. The other remarkable observation is the consistency in the polarity of the laboratory velocity records when compared with the PS10 records. The dominance of the fault parallel component over the fault normal component ( $A$  vs.  $B$ ) and ( $A'$  vs.  $B'$ ) is observed in the early portion of the experimental records although the exact level of  $1.5\times$  ratio exhibited by the PS10 records was not captured by the experimental records. Note that the PS10 fault parallel record does not exhibit a dilatational field peak prior to the arrival of the shear Mach front. This could be attributed to the fact that the lab experiment is still largely 2D-like in that there is no significant spatial variation of the rupture through depth. This point is bolstered by the results of the dynamic 3D calculations by (Dunham & Archuleta, 2004) which do not distinguish between the leading dilatational field and the shear Mach front. The experimental fault normal record also exhibits some striking similarities with the corresponding PS10 record between the points labeled  $C' \rightarrow D' \rightarrow E'$  in the laboratory FN record and the corresponding velocity swings spanning from  $C \rightarrow D \rightarrow E$  in the PS10 FN ground motion record. The magnitude of the relative velocity swings between  $C' \rightarrow D'$  and  $C \rightarrow D$  were forced to match as part of the scaling process. This then established the amplitude scaling which was applied to the fault parallel and vertical records. As noted by (Dunham & Archuleta, 2004) the almost antisymmetric nature of this part of the record at PS10 re-

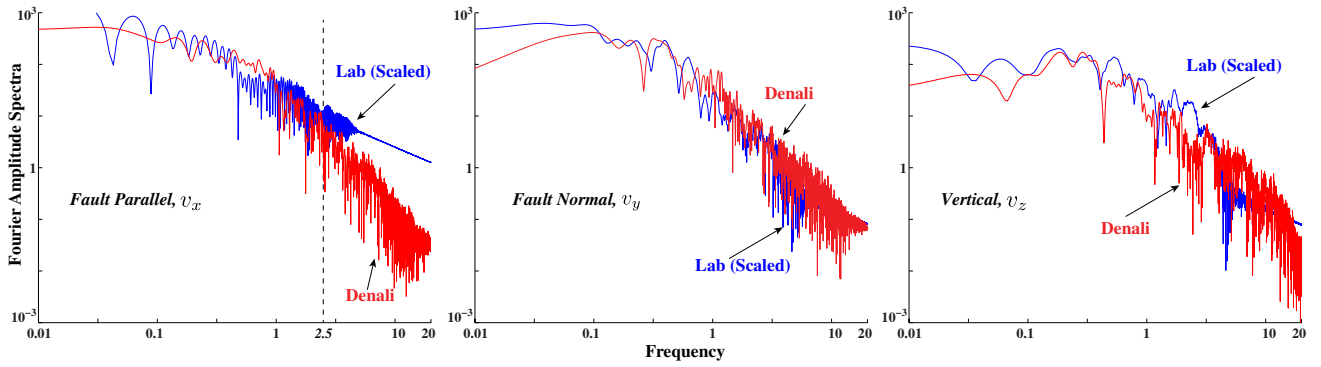


Figure 4.5: Fourier Amplitude Spectra (FAS) of the Denali Pump Station 10 record and Scaled Laboratory particle velocities

veals that the trailing Rayleigh disturbance was pulse-like. However, since a crack-like rupture resulted in the experiment, the trailing Rayleigh disturbance failed to completely heal and hence the record is not purely anti-symmetric. Nevertheless, the result captures the same general features and sense of motion observed in the corresponding portion of the PS10 fault normal ground motion record, and provides strong experimental confirmation that this portion of the PS10 record was indeed attributed to the passage of a trailing Rayleigh pulse. There is also a very nice match between the vertical record obtained in the laboratory earthquake spanning between the points  $F' \rightarrow H'$  and the PS10 ground motion record spanning the interval defined by between the points labeled  $F \rightarrow H$ .

Bizzarri et al. (2010) noted that there was no elevation of the 5% damped response spectral accelerations in the period band 0.05 - 0.4 s compared to the spectral acceleration observed at non-Mach pulse stations for earthquakes that went supershear (except for a small subset of Imperial Valley stations). To check if this is observed in the laboratory experiments we also calculate the Fourier amplitude spectra (FAS) of the velocity amplitude for both the Denali Pump Station 10 record and Scaled Laboratory particle velocities record. To make proper comparison between the PS10 and the scaled laboratory velocity records we first resampled the scaled laboratory record at the PS10 sampling rate (100 Hz) and then applied half-cosine taper to the last 10% of the signal. The results (frequency range between 0.01 and 20 Hz) are shown in Figure 4.5. First of all we note that the fault normal (FN) spectra are remarkably similar as expected because of similar rise times of the significant pulses ( $B, C, D$ ) in the PS10 record and the scaled record ( $B', C', D'$ ). The modest difference in the vertical (V) record is mainly due to the fact that the significant pulses in the lab record ( $F', G', H'$ ) have sharper peaks than their counterparts in the PS10 record ( $F, G, H$ ).

The biggest difference is seen in the fault parallel (FP) record around 2.5 Hz, and beyond, as noted by Bizzarri et al. (2010). The significant difference here is clearly the lack of the precursory dilatational field (part of the velocity field carrying  $\vec{\nabla} \cdot \vec{v}$  like motion) in the PS10 record. We note that this field actually represents the volumetric strain rate (first invariant of the strain rate tensor) i.e.  $\vec{\nabla} \cdot \vec{v} = \dot{\epsilon}_{xx} + \dot{\epsilon}_{yy} + \dot{\epsilon}_{zz}$ . In the supershear

regime even though the dilatational wave field is not being shocked it is approaching conditions close to it and consequently variations in the volumetric strain rate increases quite dramatically. In soils and brittle materials, like rocks, this, possibly dynamic, variations in volumetric strain rates will invariably lead to non-linear response (in soils) or comminution (in rocks). We strongly suspect this is the reason why this dilatational field was never recorded at PS10 and hence the lack of elevation of the 5% damped response spectral accelerations in the period band 0.05 - 0.4 s.

Nevertheless, the fact that scaled dynamic rupture experiments in brittle polymeric surrogates are capable of qualitatively reproducing all the significant features of the PS10 record is simply remarkable. It suggests that at near-source distances the strong singular elastodynamic nature of both the supershear and the trailing Rayleigh pulses swamp the near-source velocity field and the inherent inhomogeneities of the earth's crust do not contribute much to the dominant features of the ground motion.

The laboratory earthquake and the near-fault measurements presented here should thus be viewed as faithful physical analogs to the Denali event and to the resulting PS10 ground motion records. The overall goal was to reproduce the supershear portion of the Denali rupture in a controlled and repeatable laboratory setting to capture the prominent supershear ground motion signatures and to offer a strong physical basis for the design of the experiment and the interpretation of the results. All of this was possible over 6 orders of magnitude of length scale difference between the field and the experiment. Viewed from this perspective, the analog experiments were quite successful in capturing the field reality and have performed better in many respects to the best available forward and direct numerical modeling attempts offered up to this time. The success of this approach establishes controlled, scalable experiments as credible physical analogues to field events and demonstrates their value in routinely investigating near-field ground shaking signatures in the laboratory. The lack of dense enough near-source ground motion records makes their potential value only stronger.

The direct practical consequence of the above observations are that a near field station will first experience the primary fault parallel (FP) shaking due to the arrival of the supershear rupture fields, followed by a primary fault normal (FN) shaking linked to the trailing Rayleigh pulse. Structures located near a fault hosting such a transition will effectively experience two separate, closely timed earthquake events characterized by different forms of ground-shaking (one dominated by the fault parallel component and the other by the fault normal component). The timing between these two occurrences will depend on the location of the near field station relative to the point of sub-Rayleigh-to-supershear transition. Indeed, in the future, we envision the use of such analogue experiments and scaling arguments in providing accurate and scalable ground shaking records to be used as inputs to large scale structural integrity calculations in assessing the seismic hazard of realistic buildings.

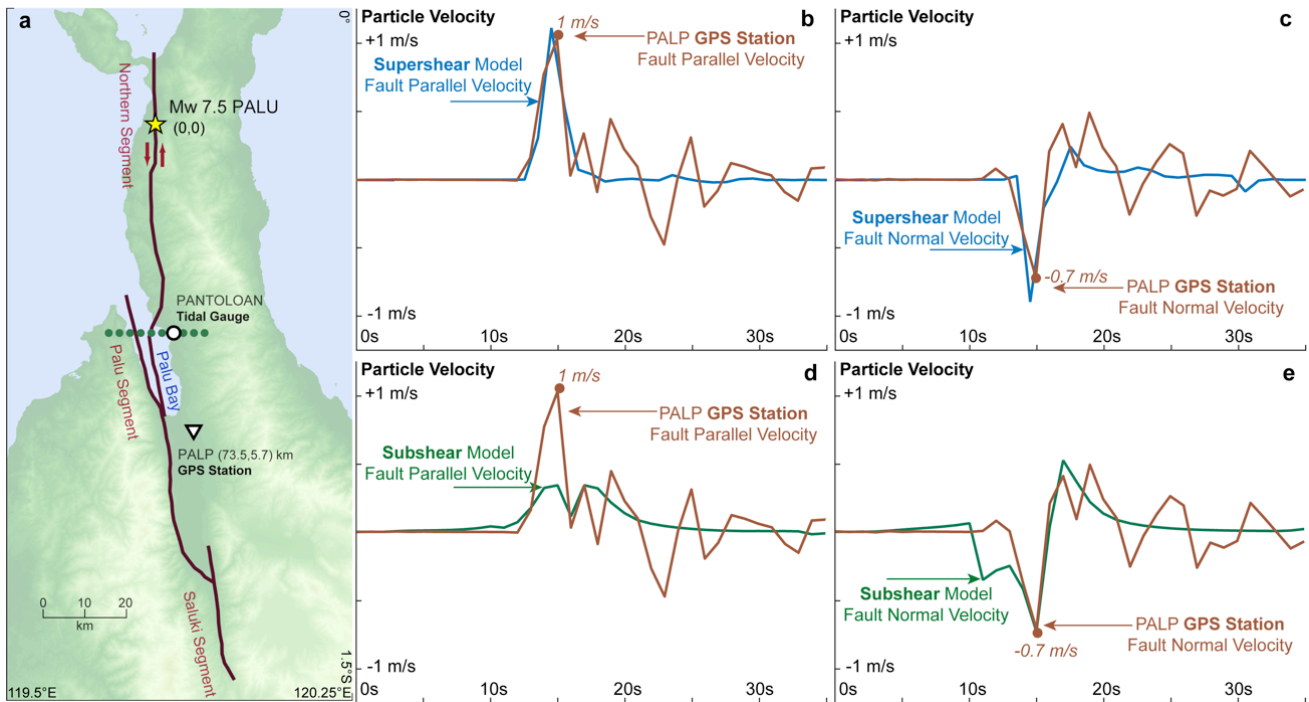


Figure 4.6: **The earthquake rupture and near-field evidence of supershear.** **a**, The Palu-Koro fault system, where the Pantoloan tidal gauge and the PALP GPS station are marked. The green line of dots represents the slice of the bay considered for the tsunami model employed in this study. **b**, Comparison between the fault parallel particle velocities recorded at the PALP station with those generated by the numerical supershear rupture model of Dunham & Bhat (2008). **c**, Comparison between the corresponding fault normal particle velocities. **d,e**, Same as (b,c) but for a subshear rupture.

#### 4.1.2 The 2018 $M_w$ 7.5 Palu Earthquake

The most unmistakable signature of a supershear rupture is that the fault parallel particle velocity dominates over the fault normal velocity (Dunham & Archuleta, 2005; Mello et al., 2014) (when the rupture velocity  $v$  is greater than  $\sqrt{2}c_s$  for a shear wave speed  $c_s$ ). The opposite signature is expected for a subshear rupture. Figure 4.6a shows the Palu-Koro fault system along with the location of the high-rate, 1Hz, PALP GPS station. Figures 4.6b-c show the particle velocities recorded during the Sulawesi earthquake, clearly demonstrating a fault parallel particle velocity greater than the fault normal velocity ( $\sim 1.0\text{m/s}$  versus  $\sim 0.7\text{m/s}$ ). This proves that the rupture, as it passed by the PALP station, definitively went supershear and hence attained a speed between  $\sqrt{2}c_s$  and the P-wave speed,  $c_p$ , of the medium (the absolute limiting speed of the rupture). This represents the first-ever observation of a supershear rupture by a high-rate GPS station. Socquet et al. (2019) and (Bao et al., 2019) have also inferred that this earthquake went supershear, but mainly through far-field observations employing geodetic and teleseismic data, respectively. The only other near-field evidence of a supershear earthquake was obtained using an accelerometer (250Hz) at Pump Station 10 (PS10) during the 2002 Mw 7.9 Denali earthquake (Ellsworth et al., 2004a; Mello et al., 2014).

We can further compare the PALP records against a 3D supershear earthquake simulation (Dunham & Bhat, 2008) whose rupture propagates at a speed of  $v = 1.6c_s$  and whose corresponding particle velocities are computed at 100Hz and then decimated to match the 1Hz sampling rate of the GPS observations (see Methods for details). The synthetic data and the GPS

records are in excellent agreement for the main rupture pulse (Figures 4.6b-c). The subsequent arrivals are not as well-captured since the numerical model does not account for the local velocity structure and the detailed fault geometry. A similar comparison with synthetic velocities computed for a subshear rupture ( $v = 0.8c_s$ ) finds that they are in poor agreement with GPS data (Figures 4.6d-e). This clearly suggests that the supershear rupture speed was  $1.6c_s$  (around 5.3km/s) when it passed by the PALP GPS station (Ulrich et al. (2019) also find a speed greater than  $\sqrt{2}c_s$ ). We have thus provided the first near-field high-rate GPS-based evidence that the Sulawesi earthquake rupture actually did go supershear as claimed.

## 4.2 Far-Field Damage

### 4.2.1 The 2001 $M_w$ 7.8 Kunlun Earthquake

The Kokoxili surface rupture (Figure 4.7) has been studied by a number of workers, Xu et al. (2002), Lin et al. (2002, 2003), Lasserre et al. (2005) and Klinger et al. (2006) among others, and mapped in detail using Ikonos satellite images and supporting fieldwork by Klinger et al. (2005). Particular attention was paid to the slip-partitioned section, which is also discussed by King et al. (2005). Lin et al. (2003), Bouchon & Vallee (2003), Antolik et al. (2004), Tocheport et al. (2006) and Robinson et al. (2006a) did seismological studies of the rupture process associated with the Kokoxili event. The field team noted other interesting features, but unfortunately could not study them in detail so that we do not have careful field documentation. Thus although the observations may be consistent with rupture propagation at supershear speeds the correlation should be treated with caution.

North of the fault, bridge abutments crossing minor drainages on the Kunlun Pass to Golmud road were damaged. Since fragile walls and poorly constructed buildings were undamaged even closer to the fault and such bridges are not normally sensitive to shaking, a likely explanation is that the damage resulted from large ground strains probably in extension. The damage did not appear to be due to compression although, without more careful examination, it cannot be excluded.

South of the fault, on the road between the Kunlun Pass and Kusai Hu, extensive ground cracking occurred (Figure 4.8) oriented at approximately fault parallel as shown in Figure 4.7a. The cracking was not mapped since the cracks were too small to appear on Ikonos images. Direct mapping of a large region would have required an extended period at an altitude of nearly 4000 meters which was not possible. The extent of the region of cracking (shown in Figure 4.7) parallel to the strike of the fault is likely to be correct, but the extent perpendicular to it is simply not determined, and it is only sure that the cracking extended to the horizon on both sides of the road. Whether or not the map is accurate, the cracks were substantial distributed features that did not have the character of primary fault ruptures. The field team did not constrain the orientation of these features relative

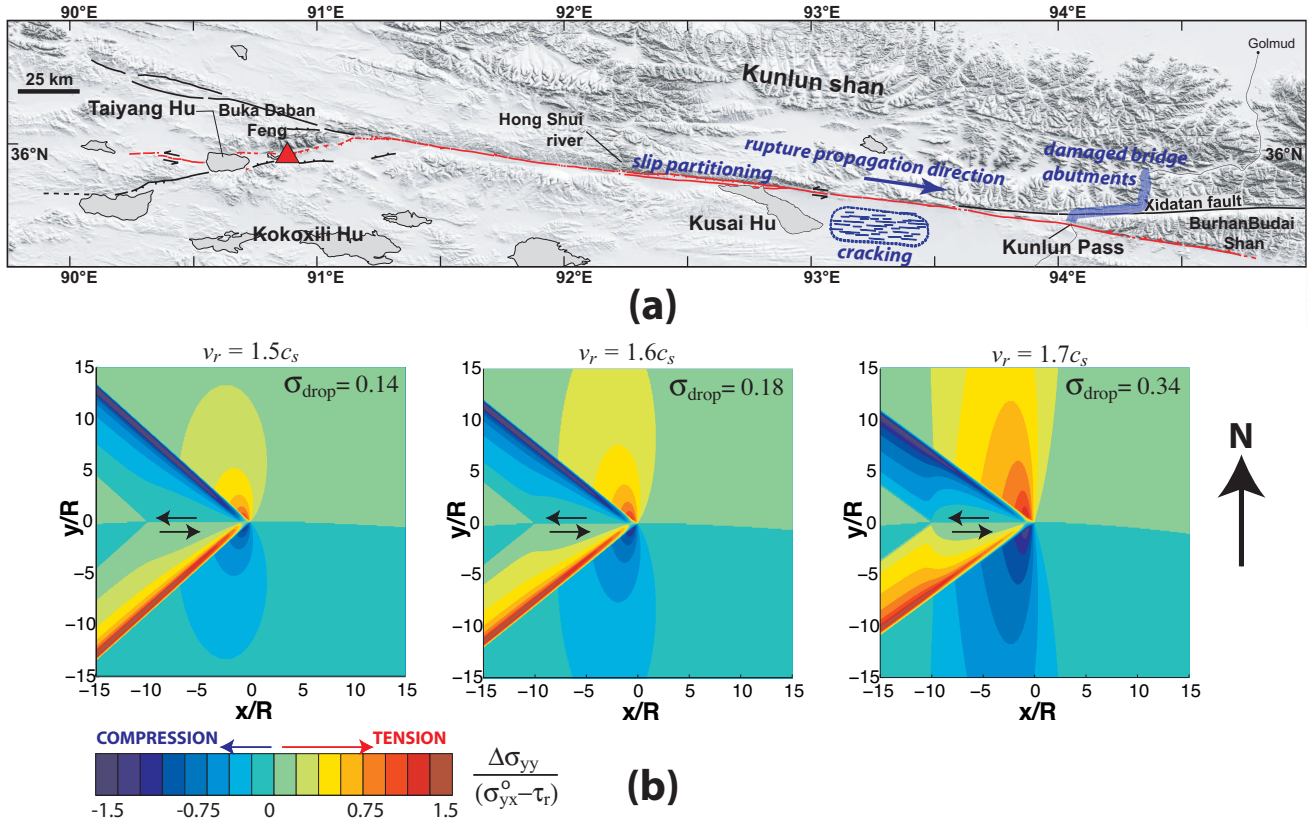


Figure 4.7: (a) Simplified map of the surface rupture (red line) for the 2002 Kokoxili earthquake (adapted from Klinger et al. (2005)). The epicentre is indicated by a red triangle so that rupture propagated mainly to the east. The slip-partitioned section extends from the Hong Shui river to north of the middle of Kusai Hu (lake). Extensive cracking was observed (with approximate crack orientations drawn by authors) from east of the Kusai Hu to about halfway to the Kunlun Pass. North of the pass (where the road to Golmud is outlined in blue) bridge abutments were damaged. The extent of the region of cracking parallel to the strike of the fault is likely to be correct, but the extent perpendicular to it is simply not determined, and it is only sure that the cracking extended to the horizon on both sides of the road. (b) Perturbation in fault normal stress,  $\Delta\sigma_{yy}/(\sigma_{yx}^0 - \tau_r)$  normalized by dynamic stress drop due to a 'left-lateral' supershear slip pulse propagating steadily at various rupture speeds,  $v_r$ . The results are for  $R/L = 0.1$  where  $R$  and  $L$  are the size of the slip weakening zone and the length of the slip pulse respectively and  $\sigma_{drop} = (\sigma_{yx}^0 - \tau_r)/(\tau_p - \tau_r)$ .

to the main Kokoxili rupture trace. However, the road track shown in Figure 4.8 is roughly oriented in the West-North-West direction (the absence of the Kunlunshan mountain range at the horizon of Figure 4.8 supports this conclusion). That means that the cracks are oriented at shallow angles to the main rupture trace. Our estimates of the far-field stresses show that, for a left-lateral supershear rupture as the Kokoxili event, the region where the cracks were observed suffered from large fault normal extensional stress perturbation ( $\Delta\sigma_{yy} \approx 5 - 15$  MPa for a 3 MPa dynamic stress drop, on the pulse, consistent with the average stress drop inferred by Rice et al. (2005) for other large, sub-Rayleigh ruptures) leading to the formation of tensile cracks oriented roughly parallel to the main rupture trace [Figure 4.7b].

Because there is only the limited constraint mentioned of the cracking direction, it is instructive to examine other possibilities. If these extensional features were oriented at some near-perpendicular angle to the main rupture trace then this could mean that the extensional features observed were created by the unloading phase following the traversal of a large compressional loading pulse. For such orientation, it would be possible that the brittle near-surface material (frozen soil sediments) could yield in compaction when the Mach front traversed through the material, and then unloaded as tensile cracks when the compressional strain was removed in the wake of the Mach front. Our estimates of far-field stresses show that at Kunlun rupture speeds the fault parallel stress perturbation ( $\Delta\sigma_{xx}$ ), is compressional and quite large ( $\approx 5 - 15$  MPa) for a 3 MPa dynamic stress drop on the



Figure 4.8: Cracks along the road from Kusai Hai to the Kunlun pass. At this point the road is several kilometers from the fault. The cracks were not mapped and their orientation was not specifically measured, but was close to the orientation shown in Figure 4.7. The cracking is consistent either with extension, or with compression and inelastic yielding followed by tensile failure when the compression was relaxed.

pulse [Figures 2.9 and 4.9]. Thus there is a plausible mechanism for any angle of the tensile cracks with respect to the main fault trace, except for angles in the vicinity of  $\pm 45^\circ$ , in which case the normal stress on these features (whether tensile or compressive) is small in magnitude.

Thus it seems most unlikely that a sub-Rayleigh rupture could have activated the normal fault structure. We thus find that at the rupture speeds for the Kunlun event normal fault activation by positive changes in Coulomb stress on the same is unlikely to happen, and no viable alternative is provided to the hypothesis that the normal faulting resulted from slip-partitioning at depth (King et al., 2005).

The value of  $\Psi$ , the principal stress angle with respect to the fault and bearing in mind that the fault is left-lateral, about 200 km to the east of the Kunlun-Xidatan junction was estimated to be between 30 and 45 degrees from orientations of active faults in the region. It was noted for Denali fault in Alaska, which has similar tectonic features as Kunlun, by Ratchkovski (2003), that the orientation of the maximum principal stress rotated about the normal to the strike as one traversed along the strike of the fault. This might be the case with Kokoxili but no similar stress direction estimate exists for the region to the east as of now. The orientation of the cracks and the existence of both normal and strike-slip structures gives us an additional constraint on  $\Psi$ . Firstly, if the cracks were created by the unloading phase following the traversal of a large compressional loading pulse then the orientation of the cracks might give us some constraint on the direction of the maximum in-plane compressive stress,  $\Psi$ . The average orientation of the cracks seem to be between 50 and 55 degrees (no precise measurements were made in the field) with respect to the fault and these features are expected to form perpendicular to the maximum in-plane compressive stress direction, provided that the stress perturbation added to that compression. This suggests that  $\Psi$  should be roughly between 35 and 40 degrees. The simultaneous existence of normal and strike-slip faulting, if interpreted (too

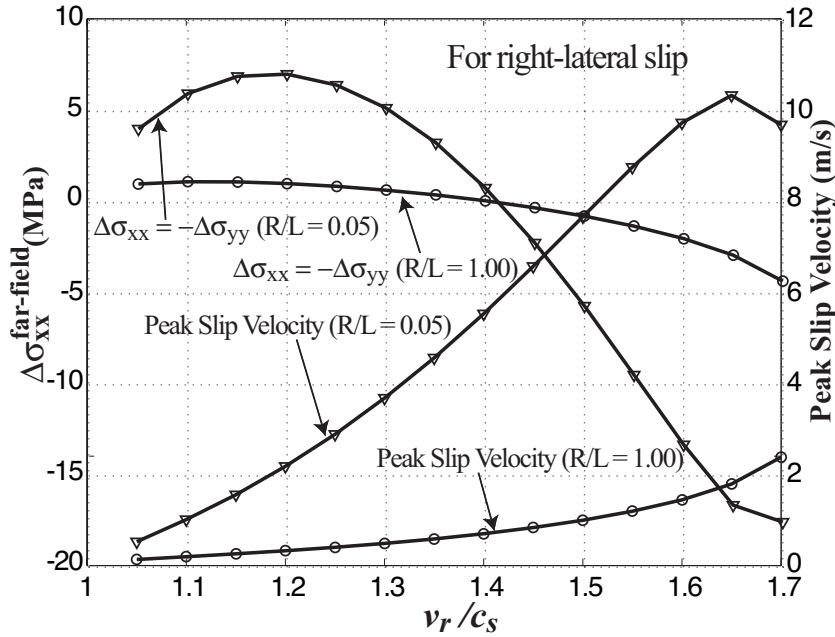


Figure 4.9: Far field perturbation in fault parallel stress,  $\Delta\sigma_{xx}$  as a function of rupture velocity calculated using the maximum slip velocities at the corresponding rupture velocities and for different values of  $R/L$ . We assume dynamic stress drop to be 3MPa, shear modulus to be 30 GPa and S-wave speed of  $3km/s$  in these calculations.

strictly) to mean that the  $\tau/\sigma$  were the same on both the structures, that  $\sigma_{zz}$ , the maximum principal compressive stress, and the remaining principal stresses be compressive and not greater than  $\sigma_{zz}$ , puts  $\Psi$  in the range of 16 to 27 degrees (for  $\tau/\sigma$  between 0.3 and 0.6). The direction  $\Psi_{\Delta\sigma}$  of the principal compression in the perturbation far-field lies between 0 and 10 degrees when  $v_r > \sqrt{2}c_s$ , specifically between 3 and 6 degrees when  $1.5c_s < v_r < 1.6c_s$ . In fact, in the far-field  $\Psi_{\Delta\sigma} = 0.5 \tan^{-1}(-\cot 2\beta)$  where  $\sin \beta = c_s/v_r$ . For the far-field compressive stress along the principal direction to become yet more compressive we must have  $\Psi - \Psi_{\Delta\sigma} < \pi/4$  which implies that  $\Psi < \pi/4 - 0.5 \tan^{-1}(\cot 2\beta) = 39^\circ$  to  $42^\circ$  when  $1.5c_s < v_r < 1.6c_s$ . Thus the above constraints on pre-stress direction make it plausible that stresses in the far-field caused the ground cracking.

### 4.3 Off-fault Damage at Transition

#### 4.3.1 The 1999 $M_w$ 7.4 Izmit ; 2001 $M_w$ 7.8 Kunlun ; 2002 $M_w$ 7.9 Denali & 2013 $M_w$ 7.5 Craig earthquakes

The theoretical analysis of the stress state at the rupture tip during the acceleration from sub-Rayleigh to supershear speeds suggests the existence of a gap in coseismic off-fault damage at the supershear transition. In nature, the extent of coseismic off-fault damage could be reflected in the spatial distribution of early near-fault aftershocks (occurring around a week after the main earthquake). When reanalysing the regions where established supershear ruptures transitioned from sub-Rayleigh to supershear speeds, the precise location of the transition should then be highlighted by a local decrease in the aftershock intensity and its spatial extent. Assuming that the nucleation of early aftershocks are mainly governed by the stress state left

in the wake of the earthquake, we analyse the spatial and temporal distribution of relocated aftershocks for three well-known supershear ruptures: the  $M_w$  7.4 1999 Izmit (Turkey) earthquake (Bouchon & Karabulut, 2008; Bouchon et al., 2001) (Figure 4.10a), the  $M_w$  7.9 2002 Denali (Alaska) earthquake (Ellsworth et al., 2004a) (Figure 4.10d), and the  $M_w$  7.5 2013 Craig (Alaska) earthquake (Yue et al., 2013) (Figure 4.10g).

For these examples, we compute the seismic moment released by the aftershocks at a distance of less than 5 km from the main fault, and, for different periods of time after the mainshock: 1-3 days, 1, 2, 3 weeks and 1 month (Figures 4.10 c, f, and i). When focusing on the region where the rupture is expected to transition supershear, we systematically observe a small region ( $\sim 5$ –15 km) characterised by reduced seismic moment release and a clear lack of aftershocks (Figure 4.10 b, c, e, f, h and i, pink boxes). This feature is spatially persistent, no matter the distance considered when computing the cumulative seismic moment released. Note that the cumulative seismic moment systematically rises after 3 weeks in this transition region, potentially related to postseismic deformation. This inferred transitional region actually co-locates with the region of maximum afterslip for each event (Ding et al., 2015; Freed et al., 2006; Hearn et al., 2009). This delayed increase in near-fault deformation confirms that the observed gap in the early aftershocks productivity (less than 3 weeks after the mainshock) is mostly related to the mainshock dynamic rupture, that is the supershear transition (see Methods Section for details in the Catalogs and statistical analysis of the results).

As high-resolution aftershocks catalogs are not available for all supershear ruptures, we explore a new method to investigate the spatial evolution of near fault coseismic damage, by focusing on the width of the damage zone generated during the earthquake. Recent developments in satellite optical image analysis and sub-pixel correlation methods now allow for the detection of displacement variations due to an earthquake down to a resolution of one meter. Noting that, for earthquakes of large magnitudes ( $M_w \geq 7$ ), fault zones (fault core and damage zone) are usually of metric- to kilometer-scale (Gold et al., 2015), we apply this method to the  $M_w$  7.8 2001 Kunlun (China) earthquake (Bhat et al., 2007; Robinson et al., 2006b; Vallée et al., 2008). Displacement profiles normal to the fault are computed using pre- and post-earthquake images and are used to infer the width of the fault zone (fault core and damage zone), produced by the earthquake (Figure 4.11, see Methods Section for details in the methodology and the Supplementary Information for details on the data employed in the analysis). While the overall mean of the fault zone width is around 238 meters, we observe a clear localised region,  $\sim 11$  km-long, where damage largely reduced down to a mean of 127 meters, located around what was previously inferred as the supershear transition zone (Vallée et al., 2008). As expected from theoretical analysis and numerical modelling, the supershear transition would be characterised by a significant reduction in damage zone width. We acknowledge here that the aftershock catalog of Robinson and colleagues Robinson et al., 2006b also alludes to the same conclusion. How-

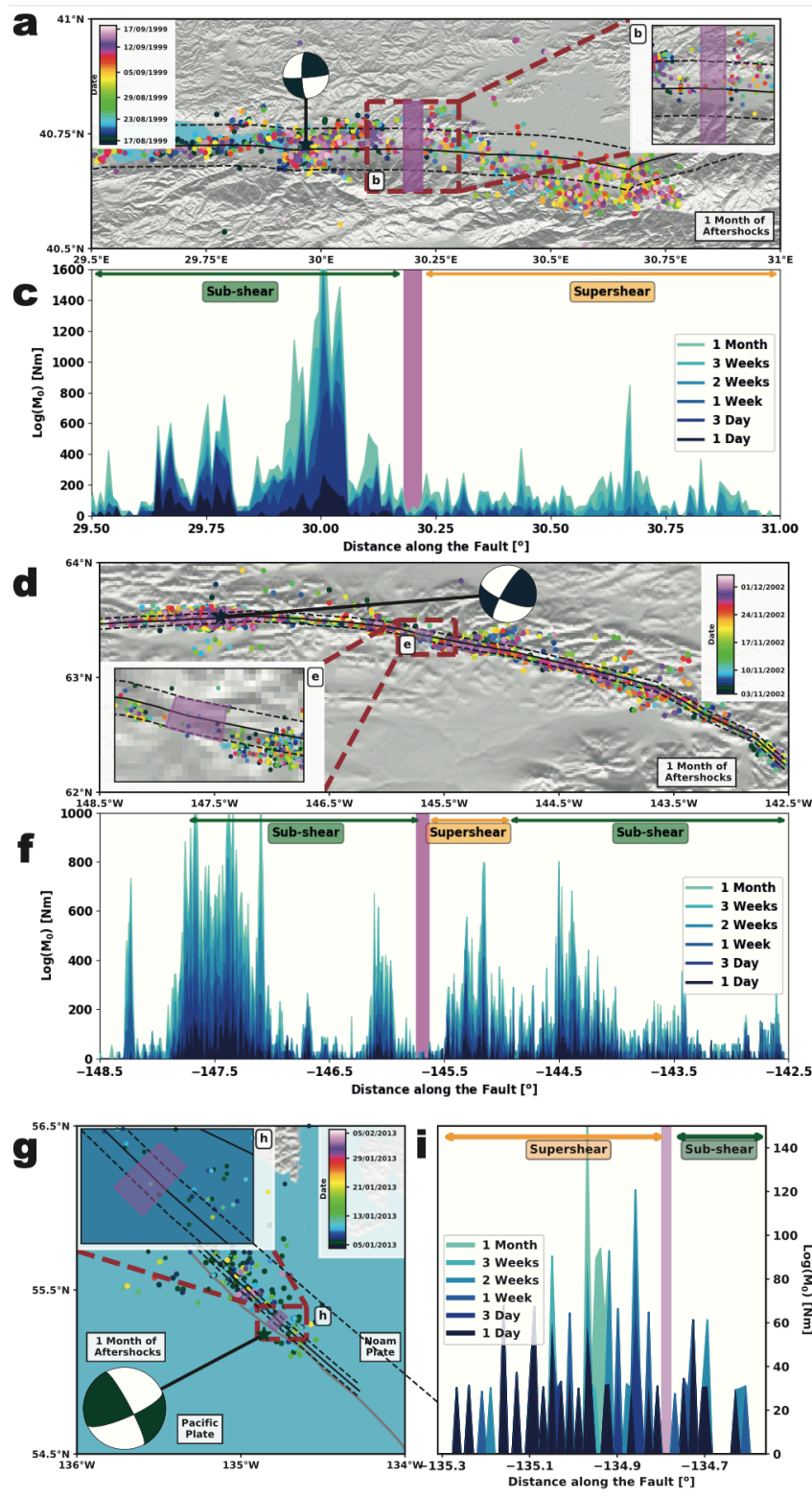


Figure 4.10: **High-Resolution Aftershock Catalog Analysis.** 1-month aftershock distribution for Izmit (a), Denali (d), and Craig (g) earthquakes, color-coded by time and indicating the respective event epicentre (color-coded star) and focal mechanism. The black continuous line denotes the surface rupture for each event. **c,f,i** Cumulative aftershock seismic moment release projected on the main fault (in log scale) at different temporal scales (1-3 days, 1-2-3 weeks and 1 month), for Izmit (c), Denali (f), and Craig (i) earthquakes. All the aftershocks within a distance of 5 km from the fault are considered in the calculation (area denoted by the black discontinuous lines in a, d and g). Color-coded arrows indicate the different speed regimes reported for each event (green for sub-Rayleigh and orange for supershear) (Bouchon & Karabulut, 2008; Ellsworth et al., 2004a; Yue et al., 2013), while the pink boxes indicate this work’s proposed Transition Zones. **b,e,h** Zoom plot of the region proposed as Transition zone in this study for each earthquake.

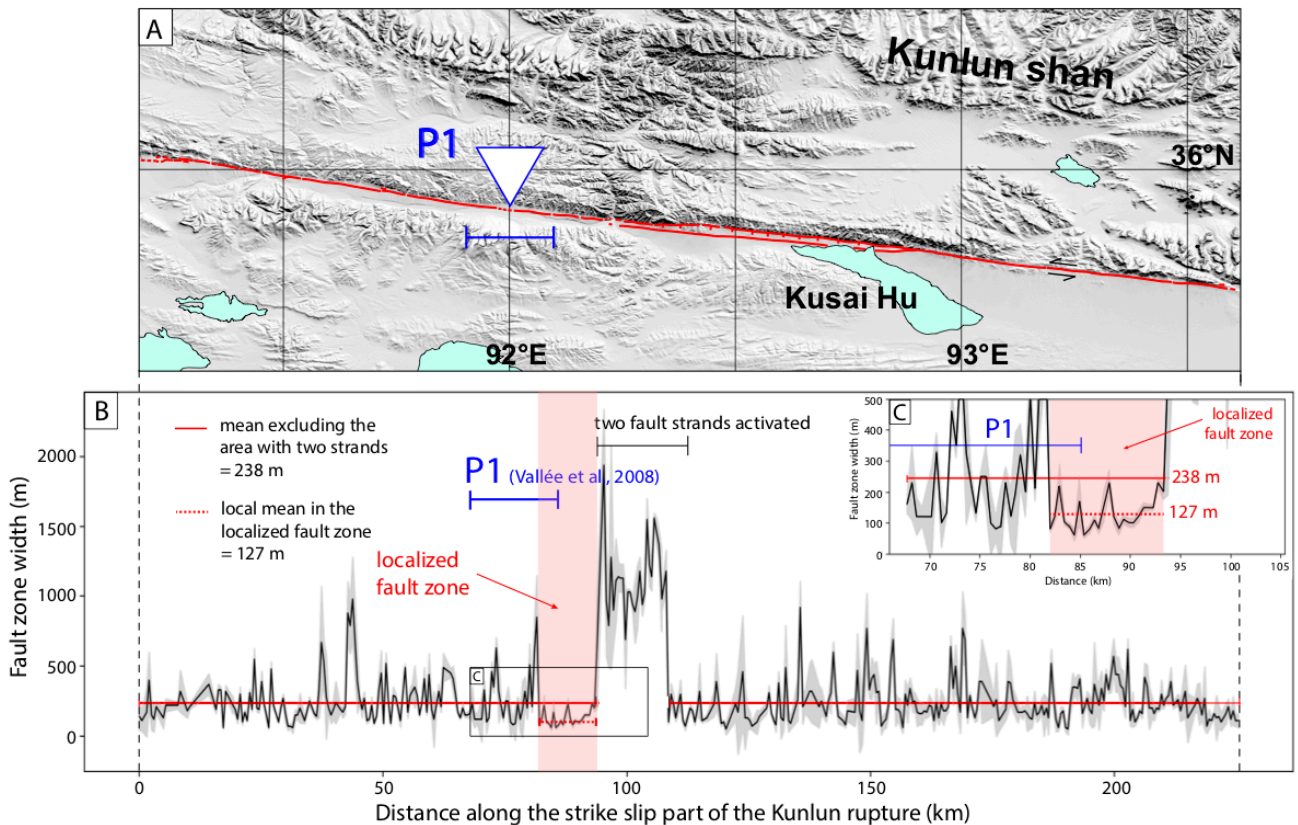


Figure 4.11: **Optical Correlation Images Analysis.** **a.** Map of the strike slip section of the  $M_w$  7.8 2001 Kunlun (China) earthquake, where P1 denotes the transition zone reported for the event from seismological far-field data (Vallée et al., 2008). **b.** Along-Strike fault zone width (black) and its associated uncertainty (grey), obtained from the analysis of 40 km-long profiles, sampling the fault zone every 500 m, on the surface displacement maps. The latter is derived from correlating pre- and post-earthquake SPOT 1-4 images. The 11 km-long red area highlighted the specific region with a mean fault width (red dashed line) of only 127 m compared to 238 m recorded for the rest of the rupture (red line). The latter excludes the area where two parallel fault strands are activated and for which the fault zone is exceptionally large ( $> 1000$  m). **c.** Zoom of the Figure 4.11 b.

ever due to the lack of high spatio-temporal density of aftershocks in their catalog we instead chose the above technique.

Using the theoretical framework to precisely estimate the location of supershear transition. When applied to known supershear ruptures, this approach allows for a better spatial localisation of the region where the earthquake accelerates from sub-Rayleigh to supershear speeds. Obviously, since we modelled the earthquake as a simple 1D planar crack, future work is necessary to evaluate the effect of 3D fault geometry in this process. Regardless, the gap in coseismic off-fault damage related to supershear transition appears well-defined in natural earthquakes (Figure 4.10), even after accounting for the uncertainty in the location of aftershocks. This approach could thus be used as a first step to precisely locate supershear transition.

The use of relocated catalogs is already substantive in this study, as past works who noticed a lack in near-fault aftershocks for supershear rupture concluded that the aftershock quiescence co-located with the entire supershear rupture (Bouchon & Karabulut, 2008). In this study, we are able to define the region of this quiescence in off-fault activity and have related it to supershear transition. This is due to the transient shrinkage in stress concentration around the rupture tip as its velocity approaches the Rayleigh wave speed. Also, the results presented in this study, are in agreement with the published kinematic models for Izmit (Bouchon et al., 2000, 2001), Denali (Dunham & Archuleta, 2004; Ellsworth et al., 2004a), Craig (Yue et al.,

2013), and Kunlun (Bouchon & Vallee, 2003; Robinson et al., 2006b; Vallée et al., 2008; Vallée & Dunham, 2012) earthquakes. The main difference here is that we are able to define more precisely the location, and the length of the transition region, through aftershock and image correlation analysis.

However, this study is limited to careful reanalysis of regions where the supershear transition was expected to happen. As we can see from the entire fault profile, local gaps in aftershock density are obviously not a necessary and sufficient condition for supershear transition. They could be related to local changes in rupture speeds, within the sub-Rayleigh speed regime, and this calls for further investigation. This study, for now, highlights the location and extent of the supershear transition, through a mechanics based analysis, as a first step to investigate the condition for such transitions.

Theoretical and numerical modelling of off-fault damage both suggest that the transition from the sub-Rayleigh to the supershear regime is characterised by a reduction in the width of the damage zone and a paucity of aftershocks. We cross-validate this predicted feature, with seismological evidence of aftershock quiescence for the Izmit, Denali and Craig supershear earthquakes, and with geodetic observations of the damage zone for the Kunlun earthquake. These results are valid for a well-developed sub-Rayleigh rupture that transitions to supershear speeds. Recent observations from the Palu earthquake hint that the rupture might have either nucleated directly at a supershear speed, or transitioned very early on (Bao et al., 2019; Socquet et al., 2019). For this particular case, further exploration is required to see if similar features can be observed in the field.

In conclusion, identifying an absence of aftershocks and decrease in off-fault damage allows us to pinpoint the location of the transition from sub-Rayleigh to supershear speeds. This work provides a new framework, guided by theoretical fracture mechanics, to precisely locate supershear transitions in the field. This approach offers the opportunity to revisit supershear transition zones in the field, in order to better characterise the local fault conditions, and further explore the mechanical conditions for such transitions.

## 4.4 Supershear Tsunamis

### 4.4.1 The 2018 $M_w$ 7.5 Palu Earthquake

Devastating tsunamis are known to predominantly occur due to subduction zone earthquakes such as the 2011  $M_w$  9.0 Tohoku-Oki earthquake in Japan. However, the 2018  $M_w$  7.5 Palu, Sulawesi (Indonesia) strike-slip earthquake generated an unexpected tsunami with disastrous and deadly effects. Since such strike-slip earthquakes are not known to generate large tsunamis, the latter's origin remains much debated. Here we present near-field observational evidence that the earthquake attained supershear speed, i.e., a rupture speed greater than the shear wave speed of the host medium.

We study the effect of this rupture phenomenon on generation of tsunamis by coupling the corresponding ground motion to a 1D non-linear shallow water wave model that accounts for both the time-dependent bathymetric displacement as well as, importantly, the bathymetric velocity. Using the local bathymetric profile of Palu bay around the Pantoloan harbour tidal gauge, our simulations clearly reproduce the motions of the observed tsunami with minimal tuning of parameters. This implies that Mach fronts, generated by a supershear earthquake, interacted with the Palu bay to cause the tsunami. Our results suggest that the speed of the rupture should also be included in the assessment of tsunami hazard.

Tsunamis are well-known to be amongst the most destructive consequences of earthquakes (Bryant, 2008; Pugh & Woodworth, 2014; Röbbke & Vött, 2017; Synolakis & Okal, 2005), and the 2018 Sulawesi earthquake was no exception: it generated a devastating tsunami (Fritz et al., 2018; Mai, 2019) in the nearby Palu bay in which hundreds were killed and tens of thousands more displaced from their homes (ASEAN Situation Update No.15 - Earthquake & Tsunami Sulawesi). However, this was an unexpected event since the earthquake was associated with the predominantly in-plane ground motion produced by strike-slip ruptures. As these motions are not known to excite significant waves, the underlying physical mechanisms behind the tsunami have largely remained a mystery (Syamsidik et al., 2019). Many studies conducted to explain the phenomenon have not arrived at definitive conclusions (Muhari et al., 2018) nor have adequately captured tidal gauge records (Heidarzadeh et al., 2019; Jamelot et al., 2019); the main consensus appears to be that some form of ground motion (e.g., landslides (Sassa & Takagawa, 2019) or the reverse-slip motion of the fault (He et al., 2019)), amplified by the bay, is to blame.

However, a key notable feature of this earthquake is that it ruptured at supershear speed (Bao et al., 2019; Socquet et al., 2019), which results in a manifestation of two shock (or Mach) fronts carrying significant vertical velocity with relatively slow attenuation over large distances (Dunham & Bhat, 2008). Although the overall tsunami behaviour at Palu is likely a combination of several effects that include these supershear dynamics as well as landslides, recent studies by Jamelot et al. (2019), Oral et al. (2020), and Ulrich et al. (2019) suggest that the influence from phenomena such as the latter may be secondary: the rupture itself may have created adequate seafloor movement to excite the tsunami, which was subsequently amplified by the shallow and narrow 2D/3D geometric features of the Palu bay. Jamelot et al. (2019) capture amplitudes recorded by the Pantoloan tidal gauge, but not the first phases and motions—ultimately conceding that a dynamic study should be conducted to better understand the influence of supershear. The model-based study of Ulrich et al. (2019), which incorporates some dynamics of supershear in the form of time-dependent ground displacement, better captures tidal gauge records but, again, there remains a mismatch in the first phases and arrival.

Hence the primary objective of this work is to provide the missing link in

explaining these discrepancies and more fully understand the role played by supershear rupture dynamics on the generation of the Palu tsunami. In particular, we incorporate a neglected feature in the above-cited works that is a defining characteristic of supershear earthquakes: the *velocity* of the ground motion (Dunham & Bhat, 2008). Using a model validated by the first near-field evidence of supershear at Palu, our results imply that ground speeds, which better represent the intricacies of the Mach fronts, may further explain the observed motions of the tsunami. Since other studies (including those investigating landslides and liquefaction) have adequately captured much of the observed run-up amplitudes and some local inundations, the scope of this paper is to focus on the first phases and arrival in the Pantoloan records.

### Modelling the effect of supershear velocity on tsunami generation

Using the synthetic particle motions (which, again, agree with PALP GPS records and are generated by the 3D supershear earthquake model), a 1D non-linear shallow water wave model incorporating time dependent bathymetry movements in ground velocity and displacement (Dutykh & Clamond, 2016) has been utilized to simulate the generation and propagation of the tsunami. This employs the depth-averaged shallow water approximation of the Euler equations that can be written as a system of coupled hyperbolic partial differential equations given by

$$\frac{\partial H}{\partial t} + \frac{\partial(Hu)}{\partial y} = 0 \quad (4.2)$$

$$\frac{\partial(Hu)}{\partial t} + \frac{\partial(Hu^2)}{\partial y} + gH \frac{\partial \eta}{\partial y} = 0 \quad (4.3)$$

The domain of validity is given by  $0 \leq y \leq L$ ;  $t \geq 0$ . Here,  $u(y, t)$  is the fluid velocity,  $\eta(y, t)$  is the sea surface height and  $H(y, t) = h_0(y) + h(y, t) + \eta(y, t)$  is the absolute height from the bed-level to the water surface for an initial at-rest bathymetry  $h_0(y)$ . The entire domain of length  $L$  is subjected to a time-dependent ground perturbation  $h(y, t)$  which— together with the corresponding ground velocity  $\partial h(y, t)/\partial t$  included in system (4.2)—sources the subsequent tsunami dynamics. In what follows, these values are determined from the 3D supershear earthquake model (Dunham & Bhat, 2008). The constant  $g$  is the acceleration due to gravity.

The specific Palu bay configuration is outlined in Figure 4.12a along with the governing equations defined on the horizontal  $y$ -axis, where  $z = \eta(y, t)$  represents the water height relative to the background sea level. The bathymetry shape closely approximates that of the segment demarcated by the green dotted line near the Pantoloan tidal gauge in Figure 4.6a (basin width 9.2km, maximum depth 710m and an average slope of  $7^\circ$  to the east and  $27^\circ$  to the west of the bay). The shallowest part is taken to be 1m, and the distance between the virtual gauge and the fault is 4.3km. The complete computational domain is taken to be twice the basin width ( $L = 18.4$ km). Figure 4.12b presents a temporal snapshot in the  $(x, y)$ -plane (the ground surface) illustrating the dynamic vertical velocity field (and the associated Mach fronts)

which is input as a synthetic source in conjunction with its corresponding time-dependent displacement field. The fault and the sense of slip (left-lateral) are indicated in red, and the data applied to perturb the bathymetry is taken along the line demarcated by dark green circles (whose locations correspond to the same markers indicated in the model domain of Figure 4.12a). For an example point located at  $(x_0, y_0)$  and highlighted in a larger light green circle, the plots of Figure 4.12c additionally present the temporal evolution of both the vertical velocity (which can reach  $\sim 1\text{m/s}$  along the domain) as well as its corresponding ground displacement (which, in the 1D setting, can reach  $\sim 40\text{cm}$ ). As already noted the shapes and the maximum values of these profiles remain fairly unattenuated at large distances from the original earthquake—a hallmark of the energy carried by supershear shock fronts (Dunham & Bhat, 2008). For the results that subsequently follow, Figures 4.12d-e additionally present the analogous inputs for classical modelling of seismogenic tsunamis. In a classical setting (Pedlosky, 2013), the earthquake source is often modelled as a static displacement perturbation applied to the bathymetry (rather than dynamic ground motion), i.e., a static  $h(y, t) = h(y)$  that neither accounts for the time-dependence nor the velocity of the sea floor (other simple approximations to more complicated sources are also standard (Kajiura, 1963; Tanioka & Satake, 1996)). From the supershear earthquake results, this corresponds to the final, permanent ground displacement at the end of the temporal profiles in Figure 4.12c and is expectedly on the order of a few centimeters.

### Capturing first motions and arrival recorded at Pantoloan

Numerical solution of the non-linear shallow water wave equations has been facilitated by a spectral Fourier continuation (FC) methodology (Amrani & Bruno, 2016; Lyon & Bruno, 2010) employing a bathymetry that closely resembles the Palu bay near the Pantoloan tidal gauge (see Figures 4.6, 4.12). Through use of a discrete periodic extension in space and explicit integration in time, such a solver enables high-order accuracy, mild Courant-Friedrichs-Lewy (CFL) constraints on the temporal discretisation and nearly dispersionless resolution of propagating waves over large distances (see Methods). Figure 4.13 presents simulation results in the  $(t, y)$ -plane (time and space) of the water height  $z = \eta(y, t)$  and, more importantly, presents a comparison between observations recorded every minute by the Pantoloan tidal gauge (whose geographic location is indicated in Figure 4.6a) with that predicted by the dynamic source model (plotted in Figure 4.13 at the same frequency). The numerical modelling has been conducted at a much higher temporal resolution (on the order of 10 milliseconds), and the Pantoloan records have been obtained and processed by the Agency for Geospatial Information (BIG), Indonesia (<http://tides.big.go.id>). Remarkably, both the first motions and phases from the observation records are in excellent agreement with the 1D approximation generated by excitation from the dynamic supershear earthquake. Later phases, which can be attributed to tsunami wave reflections within the Palu bay, are not as well-captured since our model does not fully account for the localised effects of

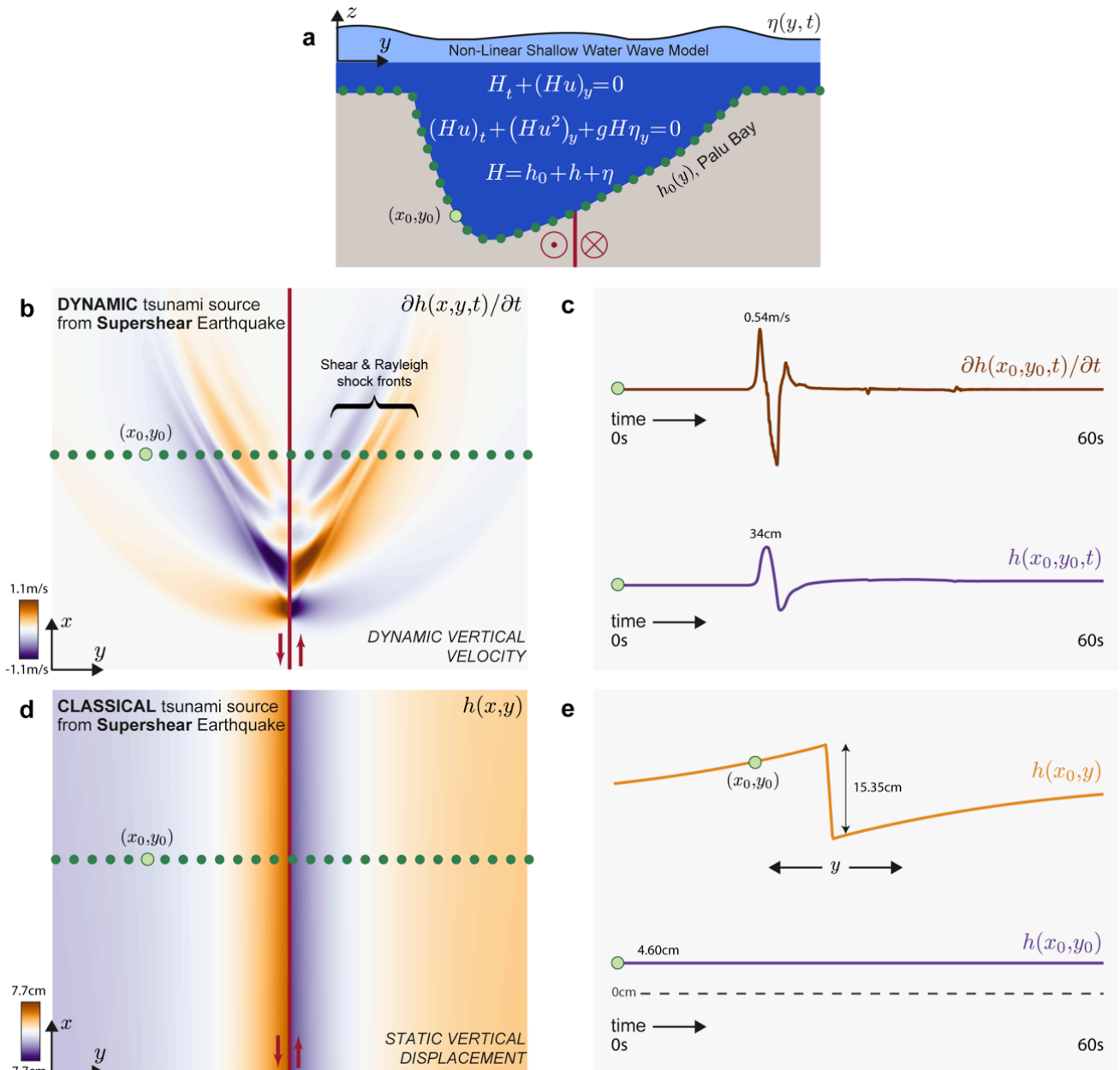


Figure 4.12: **The non-linear tsunami model setup that incorporates displacement and velocity ground dynamics.** The strike-slip fault and its sense of motion are indicated in red in all the panels. **a**, Snapshot of the dynamic vertical velocity from a supershear earthquake with, **b**, its temporal evolution at an example point  $(x_0, y_0)$  (light green). **c**, The static displacement field due to a supershear earthquake. **d**, A diagram of the non-linear shallow water wave system for tsunami height  $\eta$ , initial bathymetry  $h_0$  and bathymetry perturbation (source)  $h$ . The dark green dots on the supershear earthquake data in **(a,c)** correspond to the source locations used to perturb the bathymetry domain in **(d)**. **e**, The spatial profile in  $y$  of the static displacement field due to a supershear earthquake.

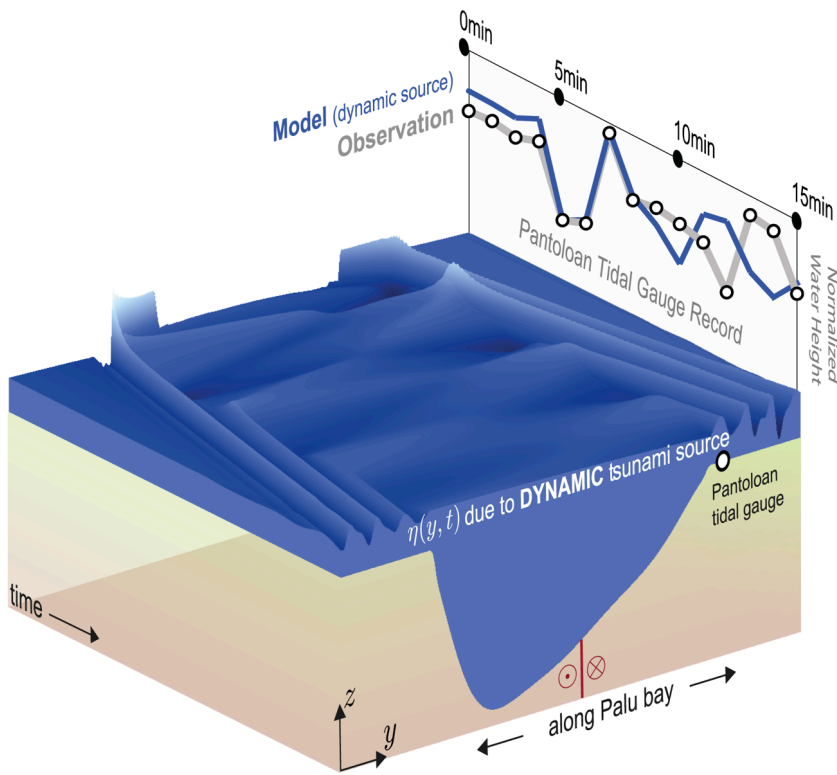


Figure 4.13: **Simulated tsunami using dynamic ground motion (including velocity)**. Spatio-temporal evolution  $\eta(y, t)$  of the tsunami along the Palu bay due to dynamic bathymetry velocity and displacement from a supershear earthquake. Normalised Pantoloan tidal gauge records during the event are overlaid with model predictions.

the 2D/3D bathymetric profile. Nevertheless, the tsunami arrival and primary dynamics are correctly reproduced.

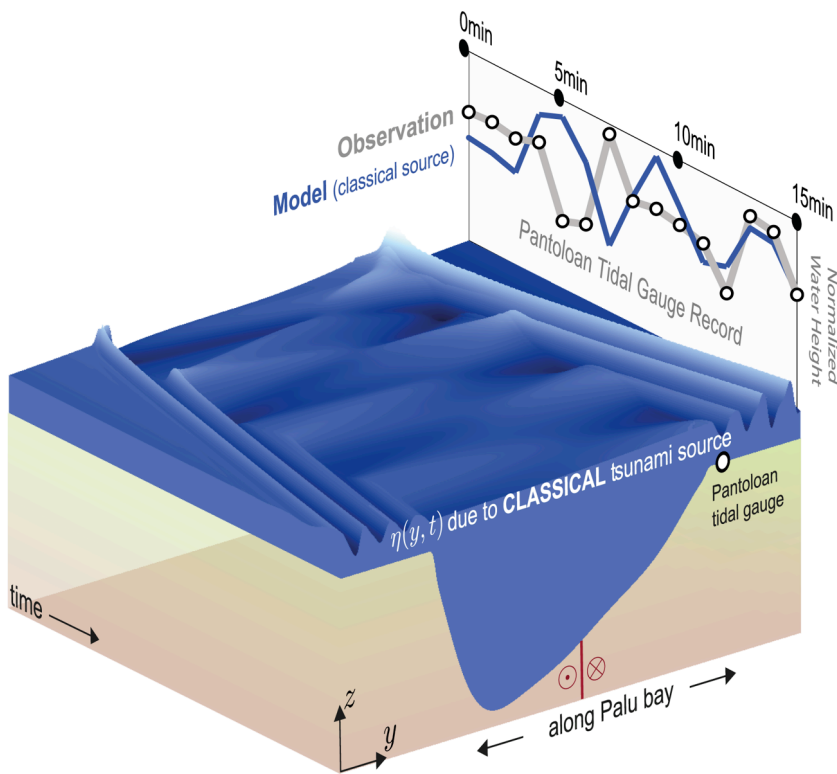


Figure 4.14: **Simulated tsunami using classical (static) displacement**. Spatiotemporal evolution  $\eta(y, t)$  of the tsunami along the Palu bay due to static displacement from a supershear earthquake. Normalised Pantoloan tidal gauge records during the event are overlaid with model predictions.

For comparison, Figure 4.14 presents the corresponding simulations that are classically-sourced by the final (static) vertical displacement given by the same supershear earthquake simulation. Although a tsunami is generated, there are large contrasts in phase, width and particularly the sign (Figure 4.14) when compared to the Pantoloan tidal gauge observations. This implies that the complex ground motion (which is not accounted for by classical tsunami models) must be incorporated in order to correctly predict the tsunami dynamics as in Figure 4.13. We note that we have normalized water heights by their corresponding maxima for comparison throughout: since more energy is carried *along* the fault (Dunham & Bhat, 2008) running in the direction  $x$  (Figure 4.12), the 1D model in  $y$  will naturally generate lower amplitudes (of the order of half a meter). However, similar tsunami signatures can still be expected and, indeed, Jamelot et al. (2019) incorporated a more comprehensive (classical) model treating localised effects of the 2D/3D bathymetry but generated the same mismatches in phase as those in Figure 4.14.

## Conclusions

Hence we confirm that the Sulawesi earthquake went supershear via the first near-field high-rate GPS-based evidence of such a rupture and that, by modelling the corresponding effect on the generation of tsunamis in a shallow geometry, we conclude that the ground motion resulting from the associated Mach fronts (which carry minimally attenuated velocities to large distances) may well have caused the Palu tsunami. Since nothing geologically specific about the bay has been introduced, our results signify the importance of such configurations for tsunami hazard assessment due to strike-slip earthquakes. The same physical ingredients (supershear rupture and a shallow bay) may combine to produce similar effects elsewhere, including the Tomales bay in California (which is crossed offshore by the San Andreas fault system (Johnson & Beeson, 2019)) and the Izmit bay in Turkey (which is crossed by the North Anatolian fault (Altinok et al., 2001)). Both these regions, as well as the Palu bay, have suffered from historical tsunamis. On the contrary, the 2012 Off Northern Sumatra earthquake and the 2013 Craig, Alaska earthquake both went supershear but caused negligible (or no) tsunamis since they occurred in deep ocean without any shallow bay near them. Additionally, the 1999 Izmit earthquake was subshear as it passed through the Izmit bay and thus generated only a negligible tsunami. Hence we reemphasise that supershear rupture *and* a shallow bay are key to generate significant tsunamis. We thus suggest that any rapid assessment of tsunami hazard after a strike-slip earthquake should also involve a rapid assessment of the earthquake rupture velocity as we have shown that ultimately the focal mechanism, the depth *and* the speed of the rupture all contribute towards the generation of tsunamis.

# 5

## CONCLUSIONS

In this thesis I have laid out the theoretical models of a supershear rupture which highlighted the following key signatures of a supershear rupture.

- Supershear ruptures are stable above the Eshelby speed,  $\sqrt{2}c_s$ .
- The near field particle velocity is dominated by the fault parallel component for such ruptures. The opposite is true for sub-Rayleigh/ sub-shear ruptures.
- There is a clear separation of the dilatational and the shear fields which manifest in the ground motion.
- Supershear ruptures are, usually, trailed by a pulse traveling exactly at the Rayleigh wave speed. This pulse has dominantly fault normal motion.
- In 3D, supershear ruptures manifest Rayleigh Mach fronts, in addition to the shear ones. The Rayleigh Mach fronts suffer no attenuation with distance from the fault for an ideal medium.
- At the location of transition from sub to supershear speeds, severe Lorentz-like contraction of the stress field should lead to minimal off-fault damage.
- The Rayleigh mach fronts can induce large tsunamis in a bay-like bathymetry and will manifest as a unique signature in the tidal gauge records.

I have systematically presented experimental evidence and natural observations that support all of the above salient features of a supershear rupture. Suffice to say, **dynamic shear ruptures can indubitably attain supershear speeds.**

अंतः अस्ति प्रारंभः

The end is the beginning



# BIBLIOGRAPHY

- Aagaard, B. T. & T. H. Heaton (2004). “Near-source ground motions from simulations of sustained intersonic and supersonic fault ruptures”. *Bull. Seism. Soc. Am.* 94 (6), pp. 2064–2078. DOI: 10.1785/0120030249 (See pp. 51, 56).
- Agnew, D. C. (2002). “History of seismology”. *International handbook of earthquake and engineering seismology*. Ed. by W. H. K. Lee, H. Kanamori, P. C. Jennings, & C. Kisslinger. Vol. 81. Elsevier Science & Technology Books, pp. 3–11. DOI: 10.1016/S0074-6142(02)80203-0 (See p. 12).
- Aki, K. & P. G. Richards (2002). “Quantitative Seismology”. University Science Books (See p. 29).
- Altinok, Y, S Tinti, B Alpar, A. C. Yalciner, Ş Ersoy, E Bortolucci, & A Armigliato (2001). “The tsunami of August 17, 1999 in Izmit bay, Turkey”. *Natural Hazards* 24, pp. 133–146. DOI: 10.1023/A:1011863610289 (See p. 142).
- Amlani, F. & O. P. Bruno (2016). “An FC-based Spectral Solver for Elastodynamic Problems in General Three-dimensional Domains”. *J. Comput. Phys.* 307, pp. 333–354. DOI: 10.1016/j.jcp.2015.11.060 (See p. 139).
- Amlani, F., H. S. Bhat, W. J. F. Simons, A. Schubnel, C. Vigny, A. J. Rosakis, J. Efendi, A. Elbanna, & H. Z. Abidin (2020). “Supershear Tsunamis and insights from the  $M_w$  7.5 Palu Earthquake”. *to appear in Nat. Geosci.* (See p. 19).
- Andrews, D. J. (1976). “Rupture velocity of plane strain shear cracks”. *J. Geophys. Res.* 81, pp. 5679–5689. DOI: 10.1029/JB081i032p05679 (See pp. 17, 47–48, 54–55, 72–73).
- (1985). “Dynamic Plane-Strain Shear Rupture With A Slip-Weakening Friction Law Calculated By A Boundary Integral Method”. *Bull. Seism. Soc. Am.* 75 (1), pp. 1–21 (See pp. 53, 73).
- Antolik, M., R. E. Abercrombie, & G. Ekstrom (2004). “The 14 November 2001 Kokoxili (Kunlunshan), Tibet, earthquake: Rupture transfer through a large extensional step-over”. *Bull. Seism. Soc. Am.* 94 (4), pp. 1173–1194. DOI: 10.1785/012003180 (See p. 129).
- Archuleta, R. J. (1984). “A faulting model for the 1979 Imperial Valley earthquake”. *J. Geophys. Res.* 89, pp. 4559–4586. DOI: 10.1029/JB089iB06p04559 (See p. 18).
- Aristotle (350 B.C.E.). “Meteorologica” (See p. 11).
- Bao, H., J.-P. Ampuero, L. Meng, E. J. Fielding, C. Liang, C. W. D. Milliner, T. Feng, & H. Huang (2019). “Early and persistent supershear rupture of the 2018 magnitude 7.5 Palu earthquake”. *Nat. Geosci.* 12, pp. 200–205. DOI: 10.1038/s41561-018-0297-z (See pp. 19, 128, 136–137).
- Barenblatt, G. I. (1962). “The mathematical theory of equilibrium cracks in brittle fracture”. *Adv. Appl. Mech.* 7, pp. 55–129. DOI: 10.1016/S0065-2156(08)70121-2 (See p. 31).
- Ben-David, O., G. Cohen, & J. Fineberg (2010). “The Dynamics of the Onset of Frictional Slip”. *Science* 330, pp. 211–214. DOI: 10.1126/science.1194777 (See p. 116).

- Ben-Menahem, A. & S. J. Singh (1987). “Supershear accelerations and Mach-waves from a rupturing front: I-Theoretical-model and implications”. *J. Phys. Earth* 35 (5), pp. 347–365. DOI: 10.4294/jpe1952.35.347 (See pp. 50, 68–69).
- Benioff, H. (1955). “Mechanism and strain characteristics of the White Wolf fault as indicated by the aftershock sequence”. *Earthquakes in Kern County, California during 1952*, vol. 171. Div. Mines Bull., pp. 199–202 (See p. 16).
- Bernard, P. & D. Baumont (2005). “Shear Mach wave characterization for kinematic fault rupture models with constant supershear rupture velocity”. *Geophys. J. Int.* 162 (2), pp. 431–447. DOI: j.1365-246X.2005.02611.x (See pp. 51, 69).
- Bhat, H. S., R. Dmowska, G. C. P. King, Y. Klinger, & J. R. Rice (2007). “Off-fault damage patterns due to supershear ruptures with application to the 2001  $M_w$  8.1 Kokoxili (Kunlun) Tibet earthquake”. *J. Geophys. Res.* B06301. DOI: 10.1029/2006JB004425 (See pp. 19, 32, 51–53, 61–62, 65–66, 68, 72, 133).
- Bhat, H. S., R. L. Biegel, A. J. Rosakis, & C. G. Sammis (2010). “The Effect of Asymmetric Damage on Dynamic Shear Rupture Propagation II: With Mismatch in Bulk Elasticity”. *Tectonophysics* 493, pp. 263–271. DOI: 10.1016/j.tecto.2010.03.016 (See p. 86).
- Bhat, H. S., A. J. Rosakis, & C. G. Sammis (2012). “A Micromechanics Based Constitutive Model For Brittle Failure at High Strain Rates”. *J. Appl. Mech.* 79. DOI: 10.1115/1.4005897 (See p. 77).
- Biegel, R. L., H. S. Bhat, C. G. Sammis, & A. J. Rosakis (2010). “The Effect of Asymmetric Damage on Dynamic Shear Rupture Propagation I: No Mismatch in Bulk Elasticity”. *Tectonophysics* 493, pp. 254–262. DOI: 10.1016/j.tecto.2010.03.020 (See p. 86).
- Bizzarri, A., E. M. Dunham, & P. Spudich (2010). “Coherence of Mach fronts during heterogeneous supershear earthquake rupture propagation: Simulations and comparison with observations”. *J. Geophys. Res.* 115. DOI: 10.1029/2009JB006819 (See p. 126).
- Bouchon, M. & H. Karabulut (2008). “The Aftershock Signature of Supershear Earthquakes”. *Science* 320, p. 1323. DOI: 10.1126/science.1155030 (See pp. 133–135).
- Bouchon, M. & M. Vallee (2003). “Observation of long supershear rupture during the magnitude 8.1 Kunlunshan earthquake”. *Science* 301 (5634), pp. 824–826. DOI: 10.1126/science.1086832 (See pp. 129, 136).
- Bouchon, M., N. Toksöz, H. Karabulut, M. P. Bouin, M. Dietrich, M. Aktar, & M. Edie (2000). “Seismic imaging of the 1999 Izmit (Turkey) rupture inferred from the near-fault recordings”. *Geophys. Res. Lett.* 27, pp. 3013–3016. DOI: 10.1029/2000GL011761 (See p. 135).
- Bouchon, M., M. P. Bouin, H. Karabulut, M. N. Toksoz, M. Dietrich, & A. J. Rosakis (2001). “How fast is rupture during an earthquake? New insights from the 1999 Turkey earthquakes”. *Geophys. Res. Lett.* 28 (14), pp. 2723–2726. DOI: 10.1029/2001GL013112 (See pp. 18, 133, 135).
- Bouchon, M., H. Karabulut, M.-P. Bouin, J. Schmittbuhl, M. Vallée, R. Archuleta, S. Das, F. Renard, & D. Marsan (2010). “Faulting characteristics of supershear earthquakes”. *Tectonophysics* 493, pp. 244–253. DOI: 10.1016/j.tecto.2010.06.011 (See p. 118).
- Brace, W. F. & J. D. Byerlee (1966). “Stick-slip as a mechanism for earthquakes”. *Science* 153, pp. 990–992. DOI: 10.1126/science.153.3739.990 (See pp. 13, 15, 112).
- Broberg, K. B. (1960). “The propagation of a brittle crack”. *Ark. Fys.* 18, pp. 159–92 (See p. 55).
- (1978). “On transient sliding motion”. *Geophys. J. R. astr. Soc.* 52, pp. 397–432. DOI: 10.1111/j.1365-246X.1978.tb04240.x (See p. 31).

- (1989). “The near-tip field at high crack velocities”. *Int. J. Fract.* 39, pp. 1–13. DOI: [https://doi.org/10.1007/978-94-009-0927-4\\_1](https://doi.org/10.1007/978-94-009-0927-4_1) (See pp. 21, 30–32, 35).
- (1994). “Intersonic Bilateral Slip”. *Geophys. J. Int.* 119 (3), pp. 706–714. DOI: 10.1111/j.1365-246X.1994.tb04010.x (See p. 49).
- (1996). “How fast can a crack go?” *Mater. Sci.* 32, pp. 80–86. DOI: 10.1007/BF02538928 (See p. 21).
- (1999). “Cracks and Fracture”. Academic Press (See pp. 21, 31, 55).
- Bruhat, L., Z. Fang, & E. M. Dunham (2016). “Rupture complexity and the supershear transition on rough faults”. *J. Geophys. Res.* 121. DOI: 10.1002/2015JB012512 (See p. 72).
- Bryant, E. (2008). “Tsunami: The Underrated Hazard”. Springer Berlin Heidelberg (See p. 137).
- Burridge, R. (1973). “Admissible speeds for plane-strain self-similar shear cracks with friction but lacking cohesion”. *Geophys. J. R. astr. Soc.* 35, pp. 439–455. DOI: 10.1111/j.1365-246X.1973.tb00608.x (See pp. 16–17, 47, 49, 72).
- Burridge, R., G. Conn, & L. B. Freund (1979). “Stability Of A Rapid Mode-II Shear Crack With Finite Cohesive Traction”. *J. Geophys. Res.* 84 (NB5), pp. 2210–2222. DOI: 10.1029/JB084iB05p02210 (See pp. 17–18, 21, 47, 53, 72).
- Byerlee, J. (1967). “Frictional characteristics of granite under high confining pressure”. *J. Geophys. Res.* 72, pp. 3639–3648. DOI: 10.1029/JZ072i014p03639 (See p. 15).
- Candela, T., F. Renard, Y. Klinger, K. Mair, J. Schmittbuhl, & E. E. Brodsky (2012). “Roughness of fault surfaces over nine decades of length scales”. *J. Geophys. Res.* 117, B08409. DOI: 10.1029/2011JB009041 (See p. 116).
- Coker, D. & A. J. Rosakis (2001). “Experimental observations of intersonic crack growth in asymmetrically loaded unidirectional composite plates”. *Philos. Mag. A* 81 (3), pp. 571–595. DOI: 10.1080/01418610108212160 (See p. 83).
- Coker, D., A. J. Rosakis, & A. Needleman (2003). “Dynamic crack growth along a polymer composite-Homalite interface”. *J. Mech. Phys. Solids* 51 (3), pp. 425–460. DOI: 10.1016/S0022-5096(02)00082-0 (See p. 83).
- Craggs, J. W. (1960). “On the propagation of a crack in an elastic-brittle material”. *J. Mech. Phys. Solids* 8, pp. 66–75. DOI: 10.1016/0022-5096(60)90006-5 (See pp. 16–17).
- Dalguer, L. A. & S. Day (2007). “Staggered-Grid Split-Node method for spontaneous rupture simulation”. *J. Geophys. Res.* 112, B02302. DOI: 10.1029/2006JB004467 (See p. 54).
- Das, S. (2007). “The Need to Study Speed”. *Science* 317, pp. 905–906. DOI: 10.1126/science.1142143 (See p. 117).
- Das, S. & K. Aki (1977). “A numerical study of two-dimensional spontaneous rupture propagation”. *Geophys. J. R. astr. Soc.* 50, pp. 643–668. DOI: 10.1111/j.1365-246X.1977.tb01339.x (See p. 17).
- Das, S. (2015). “Supershear Earthquake Ruptures—Theory, Methods, Laboratory Experiments and Fault Superhighways: An Update”. *Perspectives on European Earthquake Engineering and Seismology*. Ed. by A. Ansal. Springer, pp. 1–20. DOI: 10.1007/978-3-319-16964-4\_1 (See pp. 16, 18).
- Davison, C. (1921). “Founders of Seismology.—I. John Michell”. *Geological Magazine* 58, pp. 98–107. DOI: 10.1017/S0016756800090312 (See p. 12).
- Ding, K., J. T. Freymueller, Q. Wang, & R. Zou (2015). “Coseismic and Early Post-seismic Deformation of the 5 January 2013 Mw 7.5 Craig Earthquake from Static and Kinematic GPS Solutions”. *Bull. Seism. Soc. Am.* 105, pp. 1153–1164. DOI: 10.1785/0120140172 (See p. 133).
- Dunham, E. M. (2007). “Conditions governing the occurrence of supershear ruptures under slip-weakening friction”. *J. Geophys. Res.* 112. DOI: 10.1029/2006JB004717 (See pp. 17, 73).

- Dunham, E. M. & R. J. Archuleta (2004). "Evidence for a supershear transient during the 2002 Denali fault earthquake". *Bull. Seism. Soc. Am.* 94 (6), S256–S268. DOI: 10.1785/0120040616 (See pp. 18, 21, 47, 49, 51, 72, 119–120, 125, 135).
- (2005). "Near-source ground motion from steady state dynamic rupture pulses". *Geophys. Res. Lett.* 32. DOI: 10.1029/2004GL021793 (See pp. 21, 30–33, 36, 39, 43, 45, 51, 53, 56, 61–62, 65, 68, 111, 117, 122, 128).
- Dunham, E. M. & H. S. Bhat (2008). "Attenuation of radiated ground motion and stresses from three-dimensional supershear ruptures". *J. Geophys. Res.* 113. DOI: 10.1029/2007JB005182 (See pp. 19, 117, 128, 137–139, 142).
- Dunham, E. M., P. Favreau, & J. M. Carlson (2003). "A supershear transition mechanism for cracks". *Science* 299 (5612), pp. 1557–1559. DOI: 10.1126/science.1080650 (See pp. 47, 72, 121, 123).
- Dutykh, D. & D. Clamond (2016). "Modified shallow water equations for significantly varying seabeds". *Appl. Math. Model.* 40, pp. 9767–9787. DOI: 10.1016/j.apm.2016.06.033 (See p. 138).
- Eberhart-Phillips, D. et al. (2003). "The 2002 Denali fault earthquake, Alaska: A large magnitude, slip-partitioned event". *Science* 300 (5622), pp. 1113–1118. DOI: 10.1126/science.1082703 (See p. 65).
- Ellsworth, W. L., M. Celebi, J. R. Evans, E. G. Jensen, R. Kayen, M. C. Metz, D. J. Nyman, J. W. Roddick, P. Spudich, & C. D. Stephens (2004a). "Near-field ground motion of the 2002 Denali fault, Alaska, earthquake recorded at pump station 10". *Earthq. Spectra* 20, pp. 597–615. DOI: 10.1193/1.1778172 (See pp. 18, 51, 117–119, 128, 133–135).
- Ellsworth, W. L., M. Celebi, J. R. Evans, E. G. Jensen, D. J. Nyman, & P. Spudich (2004b). "Processing and modeling of the pump station 10 record from the November 3, 2002, Denali fault, Alaska earthquake". *Proceedings, 11th Intern. Conf. Soil Dynam. Earthq. Eng* 1, pp. 471–477 (See p. 119).
- Eshelby, J. D. (1949). "Uniformly Moving Dislocations". *Proc. Phys. Soc. Lond. A* 62 (353), pp. 307–314. DOI: 10.1088/0370-1298/62/5/307 (See pp. 30, 53).
- (1969). "The elastic field of a crack extending non-uniformly under general anti-plane loading". *J. Mech. Phys. Solids* 17, pp. 177–199. DOI: 10.1016/0022-5096(69)90032-5 (See p. 15).
- Favreau, P., M. Campillo, & I. R. Ionescu (2002). "Initiation of shear instability in three-dimensional elastodynamics". *J. Geophys. Res.* 107, pp. 2147–2164. DOI: 10.1029/2001JB000448 (See p. 54).
- Field, E. H., T. E. Dawson, K. R. Felzer, A. D. Frankel, V. Gupta, T. H. Jordan, T. Parsons, M. D. Petersen, R. S. Stein, R. Weldon, et al. (2009). "Uniform California earthquake rupture forecast, version 2 (UCERF 2)". *Bull. Seism. Soc. Am.* 99, pp. 2053–2107. DOI: 10.1785/0120080049 (See p. 117).
- Fliss, S., H. S. Bhat, R. Dmowska, & J. R. Rice (2005). "Fault branching and rupture directivity". *J. Geophys. Res.* B06312. DOI: 10.1029/2004JB003368 (See p. 67).
- Fossum, A. F. & L. B. Freund (1975). "Nonuniformly moving shear crack model of a shallow focus earthquake mechanism". *J. Geophys. Res.* 80, pp. 3343–3347. DOI: 10.1029/JB080i023p03343 (See p. 18).
- Freed, A. M., R. Bürgmann, E. Calais, J. Freymueller, & S. Hreinsdóttir (2006). "Implications of deformation following the 2002 Denali, Alaska, earthquake for post-seismic relaxation processes and lithospheric rheology". *J. Geophys. Res.* 111, B01401. DOI: 10.1029/2005JB003894 (See p. 133).
- Freund, L. B. (1972). "Crack Propagation in an Elastic Solid Subjected to General Loading-II. Non-Uniform Rate of Extension". *J. Mech. Phys. Solids* 20, pp. 141–152. DOI: 10.1016/0022-5096(72)90007-5 (See pp. 73–74).
- (1979). "Mechanics Of Dynamic Shear Crack-Propagation". *J. Geophys. Res.* 84 (NB5), pp. 2199–2209. DOI: 10.1029/JB084iB05p02199 (See pp. 18, 21–22, 25, 31, 35, 73, 110).

- (1990). “Dynamic Fracture Mechanics”. Cambridge: Cambridge University Press (See pp. 22, 25, 55).
- Fritz, H. M., C Synolakis, N Kalligeris, V Skanavis, F Santoso, M Rizal, G. S. Prasetya, Y. Liu, & P. L. F. Liu (2018). “Field survey of the 28 September 2018 Sulawesi tsunami”. *AGU Fall Meeting Abstracts* (See p. 137).
- Gabuchian, V., A. J. Rosakis, N. Lapusta, & D. D. Oglesby (2014). “Experimental investigation of strong ground motion due to thrust fault earthquakes”. *J. Geophys. Res.* 119, pp. 1316–1336. DOI: 10.1002/2013JB010409 (See p. 87).
- Gabuchian, V., A. J. Rosakis, H. S. Bhat, R. Madariaga, & H. Kanamori (2017). “Experimental evidence that thrust earthquake ruptures might open faults”. *Nature* 545. DOI: 10.1038/nature22045 (See p. 87).
- Gao, H., Y. Huang, P. Gumbsch, & A. Rosakis (1999). “On radiation-free transonic motion of cracks and dislocations”. *J. Mech. Phys. Solids* 47, pp. 1941–1961. DOI: 10.1016/S0022-5096(98)00126-4 (See p. 30).
- Georgiadis, H. G. & G. Lykotrafitis (2001). “A Method Based on the Radon Transform for Three-Dimensional Elastodynamic Problems of Moving Loads”. *J. Elasticity* 65, pp. 87–129. DOI: 10.1023/A:1016135605598 (See pp. 52, 62).
- Gilbert, G. K. (1884). “A theory of the earthquakes of the Great Basin, with a practical application”. *American Journal of Science* 27, pp. 49–53 (See p. 13).
- Gold, R. D., N. G. Reitman, R. W. Briggs, W. D. Barnhart, G. P. Hayes, & E. Wilson (2015). “On- and off-fault deformation associated with the September 2013 Mw 7.7 Balochistan earthquake: Implications for geologic slip rate measurements”. *Tectonophysics* 660, pp. 65–78. DOI: 10.1016/j.tecto.2015.08.019 (See p. 133).
- Graff, K. F. (1991). “Wave motion in elastic solids”. Dover publications (See p. 23).
- Griffith, W. A., A. J. Rosakis, D. D. Pollard, & C. W. Ko (2009). “Dynamic rupture experiments elucidate tensile crack development during propagating earthquake ruptures”. *Geology* 37, pp. 795–798. DOI: 10.1130/G30064A.1 (See p. 86).
- Guatteri, M. & P. Spudich (2000). “What can strong-motion data tell us about slip-weakening fault-friction laws”. *Bull. Seism. Soc. Am.* 90, pp. 98–116. DOI: 10.1785/0119990053 (See p. 56).
- Haeussler, P. J. et al. (2004). “Surface rupture and slip distribution of the Denali and Totschunda faults in the 3 November 2002 M 7.9 earthquake, Alaska”. *Bull. Seism. Soc. Am.* 94, S23–S52. DOI: 10.1785/0120040626 (See p. 118).
- Harris, R. A., R. J. Archuleta, & S. M. Day (1991). “Fault steps and the dynamic rupture process: 2-D numerical simulations of a spontaneously propagating shear fracture”. *Geophys. Res. Lett.* 18, pp. 893–896. DOI: 10.1029/91GL01061 (See p. 67).
- He, L., G. Feng, Z. Li, Z. Feng, H. Gao, & X. Wu (2019). “Source parameters and slip distribution of the 2018 Mw 7.5 Palu, Indonesia earthquake estimated from space-based geodesy”. *Tectonophysics* 772, p. 228216. DOI: 10.1016/j.tecto.2019.228216 (See p. 137).
- Hearn, E. H., S. McClusky, S. Ergintav, & R. E. Reilinger (2009). “Izmit earthquake postseismic deformation and dynamics of the North Anatolian Fault Zone”. *J. Geophys. Res.* 114, B08405. DOI: 10.1029/2008JB006026 (See p. 133).
- Heaton, T. H. (1990). “Evidence for and implications of self-healing pulses of slip in earthquake rupture”. *Phys. Earth Planet. In.* 64, pp. 1–20. DOI: 10.1016/0031-9201(90)90002-F (See p. 44).
- Heidarzadeh, M., A. Muhari, & A. B. Wijanarto (2019). “Insights on the Source of the 28 September 2018 Sulawesi Tsunami, Indonesia Based on Spectral Analyses and Numerical Simulations”. *Pure Appl. Geophys.* 176, pp. 25–43. DOI: 10.1007/s00024-018-2065-9 (See p. 137).

- Ida, Y. (1972). “Cohesive force across tip of a longitudinal-shear crack and Griffiths specific surface-energy”. *J. Geophys. Res.* 77, pp. 3796–3805. DOI: 10.1029/JB077i020p03796 (See p. 31).
- Jamelot, A., A. Gailler, P. Heinrich, A. Vallage, & J. Champenois (2019). “Tsunami Simulations of the Sulawesi Mw 7.5 Event: Comparison of Seismic Sources Issued from a Tsunami Warning Context Versus Post-Event Finite Source”. *Pure Appl. Geophys.* 176, pp. 3351–3376. DOI: 10.1007/s00024-019-02274-5 (See pp. 137, 142).
- Jara, J., L. Bruhat, S. Antoine, K. Okubo, M. Y. Thomas, Y. Klinger, R. Jolivet, & H. S. Bhat (2020). “Signature of supershear transition seen in damage and aftershock pattern”. *submitted to Nat. Comm.* (See p. 19).
- Johnson, S. Y. & J. W. Beeson (Mar. 2019). “Shallow Structure and Geomorphology along the Offshore Northern San Andreas Fault, Tomales Point to Fort Ross, California”. *Bull. Seismol. Soc. Am.* 109, pp. 833–854. DOI: 10.1785/0120180158 (See p. 142).
- Kajiura, K. (1963). “The leading wave of a tsunami”. *Bull. Earthquake Res. Inst.* 41, pp. 535–571 (See p. 139).
- Kavaturu, M., A. Shukla, & A. J. Rosakis (1998). “Intersonic crack propagation along interfaces: Experimental observations and analysis”. *Exp. Mech.* 38 (3), pp. 218–225. DOI: 10.1007/BF02325746 (See p. 83).
- King, G., Y. Klinger, D. Bowman, & P. Tapponnier (2005). “Slip partitioned surface breaks for the 2001 Kokoxili earthquake, China ( $M_w$  7.8)”. *Bull. Seism. Soc. Am.* 95, pp. 731–738. DOI: 10.1785/0120040101 (See pp. 129, 131).
- Klinger, Y., X. Xu, P. Tapponnier, J. Van der Woerd, C. Lasserre, & G. King (2005). “High-resolution satellite imagery mapping of the surface rupture and slip distribution of the  $M_w \sim 7.8$ , 14 November 2001 Kokoxili earthquake, Kunlun fault, northern Tibet, China”. *Bull. Seism. Soc. Am.* 95, pp. 1970–1987. DOI: 10.1785/0120040233 (See pp. 129–130).
- Klinger, Y., R. Michel, & G. C. P. King (2006). “Evidence for an earthquake barrier model from  $M_w \sim 7.8$  Kokoxili (Tibet) earthquake slip-distribution”. *Earth Planet. Sc. Lett.* 242, pp. 354–364. DOI: 10.1016/j.epsl.2005.12.003 (See p. 129).
- Klinger, Y. et al. (2018). “Earthquake damage patterns resolve complex rupture processes”. *Geophys. Res. Lett.* DOI: 10.1029/2018GL078842 (See p. 75).
- Kostrov, B. V. (1964). “Selfsimilar problems of propagation of shear cracks”. *J. Appl. Math. Mech.-USS.* 28, pp. 1077–1087. DOI: 10.1016/0021-8928(64)90010-3 (See pp. 15–17, 21).
- Kostrov, B. (1966). “Unsteady propagation of longitudinal shear cracks”. *J. Appl. Math. Mech.-USS.* 30, pp. 1241–1248. DOI: 10.1016/0021-8928(66)90087-6 (See p. 15).
- Koto, B. (1893). “On the cause of the great earthquake in central Japan, 1891”. *J. Coll. Sci. Imp. Univ. Tokyo* 5 (See p. 14).
- Kristek, J., P. Moczo, & R. J. Archuleta (2002). “Efficient methods to simulate planar free surface in the 3D 4th-order staggered-grid finite-difference schemes”. *Stud. Geophys. Geod.* 46, pp. 355–381. DOI: 0.1023/A:1019866422821 (See p. 54).
- Lambros, J. & A. J. Rosakis (1995). “Shear Dominated Transonic Interfacial Crack-Growth In A Bimaterial .1. Experimental-Observations”. *J. Mech. Phys. Solids* 43 (2), pp. 169–188. DOI: 10.1016/0022-5096(94)00071-C (See p. 83).
- Lansing, D. L. (1966). *The displacements in an elastic half-space due to a moving concentrated normal load*. Tech. rep. NASA (See pp. 52, 62).
- Lasserre, C., G. Peltzer, F. Crampé, Y. Klinger, J. Van der Woerd, & P. Tapponnier (2005). “Coseismic deformation of the 2001  $M_w = 7.8$  Kokoxili earthquake in Tibet, measured by synthetic aperture radar interferometry”. *J. Geophys. Res.* 110 (B12408). DOI: 10.1029/2004JB003500 (See p. 129).

- Lee, W. H. K., H. Kanamori, P. C. Jennings, & C. Kisslinger (2002). "International Handbook of Earthquake and Engineering Seismology-Part A". Elsevier Science & Technology Books (See p. 13).
- Lin, A., B. Fu, J. Guo, Q. Zeng, G. Dang, W. He, & Y. Zhao (2002). "Co-seismic strike-slip and rupture length produced by the 2001  $M_s$  8.1 central Kunlun earthquake". *Science* 296, pp. 2015–2016. DOI: 10.1126/science.1070879 (See p. 129).
- Lin, A., M. Kikuchi, & B. Fu (2003). "Rupture segmentation and process of the 2001  $M_w$  7.8 central Kunlun, China, earthquake". *Bull. Seism. Soc. Am.* 93, pp. 2477–2492. DOI: 10.1785/0120020179 (See p. 129).
- Liu, C., Y. Huang, & A. J. Rosakis (1995). "Shear dominated transonic interfacial crack-growth in a bimaterial. 2. Asymptotic fields and favorable velocity regimes". *J. Mech. Phys. Solids* 43 (2), pp. 189–206. DOI: 10.1016/0022-5096(94)00072-D (See p. 30).
- Liu, C., A. Bizzarri, & S. Das (2014). "Progression of spontaneous in-plane shear faults from sub-Rayleigh to compressional wave rupture speeds". *J. Geophys. Res.* 119, pp. 8331–8345. DOI: 10.1002/2014JB011187 (See p. 72).
- Liu, Y. & N. Lapusta (2008). "Transition of mode II cracks from sub-Rayleigh to intersonic speeds in the presence of favorable heterogeneity". *J. Mech. Phys. Solids* 56, pp. 25–50. DOI: 10.1016/j.jmps.2007.06.005 (See pp. 47, 72, 121).
- Lu, X. (2009). "Combined experimental and numerical study of spontaneous dynamic rupture on frictional interfaces". PhD thesis. California Institute of Technology (See pp. 87, 120).
- Lu, X., N. Lapusta, & A. J. Rosakis (2007). "Pulse-like and crack-like ruptures in experiments mimicking crustal earthquakes". *P. Natl. Acad. Sci. USA* 104, pp. 18931–18936. DOI: 10.1073/pnas.0704268104 (See pp. 87, 121).
- Lu, X., N. Lapusta, & A. Rosakis (2010). "Pulse-like and crack-like dynamic shear ruptures on frictional interfaces: experimental evidence, numerical modeling, and implications". *Int. J. Fract.* Pp. 1–13. DOI: 10.1007/s10704-010-9479-4 (See p. 87).
- Lykotrafitis, G. & A. J. Rosakis (2006a). "Dynamic sliding of frictionally held bimaterial interfaces subjected to impact shear loading". *Proc. R. Soc. A* 462 (2074), pp. 2997–3026. DOI: 10.1098/rspa.2006.1703 (See p. 87).
- (2006b). "Sliding along frictionally held incoherent interfaces in homogeneous systems subjected to dynamic shear loading: a photoelastic study". *Int. J. Fract.* 140 (1-4), pp. 213–233. DOI: 10.1007/s10704-005-6103-0 (See p. 87).
- Lykotrafitis, G., A. J. Rosakis, & G. Ravichandran (2006). "Particle velocimetry and photoelasticity applied to the study of dynamic sliding along frictionally-held bimaterial interfaces: Techniques and feasibility". *Exp. Mech.* 46 (2), pp. 205–216. DOI: 10.1007/s11340-006-6418-4 (See p. 87).
- Lyon, M. & O. P. Bruno (2010). "High-order unconditionally stable FC-AD solvers for general smooth domains II. Elliptic, parabolic and hyperbolic PDEs; theoretical considerations". *J. Comput. Phys.* 229, pp. 3358–3381. DOI: 10.1016/j.jcp.2010.01.006 (See p. 139).
- Madariaga, R. (2012). "The birth of forward models: From Coulomb criterion to cohesive force laws". *The mechanics of faulting: From laboratory to earthquakes*. Ed. by A. Bizzarri & H. S. Bhat. Research Signpost (See p. 15).
- Mai, P. M. (2019). "Supershear tsunami disaster". *Nat. Geosci.* 12, p. 150. DOI: 10.1038/s41561-019-0308-8 (See p. 137).
- Marcinkovich, C. & K. B. Olsen (2003). "On the implementation of perfectly matched layers in a three-dimensional fourth-order velocity-stress finite difference scheme". *J. Geophys. Res.* 108, 2276. DOI: 10.1029/2002JB002235 (See p. 55).
- Marone, C. (1998). "Laboratory-derived friction laws and their application to seismic faulting". *Ann. Rev. Earth Planet. Sci.* 26, pp. 643–696. DOI: 10.1146/annurev.earth.26.1.643 (See p. 15).

- Mello, M., H. S. Bhat, A. J. Rosakis, & H. Kanamori (2010). “Identifying the unique ground motion signatures of supershear earthquakes: Theory and experiments”. *Tectonophysics* 493, pp. 297–326. DOI: 10.1016/j.tecto.2010.07.003 (See pp. 36, 93, 103, 117, 120–121, 123).
- (2014). “Reproducing The Supershear Portion Of The 2002 Denali Earthquake Rupture In Laboratory”. *Earth Planet. Sc. Lett.* 387, pp. 89–96. DOI: 10.1016/j.epsl.2013.11.030 (See pp. 19, 48–49, 72, 87, 128).
- Mello, M., H. S. Bhat, & A. J. Rosakis (2016). “Spatiotemporal properties of sub-Rayleigh and supershear rupture velocity fields : Theory and Experiments”. *J. Mech. Phys. Solids* 93, pp. 153–181. DOI: 10.1016/j.jmps.2016.02.031 (See p. 19).
- Michell, J. (1760). “Conjectures concerning the cause, and observations upon the phaenomena of earthquakes; particularly of that great earthquake of the first of November, 1755, which proved so fatal to the city of Lisbon, and whose effects were felt as far as Africa, and more or less throughout almost all Europe”. *Phil. Trans. Roy. Soc. London* 51. DOI: 10.1098/rstl.1759.0057 (See p. 12).
- Muhari, A., F. Imamura, T. Arikawa, A. R. Hakim, & B. Afriyanto (2018). “Solving the Puzzle of the September 2018 Palu, Indonesia, Tsunami Mystery: Clues from the Tsunami Waveform and the Initial Field Survey Data”. *J. Disaster Res.* 13 Sci. Comm. sc20181108. DOI: 10.20965/jdr.2018.sc20181108 (See p. 137).
- Muskhelishvili, N. I. (1953). “Singular integral equations: Boundary problems of function theory and their application to mathematical physics. Translation from Russian edited by J. R. M. Radok”. P. Nordoff, Groningen (See pp. 31, 41).
- Nielsen, S. B. & J. M. Carlson (2000). “Rupture pulse characterization: self-healing, self-similar, expanding solutions in a continuum model of fault dynamics”. *Bull. Seism. Soc. Am.* 90, pp. 1480–1497. DOI: 10.1785/0120000021 (See p. 120).
- Obrezanova, O. & J. R. Willis (2003). “Stability of intersonic shear crack propagation”. *J. Mech. Phys. Solids* 51 (11-12), pp. 1957–1970 (See pp. 21, 53).
- Ohnaka, M. & L.-f. Shen (1999). “Scaling of the shear rupture process from nucleation to dynamic propagation: Implications of geometric irregularity of the rupturing surfaces”. *J. Geophys. Res.* 104, pp. 817–844. DOI: 10.1029/1998JB900007 (See p. 115).
- Okubo, K., H. S. Bhat, E. Rougier, S. Marty, A. Schubnel, Z. Lei, E. E. Knight, & Y. Klinger (2019). “Dynamics, radiation and overall energy budget of earthquake rupture with coseismic off-fault damage”. *J. Geophys. Res.* 124. DOI: 10.1029/2019JB017304 (See pp. 75–76).
- Okubo, P. G. & J. H. Dieterich (1984). “Effects of physical fault properties on frictional instabilities produced on simulated faults”. *J. Geophys. Res.* 89, pp. 5817–5827. DOI: 10.1029/JB089iB07p05817 (See p. 115).
- Oral, E., H. Weng, & J. P. Ampuero (2020). “Does a Damaged-Fault Zone Mitigate the Near-Field Impact of Supershear Earthquakes?—Application to the 2018 7.5 Palu, Indonesia, Earthquake”. *Geophys. Res. Lett.* 47, e2019GL085649. DOI: 10.1029/2019GL085649 (See p. 137).
- Palmer, A. C. & J. R. Rice (1973). “Growth Of Slip Surfaces In Progressive Failure Of Over-Consolidated Clay”. *Proc. R. Soc. Lond. Ser-A* 332 (1591), pp. 527–548. DOI: 10.1098/rspa.1973.0040 (See pp. 31, 33).
- Passelègue, F. X., A. Schubnel, S. Nielsen, H. S. Bhat, & R. Madariaga (2013). “From Sub-Rayleigh to Supershear Ruptures During Stick-Slip Experiments on Crustal Rocks”. *Science* 340, pp. 1208–1211. DOI: 10.1126/science.1235637 (See pp. 18–19).
- Pedlosky, J. (2013). “Geophysical Fluid Dynamics”. Springer Science & Business Media (See p. 139).

- Poliakov, A. N. B., R. Dmowska, & J. R. Rice (2002). “Dynamic shear rupture interactions with fault bends and off-axis secondary faulting”. *J. Geophys. Res.* 107. DOI: 10.1029/2001JB000572 (See p. 40).
- Pugh, D. & P. Woodworth (2014). “Sea-level science: understanding tides, surges, tsunamis and mean sea-level changes”. Cambridge University Press (See p. 137).
- Ratchkovski, N. A. (2003). “Change in stress directions along the central Denali fault, Alaska after the 2002 earthquake sequence”. *Geophys. Res. Lett.* 30, p. 2017. DOI: 10.1029/2003GL017905 (See p. 131).
- Rice, J. R., C. G. Sammis, & R. Parsons (2005). “Off-fault secondary failure induced by a dynamic slip pulse”. *Bull. Seism. Soc. Am.* 95, pp. 109–134. DOI: 10.1785/0120030166 (See pp. 40, 43–44, 51, 55, 59, 63, 71, 122, 130).
- Robinson, D. P., S. Das, & A. B. Watts (2006a). “Earthquake rupture stalled by a subducting fracture zone”. *Science* 312, pp. 1203–1205. DOI: 10.1126/science.1125771 (See pp. 116, 129).
- Robinson, D. P., C. Brough, & S. Das (2006b). “The  $M_w$  7.8, 2001 Kunlunshan earthquake: Extreme rupture speed variability and effect of fault geometry”. *J. Geophys. Res.* 111. DOI: 10.1029/2005JB004137 (See pp. 133, 136).
- Röbke, B. & A. Vött (2017). “The tsunami phenomenon”. *Progress in Oceanography* 159, pp. 296–322. DOI: 10.1016/j.poccean.2017.09.003 (See p. 137).
- Romanet, P. (2017). “Fast algorithms to model quasi-dynamic earthquake cycles in complex fault networks”. PhD thesis. Institut de Physique du Globe de Paris (See p. 14).
- Rosakis, A. J. (2002). “Intersonic shear cracks and fault ruptures”. *Adv. Phys.* 51 (4), pp. 1189–1257. DOI: 10.1080/00018730210122328 (See pp. 21, 77, 117, 119, 123).
- Rosakis, A. J., O. Samudrala, R. P. Singh, & A. Shukla (1998). “Intersonic crack propagation in bimaterial systems”. *J. Mech. Phys. Solids* 46 (10), pp. 1789–1813. DOI: 10.1016/S0022-5096(98)00036-2 (See p. 83).
- Rosakis, A. J., O. Samudrala, & D. Coker (1999). “Cracks faster than the shear wave speed”. *Science* 284 (5418), pp. 1337–1340. DOI: 10.1126/science.284.5418.1337 (See pp. 18, 83).
- Rosakis, A. J., H. Kanamori, & K. W. Xia (2006). “Laboratory earthquakes”. *Int. J. Fract.* 138 (1-4), pp. 211–218. DOI: 10.1007/s10704-006-0030-6 (See p. 86).
- Rosakis, A. J., K. W. Xia, G. Lykotrafitis, & H. Kanamori (2007). “Dynamic shear rupture in frictional interfaces: Speeds, Directionality and Modes”. *Treatise on Geophysics*. Ed. by G. Schubert. Vol. 4. Elsevier, pp. 153–192. DOI: 10.1016/B978-0-444-53802-4.00072-5 (See pp. 35, 86, 117, 119–121, 123).
- Rougier, E., E. E. Knight, Z. Lei, & A. Munjiza (2016). *HOSS.edu2.x (Hybrid Optimization Software Suite - Educational Version, Second Generation)* (See p. 75).
- Rubino, V., A. J. Rosakis, & N. Lapusta (2017). “Understanding dynamic friction through spontaneously evolving laboratory earthquakes”. *Nat. Commun.* 8. DOI: 10.1038/ncomms15991 (See p. 87).
- Samudrala, O. & A. J. Rosakis (2003). “Effect of loading and geometry on the subsonic/intersonic transition of a bimaterial interface crack”. *Eng. Fract. Mech.* 70 (2), pp. 309–337. DOI: 10.1016/S0013-7944(02)00025-5 (See p. 83).
- Samudrala, O., Y. Huang, & A. J. Rosakis (2002a). “Subsonic and intersonic mode II crack propagation with a rate-dependent cohesive zone”. *J. Mech. Phys. Solids* 50 (6), pp. 1231–1268. DOI: 10.1016/S0022-5096(01)00129-6 (See pp. 21, 32, 35).
- (2002b). “Subsonic and intersonic shear rupture of weak planes with a velocity weakening cohesive zone”. *J. Geophys. Res.* 107. DOI: 10.1029/2001JB000460 (See pp. 21, 32, 35, 122).
- Sassa, S. & T. Takagawa (2019). “Liquefied gravity flow-induced tsunami: first evidence and comparison from the 2018 Indonesia Sulawesi earthquake and tsunami

- disasters". *Landslides* 16, pp. 195–200. DOI: 10.1007/s10346-018-1114-x (See p. 137).
- Schubnel, A., S. Nielsen, J. Taddeucci, S. Vinciguerra, & S. Rao (2011). "Photo-acoustic study of subshear and supershear ruptures in the laboratory". *Earth Planet. Sc. Lett.* 308, pp. 424–432. DOI: 10.1016/j.epsl.2011.06.013 (See p. 114).
- Segall, P. (2010). "Earthquake and volcano deformation". Princeton University Press (See pp. 13–14).
- Sibson, R. H. (1985). "Stopping of earthquake ruptures at dilational fault jogs". *Nature* 316, pp. 248–251. DOI: 10.1038/316248a0 (See p. 116).
- Singh, R. P., J. Lambros, A. Shukla, & A. J. Rosakis (1997). "Investigation of the mechanics of intersonic crack propagation along a bimaterial interface using coherent gradient sensing and photoelasticity". *Proc. R. Soc. Lond. A* 453 (1967), pp. 2649–2667. DOI: 10.1098/rspa.1997.0141 (See p. 83).
- Socquet, A., J. Hollingsworth, E. Pathier, & M. Bouchon (2019). "Evidence of supershear during the 2018 magnitude 7.5 Palu earthquake from space geodesy". *Nat. Geosci.* 12, pp. 192–199. DOI: 10.1038/s41561-018-0296-0 (See pp. 19, 128, 136–137).
- Solares, J. M. M. & A. L. Arroyo (2004). "The great historical 1755 earthquake. Effects and damage in Spain". *J. Seismology* 8, pp. 275–294. DOI: 10.1023/B:JOSE.0000021365.94606.03 (See p. 11).
- Somerville, P. G., N. F. Smith, R. W. Graves, & N. A. Abrahamson (1997). "Modification of empirical strong ground motion attenuation relations to include the amplitude and duration effects of rupture directivity". *Seismol. Res. Lett.* 68, pp. 199–222. DOI: 10.1785/gssr1.68.1.199 (See p. 51).
- Spudich, P. & E. Cranswick (1984). "Direct observation of rupture propagation during the 1979 Imperial Valley earthquake using a short baseline accelerometer array". *Bull. Seism. Soc. Am.* 74, pp. 2083–2114 (See p. 18).
- Spudich, P. & M. Guatteri (2004). "The effect of bandwidth limitations on the inference of earthquake slip-weakening distance from seismograms". *Bull. Seism. Soc. Am.* 94, pp. 2028–2036. DOI: 10.1785/0120030104 (See p. 56).
- Steketee, J. A. (1958). "Some geophysical applications of the elasticity theory of dislocations". *Can. J. Phys.* 36, pp. 1168–1198. DOI: 10.1139/p58-123 (See p. 14).
- Svetlizky, I. & J. Fineberg (2014). "Classical shear cracks drive the onset of dry frictional motion". *Nature* 509, pp. 205–208. DOI: 10.1038/nature13202 (See p. 74).
- Syamsidik, Benazir, M. Umar, G. Margaglio, & A. Fitrayansyah (2019). "Post-tsunami survey of the 28 September 2018 tsunami near Palu Bay in Central Sulawesi, Indonesia: Impacts and challenges to coastal communities". *Int. J. Disaster Risk Reduc.* 38, p. 101229. DOI: 10.1016/j.ijdrr.2019.101229 (See p. 137).
- Synolakis, C. E. & E. A. Okal (2005). "1992–2002: perspective on a decade of post-tsunami surveys". *Tsunamis*. Springer, pp. 1–29 (See p. 137).
- Tanioka, Y. & K. Satake (1996). "Tsunami generation by horizontal displacement of ocean bottom". *Geophys. Res. Lett.* 23, pp. 861–864. DOI: 10.1029/96GL00736 (See p. 139).
- Thomas, M. Y., H. S. Bhat, & Y. Klinger (2017). "Effect of Brittle off-fault Damage on Earthquake Rupture Dynamics". *Fault Zone Dynamic Processes : Evolution of Fault Properties During Seismic Rupture, Geophysical Monograph 227*. Ed. by M. Y. Thomas, H. S. Bhat, & T. M. Mitchell. American Geophysical Union (AGU), pp. 255–280. DOI: 10.1002/9781119156895.ch14 (See p. 75).
- Thomas, M. Y. & H. S. Bhat (2018). "Dynamic evolution of off-fault medium during an earthquake: a micromechanics based model". *Geophys. J. Int.* 214, pp. 1267–1280. DOI: 10.1093/gji/ggy129 (See pp. 75–77).
- Tocheport, A., L. Rivera, & J. Van der Woerd (2006). "A Study of the 14 November 2001 Kokoxili earthquake: History and geometry of the rupture from teleseismic

- data and field observations". *Bull. Seism. Soc. Am.* 96, pp. 1729–1741. DOI: 10.1785/0120050200 (See p. 129).
- Udias, A. (1999). "Principles of seismology". Cambridge University Press (See p. 11).
- Udias, A., R. Madariaga, E. Buforn, et al. (2014). "Source Mechanisms of Earthquakes: Theory and Practice". Cambridge University Press (See p. 11).
- Ulrich, T., S. Vater, E. H. Madden, J. Behrens, Y. van Dinther, I. Van Zelst, E. J. Fielding, C. Liang, & A.-A. Gabriel (2019). "Coupled, physics-based modeling reveals earthquake displacements are critical to the 2018 Palu, Sulawesi Tsunami". *Pure Appl. Geophys.* 176, pp. 4069–4109. DOI: 10.1007/s00024-019-02290-5 (See pp. 129, 137).
- Vallée, M., M. Landès, N. M. Shapiro, & Y. Klinger (2008). "The 14 November 2001 Kokoxili (Tibet) earthquake: High-frequency seismic radiation originating from the transitions between sub-Rayleigh and supershear rupture velocity regimes". *J. Geophys. Res.* 113. DOI: 10.1029/2007JB005520 (See pp. 133, 135–136).
- Vallée, M. & E. M. Dunham (2012). "Observation of far-field Mach waves generated by the 2001 Kokoxili supershear earthquake". *Geophys. Res. Lett.* 39. DOI: 10.1029/2011GL050725 (See pp. 19, 136).
- Weertman, J (1969). "Dislocation motion on an interface with friction that is dependent on sliding velocity". *J. Geophys. Res.* 74, pp. 6617–6622. DOI: 10.1029/JB074i027p06617 (See p. 16).
- Williams, M. L. (1957). "On the stress distribution at the base of a stationary crack". *J. Appl. Mech.* 24, pp. 109–114. DOI: 10.1115/1.3640470 (See p. 73).
- Wong, T.-f. (1982). "Shear fracture energy of Westerly granite from post-failure behavior". *J. Geophys. Res.* 87, pp. 990–1000. DOI: 10.1029/JB087iB02p00990 (See p. 115).
- Wu, F. T., K. Thomson, & H. Kuenzler (1972). "Stick-slip propagation velocity and seismic source mechanism". *Bull. Seism. Soc. Am.* 62, pp. 1621–1628 (See p. 16).
- Xia, K. W., A. J. Rosakis, & H. Kanamori (2004). "Laboratory earthquakes: The sub-Rayleigh-to-supershear rupture transition". *Science* 303 (5665), pp. 1859–1861. DOI: 10.1007/s10704-006-0030-6 (See pp. 18, 83, 86, 117, 119–121).
- Xia, K. W., A. J. Rosakis, H. Kanamori, & J. R. Rice (2005a). "Laboratory earthquakes along inhomogeneous faults: Directionality and supershear". *Science* 308 (5722), pp. 681–684. DOI: 10.1126/science.1108193 (See p. 86).
- Xia, K. W., A. J. Rosakis, & H. Kanamori (2005b). "Supershear and sub-Rayleigh to supershear transition observed in laboratory earthquake experiments". *Exp. Tech.* 29 (3), pp. 63–66. DOI: 10.1111/j.1747-1567.2005.tb00220.x (See pp. 83, 86).
- Xu, X., W. Chen, W. Ma, G. Yu, & G. Chen (2002). "Surface rupture of the Kunlunshan earthquake ( $M_s$  8.1), northern Tibetan plateau, China". *Seismol. Res. Lett.* 73, pp. 884–892. DOI: 10.1785/gssr1.73.6.884 (See p. 129).
- Yue, H., T. Lay, J. T. Freymueller, K. Ding, L. Rivera, N. A. Ruppert, & K. D. Koper (2013). "Supershear rupture of the 5 January 2013 Craig, Alaska (Mw 7.5) earthquake". *J. Geophys. Res.* 118, pp. 5903–5919. DOI: 10.1002/2013JB010594 (See pp. 18, 133–135).
- Zhan, Z., D. V. Helmberger, H. Kanamori, & P. M. Shearer (2014). "Supershear rupture in a Mw 6.7 aftershock of the 2013 Sea of Okhotsk earthquake". *Science* 345, pp. 204–207. DOI: 10.1126/science.1252717 (See p. 18).